

Formulation of electrostrictive materials for vibrational energy recovery and development of high sensitivity stress sensors

Mickaël Pruvost

▶ **To cite this version:**

Mickaël Pruvost. Formulation of electrostrictive materials for vibrational energy recovery and development of high sensitivity stress sensors. Chemical Physics [physics.chem-ph]. Université Paris sciences et lettres, 2018. English. NNT : 2018PSLET027 . tel-02506398

HAL Id: tel-02506398
https://pastel.hal.science/tel-02506398

Submitted on 12 Mar 2020

HAL is a multi-disciplinary open access archive for the deposit and dissemination of scientific research documents, whether they are published or not. The documents may come from teaching and research institutions in France or abroad, or from public or private research centers.

L'archive ouverte pluridisciplinaire **HAL**, est destinée au dépôt et à la diffusion de documents scientifiques de niveau recherche, publiés ou non, émanant des établissements d'enseignement et de recherche français ou étrangers, des laboratoires publics ou privés.

THÈSE DE DOCTORAT

de l'Université de recherche Paris Sciences et Lettres
PSL Research University

Préparée à l'Ecole Supérieure de Physique et de Chimie Industrielles de la Ville de Paris – ESPCI Paris

Formulation of electrostrictive materials for vibrational energy recovery and development of high sensitivity stress sensors

Ecole doctorale n°397
PHYSIQUE ET CHIMIE DES MATERIAUX

Spécialité : PHYSICO-CHIMIE

Soutenue par Mickaël PRUVOST
le 19 octobre 2018

Dirigée par **Annie Colin**
Cécile Monteux

COMPOSITION DU JURY :

M. LALLART Mickaël
INSA Lyon, Rapporteur

M. BROCHON Cyril
ENSCBP, Rapporteur

M. BAUMBERGER Tristan
Sorbonne Université, Président du Jury

M. CRETON Costantino
ESPCI Paris, Examinateur

M. NICU Liviu
LAAS, Examinateur

M. POULIN Philippe
CRPP, Examinateur

Mme. COLIN Annie
ESPCI Paris, Directrice de thèse

Mme. MONTEUX Cécile
ESPCI Paris, Directrice de thèse

ESPCI PARIS
EDUCATION SCIENCE INNOVATION

PSL
RESEARCH UNIVERSITY PARIS

Laboratoire “Chimie Biologie Innovations”

Equipe MIE

ESPCI Paris, 10 rue Vauquelin

75005, Paris

“As people find more ways to incorporate these inexpensive, flexible and customizable devices into their lives, the computers themselves will gradually ‘disappear’ into the fabric of our lives.”

"The Disappearing Computer" by Bill Gates, 2003

Introduction

Innovations are expected to emerge from soft matter when its development is done at the interface between several domains. In particular, electrical properties joined with soft matter allowed the realization of a new class of materials: the electroactive polymers. Their interest has been put forward in many industrial fields (robotic, energy, eHealth, etc.) where sensors, energy harvesters, haptic technologies, actuators are required. All these applications involve advances in the synthesis of dielectric materials meeting the electric, mechanical, cost, and scalability supplies. Definitely, the emergence of successful materials will be based on breakthroughs in their formulation and soft matter offers a range of tools to do so.

In this Manuscript, we develop new formulation paths for improving the electromechanical properties of electrostrictive materials, a class of electroactive materials. Until now, electrostrictive materials suffer from limited dielectric properties: high dielectric losses, high elastic modulus, and low dielectric constant, leading to poor assets for practical applications. We proposed to develop composites with emulsion approaches and conductive fillers. The emulsion versatility combined with the superlative properties of reduced graphene oxides and carbon black lead to tunable soft materials. We provide a particular interest in formulation parameters for meeting the electrical and mechanical requirements.

Research efforts, in the integration of our electrostrictive materials into real-life applications, have been ensured to show their practical potential. First, the use of vibrating structures have been used to characterize the electromechanical performances of our materials and proving the possibility of harvesting mechanical energy with them. Then, we succeed in using our electrostrictive materials as highly sensitive pressure sensors. The materials are successfully employed to assess the pulse frequency and to measure human blood pressure.

The following outline illustrates our scientific approach, starting from the formulation then the characterization and finally the integration into concrete applications.

Chapter 1: General introduction.

The first Chapter lays down the framework of the study, dealing with state of the art of electroactive polymers in mechanical energy harvesting and sensing technologies. We introduce general concepts focusing on the most relevant mechanisms of energy harvesting and sensing. Finally, we present the paths we decided to follow to create new electroactive polymers based on electrostrictive effects.

Chapter 2: Materials and methods for the realization of electrostrictive composites and their characterization.

The second Chapter is devoted to the impedance measurements and material synthesis. We developed characterization methods and setups for the measurement of the electrostrictive coefficients and the power recovering of dielectric materials. Finally, we expose two new routes to synthesize electroactive composites via emulsions templating effects.

Chapter 3: Electrostrictive response and piezoresistivity of r-GO composites based on an (O/W) emulsion template.

In the third Chapter, we report the preparation of polymer-reduced graphene oxide (rGO) composites. Using an O/W emulsion road, we introduce conductive nanoparticles into polymer matrices that enhance the electronic properties of the material. We study the dielectric properties and the electrostriction coefficients for different filler concentration.

Chapter 4: Microporous electrostrictive materials for vibrational energy harvesting.

This Chapter deals with the realization of microporous electrostrictive composites with improved properties for vibrational energy harvesting. These systems are made of carbon black particles dispersed in a porous PDMS matrix thanks to an inverted emulsion templating. We succeeded in evaluating the energy scavenging abilities of these composites.

Chapter 5: Integration of electrostrictive materials in a cantilever device.

In this part, electrostrictive porous are integrated into a real-life application of mechanical energy harvesting. We produce a mechanical energy harvester with a cantilever approach. The energy scavenging abilities of the cantilever is discussed.

Chapter 6: Highly sensitive flexible pressure sensors based on electrostrictive materials.

In this Chapter, we presented highly sensitive flexible pressure and strain sensors based on electrostrictive materials. We report the realization of a capacitive pressure sensor tested over thousands of cycles. Then, we demonstrate the possibility of continuously recording arterial pulse waves in a noninvasive way. The pressure sensor is successfully employed to assess the pulse frequency and to measure systolic and diastolic peaks.

Conclusion and perspectives.

Finally, we present some conclusions and perspectives which are rooted in the context of this manuscript.

Contents

Chapter 1: General introduction.

1 Introduction to electroactive polymers: 14
2 The energy harvesting: 15
2.1 Energy harvesting for powering the Internet of things: 15
2.2 Comparison between energy sources: 18
2.3 Mechanical energy harvesting: 19
2.3.1 Piezoelectric harvester: 22
2.3.2 Triboelectricity: 24
2.3.3 Variable capacitors: 26
3 Electroactive polymers for mechanical energy harvesting: 31
3.1.1 Piezoelectric polymers: 32
3.1.2 Electrostrictive polymers: 33
3.1.3 Conversion roads: 37
3.1.4 Performance parameters of electrostrictive materials for mechanical energy harvesting: 38
4 Electroactive polymers for sensor technologies: 45
4.1 Future of sensing : 45
4.2 Transduction methods: 45
4.2.1 Piezoresistivity: 45
4.2.2 Piezocapacity: 48
4.2.3 Our strategy: 52

Chapter 2: Materials and methods for the realization of electrostrictive composites and their characterization.

1.1 Impedance measurements: 61
1.1.1 General considerations on dielectric materials: 61
1.1.2 Impedance: 62
1.1.3 Compensation procedure: 63
1.1.4 Relation between capacitance, resistance and conductivity, permittivity: 65
1.1.5 Dielectric loss: 67
1.1.6 Practical procedure for measuring ε', σ and tan δ as a function of frequency: 67
1.2 Determination of electromechanical performances: 68
1.2.1 Measurement and calculation of the intrinsic electrostrictive modulus in static configurations: 68
1.2.2 Vibrational energy harvesting setup: 69
1.3 Formulation of the emulsion based electrostrictive composites: 70
1.3.1 Oil in water emulsion: 70
1.3.2 Water in oil emulsion: 71
1.4 Scanning Electron Microscopy (SEM) analysis: 72
1.5 Sensibility measurements: 72

Chapter 3: Electrostrictive response and piezoresistivity of r-GO composites based on an (O/W) emulsion template.

1 Introduction: 76
1.1 Percolation theory: 77
1.1.1 Evolution of the conductivity: 77
1.1.2 Evolution of the permittivity: 77
1.1.3 Variable permittivity (electrostriction): 78
1.2 Interest of reduced graphene oxide flakes: 79
1.2.1 Description and properties: 79
1.2.2 Self assemblage of the GO flakes: a way for decreasing electrical losses: 80

1.3 Strategies to disperse conductive fillers: 81
1.4 Our approach: 82
1.4.1 Reduction paths: 82
1.4.2 Dispersion process: 82
2 Results and discussion: 84
2.1 Microscopy and emulsion distribution: 84
2.2 Dielectric measurements: 85
2.2.1 Influence of the reduction on the dielectric properties: 85
2.2.2 Dielectric response as a function of the filler concentration: 86
2.2.3 Comparison with CNT/PDMS composites: 87
2.2.4 Dielectric response as a function of the electrical frequency: 88
2.2.5 Influence of the r-GO concentration on the electrostriction modulus: 90
2.2.6 Piezoresistivity: 91

Chapter 4: Microporous electrostrictive materials for vibrational energy harvesting.

1 Introduction: 98
2 Our strategy: 98
3 Carbon black/PDMS composites based on a W/O emulsion template: 99
3.1 Carbon black as conductive fillers: 99
3.2 Dispersion and coating processes: 100
3.2.1 Water solubilization of carbon black: 100
3.2.2 Water in oil dispersion: 100
3.2.3 Emulsion coating and curing parameters: 101
3.3 Interest in porous structures: 102
3.4 Microscopic analysis: 102
3.5 Dielectric response: 103

3.5.1 Frequency dependence: 103
3.5.2 Influence of the formulation on dielectric properties: 105
3.5.3 Conclusion on dielectric response of porous BC/PDMS composites: 106
4 Interest of bilayer composites: 107
4.1 Bilayer composites: 107
4.2 Effective impedance of the bilayer composites: 107
4.3 Theoretical plots: 109
4.4 Experimental dielectric response of bilayer composites: 111
4.4.1 Isolating layer deposition: 111
4.4.2 Dielectric response of bilayer composites: 111
5 Harvesting mechanical energy with electrostrictive materials: 114
5.1 General considerations: 114
5.2 Theoretical calculation of the harvested current: 115
5.3 Expression of the harvested power: 116
5.4 Loss power and efficiency: 117
5.5 Dynamic measurement of electrostrictive modulus: 119
5.6 Energy harvesting results: 119
5.6.1 Figure of merit: 119
5.6.2 Power harvested: 120
5.6.3 Influence of the load resistance on the harvested current: 121
5.7 Discussion: 122
5.8 Conclusion: 123

Chapter 5: Integration of electrostrictive materials in a cantilever device.

1 Introduction: 129

2 Materials and methods: 129
2.1 Cantilever fabrication : 129
2.2 Static characterization: 130
2.3 Dynamic characterization: 131
3 Results and discussion: 132
3.1 Recovering power optimization: 132
3.2 Electrical balance: 136
3.2.1 Leak resistance: 136
3.2.2 Loss power: 136
4 Conclusion : 138
Chapter 6: Highly sensitive flexible pressure sensors based on electrostrictive materials.
1 Introduction: 143
2 Materials and methods: 145
3 Results: 148
4 Discussion and conclusion: 156
5 Outlooks: 157
Conclusion and perspectives.

1. General introduction

Summary:

This first chapter is devoted to the state of art of electroactive polymers in the context of mechanical energy harvesting and sensing. We present general concepts and orders of magnitude. In the two main sections, we also provide a particular interest in the most relevant mechanisms of energy harvesting and sensing, focusing on the use of electroactive polymers. Finally, we will detail our approach based on the use of electrostrictive materials.

1 Introduction to electroactive polymers:

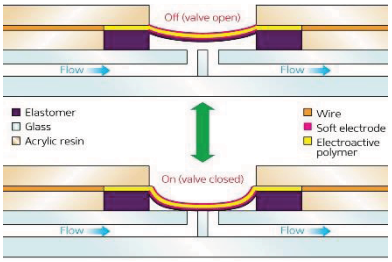
The need to replace conventional materials (wood, ceramics, metals, etc.) with new materials has become a major industrial issue. The hopes placed in these new materials are immense because they will be closely linked to future technological developments and their novel properties will be a response to contemporary issues. Self-healing polymers [1], self-cleaning glass [2] or, more recently, vitrimers [3] (polymers combining the properties of glass and plastics) are few examples of applications that have been made possible through research in materials science.

In this mosaic of new materials, an active search is taking place in the field of electroactive polymers. The electroactive polymers (EAPS) are a class of polymers with a strong coupling between electrical and mechanical properties. As a consequence when a voltage is applied to them, their shape is modified. Their similarities with biological tissues in terms of achievable strain make them good candidates for "artificial muscles" in the field of robotics, where large movement is often needed. Traditional mechanical actuators including motors, pneumatic and hydrolytic technologies have many restrictions in terms of weight, size and price (**FIG. 1.1**). As a contrast, EAPS present interesting inherent properties such as lightweight, easy to process, high compliance and are generally low cost (**FIG. 1.1** b)).

a)  b) 

FIG. 1.1 - Comparison between two equivalent walking robots. a) HEBI Robotics based on mechanical actuators b) Electroactive robot [4].

Numerous results have been achieved in the fields of microfluidics (pumps, valves [5], **FIG. 1.2** a)) and optics (variable lenses [6]) thanks to EAPS, making them close to commercial products. Even the NASA (**FIG. 1.2** b)) has developed and integrated EAPS for finely controlling the tension of membrane structures in space.

a) 

b) 

FIG. 1.2 - a) Microfluidic valve based on EAP b) NASA membrane structure.

All these applications use EAPS as actuators, meaning that electrical energy is furnished to materials for changing their shape, controlling thus a mechanism or a system. However, EAPS revealed possibilities in the reverse direction (generator mode) with two main applications: vibrational energy harvesting and pressure/strain sensors. Both fields have received less attention than actuation but could pave the way for the design of multifunctional materials integrating high sensitivity and energy autonomy. That is the reason why we have chosen to focus our research on designing new electroactive materials for these two promising specific applications.

This first chapter is devoted to the state of art of EAPS in the context of mechanical energy harvesting and sensing. In both sections, we will describe the most relevant mechanisms of energy harvesting and sensing, focusing on electroactive polymers. Finally, we will detail our approach based on the use of electrostrictive materials.

2 The energy harvesting:

Before we focus on electroactive polymers in the context of mechanical energy harvesting, let us take this section to recall what energy harvesting is and on which technologies it is based. We will evaluate the advantages and disadvantages of each technology and pay particular attention to their power generation capabilities.

2.1 Energy harvesting for powering the Internet of things:

The Internet of Things (IoT) is a new and fast-growing concept which aims at connecting everyday physical objects into the Internet or other networks without any human interaction [7–9]. “Things” or “objects” such as sensors, actuators, etc. would be able to send or receive information from environment and cooperate to reach common goals. Their development will significantly impact many fields of future day-day life. Energy management, e-health [10], predictive maintenance [11] or building automation [12] are just a few examples of field in which the IoT will play a prominent role (**FIG. 1.4**).

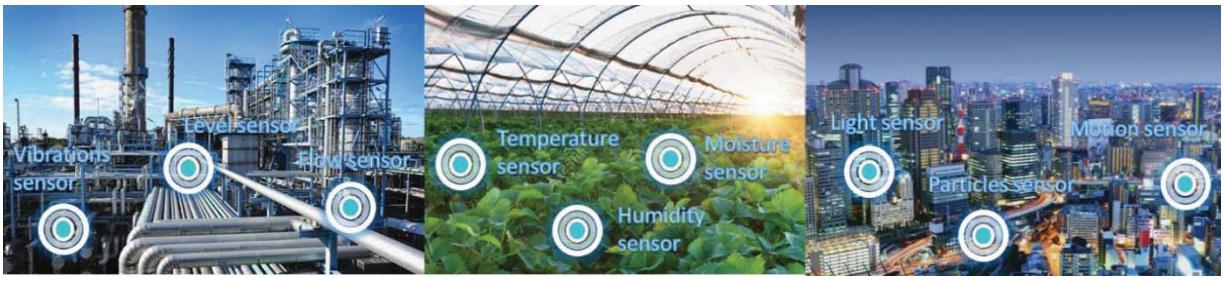


FIG. 1.4 - Examples of fields where IoT will play a prominent role.

In 2020, Cisco Company predicts that more than 50 billion objects will be connected to the world [13].

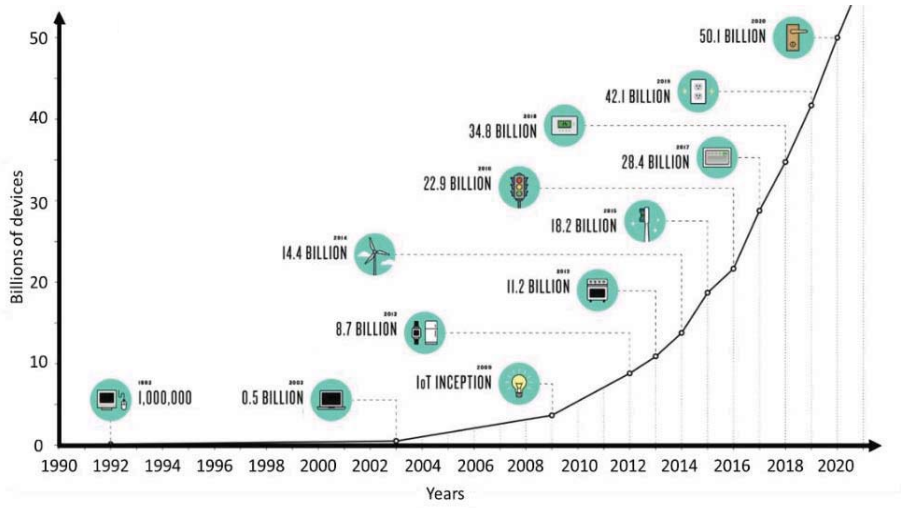


FIG. 1.5 - Evolution of The Internet of Things based on Cisco data [13].

Indeed, the IoT requires the usage of numerous wireless objects working in the network. Plus, these objects need to achieve several years of unattended operation. Thus, providing the electrical energy to run this huge number of wireless objects is a major concern and a limiting factor for the massive deployment of the Internet of Things. Use of batteries with limited lifetime is a severe constraint because replacing (i.e. alkaline pile) or recharging (i.e. lithium ion) batteries is a time and human cost for a large-scale network. Moreover, wires can be difficult to integrate and unsuited for example inside walls or on rotating parts. Two promising directions would address this energy challenge. The first would be to design ultra-low power hardware making batteries time viable. In the last decades, significant progress has been achieved in electronics technologies for the development of low-consumption and miniaturized sensors. For example, the Phoenix processor [14,15] has a sleep power consumption of only 30 pW and 200 nW in active mode. Yu-Shiang Lin and collaborators developed an ultra-low power temperature sensor which consumes only 220nW [16]. The second direction is the use of energy from the environment to make IoT devices self-powered, thus decreasing even eliminating their dependence on batteries. Extracting energy from the surrounding environment and converting it into electrical energy is known as “energy harvesting”. In fact, we live in a world where untapped energy sources surround us. These sources can come from human activities or derive from ambient energies such as chemical energy (chemistry, biochemistry), thermal energy (temperature gradients or variations), radiant energy (sun, infrared, RF) and mechanical energy (vibrations, deformations). Energy harvesting technologies are often based on well-established principles such as the photovoltaic, electrodynamic, and thermoelectric effects. Contrary to batteries, they are not time-dependent and can deliver power for long periods when ambient energy is available.

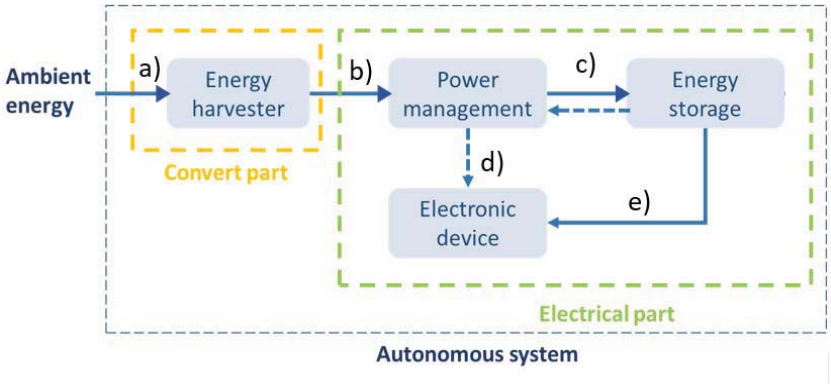


FIG. 1.6 - Blocks diagram of an autonomous system.

Energy harvesting from environment is not recent: people have been harvesting energy for centuries at large scale with windmills and nowadays with wind turbines. Thanks to progresses in electronic, small-scale applications are now conceivable. **FIG. 1.6**, presents the most common block diagram of an autonomous system, integrating a converting part (yellow box) and an electrical part (green box). The ambient energy is converting into electrical energy thanks to the harvester with a definite efficiency. The electrical energy can either power low consumption electronic systems directly (**FIG. 1.6**, d)), or charge an electrical storage reservoir (battery, capacitor, supercapacitor) that can be used to produce power pulses at time intervals (**FIG. 1.6**, e)). The harvesters aim at powering small devices, low consumer of electricity, they do not seek in any case to power large systems that require massive quantities of electricity (computer, electrical cars, etc.).

To set the orders of magnitude, **FIG. 1.7** gives an estimate of the powers required to make systems of everyday life working. The powers targeted by the harvesting energy are between the nW and the mW, typically enough to supply sensor-type electronic components. Power is directly linked to the frequency of operations that the small

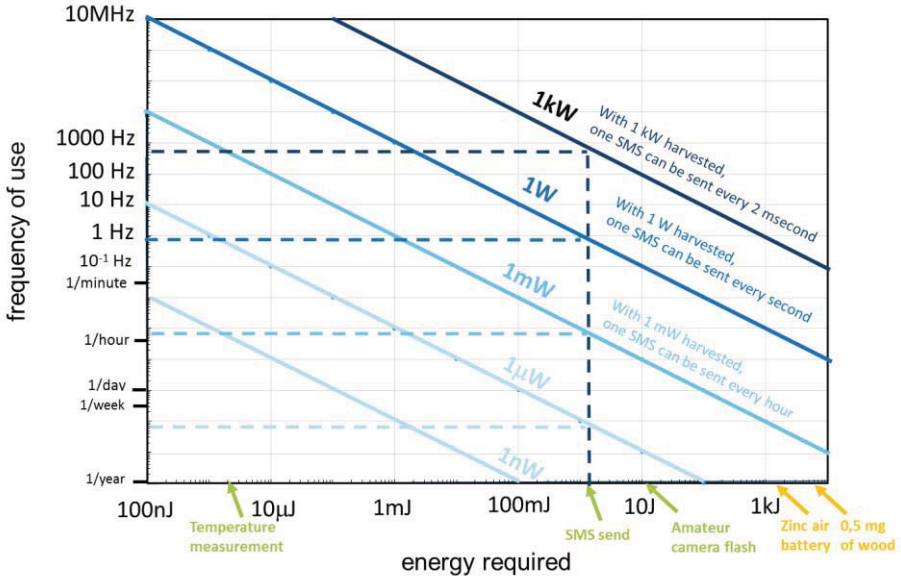


FIG. 1.7- Power consumption of some operations.

electronics will be able to make. For example, sending a short message required 1J, meaning that for a harvester powering 1 W, one message will be sent every second whereas for 1 mW, only one message will be sent every hour. It means that whatever the power harvested, every operation will be achievable but at a frequency which could be around hertz to once per year.

For a clear comparison between energy sources and energy harvesters, performances of harvesters must be discussed in terms of power density (nW, µW, mW /cm^3 - cm^2) meaning than a certain amount of energy is converted by a certain quantity of time per volume or a surface of the harvester. Indeed, power density is a decisive consideration because space is often constrained in small devices.

2.2 Comparison between energy sources:

Before comparing energy sources, it is important to keep in mind that every device will not be exploited in the same environmental conditions, meaning under the same energy sources. Indeed, the energy to be harvested depends on the working environment of the device. For example, if a device is used under the light, solar energy would be a usual choice. In the case of a device used near machines, possibly in the dark, harvesting mechanical vibration energy would be the best choice.

FIG. 1.8, compares the availability of different energy sources [17]. Collecting energy from the visible light is probably the most common way of harvesting energy from environment. Indeed, photovoltaic devices, using semiconductor materials, provide high photo-conversion over a broad range of wavelengths. These devices are typically low cost and provide power levels that are in the range of those required for microelectronic circuits. Outdoor solar energy can provide a power density of 15,000 µW/cm^3, making solar energy, the highest source of energy harvesting. While solar energy is abundant in some applications, it is a less attractive source for indoor environments as the power density drops down to as low as 100 µW/cm^3.

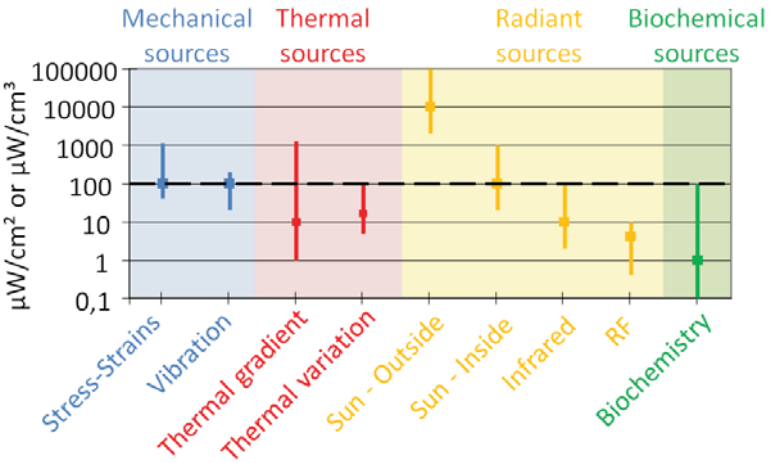


FIG. 1.8 - Environmental sources of energy [17]. 100 µW/cm^3 or µW/cm^2 is highlighted by a dashed black line.

Recent progress has been reported in the field of PV especially in terms of efficiency. In 2017, K.Yamamoto *et al*. succeed in developing a silicon-based solar cell with a photo-conversion efficiency over 26%, approaching thus the theoretical limit of Si solar cells (29.1%) [18]. However, the world record for solar cell efficiency is 46.0% and was achieved by using multi-junction concentrator solar cells [19]. This technology, based on exotic materials such as gallium arsenide, is until now not economically viable.

After the mechanical energy source, which will be discussed later, thermal sources appear to be a common energy source. From human body warm, automobile engines waste heat to more integrated systems such as photovoltaic cells, many thermal sources are present in our environment. Most of the thermal harvesters are based on a thermoelectric effect (Seebeck effect) [20] which is a physical phenomenon present in some materials: it links the flow of heat that passes through them to the electric current flowing through them. These systems require two dissimilar semiconductors (p- and n-type materials). A high temperature is exposed at one end (waste heat), while the other end has a lower temperature (ambient). The differences in temperature generate potential differences between them (**FIG. 1.9**). The performances of the thermoelectric generators are governed by temperature difference and thermoelectric material properties. Until now, low output powers have been described [21]. First, because harvesters need high temperature difference. The practical temperature between the human body and the atmosphere is too low (ΔT=5-15°C), leading to power density around 30 $\mu W/cm^2$ [22]. Second, because the maximum efficiency of the thermal harvester is currently around 5–10% [23] primarily due to the low performance materials which need to have contradictive properties (high electrical conductivity and low thermal conductivity) to perform.

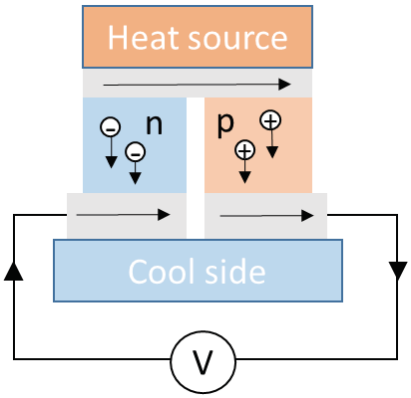


FIG. 1.9 - Seebeck effect.

2.3 Mechanical energy harvesting:

Of the many ambient environmental sources of energy available, vibrations are the second [17] and the concern of this thesis. Mechanical energy can be found almost anywhere: from human bodies to industrial installations. The sources of mechanical energy can be a vibrating structure (a bridge, a window in a noisy street, etc.), a moving object (washing machines) or movement induced by flow (air or water). **TAB. 1.1**, shows examples where mechanical energy can be harvested [24].

TAB. 1.1 - Examples of mechanical sources:

Human body/motion	**Transportation**	**Infrastructure**	**Industry**	**Environment**
Breathing, blood, walking, arm/finger motion, jogging, talking	Cars, trains, noises, tires, brakes, turbines	Bridges, roads, floors, tunnels, pipes	Motors, machines,windows	Air flow, ocean waves

These numerous sources make converting mechanical energy from vibrations into electrical energy an attractive approach for powering wireless devices. Each vibrations are characterized by a frequency, an acceleration and an amplitude. The amount of harvestable energy depends on these mechanical characteristics. Williams and Yates [25], proposed a simple model to predict the mechanical power generated by vibrations. The system consists of an inertial device where a seismic mass, m, on a spring, k, is attached to a housing system (**FIG. 1.10**).

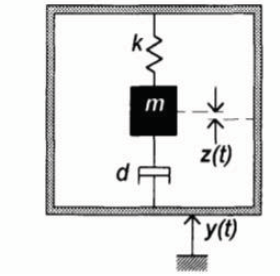


FIG. 1.10 - Schematic diagram of the inertial device.

When the housing is vibrating, the mass is moving so that there is a movement between the mass and the housing. The differential equation (**EQ. 1.1**) that describes the movement of the mass is derived from the dynamic forces of the mass :

$$m\ddot{z}(t) + d\dot{z}(t) + kz(t) = -m\ddot{y}(t) \tag{1.1}$$

Where y(t) is the displacement of the vibrating housing, z(t) is the relative motion of the mass with respect to the housing, m is the seismic mass, k is the spring constant and d is the damping constant. The analytical expression for the mechanical power |P| owes to a sinusoidal vibration is given by (**EQ. 1.2**).

$$Generated\ power = \frac{m\zeta_t Y_0^2 \left(\frac{\omega}{\omega_n}\right)^3 \omega^3}{\left[1 - \left(\frac{\omega}{\omega_n}\right)^2\right]^2 + \left[2\zeta_t \frac{\omega}{\omega_n}\right]^2} \tag{1.2}$$

where ζt the damping factor, ω the input frequency and ω_n is the natural frequency of the spring mass and Y_0 is the amplitude of vibration. This result holds for any type of electrical conversion technology, and so the choice of a transducer does not affect,

theoretically, the amount of mechanical power. From the analysis, it can be seen that the amount of power generated is proportional to the cube of the vibration frequency.

At resonant frequency, **EQ. 1.2** can be simplified by:

$$Generated\ power = \frac{mY_0^2\omega_n^3}{4\zeta_t} \tag{1.3}$$

TAB. 1.2 gives estimations of the generated mechanical power of some common activities. Regarding these values even basic activity like walking can constitute a high source of mechanical energy (67 W).

TAB. 1.2 - Mechanical power generated from common activities [26] :

Activity	Mechanical power generated (W)
Fingers (type)	0,01
Breath	0,83
Blood flow	0,93
Exhalation	1,00
Walk	67,00

The Williams and Yates model provides general information on the main parameters involved in the generation of mechanical energy from ambient vibrations but do not

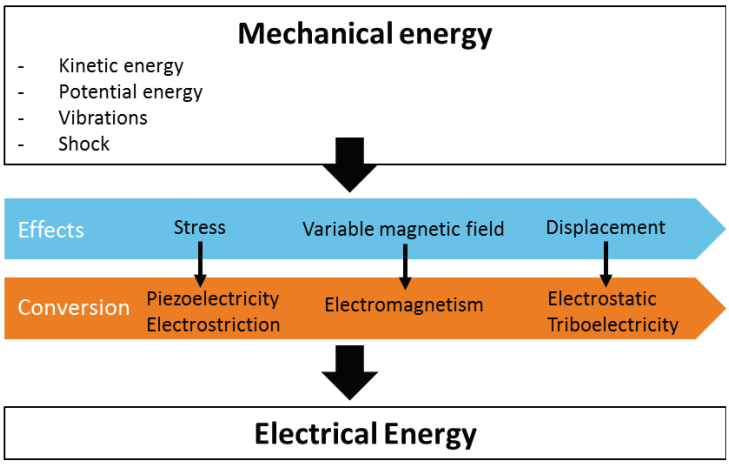


FIG. 1.11 - Conversion methods for mechanical energy.

discuss the ways of converting the mechanical energy into electricity. Several technologies have been developed for converting mechanical waste energy. They present different advantages or disadvantages, in particular according to the intended application. The most classic systems are based on the effect of electromagnetic, piezoelectric or electrostatic systems (**FIG. 1.11**). Although the formers are studied for decades, new harvesters are emerging, exploiting triboelectricity or electrostriction effects.

In the next parts, the main mechanical harvesters will be presented with a description of the technologies including working principles, last performances reported and applications.

2.3.1 Piezoelectric harvester:

Piezoelectric materials have the ability to produce voltage when deformed due to vibrations (direct effect), and conversely, they deform when subjected to an externally applied electric voltage (converse effect). For energy harvesting, it is the direct effect which is involved. Piezoelectric materials are numerous and very diverse. They include crystals (quartz SiO_2) ceramics (lead zirconate titanate (LZT sometimes PZT) or barium titanate BaTiO3), composites (Macro-Fiber Composite (MFC)), even polymers such as polyvinylidene fluoride (PVDF). Piezoelectric polymers, as electroactive polymers, will be discussed, further. In all cases, the piezoelectricity appears due to a strong asymmetry of the crystal lattice in a non-coincidence centroids positive and negative charges. Generally, piezoelectric harvesters are based on a basic cantilever beam structure designed using MEMS techniques (**FIG. 1.12**). Piezoelectric materials are attached to a non-piezoelectric substrate to provide strength to the materials. The harvester is attached to a vibrating source to generate alternating voltage. The generated potential difference from a piezoelectric material is directly proportional to the involved mechanical strain at the cantilever.

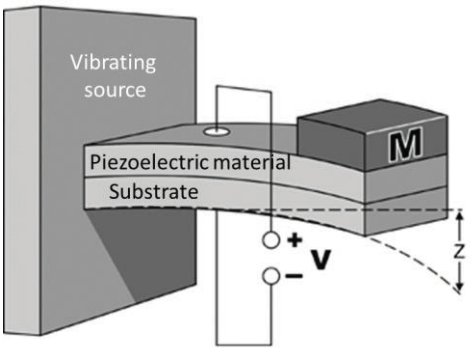


FIG. 1.12 - Piezoelectric harvester based on cantilever structure.

The system of equations (**EQ. 1.4**) summarizes the couplings within a piezoelectric material [27].

$$S_{ij} = s^E_{ijkl}\tau_{kl} + d_{kij}E_k$$
$$D_i = d_{ikl}\tau_{kl} + \varepsilon^\tau_{ik}E_k \quad (1.4)$$

Where S_{ij} is the mechanical strain, τ_{kl} the mechanical stress, D_i the electrical displacement, E_k the electric field, ε^τ_{ik} the permittivity, s^E_{ijkl} the elastic compliance and, d_{kij} the piezoelectric strain constant. The superscripts E and τ denote that the respective constants are evaluated at constant electric and constant stress. The material can be used according to the mode 33 or mode 31 depending on the mechanical stress is perpendicular or parallel to the electrodes. Usually, the 33 mode shows better

performance in terms of electromechanical performance than in the 31 mode [28]. The electromechanical coupling coefficient k_{ij} is typically used to attest to the quality of the electromechanical conversion and the choice of a piezoelectric material for energy recovery. For a mechanical stress perpendicular to electrodes, k_{ij} can be expressed by (**EQ. 1.5**)

$$k^2{}_{33} = \frac{{d_{33}}^2}{\varepsilon_{33}^{\sigma} s_{33}^{E}} \tag{1.5}$$

Where $\varepsilon_{33}^{\sigma}$ is the permittivity, s_{33}^{E} is the elastic compliance and d_{33} is the piezoelectric charge coefficient. The square value of k_{33} corresponds to the efficiency of energy conversion (**EQ. 1.6**) which constitutes an important constant used for assessing the interest of piezoelectric materials.

$$k^2{}_{33} = \frac{electrical\ energy}{mechanical\ energy} \tag{1.6}$$

PZT ceramics were used for a long time for electromechanical conversion due to their high piezoelectric coefficients (**TAB. 1.3**). S.Sugiyama *et al*. [29] reported the realization of piezoelectric harvesters using wafer-level microfabrication techniques. Piezoelectric harvesters were fabricated at the wafer level by bonding a single bulk PZT sheet onto a silicon-on-insulator wafer using a low-temperature process. A single harvester (0.4 mm^3) exhibited a power density of 29 mW/cm^3 when excited at 1 g at a resonant frequency of 514 Hz. This is the highest power density reported in the reported literature for a piezoelectric cantilever [30].

TAB. 1.3 - Piezoelectric properties of usual materials:

Properties	PZT-5H	PZT-5A	$BaTiO_3$	MFC
d_{33} (pC/N)	593	374	149	460
d_{31} (pC/N)	-274	-171	78	-200
k_{33}	75%	71%	48%	60%
k_{31}	39%	31%	21%	-
ε_r	3400	1700	1700	-
Y (Gpa)	65	65	120	30

However, PZT materials present high rigidity and limited strain making them unsuitable for applications where large strain and low frequency are required. Additionally, as PZT are composed of lead, they are very dangerous for the environment. That is why researchers make effort to develop lead-free materials such as barium titanate $BaTiO_3$. Park et al. [31] established a flexible $BaTiO_3$ generator using soft lithographic methods which offered power conversion of up to 7 mW/cm^3. However, the $BaTiO_3$ deposition

process requires high temperature (700-900 °C) [31,32] which is not compatible with most of substrate materials.

Additionally to research for developing lead free materials, other efforts have been dedicated to extending the operating frequency ranges. Indeed, the harvested power is highly dependent on the vibration of the piezoelectric cantilever and is maximized in resonance. A few frequency offset can lead to a huge decrease in output power (**FIG. 1.13**, [33]). Therefore, adjusting resonance frequency into a larger operating bandwidth is a condition for more realistic piezoelectric structures.

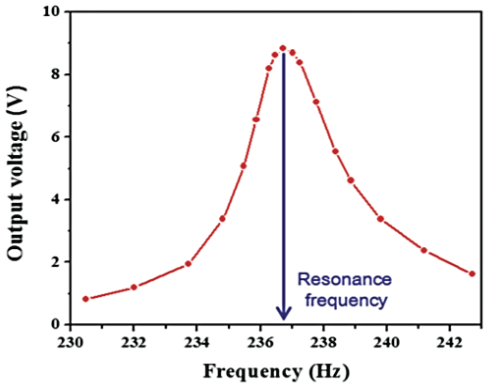


FIG. 1.13 - Resonance frequency in cantilever harvesters.

A major idea to improve the electromechanical efficiency is to modify the traditional cantilever structure. For example, a configuration of doubly clamped beams approach (**FIG. 1.14** a)) can provide a huge deflection by making two types of strains (bending and stretching strains), which lead to a wider resonance bandwidth (**FIG. 1.14** b)). This configuration provides a very high level of power generation of up to 2000 mW/cm^3 (at 1050 Hz, power of 80 µm) according to Hajati *et al.* [34]. However, the excitation frequencies are clearly not adapted to ambient vibrational energies as these sources developed lower frequencies [24].

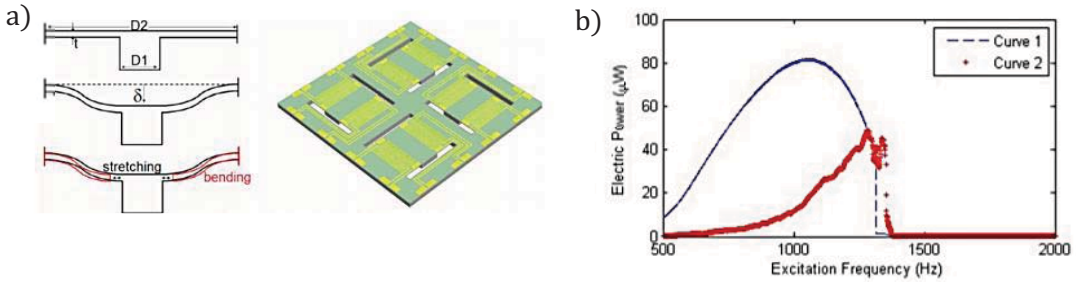


FIG. 1.14 - a) Doubly clamped beams structure b) resonance bandwidth (blue curve).

2.3.2 Triboelectricity:

The use of triboelectricity for mechanical energy harvesting was first reported by Wang and co-workers in 2012 [35]. Usually, tribo-electric effect is considered as a negative effect regarding the industrial risk that can constitute the static charges. Nevertheless, this effect can be smart use to convert mechanical energy into electricity. Triboelectric

generators (TEG) always contain two different materials that are assembled face to face. When materials are in contact, mostly by friction, opposite static charges appear on the surfaces due to contact electrification. The mechanism at play is still a matter of debate [36]. Materials having large electronegativity will gain charge while the other which with less electronegativity will lose charges regarding the triboelectric series [37]. If the back side of the materials has an electrode, the charges can flow between two electrodes through an external circuit and a potential difference is created as the materials are separated. When a motion is made between the two materials, an induced current is created therefore converting mechanical energy into electrical energy. Main operation modes of TEGs are presenting **FIG. 1.15 a)** and have been adapted to different applications.

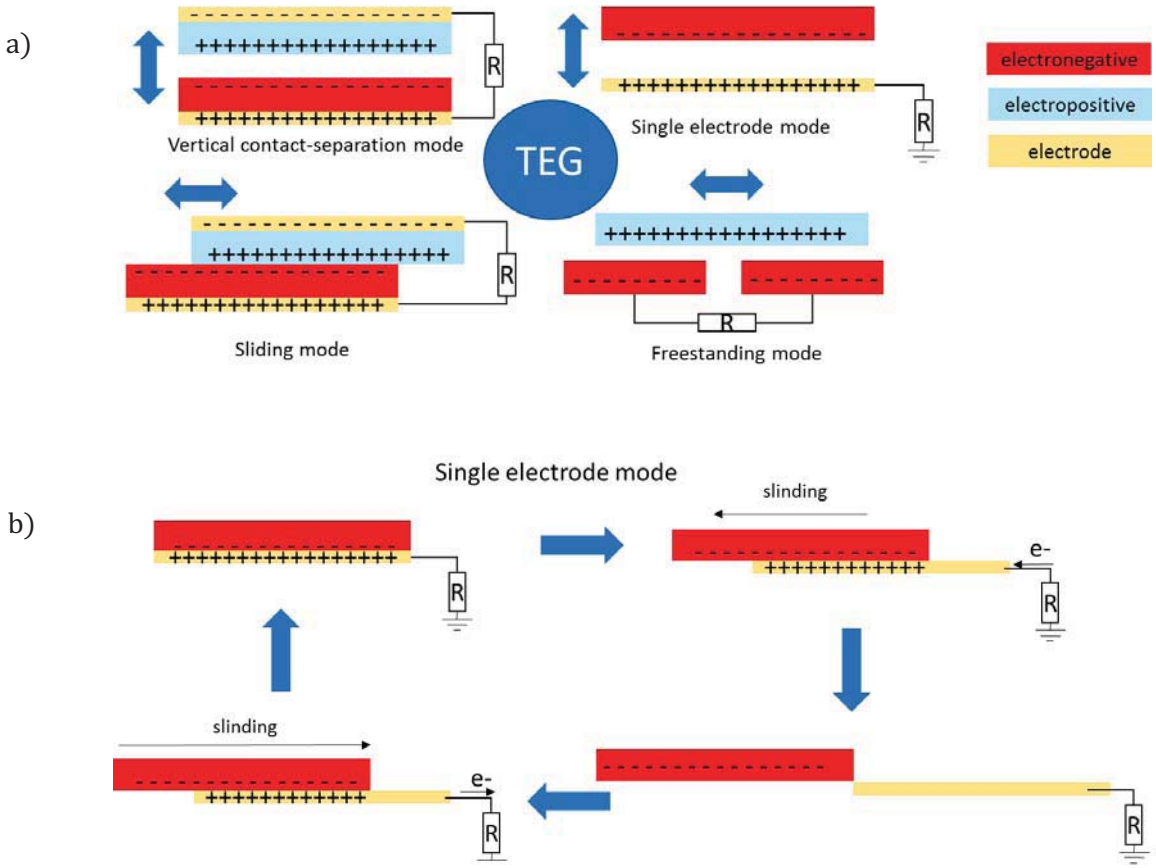


FIG. 1.15 – a) Main triboelectric modes b) Single electron mode in sliding configuration.

FIG. 1.15 b) illustrates the single electron mode in sliding configuration. Electrode on the bottom part of the TEG is grounded. Electrons exchange between the bottom electrode and the ground when top electrode is sliding. An alternative current is thus generated.

The performance of TEG majorly depends on two factors: choice of triboelectric materials and surface topography of the triboelectric layers. Choice of materials affects the amount of surface charges regarding the triboelectric series [37] and surface topography is predominant for large contact area. Since 2012, various methods have been developed [38] to optimize performance of TEG. This includes changes in materials (polytetrafluoroethylene (PTFE), polyvinylidene fluoride (PVDF), silk, etc.) and changes in structural design [39].



FIG. 1.16 - Recent progress in triboelectric technologies.

Wang *et al.* summarized the last progresses in the performance of TEG in terms of area output power density (**FIG. 1.16**) [39]. From the first reported work on TEG in 2012[38], where 10 mW/cm^3 were successfully harvested with kapton/PET in sliding mode (**FIG. 1.17** a)), a large progress has been reported. Now the highest area power density reaches 50 mW/cm^2, meaning a volume power density of 15 W/cm^3[40]. This result has been obtained by using a thin-film-based micro-grating method (**FIG. 1.17** b)).

They harvest energy from sliding motion (10 m/s) between complementary micro-sized surfaces of metal and PTFE.

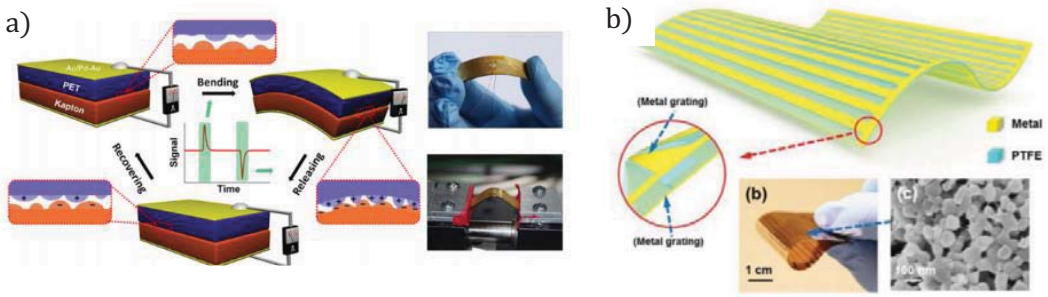


FIG. 1.17 - a) First reported work on TEG [38] b) TEG with the highest reported area power density [40].

Additionally, different mechanical sources of energy have been investigated comprising wind, water and sound-based energy harvesters. X.Fan *et al.* have developed a rollable paper-based triboelectric nanogenerator (PTFE/Cu/paper) for harvesting sound wave energy (acoustic energy). It is capable of delivering a maximum power density of 1mW/cm^3 [41]. More recently, an innovative design was proposed by Chen *et al.* [42] to connect multiple TEG units into a network of large scale kinetic water energy harvesting (**FIG. 1.18** a)). Each unit harvest around 0.1 mW/cm^2, consequently, the network is expected to give an average power output of 1 MW from 1 km^2 surface area (**FIG. 1.18**, b)).

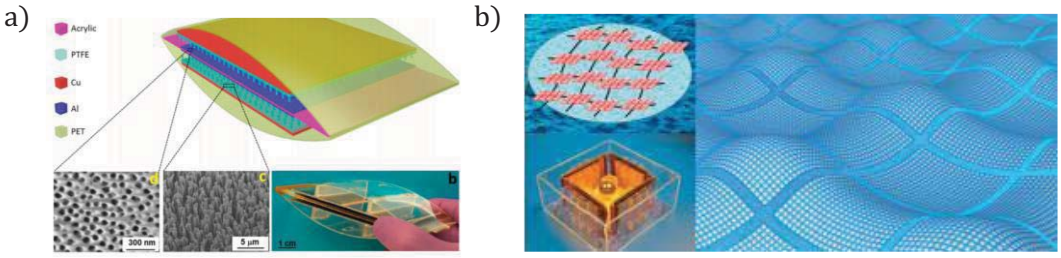


FIG. 1.18 - a) TEG units for harvesting kinetic water energy b) TEG units into a network for large scale applications.

Although, triboelectric harvesters present good electromechanical performances, are easily processed and low cost, some potential issues still need to be solved. This includes a comprehension of the fundamental mechanism of contact electrification and the development of materials with stable and durable characteristics [38].

2.3.3 Variable capacitors:

The conversion of mechanical energy into electricity using variable capacitors is based on electrostatic concepts. We consider a capacitor consisted of two parallel electrodes which are electrically isolated from each other by a dielectric material (typically air or vacuum) **FIG. 1.19**.

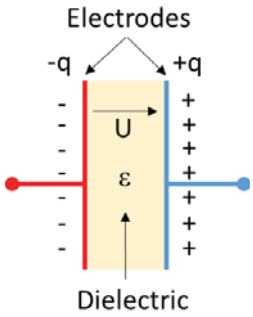


FIG. 1.19 - Structure of a parallel plates capacitor.

The capacitance C of such a parallel electrode capacitor is determined by the overlapping area A and the distance d of the electrodes as well as by the material permittivity ε' between the electrodes according to **EQ. 1.7**

$$C = \frac{\varepsilon' A}{d} \tag{1.7}$$

The permittivity ε, can be expressed as a function of the permittivity of vacuum ε_0 and of the relative permittivity of the material ε'_r (dimensionless number) such as $\varepsilon' = \varepsilon'_r \varepsilon_0$. When subjected to an external voltage U, the electrodes acquire charges of opposite sign q proportionally to the capacitance **EQ. 1.8**.

$$q = CU \tag{1.8}$$

A variation of the parameters A, d or ε' results in a change of capacitance. For a constant charge q, a change in the capacitance C (for example, by changing the distance d between the electrodes) will lead to a change in the voltage U. Similarly, if the voltage U is constant, a change in the capacitance will lead to a change in the charge q. This is the working principle of the variable capacitor harvester.

Usually, the area and the distance are commonly varied to realize a variable capacitor. Indeed, these geometric parameters can be easily modified by the kinetic motion (**FIG. 1.20**).

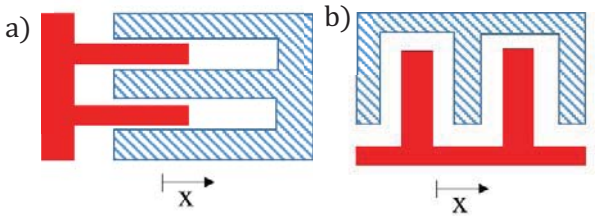


FIG. 1.20 - Top view of the two main electrode geometries for variable capacitors. Red electrode is stationary while shaded electrode is movable. (a) Interdigitated area changing electrodes. (b) Interdigitated distance changing electrode.

These two common geometries are usually employed to make mechanical motion sensors (i.e. accelerometers, gyroscopes) but may be adapted for electrostatic energy harvesting devices. In this case, energy cycles, made of charges and discharges of the capacitor, must be employed for mechanical-electrical energy conversion. The general idea is to place a certain amount of energy in the variable capacitor (initially charge) and to use the ambient vibratory energy to decrease or increase the capacitance by using mechanical work. It is worth mentioning that the electrostatic harvesters are not self-driven contrary to piezoelectric harvesters, and require an external power source to initially charge the capacitor. The two commonly energy cycles are at constant charge or voltage.

Both cycles are presented to discuss the principles of energy conversion in variable capacitors.

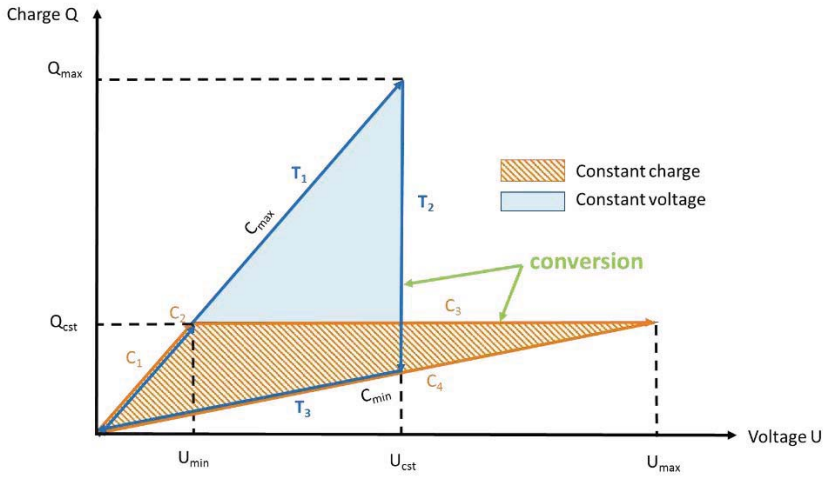


FIG. 1.21 - Conversion cycles with variable capacitors.

- Constant charge conversion cycle:

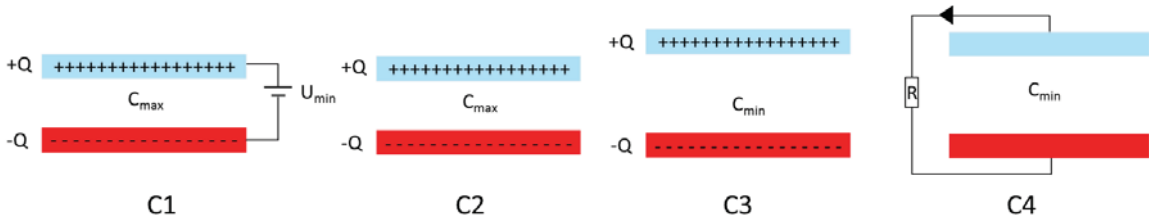


FIG. 1.22 - Constant charge conversion

The cycle begins when the value of the capacitance is maximum (C_{max}). The electrodes are loaded up to a voltage polarization Umin thanks to an external source. An electric charge is stored in the capacity $Q_{cst} = U_{min}\ C_{max}$ (C_1). The electrical system is then left in open circuit (C_2), the electrical charge stored in the capacitance is therefore constant. Thanks to the vibrations, the upper electrode moves with respect to the lowest electrode. The charge is constant during this step and the capacitance decreases to reach a value C_{min} (C_3), which leads to an increase in the voltage at terminals of the capacity $U_{max} = Q_{cst} / C_{min}$. The electrical charges are then removed from the structure throw a resistance (C_4). Recovered energy is the shaded orange area which leads to harvested energy (**FIG. 1.21**):

$$E_{Qcst} = \frac{1}{2} U_{max} U_{min} (C_{max} - C_{min}) = \frac{1}{2} U_{max} U_{min} \Delta C \qquad (1.9)$$

Then the system is recharged at U_{min} for cycling.

- Constant voltage conversion cycle:

The cycle also begins when the value of the capacitance is maximal (C_{max}). An electric charge is injected in the structure via management electronics from a storage element, for example a battery (T1). Vibrations cause the electrode to move higher with respect to the lower electrode and induce a decrease of the capacitance. This decrease in capacity is made maintaining the polarization voltage: the charge decreases $Q = CU$, hence the appearance of a flow of current from capacitor which recharges the battery (T2). Then, when the capacity reaches its minimum value, the charge still present in the capacity is totally transferred to the battery (T3) in a short time with regard to mechanical movement. Recovered energy is the blue area which leads to harvested energy (**FIG. 1.21**):

$$E_{Ucst} = \frac{1}{2}U^2(C_{max} - C_{min}) = \frac{1}{2}U^2\Delta C \qquad (1.10)$$

Still based on the principle of variable capacitance, recent research [43–46] shows the possibility to change capacitance by using liquid movement. Indeed, it is well known [47] that electrodes in contact with an electrolyte acquire electronic charges on their surfaces. The electrode-electrolyte interface has been shown experimentally to behave like a capacitor, and a model of the interfacial region similar to a capacitor can be used (**FIG. 1.23**) [47]. This system is called an electrochemical double layer (ECDL).

The charge of the metal is negative or positive with respect to the solution and depends on the potential across the interface and the composition of the solution. At all times, however, q_m=-q_s. The charge of the metal, q_M, represents an excess or deficiency of electrons on the metal surface. The charge of the solution, q_s, is made up of an excess of either cations or anions in the vicinity of the electrode surface.

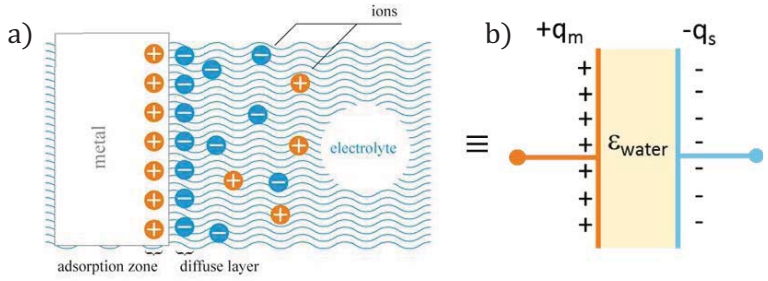


FIG. 1.23 - (a) Schematic representation of the electrochemical double layer and (b) its electrical equivalent.

Using the potential of electrochemical double layers, H.K Pak and collaborators [45] proposed a new method for electrical power generation. Indeed, they succeed in modulating charges from electrochemical double layers, creating a capacitive current, by using mechanical energy.

In this system, a water bridge is formed between two electrodes (**FIG. 1.24** (a)). At the two interfaces electrode-electrolyte, an ECDL is created (**FIG. 1.24** (b,c)) which are characterized by a capacitance. One of the interface is hydrophilic while the other one is hydrophobic. Both capacities depend on the contact area, but for the hydrophilic interface, capacitance is considered fixed. When the distance between the two electrodes is mechanically modulated, it leads to a modulated contact area for the hydrophobic surface. Consequently, the two interfacial areas are continuously charged and discharged from each other, thus generating AC electric current. The harvesting system can be fully understood by only using variable capacitor considerations.

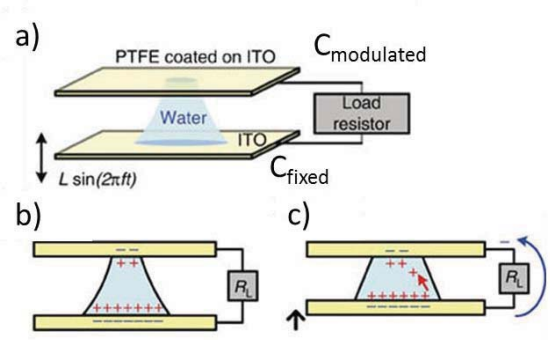


FIG. 1.24 - (a) Diagram of the experiment [45].

In this experiment, they succeed in generating about 1.5 µW of the power leading to a power density of 0.3 $\mu W.cm^{-2}$ for a fixed vibration frequency of f=30 Hz. Even if industrially speaking, confining a water droplet between two surfaces is not easy, this approach stays environmentally friendly and promising.

R.Evans & E.Skafidas [43] made an improvement on the ECDL approach. Instead of using, the movement of electrodes, they achieved the variation of the capacitance by moving the liquid itself (NaCl solution) (**FIG. 1.25** a)). They slide ionic droplets on hydrophobic interdigitated electrodes and use a low bias voltage to increase the ions accumulation and thus the global charge. They succeed in harvesting 0.1 mW/cm^2 at a low frequency of 6 Hz using a bias voltage of 1.2V. This work demonstrates the possibility of harvest mechanical energy from droplets, this concept could be coupled with photovoltaic devices which could still harvest energy in rainy conditions.

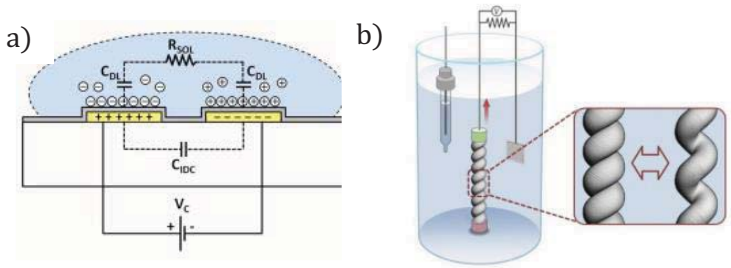


FIG. 1.25 - a) Power generator based on moving liquid [43] b) power generator from carbon nanotubes yarn twist [48].

Recently, S.H Kim et *al.* reported carbon nanotubes yarn harvesters [48] (**FIG. 1.25** b)) that electrochemically convert tensile or torsional mechanical energy into electricity without requiring external bias voltage. In fact, this is still a harvester based on a variable capacitance. When twisted, the harvester capacitance decreases while untwisted the capacitance increases. Because a chemical potential exists between the harvester and the electrolyte, there is an apparition of charges at the interface based on an effect of electrochemical double layer.

To sum up, the last reported results have shown the vast potential of variable capacitors for mechanical energy harvesting. Liquid based variable capacitors are promising technologies and will probably start replacing previous metallic variable capacitors due to the absence of voltage bias. Nevertheless, these technologies still have to demonstrate their long-term viability. Particularly, the use of liquid could lead to electrochemical reactions which could decrease the performances of harvesters over time.

3 Electroactive polymers for mechanical energy harvesting:

Compared to inorganic materials, electroactive polymers are lightweight and flexible materials making them good candidates for developing flexible generators [49]. The basic structure of an EAP harvester is quite simple. Usually, the EAP polymer film, typically an elastomer, is sandwiched between two compliant electrodes and submitted to an electric field. This field induces stresses and strains in dielectric polymers under three sources: piezoelectric effect, intrinsic electrostriction and Maxwell's stress. The mechanical response can be linear to the electric field (piezoelectricity) or nonlinear (intrinsic electrostriction and Maxwell's stress). The piezoelectric effect does not exist in all dielectric polymers, however electrostrictive effect exists in all dielectric materials even in piezoelectric materials.

3.1.1 Piezoelectric polymers:

Besides piezoelectric ceramics, there are different polymer classes that can be considered piezoelectric [50] and they obey analogous operation principles. The first class are bulk polymers. There are solid polymer films that have the piezoelectric mechanism through their molecular structure. Semi crystalline PVDF and its copolymer [P(VDF-TrFE)] and terpolymer [P(VDF-TrFE-CFE)] are the most used and studied piezoelectric bulk polymers for electromechanical devices. They have the advantages of mechanical flexibility compared to inorganic materials but present lower piezoelectric constants (d_{33}=-13–28 pC/N for PVDF compared to -593 pC/N for PZT-5A).

PVDF can present five distinct crystalline phases related to different chain conformations. The most investigated are presented **FIG. 1.26**. PVDF needs structural requirements (β-crystalline phase) for developing a high dipolar moment and thus piezoelectric properties otherwise low piezoelectric properties are measured.

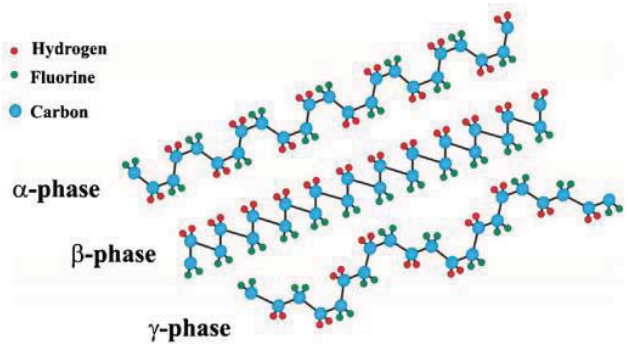


FIG. 1.26 - Crystalline phases of PVDF [51].

The β-phase can be induced by several techniques, including mechanical stretching [52] of the α-phase, addition of nucleating fillers [53] and the use of external electric field [54]. This post synthesis treatment increases the cost and time processing. Contrary to PVDF, copolymers [P(VDF-TrFE)] always presents the piezoelectric β-crystalline phase, induced by the addition of a third fluoride (TrFE monomer unit) with a large steric effect. PVDF has also been modified by the introduction of chloride trifluoride ethylene (CTFE) on the polymer chain, producing the P(VDF-CTFE) copolymer. The piezoelectric constant, d_{33} for this copolymer reaches the value of -140 pC/N[55] which is a huge increase compared to pure PVDF (**TAB. 1.4**).

TAB. 1.4 - Piezoelectric properties of some PVDF compounds:

Properties	PVDF	P(VDF-TrFE)	P(VDF-HFP)	P(VDF-CTFE)	P(VDF-TrFE-CFE)
d_{33} (pC/N)	-24 to -34	-38	-24	-140	-
d_{31} (pC/N)	8 to 22	12	30	-	-
k_{33}	20%	29%	36%	39%	55%
ε_r	6 to 12	18	11	13	55
Y (Gpa)	2,1	1,5	-	-	0,5 to 1,1

Moreover, the introduction of CFE in P(VDF-TrFE) gives rise to enhanced dielectric properties with a dielectric constant larger than 55, which is more than 5 times higher than that of PVDF.

The integration of piezoelectric polymers was studied by Paradiso and Starner [56], who developed a system to harvest the energy generated by a human being walking (**FIG. 1.27**). They used piezoelectric elements (PVDF) beneath the insole of running sneakers. They were able to produce an average power of 1.3 mW at 0.9 Hz walking pace, employing a stack of PVDF layers at the toes.

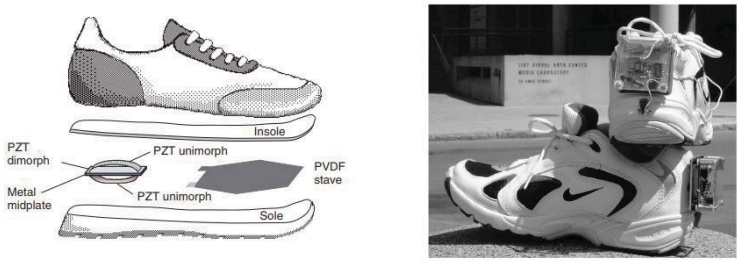


FIG. 1.27 - Integration of piezoelectric polymers in a heel.

The performances of piezoelectric polymers for mechanical energy harvesting are mainly limited by the high Young's modulus of these materials (~ GPa), which leads to low strain, and their low piezoelectric charge coefficient d_{33}. An alternative solution to harvest and convert mechanical energy would be to use *electrostrictive polymers* which can develop lower Young's modulus (~ MPa to kPa) besides high dielectric constant. These materials can be used as a soft dielectric layer in variable capacitors.

3.1.2 Electrostrictive polymers:

3.1.2.1. Theoretical considerations:

The piezoelectric effect cannot exist in a polymer that possesses the inversion symmetry. By contrast, electrostrictive effect exists in all dielectric materials even in piezoelectric materials. This is a quadratic dependence of strain on polarization P, **EQ. 1.11**.

$$S_{ij} = Q_{ijkl} P_k P_l \tag{1.11}$$

where Q_{ijkl} is the charge-related electrostrictive coefficient. **EQ. 1.11** can be expressed using a quadratic dependence of a strain on the electric field E.

$$S_{ij} = M_{ijkl} E_k E_{\ l} \tag{1.12}$$

where M_{ijkl} is the electric field-related electrostrictive coefficient.

Subjected to an electric field, the total strain S_{ij} consists of a mechanical S_{ij}^{mech}(elastic strain) and an electrostatic strain S_{ij}^{elec}. The mechanical strain is the strain in the absence of an electric field which for linear-elastic materials is determined by Hooke's law. Applying an electric field introduces electrostatic strain into the total strain. The electrostatic strain can be separated into two distinct contributions: the Maxwell strain and the intrinsic electrostriction strain.

Finally, the total strain S_{33} along the electric field in the 3-direction can be written as

$$S_{33} = S_{33}^{mech} + S_{33}^{elec} = \frac{\sigma_3}{Y} + \left(M_{33}^{electrostriction} + M_{33}^{Maxwell}\right)E_3^2 \quad (1.13)$$

Where σ_3 is the stress, Y is the Young's modulus, $M_{33}^{electrostriction}$ and $M_{33}^{Maxwell}$ are the electric field-related electrostrictive coefficient for respectively intrinsic electrostriction effect and Maxwell effect.

S^{elec} can be expressed in a different formula [57,58]

$$S^{elec} = -\frac{1}{2Y}\varepsilon\varepsilon_0((1+2\nu) - \frac{a_1+a_2(1-2\nu)}{\varepsilon})E^2 \quad (1.14)$$

where ε is the permittivity of the undeformed material, ν is Poisson's ratio and a_1, a_2 are parameters describing the variation in dielectric properties of the material with deformation, they are function of the temperature and the field frequency.

With incompressible materials (Poisson's ratio=0.5), **EQ. 1.14** becomes:

$$S^{elec} = (-\frac{\varepsilon\varepsilon_0}{Y} + \frac{a_1}{2Y\varepsilon})E^2 \quad (1.15)$$

In this case, for a strain along the electric field in the 3-direction and in comparison with **EQ. 1.13**:

$$M_{33}^{Maxwell} = -\frac{\varepsilon_r\varepsilon_0}{Y}$$
$$M_{33}^{electrostriction} = \frac{\varepsilon_0 a_1}{2Y} \quad (1.16)$$

3.1.2.2. Intrinsic electrostriction:

Intrinsic electrostriction describes the variation of dielectric properties of a material with deformation. Deformation affects the relative positions of the dipoles (**FIG. 1.28**) and the local electric field of the material, which leads to a change in dielectric properties.

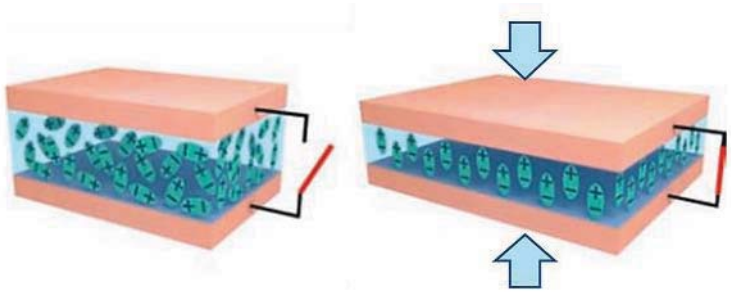


FIG. 1.28 - Intrinsic electrostriction effect that originates from direct coupling between the polarization and mechanical response.

A stressed material is anisotropic and its dielectric properties are described by a second order tensor ε_{ij}

$$\varepsilon_{ij} = \varepsilon\delta_{ij} + a_1 S_{ij} + a_2 S_{kk}\delta_{ij} \tag{1.17}$$

where ε is the permittivity of the undeformed material, a_1, a_2 are the same parameters as those used **EQ. 1.14**

$$\Delta\varepsilon_{ij} = (\varepsilon_{ij} - \varepsilon\delta_{ij}) = a_1 S_{ij} + a_2 S_{kk}\delta_{ij} \tag{1.18}$$

In the case where a material is subjected to uniaxial compression (3-direction) and that the material tested is linearly elastic **EQ. 1.18** becomes.

$$\Delta\varepsilon_{33} = (\varepsilon_{33} - \varepsilon) = a_1 S_3 + (1 - 2\nu) a_2 S_3 \tag{1.19}$$

For incompressible materials (Poisson's ratio=0.5)

$$\Delta\varepsilon_{33} = (\varepsilon_{33} - \varepsilon) = a_1 S_3 \tag{1.20}$$

For linear dielectrics, and this is the case for electrostrictive polymers, the dielectric displacement **D** is related to **E** by the second order dielectric tensor.

$$D_i = \varepsilon_0 \varepsilon_{ik} E_k \tag{1.21}$$

Which becomes for 3-uniaxial compression

$$D_3 = \varepsilon_0 \varepsilon_{33} E_3 = \varepsilon\varepsilon_0 E_3 + a_1 \varepsilon_0 S_3 E_3 \tag{1.22}$$

Using the same notation as **EQ. 1.16**, **EQ. 1.22** becomes

$$D_3 = \varepsilon_0 \varepsilon_{33} E_3 = \varepsilon \varepsilon_0 E_3 + 2\, M_{33}^{electrostriction}\, Y S_3 E_3 = \varepsilon \varepsilon_0 E_3 + 2\, M_{33}^{electrostriction}\, \sigma_3 E_3 \quad (1.23)$$

Consequently, the $M_{33}^{electrostriction}$ can be related to the variation of permittivity when a stress S_3 is applied.

$$M_{33}^{electrostriction} = \frac{\varepsilon_0 \Delta\varepsilon_{33}}{2 Y S_3} = \frac{\varepsilon_0 \Delta\varepsilon_{33}}{2\sigma_{33}} \quad (1.24)$$

This last equation shows that intrinsic electrostriction can be seen as a variation of permittivity when a stress is applied on materials. The direct consequence is the possibility to use electrostrictive materials as a variable dielectric layer. The addition of a high electrostricitve modulus and low Young's modulus could lead to huge variation of capacitance due to changes in distance and change in materials' dielectric properties.

3.1.2.3. Maxwell stress:

A dielectric polymer can be described as a dielectric layer in a capacitor. When such a capacitor is charged, positive charges from one electrode are attracted by negative charges from the other electrode by Colombian attraction(**FIG. 1.29**).

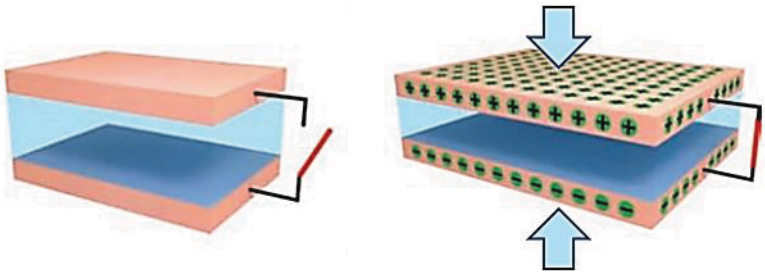


FIG. 1.29 - Maxwell stress that originates from the Coulomb interaction between oppositely charged compliant electrodes.

The resulting stress is known as the Maxwell stress and tends to squeeze the polymer between the charged electrodes, decreasing its thickness and expending its area. These dimensional changes happen as dielectric polymers are incompressible materials (Poisson's ratio=0.5).

In this case, the strain S_M due to the Maxwell stress in the thickness direction (3-direction) can be expressed as [59]:

$$S_M = -\frac{\varepsilon_r \varepsilon_0}{Y} E^2 = M_{Maxwell} E^2 = \frac{\Delta e}{e_0} \quad (1.25)$$

Where Y is the Young's modulus of the dielectric material, ν is the Poisson's ratio, $M_{Maxwell}$ is the Maxwell electrostriction modulus and $\frac{\Delta e}{e_0}$ the relative thickness change. In the case of a compressible material and taking account the Poisson's ratio of the dielectric material **EQ.1.25** would become [58]:

$$S_M = -\frac{1}{2}\frac{\varepsilon_r \varepsilon_0}{Y}(1+2\nu)E^2 = M_{Maxwell}E^2 \tag{1.26}$$

In both cases and for a more rigorous approach, it would be necessary to invoke the tensor notation but considering an isotropic polymer, the dielectric tensor is reduced to one permittivity ε.

Finally, we get the intrinsic equations of electrostriction by combining **EQ. 1.23** and **EQ. 1.13** which define the electromechanical response of materials:

$$\begin{aligned} D_3 &= \varepsilon\varepsilon_0 E_3 + 2\, M_{33}^{electrostriction}\, \sigma_3 E_3 \\ S_{33} &= \frac{\sigma_3}{Y} + \left(M_{33}^{electrostriction} + M_{33}^{Maxwell}\right)E_3^2 \end{aligned} \tag{1.27}$$

3.1.3 Conversion roads:

Different electromechanical conversion roads have been established for converting mechanical energy into electricity thanks to electrostrictive materials. Due to the electrostatic nature and the electromechanical activity, activated by the application of an electric field, two main roads are actually conceivable. The first one is based on electrostatic cycles (constant charge or voltage), as presented previously in the case of variable capacitors [60–62]. For this road, electrostrictive polymers must be finely controlled and charged during different phases: stretching, charging, relaxing and discharging. It requires a constant control of the polarization source and thus a complex power circuit in addition to a well-controlled cycle of deformation. The timing of the application and removal of the charge relative to the stretching as well as the amount of charge added and removed is a critical step for maximizing the power harvested [62].

A second converting road has been recently employed, which is much easier to implement because it does not require fine control of the charge and the strain. It is based on a "pseudo-piezoelectric" behavior [49,63,64], induced by the use of an electric field bias which may be done using supercapacitors, batteries or piezoelectric elements. Indeed, electrostrictive polymers are not piezoelectric, it is necessary to induce polarization with a dc bias to obtain a pseudo-piezoelectric behavior. A better understanding of the pseudo-piezoelectric behavior can be done comparing the two systems of electric displacement equations governing electrostriction (**EQ. 1.28**) and piezoelectricity(**EQ. 1.29**).

$$D_3 = \varepsilon\varepsilon_0 E_3 + 2\, M_{33}^{electrostriction}\, \sigma_3 E_3 \tag{1.28}$$

$$D_3 = \varepsilon_{33}^{\sigma} E_3 + d_{33}\sigma_3 \tag{1.29}$$

For a piezoelectric material, the application of a constraint directly induces the creation of electric charges thanks to the piezoelectric constant d_{33}. For an electrostrictive material, this is not the case in the absence of an electric field (passive material). By identification, the "pseudo-piezoelectric" coefficient is equal to $d_{33} = 2M_{33}^{electrostriction} E_3$ [65], thus the need for a static electric field for harvesting energy can be fully understood. In this thesis, this is the pseudo-piezoelectric mode which is employed for recovering energy.

3.1.4 Performance parameters of electrostrictive materials for mechanical energy harvesting:

Several parameters influence the power harvested with electrostrictive polymers including material properties (${M_{33}}^*$, Y, ε_r) and external parameters such as sample geometry or measurement parameters (bias voltage, frequency, etc.). These different operating conditions make the true comparison of electromechanical performances of materials quite difficult. That is why the energy conversion capability of electrostrictive polymers is preferably estimated by using a Figure of Merit (FoM). This is a number used to characterize the performance of materials independently of external parameters. In a word, higher will be the FoM, higher will be the power harvested. Earlier publications [49,66], shown that the FoM of electrostrictive composites is equal to $M^* \cdot Y$ and proportional to $(\varepsilon_0(\varepsilon_r - 1)^2/Y\varepsilon_r)$ leading to a rough proportionality between FoM and ε_r. However, some materials such as (PANI)/polyurethane (PU) [67] composites do not respect this proportionality and show its limitation. M.Lallart *et al.* [68] proposed a new FoM where external parameters are not taken into account, which is equal to the square product of the intrinsic electrostrictive modulus by the Young's modulus, divided by the permittivity.

$$\text{FoM} = \left(\frac{2\pi}{\varepsilon}\right)({M_{33}}^* Y)^2 \quad (\text{J m}^{-1}\,\text{V}^{-2}\,\text{cycle}^{-1}) \tag{1.30}$$

They demonstrate the accuracy of this new criterion by comparing it with the evolution of the harvested power and finally find a linear fit. However no proportionality was found by using the FoM, $M^* \cdot Y$, meaning that the evaluation was false. The main drawback of this figure is that it does not take into account the losses of the studied dielectric material. In the same way as permittivity, the material's conductivity is a critical parameter for energy harvesting applications. Indeed, if the material is conductive, it will not be possible to use it as a dielectric layer in variable capacitors. Usually, the losses are characterized by the loss tangent defined as

$$\tan\delta = \frac{\sigma}{\omega\varepsilon_0\varepsilon_r} \tag{1.31}$$

Where σ is the net conductivity (imaginary part of the permittivity plus conductivity from the free charges), ε_r is the relative permittivity, ω the electric pulsation. For lossless material (perfect dielectric), there is no loss and $\tan\delta \to 0$. It means that the loss tangent must be maintained as low as possible for dielectric materials. The FoM proposed by Lallart et al. (**EQ. 1.30**) tends to be generalized for true comparison between electrostrictive materials (**FIG. 1.30**) but for a full vision of material capacities, this figure must be compared with the loss tangent and that is what we will strive to do in this thesis. Until now the highest reported FoM was for a composite based on P(VDF-TrFE-CFE)/CB with a value of 31.5 10^{-9} J m^{-1} V^{-2} $cycle^{-1}$ [68] (**FIG. 1.30**).

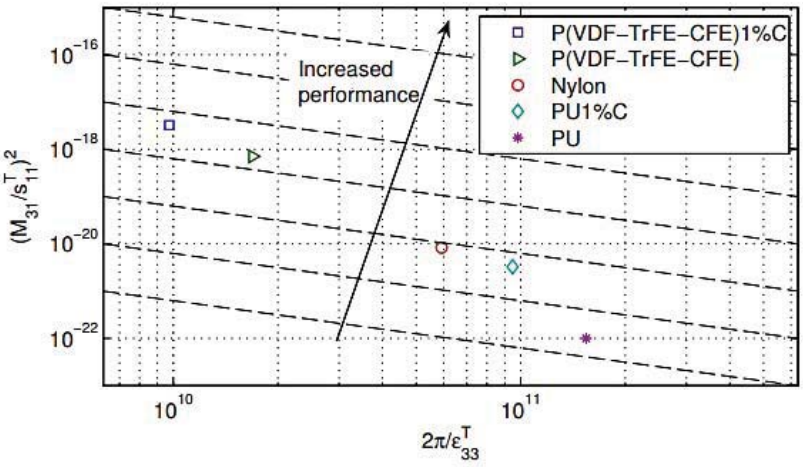


FIG. 1.30 - Comparison of electrostrictive materials based on the FoM value.

3.1.4.1. Available electrostrictive polymers:

As we have seen previously, the performances of electroactive polymers for energy harvesting purposes are directly dependent on the material properties (i.e. permittivity, electrostrictive modulus and Young's modulus). Better performances can be obtained by increasing the permittivity and the electrostrictive modulus while keeping the Young's modulus as low as possible. There are many electroactive materials that have been developed, but few that come close to meeting all of these goals. Two strategies have been explored to do so: new synthetic polymers and composites. For example, it has been demonstrated that ferroelectric P(VDF-TrFE) polymers can be converted to large electrostrictive polymers by the introduction of non polar molecular structure in the ferroelectric phase[69].

Instead of playing on polymer chemistry, a more versatile approach is to make composites with conductive fillers, dispersed in an insulating matrix (polymer). These composites combine high strain capability and have shown good conversion efficiency.

Actually, the addition of conductive fillers enhances the ability of the composites to be polarized due to the Maxwell-Wagner polarization effect [70]. This polarization intensely contributes to the permittivity of composites. The realization of composites is based on a mechanical approach where fillers are dispersed with the use of a mechanical force. In this case, homogeneously dispersed fillers inside the matrix is a challenge and can lead to a poor dispersion. Additionally, the filler addition must be done without reaching the percolation threshold, otherwise the composite become conductive ($\tan\delta \gg 1$). A variety of composites have been realized to come close to the meeting of all of the goals. This includes a variety of polymer matrix (polyurethane, polyvinylidene fluoride, polydimethylsiloxane etc.) and fillers (carbon nanotubes, graphene oxide, carbon black particles, polyaniline etc.).

N.Muensit *et al.*[67] studied electrostriction and energy harvesting performances of polyaniline(PANI)/polyurethane(PU) composites at low fillers concentration. As expected, the intrinsic electrostriction modulus increases by a factor 1.6 compared to pure polyurethane. The material get a value of M_{33} of $-6.12\,10^{-16}\,m^2.V^{-2}$ and M_{31} of $2.77\,10^{-18}\,m^2.V^{-2}$ for a PANI concentration of 2 wt% at 2V/µm.

D. Guyomar *et al.*[71] investigated carbon black/P(VDF-TrFE-CFE) composites fabricated via a simple blending method. This is a middle material based on a piezoelectric polymer filled with carbon particles. Fillers aim at increasing the dielectric constant and thus the electrostrictive properties in addition to the piezoelectric properties of the material. The composite, with 4.7 wt% of carbon black, exhibits a permittivity of 140 and a dielectric loss of 0.05 at 100Hz compared to a permittivity of 50 and a similar dielectric loss for pure P(VDF-TrFE-CFE). If no electrostrictive coefficient was reported in this work, this composite has shown significative increase of the $M_{33} = -2.4\,10^{-15}$ with 1% of CB fillers in another investigation [68].

Until now, the highest reported electrostrictive modulus [62] based on a composite approach were on the order of $-10^{-15}\,m^2.V^{-2}$ as reported **TAB. 1.5** for PU and P(VDF-TrFE-CFE) matrix. For both matrix, the filler addition has shown significantly increase of the electrostrictive modulus compared to a neat polymer. The lake of optimization into the fillers distribution inside the polymer matrix prevents materials from highly increasing their electrostrictive modulus. Indeed, the dispersion of conductive fillers in polymers can lead to aggregates and thus decreases the material properties because of a low Maxwell-Wagner polarization effect.

TAB. 1.5 - Electrostriction properties of the reported works [62]:

Polymer	Fillers	Content (vol %)	Dielectric Constant	Frequency Measurement of Permittivity (Hz)	M_{33} (m^2/V^2) 10^{-15}	Frequency Measurement of M_{33} (Hz)
PU	No		6.8	0.1	−1	0.1
PU	SiC	0.5	10.9	0.1	−2.5	0.1
PU	CB	1	15.4	0.1	−4	0.1
P(VDF-TrFE-CFE)	No		65	0.1	−1.1	0.1
P(VDF-TrFE-CFE)	CB	1	95	0.1	−2.4	0.1
P(VDF-TrFE-CFE)	PANI	23	2,000	100	−0.15	1
P(VDF-TrFE-CFE)	PANI	12.7	600	100	−0.02	1

SiC, silicon carbide; CB, carbon black; PANI, polyaniline.

J.Yuan [72] recently succeed in achieving more controlled composites (reduced graphene oxide/PDMS) with huge electrostriction modulus around $-10^{-14}\, m^2.V^{-2}$ at 0.1 Hz by using a phase transfer method. The good electrostrictive properties result from the liquid crystal structure of reduced graphene sheets inside the PDMS matrix. This increase in electrostrictive proprieties reinforced the idea that improving the filler distribution inside the matrix could lead to remarkable progress. Nevertheless, the electrostrictive properties are associated with a relatively high dielectric loss of 2.5 which prevent the materials from being used in energy harvesting applications.

3.1.4.2. Applications and setups for vibrational energy harvesting using electrostrictive polymers:

The use of electrostrictive materials as the dielectric layer of variable capacitors can target small, medium and large-scale applications that are not easily achievable with piezoelectric or electromagnetic materials. Indeed, polymers are robust, low cost and easily scalable materials compared to conventional materials such as ceramics making them the elements of choice in some applications such as fluidic energy recovery. In this context, many prototypes have been developed which are based on the harvesting of energy from ocean waves. Indeed, oceans are huge potential sources of energy (29,500 terawatt-hours a year), according to the United Nations. Recently, Giacomo.M [73] *et al.* demonstrated the ability of a dielectric elastomer to convert the oscillating energy carried by water waves into electricity. They build a harvester prototype using a commercial polyacrylate film as electrostrictive polymer (**FIG. 1.31**). In resonant conditions, their system demonstrates a delivery power density per unit mass of 197 W/Kg (taking a polyacrylate density of 1.32g/cm^3, it means a volume density of 0.26 W/cm^3).

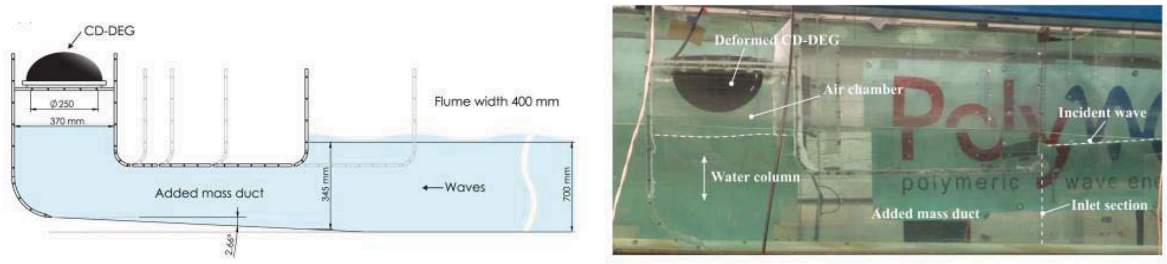


FIG. 1.31 - Large scale harvester based on electroactive polymer.

Industrials have seen the potential of waves for energy harvesting purpose and start developing projects. For example, the Bosch Company makes a demonstrator model to convert wave energy into electricity with a disruptive design (**FIG.1.32**). A float is positioned on the surface of the ocean and is firmly anchored at the bottom of the ocean. The two halves are interconnected by a thousand sheets of dielectric polymers. Every 3 to 10 seconds, these sheets are deformed by the movement of the waves and allow current to be generated .

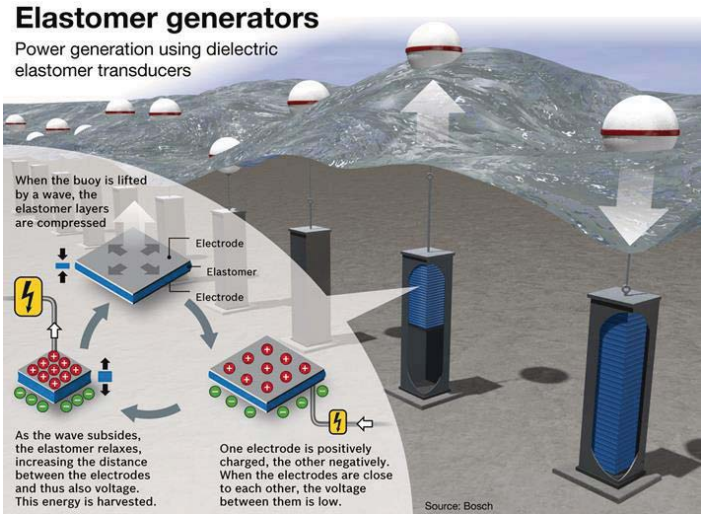


FIG.1.32 - Waves harvester from the Bosch Company based on electroactive polymers.

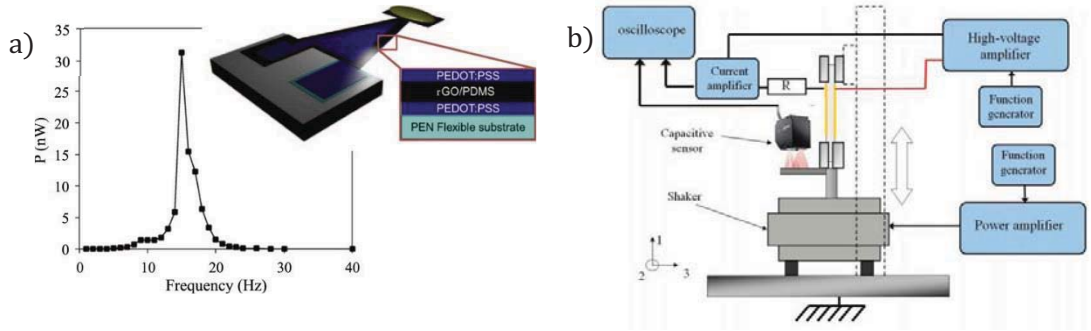


FIG.1.33 - a) Cantilever harvester based on electrostrictive polymer [74] b) clamp/clamp configuration.

At microscale, electrostrictive polymers can be used as electroactive layer in *cantilever* structures or in *clamp-clamp* setup. Hussein. N *et al*. [74] have recently presented an all-organic cantilever (**FIG.1.33** a)), integrating an electrostrictive composite based on reduced graphene oxide sheets in a PDMS matrix. Applying a sinusoidal acceleration (0,5 g, 15 Hz), they succeeded in harvesting a power density of 6 μW/cm^3. This is a good performance regarding the low frequency that was used. This output density is higher than the one extracted from polyurethane/ PANI [67] materials but lower than the one generated by P(VDF-TrFE-CFE) tepolymers, 300 μW/cm^3 [63].

Less integrated setup has been developed to harvest mechanical energy. (**FIG.1.33** b) provides a schematic representation of the setup in a clamp/clamp configuration. The

material is sandwiched between two compliant electrodes and submitted to a parallel-electrode strain produced by a shaker. This configuration caused the sample to undergo a transverse vibration (31 configuration). The clamp/clamp configuration has been used to characterize several electrostrictive materials [67,68]. The main results are reported **TAB. 1.6.**

TAB. 1.6 - Power density of several electrostrictive materials:

Sample	f(Hz)	ε_r (at f)	Y (Mpa)	volume (cm^3)	Electric field (V/μm)	Power density (μW/cm3)	FoM
PU	100	4,4	40	0,025	10	8	1,50E-11
Nylon	100	14,2	2800	0,05	10	132	4,76E-10
PU 1%C	100	7,5	40	0,025	10	172	3,08E-10
P(VDF-TrFE-CFE)	100	42,0	250	0,025	10	5840	1,11E-08
P(VDF-TrFE-CFE)+1%C	100	74,0	250	0,05	10	8240	3,03E-08

The highest value of power density was reached by Lallart et *al.* [68]using a P(VDF-TrFE-CFE)/CB composite. 8.2mW/cm^3 were successfully harvested thanks to pseudo-piezoelectric cycles. Even if high electric field was employed (10 V/μm), the material is associated with a FOM of 3 10-8 $J\,m^{-1}\,V^{-2}\,cycle^{-1}$, showing excellent conversion properties for this type of composite.

3.1.4.3. Our strategy:

Until now, electrostrictive composites have been mainly studied with polymer matrix based on high Young's modulus (polyurethane, P(VDF-TrFE-CFE)). In this research project, we propose to add conductive or high permittivity nano-fillers to very soft elastomeric polymers. Addition of such particles is expected to increase the permittivity of the polymer while keeping the material very deformable. The permittivity theoretically diverges at the percolation threshold. Although percolated composites show high conductivity and high loss tangent, near-percolated composites are expected to increase their permittivity while keeping a moderate loss tangent. Such a compromise between high permittivity and low conductivity is crucial for using electrostrictive composites in energy harvesting applications. Composites are typically produced by processing techniques such as melt-mixing or copolymerization, which provide randomly distributed particles. Our strategy is to make self-assembled near-percolated networks of conductive fillers (reduced graphene oxide and black carbon) in PDMS (polydimethylsiloxane). The self-assembly will be reached by using an emulsion approach (oil in water or water in oil). This approach could finely control the filler distribution and thus the interconnected network of conductive particles. Indeed, in the case of an oil-in-water emulsion, the fillers can be segregated between oil droplets (PDMS). For water in oil emulsions, the idea is to disperse fillers inside water droplets, dispersed in the PDMS matrix. After the water evaporation, porous materials with conductive inclusions will be obtained. This ordered structure is expected to promote the formation of microcapacitors inside the polymer matrix to afford a high increase of permittivity while keeping moderate losses.

4 Electroactive polymers for sensor technologies:

4.1 Future of sensing :

Associated with the fast expansion of the Internet of Things, flexible and stretchable electronic devices are being integrated in modern electronics at a huge increasing rate. In particular, wearable *pressure* and *strain* sensors have attracted much attention in the recent years [57–59] due to their potential for a variety of different applications.

The demand for flexible *pressure sensors*, particularly with high sensitivity in low pressure regions, is very high. They are required for healthcare and medical diagnosis systems as well as in electronic systems, in particular for so-called “e-skin” systems [78]. Pressure sensors applied on the human body [79] could provide an exceptional level of diagnostic and monitoring capabilities. The human body can generate different regimes of pressure. For example, the low pressure regime <10kPa can be produced by intracranial pressure, the medium pressure regime <100kPa is generated by the heart rate or respiration rate [80]. Detection of these low pressures has great importance in diagnostics in cardiovascular disease or respiratory disorder and the reliability of diagnostics is directly linked to the sensitivity of pressure sensors.

In contrast, the demand for *strain sensors* is required for a higher pressure regime >100kPa. They can be attached on clothing or on the human body for applications in human motion monitoring in medicine (e.g. bending movements of the hands, arms, legs, etc.). Other fields, like robotics need stretchable strain sensors. For example, robots with good sensing abilities could extend their range of applications to include complex tasks such as caring for the elderly [81].

4.2 Transduction methods:

So as to measure the magnitude of a pressure/strain stimulus, an electrical conversion must be done. Several methods for accomplishing this conversion has been studied including piezoelectricity, piezoresistivity and variable capacitance (sometimes called piezocapacitance).

4.2.1 Piezoresistivity:

There are many possibilities for a material to change its resistance in response to a pressure or a strain including changes in the geometry, changes in the contact resistance between two materials and changes due interpaticle separation in composite materials.

The resistance of a material is defined as:

$$R = \frac{\rho e}{A} = \frac{e}{\sigma A} \tag{1.32}$$

Where ρ is the resistivity, σ is the conductivity, e is the thickness and A is the area of the material. In the case of piezoresitance due to geometrical effects, the thickness or the area change with the strain induced by pressure.

Two types of sensitivity can be defined for a sensor:

- The first is the sensitivity of the resistive sensor to strain, which is usually defined by the gauge factor (GF). It is the relative change of resistance R ($\frac{\Delta R}{R0}$), where R_0 is the resistance unstrained, to the mechanical strain (ε) as

$$\mathrm{GF} = \frac{\Delta R}{\varepsilon R_0} = \frac{\Delta \rho}{\varepsilon \rho_0} + 1 + 2\nu \tag{1.33}$$

If the material does not change its resistivity under strain (ie. $\Delta\rho = 0$), the gauge factor is only due to geometrical effects and is simply

$$\mathrm{GF} = 1 + 2\nu \tag{1.34}$$

The GF is equal to 2 in the case of incompressible materials (Poisson's ratio=0.5) and for metallic strain sensors. **FIG. 1.34** shows the typical structure of a metallic strain sensor whose resistance changes when the metal foil is strained. The change in the resistance is classically characterized using a Wheatstone bridge. Due to its rigid structure, the metallic strain sensor is used for small mechanical strains in rigid engineering structures.

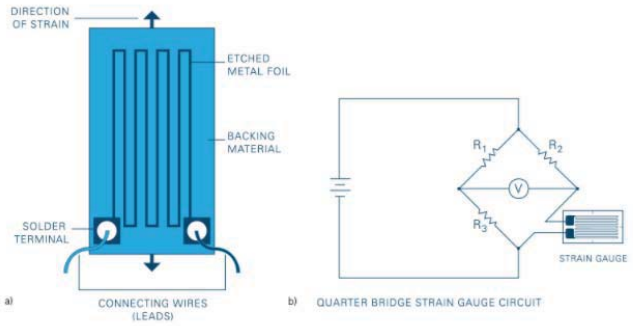


FIG. 1.34 - Metallic strain sensor.

Some other solid materials demonstrate a piezoresistive effect and develop a gauge factor superior to 2. This is the case for some semiconductors that can develop a resistive gauge factor a hundred times higher than that of metals [82]. The semiconductors generally used are germanium and silicon (amorphous or crystallized). They are based on a change of the carrier mobility (holes and electron) under strain which leads to a change in the resistivity/resistance [83]. However, solid sensors like metal or semiconductor sensors, need high pressure to be strained. Even if high GF has been

obtained, these sensors are incompatible with low strain regimes and are mainly employed in technical environments. Moreover, they only support limited strains under 5%, above the gauge mechanically fails.

- The second type of sensitivity is the sensitivity of the resistive sensor to pressure, which is usually defined by the gauge factor (GF) divided by the Young's modulus of the material.

$$\text{sensitivity to pressure } = \frac{\Delta R}{\sigma R_0} = \frac{\Delta R}{Y \varepsilon R_0} = \frac{GF}{Y} \tag{1.35}$$

Two main strategies have been explored to increase the pressure sensitivity. The first one is based on piezoresistive polymer composites which are easier integrable into small devices. The main mechanism, which leads to a change in resistivity of the composites, is the breaking and reforming of percolating pathways. These composites can be prepared by dispersing conductive fillers such as carbon black (CB), carbon nanotubes (CNT) or metallic nanoparticles into elastomers such as poly(dimethylsiloxane) (PDMS). Many of the reported resistive-type sensors function employ microstructuration of their composites. Indeed, the sensitivity to pressure can be highly improved by making materials porous with foam or sponge approaches. One of the first reported sponge structure for resistive sensors is based on porous PDMS filled with carbon nanotubes prepared by a sugar cube template (**FIG. 1.35** a)) [84]. Their material can be stretched and compressed up to 90%. Yao et al. [85] proposed a pressure sensor based on microstructure fractured graphene-wrapped PU sponge (**FIG. 1.35** b)). The resistivity changes because of the variation of the contact PU nanofibers during compressive deformation cycles. The sensitivity reported is 0.26 kPa^{-1}. However, even if the reported sensitivities are good, the complexity of controlling the pore morphology with sponges or foam is a drawback for this approach.

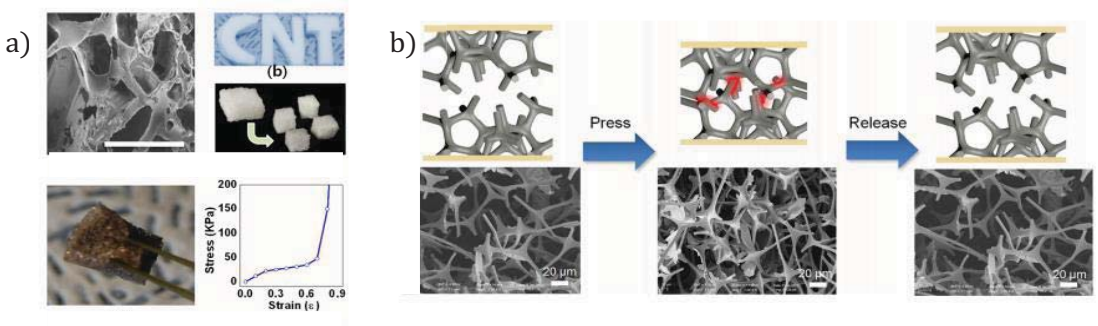
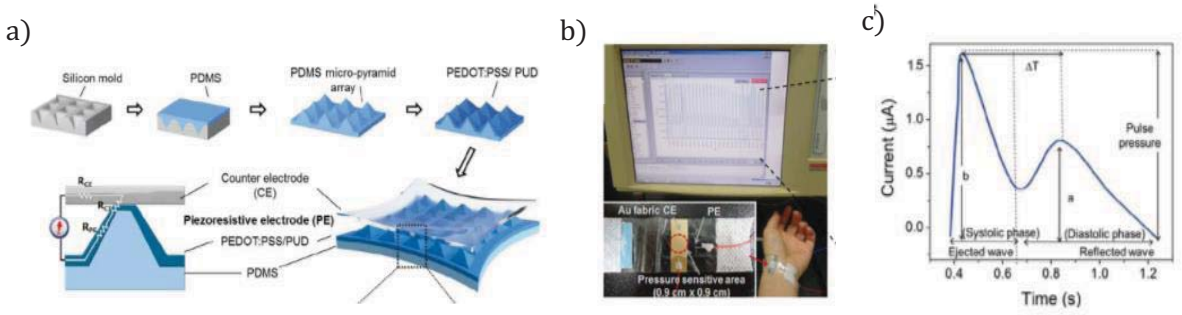


FIG. 1.35 - a) Resistive sensors based on porous PDMS filled with CNT prepared by a sugar cube template [84] b) Fractured graphene-wrapped PU sponge [85].

The second strategy is based on microstructuration of the active material. In this case, the change in resistance is due to the change of resistance in the contact interface between electrode and active material. Choong *et al.*[86] patterned PDMS with microsized pyramids (**FIG. 1.36** a)) with PEDOT:PSS coating. This structure leads to a piezoresitive electrode in which electrical resistance change with pressure. The resistive

sensor achieved a sensitivity of 10.3 kPa-1 when stretched by 40% thanks to the very small shape factor of the PDMS pyramids. They succeeded in measuring human pulse waveform thanks to their technology. Based on the same pyramid microstructuration, Zhu *et al.* [87] developed a pressure sensor with r-GO as resistive electrode with a sensitivity of -5.53 kPa^{-1} in the low pressure regime. However, the main drawback of this pyramid approach is the necessity of a very sensitive patterning process (Si mold) making the process, time consuming and less reproducibility.

FIG. 1.36 - a) Resistive pressure sensor based on PDMS microsized pyramids [86] b) Pulse wave signal recorded with PDMS pyramids sensor [86].



[80] summarized the performances of the last reported works in piezoresistive flexible pressure sensors **TAB. 1.7**. Sensitiveness of the main works are broadly dispersed from 0.26 kPa^{-1}[85] to 133 kPa^{-1} [88] with variable limits of detection.

TAB. 1.7 - Performances of the last reported piezoresistive flexible pressure sensors [80].

Active materials	Sensing mechanism	Flexibility/stretchability	Minimum detection	Maximum detection	Sensitivity
Graphene/PU sponge	Piezoresistive	Flexible	9 Pa	10 kPa	0.26 kPa^{-1}
Polypyrrole hollow-sphere	Piezoresistive	Flexible	1 Pa	11 kPa	133 kPa^{-1}
R-GO foam	Piezoresistive	Flexible	163 Pa	49 kPa	15.2 kPa^{-1}
CNT/PDMS porous	Piezoresistive	Stretchable [30%]	0.25 kPa	100 kPa	-
PEDOT:PSS/PUD micropyramid	Piezoresistive	Stretchable [50%]	23 Pa	8 kPa	10.3 kPa^{-1}
CNTs/PDMS inter-locked microdome	Piezoresistive	Flexible	0.2 Pa	59 kPa	15.1 kPa^{-1}
R-GO micropyramid	Piezoresistive	Flexible	1.5 Pa	1.4 kPa	5.5 kPa^{-1}
SWCNTs/PDMS microstructure	Piezoresistive	Flexible	0.6 Pa	1.2 kPa	1.8 kPa^{-1}
Microstructured gold thin film	Piezoresistive	Flexible	10.4 Pa	1.5 kPa	50.17 kPa^{-1}
Pressure-sensitive rubber (PSR) OFET	Piezoresistive	Flexible	10 kPa	30 kPa	–
PSR SWCNT-FET	Piezoresistive	Flexible	1 kPa	20 kPa	–
PSR nanowire (NW)-FET	Piezoresistive	Flexible	0.5 kPa	15 kPa	11.5 μS kP^{-1}

4.2.2 Piezocapacity:

Contrary to piezoresistive sensors, capacitive strain sensors are based on the variation of the capacitance. They are usually established with two stretchable electrodes between whom is placed in an elastomer dielectric film to form a well-known parallel plate capacitor.

The capacitive gauge factor is given by:

$$\mathrm{GF} = \frac{\Delta C}{\varepsilon C_0} \tag{1.36}$$

Where C_0 is the initial capacitance ($C_0 = \varepsilon_r \varepsilon_0 \frac{A}{e_0}$), ΔC is the capacitive change under the strain (ε), e_0 is the thickness at rest and A the area . The deformation brings the electrodes closer together (geometrical effect), resulting in an increase in capacitance. The theoretical value of GF for incompressible materials due to geometrical changes is

$$\mathrm{GF} = \frac{\Delta C}{\varepsilon C_0} = \frac{(1+\varepsilon)\mathrm{C}_0 - C_0}{\varepsilon C_0} = 1 \tag{1.37}$$

The development of deformable electrodes for capacitive strain sensors is one of the main requirements. Many capacitive strain sensors are based on CNT electrodes coated on elastomer such as PDMS [89,90]. Cohen *et al.* [89] developed CNT-based percolation electrodes in a capacitive strain sensor **FIG. 37**. The sensor showed reliability and linear performances with the highest reported GF (0.99 very close to the theoretical value) for a capacitive strain sensor.

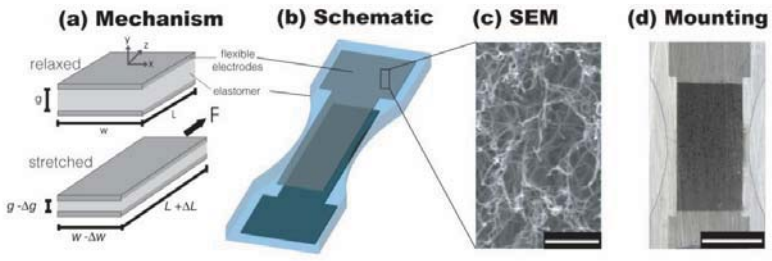


FIG. 37 - Capacitive strain sensor based on CNT electrodes [89].

Additionally, Yao and Zhu [91] described a capacitive strain sensor in which AgNWs were used as electrodes and Ecoflex as a dielectric layer. The sensor showed a linear response to large tensile strain up to 50% with a gauge factor of 0.7. The wearability of the sensor was demonstrated with the human body's movement, for example to monitor the skin strain associated with fingers.

Recently, S.R Kim *et al.* [92] developed a transparent and stretchable thin film capacitive strain sensor based on patterned Ag nanowire networks (AgNWs) on PDMS (**FIG. 1.38**).

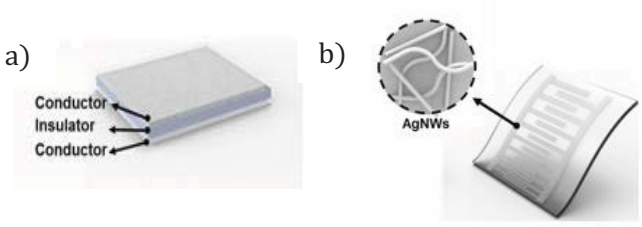


FIG. 1.38 - Capacitive strain sensor based on interdigitated AgNW electrodes [92].

Because of the interdigitated pattern, they used, for making the electrodes, the GF was increased to −2.0 and they can detect strain from 0 to 30%. The GF is larger than GF for traditional parallel plate capacitive sensor and leads to good linear response.

The majority of the reported works are based on piezocapacitance due to geometrical effects. This approach leads to small gauge factors around 1-2.

- The second type of sensitivity is the sensitivity of the capacitive sensor to pressure, which is usually defined by the gauge factor (GF) divided by the Young's modulus of the material.

$$\text{sensitivity to pressure } = \frac{\Delta C}{\sigma R_0} = \frac{\Delta C}{Y \varepsilon R_0} = \frac{GF}{Y} \qquad (1.38)$$

So as to get a high-pressure sensitivity, a low mechanical modulus is required. Therefore, dielectric polymers with small Young's modulus are traditionally used such as PDMS or Ecoflex. In this context, the capacitive sensitivity of the pyramid-structured PDMS film was investigating too. A sensitivity of 0.55 kPa^{-1} was reported compared to 0.02 kPa^{-1} for an unstructured film[93]. The structured film aims at subtly changing the permittivity value of the sensitive layer under pressure. Indeed, when the structured film is compressed the displaced volume is air, which has a lower dielectric constant (ε=1.0) than PDMS (ε~3.0). For increasing sensitivity to pressure, many groups [76,93,94] decided to integrate dielectric polymers as a gate dielectric layer in OFET (organic field effect transistor). Indeed, OFET could play the role of amplification and thus improve the sensibility. Still using the pyramid-structured PDMS and its integration in OFET, Schwartz et *al.* [76] advanced high sensitivity (8.4 kPa^{-1}) (**FIG. 1.39** a)b)).

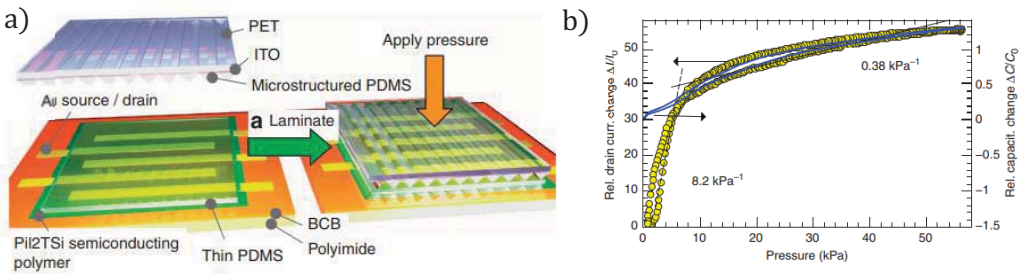


FIG. 1.39 - Pyramid-structured PDMS and its integration in OFET.

Even if low power consumption has been reported (<1 mW), the OFET needs to be used with a high bias voltage (-200 V), which could constitute a limitation for wearable electronic. Instead of using OFET, the sensitivity amplification can be obtained by using microhair structure[95]. This structure can transfer very subtile variation of pressure to sensor and maximize the contact between irregular surfaces, like skin, to sensor (**FIG. 1.40** a). Integrating pyramid-structured PDMS as sensor, C. Pang et al. developed a device with a sensitivity of 0.58 kPa^{-1}.

However, a decrease in the sensitivity and a large hysteresis were observed during consecutive runs (**FIG. 1.40** b)). This is mainly du to the slow recovery time of microhairs that are supposed to collapse after higher applied pressure.

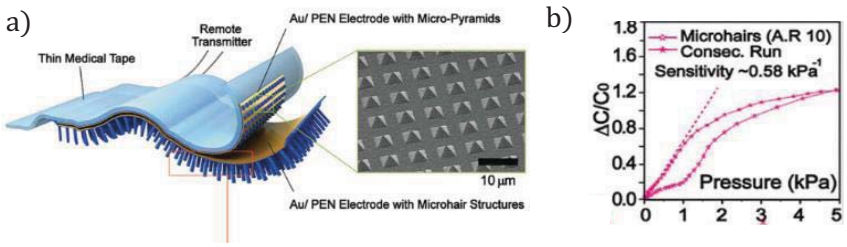


FIG. 1.40 - Pyramid-structured PDMS as sensor.

[80] summarized the performances of the last reported works in piezocapacitive flexible pressure sensors (**TAB. 1.8**). Sensitiveness of the main works are broadly dispersed from 158.6 kPa^{-1}[94] to 0.5 kPa^{-1} [93] with variable limits of detection.

TAB. 1.8 - Performances of the last reported piezocapacitive flexible pressure sensors [80].

Active materials	Sensing mechanism	Flexibility/stretchability	Minimum detection	Maximum detection	Sensitivity
Fluorosilicone/air gap	Capacitance	Flexible	0.5 kPa	190 kPa	0.91 kPa^{-1}
Ionic	Capacitance	Stretchable [500%]	1 kPa	40 kPa	–
Ecoflex	Capacitance	Stretchable [50%]	–	1.3 MPa	1.6 MPa^{-1}
Ecoflex	Capacitance	Stretchable [= 50%]	50 kPa	1 MPa	0.23MPa^{-1}
Porous PDMS/air gap	Capacitance	Stretchable [30%]	2.5 Pa	20 kPa	0.7 kPa^{-1}
PDMS microhairy	Capacitance	Flexible	–	5 kPa	0.58 kPa^{-2}
Suspended gate OFET	Capacitance	Flexible	<0.5 Pa	20 kPa	158.6 kPa^{-1}
PDMS microstructure OFET	Capacitance	Flexible	3 Pa	20 kPa	0.55 kPa^{-1}
PDMS microstructure OFET	Capacitance	Flexible	–	60 kPa	8.2 kPa^{-1}

In addition to constant efforts for improving the sensitivity, self powering the sensor is become a major concern. This unique combination of high sensitivity and energy harvesting will facilitate applications in wearable electronics. Park et *al.* [96] first reported a stretchable energy-harvesting electronic-skin device capable of detecting subtile pressure changes and generating energy from mechanical. The sensor is composed of an air gap between a porous PDMS film and a single-walled carbon nanotube (SWCNT) film (**FIG. 1.41** a)b)). The change in the capacitance is due to the change in the distance between the top and bottom electrodes. The capacitive sensor is capable of power generation through surface charges on the PDMS surface induced by UVO treatment (**FIG. 1.41** c)). Thanks to a triboelectric effect, charges are moved between the two electrodes when their distance is changed, resulting in current flow in an external circuit. A pressure sensitivity of 0.7 kPa^{-1} is achieved in the pressure region <1 kPa with power generation of tens of $\mu W/cm^2$ from a gentle finger touch.

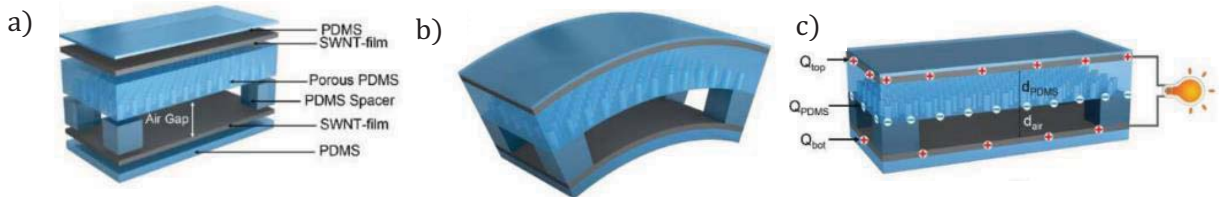


FIG. 1.41 – Capacitive sensor capable of power generation.

4.2.3 Our strategy:

Many efforts have been devoted to the developpement of flexible and wearable pressure/strain sensors for applications in human activity monitoring and personal healthcare. Sensibility has constantly been enhanced by integrating the sensor elements with an OFET or by using microstructure film. Both strategies have drawbacks. Firstly, OFET need to be used with a high bias voltage to present high sensitivity. This could, consequently, be a limitation for wearable electronic. For the second, the main drawback is the necessity of a very sensitive patterning process (Si mold) making the process time consuming and less reproductible.

Compared to piezoresistive devices piezocapacitive sensors offer some advantages such as lower power consumption and better reproducibility. The resistivity is subjected to environmental and specific conditions (humidity, temperature, damage, etc.) which could lead to unreliable data. Besides, controlling the piezoresistivity of composites is complex due to the breaking and reforming of percolating pathways. By contrast, piezocapacitive sensors are easier to process and easier to shape into different forms.

In this research project, we propose to develop capacitive pressure sensors with electrostrictive materials. Indeed, until now capacitive pressure sensors are based on variations of permittivity due to the displacement of air on pyramid-structured PDMS. We believe that taking advantages of permittivity variation of electrostrictive materials and the use of low Young's modulus elastomeric polymers, we could create highly sensitive pressure-sensor materials.

Furthermore, as electrostrictives materials can be used for mechanical energy harvesting, pressure sensors based on this approach could lead to self powered sensitive components. Without a doubt, the integration of sensors will be met through the emergence of sensing systems with power generation.

Take home message – Chapter 1

Until now, electrostrictive composites have been mainly studied for actuator applications. That is why, we have chosen to focus our research on designing new electrostrictive materials for two other promising applications: mechanical energy harvesting and sensors.

1- The first objective is to develop electrostrictive materials. We propose to add conductive or high permittivity nano-fillers to very soft elastomeric polymers. The composites will be obtained by using emulsion approaches (oil in water or water in oil). Nearly-percolated composites are expected to increase their permittivity while keeping a moderate dielectric losses and conductivity.

2- The second objective is to use the previous developed electrostrictive materials for vibrational energy harvesting. We want to measure their recovering capabilities and generate electrical energy in response to mechanical vibrations. The integration of the materials into electromechanical systems, as close to applications as possible will be pursued.

3- The last objective is to develop capacitive pressure sensors with electrostrictive materials. We believe that taking advantages of permittivity variation of electrostrictive materials and the use of low Young's modulus elastomeric polymers, we could create very pressure-sensitive materials. We want to finely characterize materials as sensors and developed a proof of concept of their relevance in this field.

[1] S. Rose, A. Prevoteau, P. Elzière, D. Hourdet, A. Marcellan, L. Leibler, Nanoparticle solutions as adhesives for gels and biological tissues, Nature. 505 (2014) 382–385. doi:10.1038/nature12806.

[2] P. Roach, N.J. Shirtcliffe, M.I. Newton, Progess in superhydrophobic surface development, Soft Matter. 4 (2008) 224–240. doi:10.1039/B712575P.

[3] D. Montarnal, M. Capelot, F. Tournilhac, L. Leibler, Silica-Like Malleable Materials from Permanent Organic Networks, Science. 334 (2011) 965–968. doi:10.1126/science.1212648.

[4] Q. Pei, M.A. Rosenthal, R. Pelrine, S. Stanford, R.D. Kornbluh, Multifunctional electroelastomer roll actuators and their application for biomimetic walking robots, in: Y. Bar-Cohen (Ed.), 2003: p. 281. doi:10.1117/12.484392.

[5] F. Xia, S. Tadigadapa, Q.M. Zhang, Electroactive polymer based microfluidic pump, Sensors and Actuators A: Physical. 125 (2006) 346–352. doi:10.1016/j.sna.2005.06.026.

[6] S. Yun, S. Park, S. Nam, B. Park, S.K. Park, S. Mun, J.M. Lim, K.-U. Kyung, An electro-active polymer based lens module for dynamically varying focal system, Applied Physics Letters. 109 (2016) 141908. doi:10.1063/1.4964426.

[7] J. Gubbi, R. Buyya, S. Marusic, M. Palaniswami, Internet of Things (IoT): A vision, architectural elements, and future directions, Future Generation Computer Systems. 29 (2013) 1645–1660. doi:10.1016/j.future.2013.01.010.

[8] F. Xia, L.T. Yang, L. Wang, A. Vinel, Internet of Things, International Journal of Communication Systems. 25 (2012) 1101–1102. doi:10.1002/dac.2417.

[9] L. Atzori, A. Iera, G. Morabito, The Internet of Things: A survey, Computer Networks. 54 (2010) 2787–2805. doi:10.1016/j.comnet.2010.05.010.

[10] V.M. Rohokale, N.R. Prasad, R. Prasad, A cooperative Internet of Things (IoT) for rural healthcare monitoring and control, in: IEEE, 2011: pp. 1–6. doi:10.1109/WIRELESSVITAE.2011.5940920.

[11] Industry 4.0: the industrial internet of things, Springer Science+Business Media, New York, NY, 2016.

[12] C. Buckl, S. Sommer, A. Scholz, A. Knoll, A. Kemper, J. Heuer, A. Schmitt, Services to the Field: An Approach for Resource Constrained Sensor/Actor Networks, in: IEEE, 2009: pp. 476–481. doi:10.1109/WAINA.2009.20.

[13] The internet of things, (n.d.). https://www.cisco.com/c/fr_fr/solutions/internet-of-things/overview.html.

[14] S. Hanson, M. Seok, Y.-S. Lin, Z. Foo, D. Kim, Y. Lee, N. Liu, D. Sylvester, D. Blaauw, A Low-Voltage Processor for Sensing Applications With Picowatt Standby Mode, IEEE Journal of Solid-State Circuits. 44 (2009) 1145–1155. doi:10.1109/JSSC.2009.2014205.

[15] H. Jayakumar, K. Lee, W.S. Lee, A. Raha, Y. Kim, V. Raghunathan, Powering the internet of things, in: ACM Press, 2014: pp. 375–380. doi:10.1145/2627369.2631644.

[16] Yu-Shiang Lin, D. Sylvester, D. Blaauw, An ultra low power 1V, 220nW temperature sensor for passive wireless applications, in: IEEE, 2008: pp. 507–510. doi:10.1109/CICC.2008.4672133.

[17] S. Boisseau, G. Despesse, B. Ahmed, Electrostatic Conversion for Vibration Energy Harvesting, in: M. Lallart (Ed.), Small-Scale Energy Harvesting, InTech, 2012. doi:10.5772/51360.

[18] K. Yoshikawa, H. Kawasaki, W. Yoshida, T. Irie, K. Konishi, K. Nakano, T. Uto, D. Adachi, M. Kanematsu, H. Uzu, K. Yamamoto, Silicon heterojunction solar cell with interdigitated back contacts for a photoconversion efficiency over 26%, Nature Energy. 2 (2017) 17032. doi:10.1038/nenergy.2017.32.

[19] F. Dimroth, M. Grave, P. Beutel, U. Fiedeler, C. Karcher, T.N.D. Tibbits, E. Oliva, G. Siefer, M. Schachtner, A. Wekkeli, A.W. Bett, R. Krause, M. Piccin, N. Blanc, C. Drazek, E. Guiot, B. Ghyselen, T. Salvetat, A. Tauzin, T. Signamarcheix, A. Dobrich, T. Hannappel, K. Schwarzburg, Wafer bonded four-junction GaInP/GaAs//GaInAsP/GaInAs concentrator solar cells with 44.7% efficiency: Wafer bonded four-junction concentrator solar cells with 44.7% efficiency, Progress in Photovoltaics: Research and Applications. 22 (2014) 277–282. doi:10.1002/pip.2475.

[20] W. He, G. Zhang, X. Zhang, J. Ji, G. Li, X. Zhao, Recent development and application of thermoelectric generator and cooler, Applied Energy. 143 (2015) 1–25. doi:10.1016/j.apenergy.2014.12.075.

[21] J. Yan, X. Liao, D. Yan, Y. Chen, Review of Micro Thermoelectric Generator, Journal of Microelectromechanical Systems. 27 (2018) 1–18. doi:10.1109/JMEMS.2017.2782748.

[22] K.T. Settaluri, H. Lo, R.J. Ram, Thin Thermoelectric Generator System for Body Energy Harvesting, Journal of Electronic Materials. 41 (2012) 984–988. doi:10.1007/s11664-011-1834-3.

[23] C.B. Vining, An inconvenient truth about thermoelectrics, Nature Materials. 8 (2009) 83–85. doi:10.1038/nmat2361.

[24] L.B. Kong, T. Li, H.H. Hng, F. Boey, T. Zhang, S. Li, Waste Mechanical Energy Harvesting (I): Piezoelectric Effect, in: Waste Energy Harvesting, Springer Berlin Heidelberg, Berlin, Heidelberg, 2014: pp. 19–133. doi:10.1007/978-3-642-54634-1_2.

[25] C.B. Williams, R.B. Yates, Analysis of a micro-electric generator for microsystems, Sensors and Actuators A: Physical. 52 (1996) 8–11. doi:10.1016/0924-4247(96)80118-X.

[26] J.L. GonzáLez, A. Rubio, F. Moll, Human Powered Piezoelectric Batteries to Supply Power to Wearable Electronic Devices, International Journal of the Society of Materials Engineering for Resources. 10 (2002) 34–40. doi:10.5188/ijsmer.10.34.

[27] A. Erturk, D.J. Inman, Piezoelectric energy harvesting, Wiley, Chichester, 2011.

[28] S.-B. Kim, H. Park, S.-H. Kim, H.C. Wikle, J.-H. Park, D.-J. Kim, Comparison of MEMS PZT Cantilevers Based on 31 and 33 Modes for Vibration Energy Harvesting, Journal of Microelectromechanical Systems. 22 (2013) 26–33. doi:10.1109/JMEMS.2012.2213069.

[29] G. Tang, J. Liu, B. Yang, J. Luo, H. Liu, Y. Li, C. Yang, D. He, V.D. Dao, K. Tanaka, S. Sugiyama, Fabrication and analysis of high-performance piezoelectric MEMS generators, Journal of Micromechanics and Microengineering. 22 (2012) 065017. doi:10.1088/0960-1317/22/6/065017.

[30] K.V. Selvan, M.S. Mohamed Ali, Micro-scale energy harvesting devices: Review of methodological performances in the last decade, Renewable and Sustainable Energy Reviews. 54 (2016) 1035–1047. doi:10.1016/j.rser.2015.10.046.

[31] K.-I. Park, S. Xu, Y. Liu, G.-T. Hwang, S.-J.L. Kang, Z.L. Wang, K.J. Lee, Piezoelectric $BaTiO_3$ Thin Film Nanogenerator on Plastic Substrates, Nano Letters. 10 (2010) 4939–4943. doi:10.1021/nl102959k.

[32] J. Ihlefeld, B. Laughlin, A. Hunt-Lowery, W. Borland, A. Kingon, J.-P. Maria, Copper Compatible Barium Titanate Thin Films for Embedded Passives, Journal of Electroceramics. 14 (2005) 95–102. doi:10.1007/s10832-005-0866-6.

[33] S. Priya, H.-C. Song, Y. Zhou, R. Varghese, A. Chopra, S.-G. Kim, I. Kanno, L. Wu, D.S. Ha, J. Ryu, R.G. Polcawich, A Review on Piezoelectric Energy Harvesting: Materials, Methods, and Circuits, Energy Harvesting and Systems. 4 (2017). doi:10.1515/ehs-2016-0028.

[34] A. Hajati, S.-G. Kim, Ultra-wide bandwidth piezoelectric energy harvesting, Applied Physics Letters. 99 (2011) 083105. doi:10.1063/1.3629551.

[35] F.-R. Fan, Z.-Q. Tian, Z. Lin Wang, Flexible triboelectric generator, Nano Energy. 1 (2012) 328–334. doi:10.1016/j.nanoen.2012.01.004.

[36] S. Niu, Y. Liu, X. Chen, S. Wang, Y.S. Zhou, L. Lin, Y. Xie, Z.L. Wang, Theory of freestanding triboelectric-layer-based nanogenerators, Nano Energy. 12 (2015) 760–774. doi:10.1016/j.nanoen.2015.01.013.

[37] D.M. Gooding, G.K. Kaufman, Tribocharging and the Triboelectric Series, in: R.A. Scott (Ed.), Encyclopedia of Inorganic and Bioinorganic Chemistry, John Wiley & Sons, Ltd, Chichester, UK, 2014: pp. 1–9. doi:10.1002/9781119951438.eibc2239.

[38] Y. Wang, Y. Yang, Z.L. Wang, Triboelectric nanogenerators as flexible power sources, Npj Flexible Electronics. 1 (2017). doi:10.1038/s41528-017-0007-8.

[39] Z.L. Wang, J. Chen, L. Lin, Progress in triboelectric nanogenerators as a new energy technology and self-powered sensors, Energy & Environmental Science. 8 (2015) 2250–2282. doi:10.1039/C5EE01532D.

[40] G. Zhu, Y.S. Zhou, P. Bai, X.S. Meng, Q. Jing, J. Chen, Z.L. Wang, A Shape-Adaptive Thin-Film-Based Approach for 50% High-Efficiency Energy Generation Through Micro-Grating Sliding Electrification, Advanced Materials. 26 (2014) 3788–3796. doi:10.1002/adma.201400021.

[41] X. Fan, J. Chen, J. Yang, P. Bai, Z. Li, Z.L. Wang, Ultrathin, Rollable, Paper-Based Triboelectric Nanogenerator for Acoustic Energy Harvesting and Self-Powered Sound Recording, ACS Nano. 9 (2015) 4236–4243. doi:10.1021/acsnano.5b00618.

[42] J. Chen, J. Yang, Z. Li, X. Fan, Y. Zi, Q. Jing, H. Guo, Z. Wen, K.C. Pradel, S. Niu, Z.L. Wang, Networks of Triboelectric Nanogenerators for Harvesting Water Wave Energy: A Potential Approach toward Blue Energy, ACS Nano. 9 (2015) 3324–3331. doi:10.1021/acsnano.5b00534.

[43] D.H. Huynh, T.C. Nguyen, P.D. Nguyen, C.D. Abeyrathne, M.S. Hossain, R. Evans, E. Skafidas, Environmentally friendly power generator based on moving liquid dielectric and double layer effect, Scientific Reports. 6 (2016) 26708. doi:10.1038/srep26708.

[44] S.-H. Kwon, J. Park, W.K. Kim, Y. Yang, E. Lee, C.J. Han, S.Y. Park, J. Lee, Y.S. Kim, An effective energy harvesting method from a natural water motion active transducer, Energy Environ. Sci. 7 (2014) 3279–3283. doi:10.1039/C4EE00588K.

[45] J.K. Moon, J. Jeong, D. Lee, H.K. Pak, Electrical power generation by mechanically modulating electrical double layers, Nature Communications. 4 (2013) 1487. doi:10.1038/ncomms2485.

[46] W. Kong, P. Cao, X. He, L. Yu, X. Ma, Y. He, L. Lu, X. Zhang, Y. Deng, Ionic liquid based vibrational energy harvester by periodically squeezing the liquid bridge, RSC Adv. 4 (2014) 19356–19361. doi:10.1039/C4RA00629A.

[47] C.G. Zoski, J. Leddy, D. Dunwoody, A.J. Bard, Electrochemical methods: fundamentals and applications, second edition [by] Allen J. Bard, Larry R. Faulkner, Wiley, New York, 2002.

[48] S.H. Kim, C.S. Haines, N. Li, K.J. Kim, T.J. Mun, C. Choi, J. Di, Y.J. Oh, J.P. Oviedo, J. Bykova, S. Fang, N. Jiang, Z. Liu, R. Wang, P. Kumar, R. Qiao, S. Priya, K. Cho, M. Kim, M.S. Lucas, L.F. Drummy, B. Maruyama, D.Y. Lee, X. Lepró, E. Gao, D. Albarq, R. Ovalle-Robles, S.J. Kim, R.H.

Baughman, Harvesting electrical energy from carbon nanotube yarn twist, Science. 357 (2017) 773–778. doi:10.1126/science.aam8771.

[49] L. Lebrun, D. Guyomar, B. Guiffard, P.-J. Cottinet, C. Putson, The Characterisation of the harvesting capabilities of an electrostrictive polymer composite, Sensors and Actuators A: Physical. 153 (2009) 251–257. doi:10.1016/j.sna.2009.05.009.

[50] K.S. Ramadan, D. Sameoto, S. Evoy, A review of piezoelectric polymers as functional materials for electromechanical transducers, Smart Materials and Structures. 23 (2014) 033001. doi:10.1088/0964-1726/23/3/033001.

[51] P. Martins, A.C. Lopes, S. Lanceros-Mendez, Electroactive phases of poly(vinylidene fluoride): Determination, processing and applications, Progress in Polymer Science. 39 (2014) 683–706. doi:10.1016/j.progpolymsci.2013.07.006.

[52] V. Sencadas, R. Gregorio, S. Lanceros-Mendez, α to β Phase Transformation and Microestructural Changes of PVDF Films Induced by Uniaxial Stretch, Journal of Macromolecular Science, Part B. 48 (2009) 514–525. doi:10.1080/00222340902837527.

[53] W. Wang, S. Zhang, L. Srisombat, T.R. Lee, R.C. Advincula, Gold-Nanoparticle- and Gold-Nanoshell-Induced Polymorphism in Poly(vinylidene fluoride), Macromolecular Materials and Engineering. 296 (2011) 178–184. doi:10.1002/mame.201000271.

[54] J. Zheng, A. He, J. Li, C.C. Han, Polymorphism Control of Poly(vinylidene fluoride) through Electrospinning, Macromolecular Rapid Communications. 28 (2007) 2159–2162. doi:10.1002/marc.200700544.

[55] Z. Li, Y. Wang, Z.-Y. Cheng, Electromechanical properties of poly(vinylidene-fluoride-chlorotrifluoroethylene) copolymer, Applied Physics Letters. 88 (2006) 062904. doi:10.1063/1.2170425.

[56] N.S. Shenck, J.A. Paradiso, Energy scavenging with shoe-mounted piezoelectrics, IEEE Micro. 21 (2001) 30–42. doi:10.1109/40.928763.

[57] H.Y. Lee, Y. Peng, Y.M. Shkel, Strain-dielectric response of dielectrics as foundation for electrostriction stresses, Journal of Applied Physics. 98 (2005) 074104. doi:10.1063/1.2073977.

[58] I. Krakovský, T. Romijn, A. Posthuma de Boer, A few remarks on the electrostriction of elastomers, Journal of Applied Physics. 85 (1999) 628–629. doi:10.1063/1.369418.

[59] Y. Bar-Cohen, ed., Electroactive polymer (EAP) actuators as artificial muscles: reality, potential, and challenges, 2nd ed, SPIE Press, Bellingham, Wash, 2004.

[60] K. Ren, Y. Liu, H. Hofmann, Q.M. Zhang, J. Blottman, An active energy harvesting scheme with an electroactive polymer, Applied Physics Letters. 91 (2007) 132910. doi:10.1063/1.2793172.

[61] Yiming Liu, Kai Liang Ren, H.F. Hofmann, Qiming Zhang, Investigation of electrostrictive polymers for energy harvesting, IEEE Transactions on Ultrasonics, Ferroelectrics and Frequency Control. 52 (2005) 2411–2417. doi:10.1109/TUFFC.2005.1563285.

[62] M. Lallart, P.-J. Cottinet, D. Guyomar, L. Lebrun, Electrostrictive polymers for mechanical energy harvesting, Journal of Polymer Science Part B: Polymer Physics. 50 (2012) 523–535. doi:10.1002/polb.23045.

[63] P.-J. Cottinet, M. Lallart, D. Guyomar, B. Guiffard, L. Lebrun, G. Sebald, C. Putson, Analysis of AC-DC conversion for energy harvesting using an electrostrictive polymer P(VDF-TrFE-CFE), IEEE Transactions on Ultrasonics, Ferroelectrics and Frequency Control. 58 (2011) 30–42. doi:10.1109/TUFFC.2011.1771.

[64] R. Liu, Q. Zhang, L.E. Cross, Experimental investigation of electrostrictive polarization biased direct apparent piezoelectric properties in polyurethane elastomer under quasistatic conditions, Journal of Applied Polymer Science. 73 (1999) 2603–2609. doi:10.1002/(SICI)1097-4628(19990923)73:13<2603::AID-APP7>3.0.CO;2-R.

[65] F. Ganet, M.Q. Le, J.F. Capsal, P. Lermusiaux, L. Petit, A. Millon, P.J. Cottinet, Development of a smart guide wire using an electrostrictive polymer: option for steerable orientation and force feedback, Scientific Reports. 5 (2016). doi:10.1038/srep18593.

[66] P.-J. Cottinet, D. Guyomar, B. Guiffard, C. Putson, L. Lebrun, Modeling and experimentation on an electrostrictive polymer composite for energy harvesting, IEEE Transactions on Ultrasonics, Ferroelectrics and Frequency Control. 57 (2010) 774–784. doi:10.1109/TUFFC.2010.1481.

[67] D. Jaaoh, C. Putson, N. Muensit, Enhanced strain response and energy harvesting capabilities of electrostrictive polyurethane composites filled with conducting polyaniline, Composites Science and Technology. 122 (2016) 97–103. doi:10.1016/j.compscitech.2015.11.020.

[68] M. Lallart, P.-J. Cottinet, L. Lebrun, B. Guiffard, D. Guyomar, Evaluation of energy harvesting performance of electrostrictive polymer and carbon-filled terpolymer composites, Journal of Applied Physics. 108 (2010) 034901. doi:10.1063/1.3456084.

[69] Q.M. Zhang, Giant Electrostriction and Relaxor Ferroelectric Behavior in Electron-Irradiated Poly(vinylidene fluoride-trifluoroethylene) Copolymer, Science. 280 (1998) 2101–2104. doi:10.1126/science.280.5372.2101.

[70] F. Kremer, A. Schönhals, eds., Broadband dielectric spectroscopy, Springer, Berlin ; New York, 2003.

[71] X. Yin, J.-F. Capsal, D. Guyomar, A comprehensive investigation of poly(vinylidene fluoride-trifluoroethylene-chlorofluoroethylene) terpolymer nanocomposites with carbon black for electrostrictive applications, Applied Physics Letters. 104 (2014) 052913. doi:10.1063/1.4864160.

[72] J. Yuan, A. Luna, W. Neri, C. Zakri, A. Colin, P. Poulin, Giant Electrostriction of Soft Nanocomposites Based on Liquid Crystalline Graphene, ACS Nano. 12 (2018) 1688–1695. doi:10.1021/acsnano.7b08332.

[73] G. Moretti, G.P.R. Papini, M. Righi, D. Forehand, D. Ingram, R. Vertechy, M. Fontana, Resonant wave energy harvester based on dielectric elastomer generator, Smart Materials and Structures. 27 (2018) 035015. doi:10.1088/1361-665X/aaab1e.

[74] H. Nesser, H. Debéda, J. Yuan, A. Colin, P. Poulin, I. Dufour, C. Ayela, All-organic microelectromechanical systems integrating electrostrictive nanocomposite for mechanical energy harvesting, Nano Energy. 44 (2018) 1–6. doi:10.1016/j.nanoen.2017.11.036.

[75] T. Yang, X. Jiang, Y. Zhong, X. Zhao, S. Lin, J. Li, X. Li, J. Xu, Z. Li, H. Zhu, A Wearable and Highly Sensitive Graphene Strain Sensor for Precise Home-Based Pulse Wave Monitoring, ACS Sensors. 2 (2017) 967–974. doi:10.1021/acssensors.7b00230.

[76] G. Schwartz, B.C.-K. Tee, J. Mei, A.L. Appleton, D.H. Kim, H. Wang, Z. Bao, Flexible polymer transistors with high pressure sensitivity for application in electronic skin and health monitoring, Nature Communications. 4 (2013) 1859. doi:10.1038/ncomms2832.

[77] S. Zhao, J. Li, D. Cao, G. Zhang, J. Li, K. Li, Y. Yang, W. Wang, Y. Jin, R. Sun, C.-P. Wong, Recent Advancements in Flexible and Stretchable Electrodes for Electromechanical Sensors: Strategies, Materials, and Features, ACS Applied Materials & Interfaces. 9 (2017) 12147–12164. doi:10.1021/acsami.6b13800.

[78] M.L. Hammock, A. Chortos, B.C.-K. Tee, J.B.-H. Tok, Z. Bao, 25th Anniversary Article: The Evolution of Electronic Skin (E-Skin): A Brief History, Design Considerations, and Recent Progress, Advanced Materials. 25 (2013) 5997–6038. doi:10.1002/adma.201302240.

[79] S. Gong, D.T.H. Lai, B. Su, K.J. Si, Z. Ma, L.W. Yap, P. Guo, W. Cheng, Highly Stretchy Black Gold E-Skin Nanopatches as Highly Sensitive Wearable Biomedical Sensors, Advanced Electronic Materials. 1 (2015) 1400063. doi:10.1002/aelm.201400063.

[80] T.Q. Trung, N.-E. Lee, Flexible and Stretchable Physical Sensor Integrated Platforms for Wearable Human-Activity Monitoringand Personal Healthcare, Advanced Materials. 28 (2016) 4338–4372. doi:10.1002/adma.201504244.

[81] J. Tegin, J. Wikander, Tactile sensing in intelligent robotic manipulation – a review, Industrial Robot: An International Journal. 32 (2005) 64–70. doi:10.1108/01439910510573318.

[82] S. Middelhoek, S.A. Audet, Silicon sensors, Acad. Pr, London, 1989.

[83] S.S. Kumar, B.D. Pant, Design principles and considerations for the 'ideal' silicon piezoresistive pressure sensor: a focused review, Microsystem Technologies. 20 (2014) 1213–1247. doi:10.1007/s00542-014-2215-7.

[84] Piezoresistive behavior of porous carbon nanotube-thermoplastic polyurethane conductive nanocomposites with ultrahigh compressibility, Applied Physics Letters. 108 (2016) 011904. doi:10.1063/1.4939265.

[85] H.-B. Yao, J. Ge, C.-F. Wang, X. Wang, W. Hu, Z.-J. Zheng, Y. Ni, S.-H. Yu, A Flexible and Highly Pressure-Sensitive Graphene-Polyurethane Sponge Based on Fractured Microstructure Design, Advanced Materials. 25 (2013) 6692–6698. doi:10.1002/adma.201303041.

[86] C.-L. Choong, M.-B. Shim, B.-S. Lee, S. Jeon, D.-S. Ko, T.-H. Kang, J. Bae, S.H. Lee, K.-E. Byun, J. Im, Y.J. Jeong, C.E. Park, J.-J. Park, U.-I. Chung, Highly Stretchable Resistive Pressure Sensors Using a Conductive Elastomeric Composite on a Micropyramid Array, Advanced Materials. 26 (2014) 3451–3458. doi:10.1002/adma.201305182.

[87] B. Zhu, Z. Niu, H. Wang, W.R. Leow, H. Wang, Y. Li, L. Zheng, J. Wei, F. Huo, X. Chen, Microstructured Graphene Arrays for Highly Sensitive Flexible Tactile Sensors, Small. 10 (2014) 3625–3631. doi:10.1002/smll.201401207.

[88] L. Pan, A. Chortos, G. Yu, Y. Wang, S. Isaacson, R. Allen, Y. Shi, R. Dauskardt, Z. Bao, An ultra-sensitive resistive pressure sensor based on hollow-sphere microstructure induced elasticity in conducting polymer film, Nature Communications. 5 (2014). doi:10.1038/ncomms4002.

[89] D.J. Cohen, D. Mitra, K. Peterson, M.M. Maharbiz, A Highly Elastic, Capacitive Strain Gauge Based on Percolating Nanotube Networks, Nano Letters. 12 (2012) 1821–1825. doi:10.1021/nl204052z.

[90] L. Cai, L. Song, P. Luan, Q. Zhang, N. Zhang, Q. Gao, D. Zhao, X. Zhang, M. Tu, F. Yang, W. Zhou, Q. Fan, J. Luo, W. Zhou, P.M. Ajayan, S. Xie, Super-stretchable, Transparent Carbon Nanotube-Based Capacitive Strain Sensors for Human Motion Detection, Scientific Reports. 3 (2013). doi:10.1038/srep03048.

[91] S. Yao, Y. Zhu, Wearable multifunctional sensors using printed stretchable conductors made of silver nanowires, Nanoscale. 6 (2014) 2345. doi:10.1039/c3nr05496a.

[92] S.-R. Kim, J.-H. Kim, J.-W. Park, Wearable and Transparent Capacitive Strain Sensor with High Sensitivity Based on Patterned Ag Nanowire Networks, ACS Applied Materials & Interfaces. 9 (2017) 26407–26416. doi:10.1021/acsami.7b06474.

[93] S.C.B. Mannsfeld, B.C.-K. Tee, R.M. Stoltenberg, C.V.H.-H. Chen, S. Barman, B.V.O. Muir, A.N. Sokolov, C. Reese, Z. Bao, Highly sensitive flexible pressure sensors with microstructured rubber dielectric layers, Nature Materials. 9 (2010) 859–864. doi:10.1038/nmat2834.

[94] Y. Zang, F. Zhang, D. Huang, X. Gao, C. Di, D. Zhu, Flexible suspended gate organic thin-film transistors for ultra-sensitive pressure detection, Nature Communications. 6 (2015). doi:10.1038/ncomms7269.

[95] C. Pang, J.H. Koo, A. Nguyen, J.M. Caves, M.-G. Kim, A. Chortos, K. Kim, P.J. Wang, J.B.-H. Tok, Z. Bao, Highly Skin-Conformal Microhairy Sensor for Pulse Signal Amplification, Advanced Materials. 27 (2015) 634–640. doi:10.1002/adma.201403807.

[96] S. Park, H. Kim, M. Vosgueritchian, S. Cheon, H. Kim, J.H. Koo, T.R. Kim, S. Lee, G. Schwartz, H. Chang, Z. Bao, Stretchable Energy-Harvesting Tactile Electronic Skin Capable of Differentiating Multiple Mechanical Stimuli Modes, Advanced Materials. 26 (2014) 7324–7332. doi:10.1002/adma.201402574.

2. Materials and methods for the production of electrostrictive composites and their characterization

Summary:

This chapter is first devoted to the impedance measurements. We present general considerations on impedance and practical methods for measuring dielectric properties of materials. We developed characterization methods and setups for the measurement of the electrostrictive coefficients and the power recovering of dielectric materials. Finally, we expose two new routes to synthesize electroactive composites via emulsions templating effects. The first is based on an oil-in-water emulsion loaded with reduced graphene oxide conductive fillers. The second is based on a water-in-oil emulsion loaded with carbon black fillers.

1.1 Impedance measurements:

1.1.1 General considerations on dielectric materials:

A dielectric is an electrical insulator that can be polarized by an applied electric field. In these materials, because very few charges are free, the circulation of a significant electric current is prevented. However, the charges present can move locally under the action of an external electric field $\boldsymbol{E}$ and cause the change of the barycenter of charges, producing a dielectric polarization $\boldsymbol{P}$.

From a microscopic point of view, several phenomena occur under the effect of an electric field, leading to the polarization [1]:

- *Electronic polarization* : this is the movement of electronic orbits compared to the nucleus.
- *Ionic polarization:* this is the movement of ions in the crystal lattice.
- *Orientation polarization:* this is the orientation of the microscopic electric dipoles.
- *The interfacial polarization:* this is the movement of free carriers at interfaces between different phases constituting the material. It mainly occurs in composite materials. This polarization is also known as Maxwell–Wagner–Sillars (MWS) polarization.

At lower frequencies, the four polarizations contribute to a high value of permittivity ε'. As the frequency increases, the contributions made by each type of polarization disappear one after the other as presented **FIG. 2.1** .

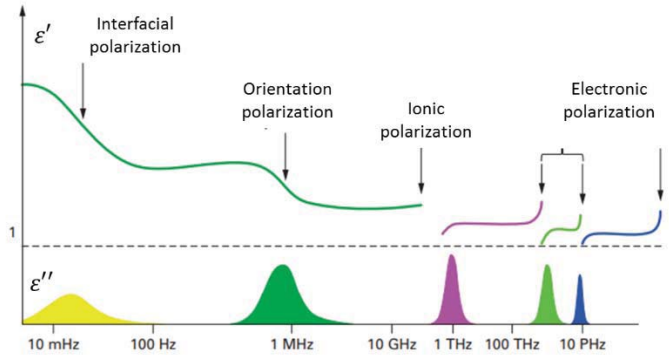


FIG. 2.1 - Frequency variations of the real and imaginary parts of the dielectric permittivity

As we are interested in the frequency range (10-10^6 Hz), interfacial and orientation polarizations will be responsible for high values of the real part of permittivity ε'. Increasing the polarization in the materials will lead to higher values of permittivity.

The permittivity can be extracted from impedance measurements. The next paragraphs are devoted to this measure.

1.1.2 Impedance:

Impedance (Z) is a crucial parameter used to characterize electronic circuits and materials. By definition, Z is the total resistance that the material offers to the flow of an alternating current (AC) at a frequency (f). This is a complex number consisting of a real part Z_{Re} and an imaginary part Z_{Im} as defined by (**EQ. 2.1**) [2]

$$Z^* = Z_{Re} + jZ_{Im} = \frac{U}{I} \tag{2.1}$$

With $|j|^2 = -1$, U is the complex voltage and I complex current.

Because impedance is a complex value, at least two values must be measured to find the impedance. Modern impedance meters measure the real and the imaginary parts of the impedance and convert them into the chosen parameters such as the capacitance (C) and the resistance (R).

In a perfect world, capacitors would only store and release electrical energy, without any dissipation. However, real capacitors are not purely capacitive and can deviate from an ideal behavior in a number of ways. The main parasitic effect is the leakage current due to a finite material's resistance. Consequently, some amount of current pass through the capacitor when a constant voltage is applied.

Impedance of an ideal capacitor, impedance Z_c is given by:

$$Z_c^* = \frac{1}{jC\omega} \tag{2.2}$$

Where C is the capacitance and ω the angular frequency ($\omega = 2\pi f$). But for a non-ideal (real) behavior, leakages are modeled as resistance R in parallel with an ideal capacitor C, as represented **FIG. 2.2.**

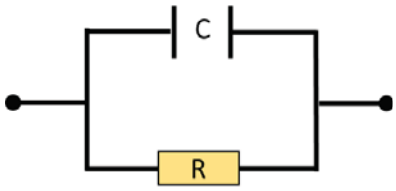


FIG. 2.2 - Ideal capacitor in parallel with a resistance.

In this model, the equivalent impedance Z_{eq}^* for a parallel configuration is given by **EQ. 2.3.**

$$\frac{1}{Z_{eq}^*} = jC\omega + \frac{1}{R} \tag{2.3}$$

EQ. 2.3 can be rewritten for emphasizing the real and imaginary part of the equivalent impedance:

$$Z_{eq}^{*} = \frac{R}{1 + R^2 C^2 \omega^2} - j\frac{R^2 C\omega}{1 + R^2 C^2 \omega^2} \tag{2.4}$$

Consequently, the resistance R and the capacitance C values of the sample can be calculated using real $Re\left(Z_{eq}^{*}\right)$ and imaginary part $Im\left(Z_{eq}^{*}\right)$ of the impedance as follows:

$$\begin{aligned} R &= Re\left(Z_{eq}^{*}\right)\left(1 + \frac{Im^2\left(Z_{eq}^{*}\right)}{Re^2\left(Z_{eq}^{*}\right)}\right) \\ C &= \frac{-Im\left(Z_{eq}^{*}\right)}{\omega\left(Re^2\left(Z_{eq}^{*}\right) + Im^2\left(Z_{eq}^{*}\right)\right)} \end{aligned} \tag{2.5}$$

1.1.3 Compensation procedure:

The measured value by the impedance meter is always a combination of the real value and the instrument's residual impedance [3]. It contains errors compared to the real value. Many artefacts affect the value of impedance due to residual impedance of the measurement circuit. For example, wires, electrodes and test fixtures add residual impedances to the impedance we want to measure. As the goal of the measurement is to have the real impedance value of materials, a compensation must be operated. To do so, an equivalent circuit (quadripole) for the experimental impedance device must be considered (**FIG. 2.3**).

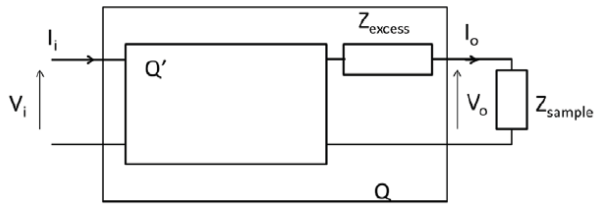


FIG. 2.3 - Impedance equivalent circuit

In this equivalent circuit, each contribution of the parasitic impedances can be distinguished:

- $Z_{Q'}$ includes the impedance generated by the cables and plugging, as represented **FIG. 2.3** by the circuit Q'. $Z_{Q'}$ can be reduced by shortening the length of the cables leading to the electrodes or by using coaxial wires.

- Z_Q includes the impedance generated by polarization at the electrodes Z_{excess} and $Z_{Q'}$, as represented **FIG. 2.3** by the circuit Q. This impedance is positioned between the input reference plan (Z_i, V_i, I_i) and the material (Z_o, V_o, I_o).

The goal of the compensation procedure is to remove the parasitic impedance Z_Q, $Z_{Q'}$ from the measurements to get Z_{sample}, the real impedance of the tested material.

The determination of the different terms of the circuit Q, leads to the resolution of the hybrid matrix defined as follows (**EQ. 2.6**) [3]:

$$\begin{pmatrix} V_i \\ I_o \end{pmatrix} = \begin{pmatrix} H_{11} & H_{12} \\ H_{21} & H_{22} \end{pmatrix} \begin{pmatrix} I_i \\ V_o \end{pmatrix} \tag{2.6}$$

Where H_{ij} are the terms of the hybrid matrix (H_{11} is an impedance, H_{22} is an admittance, H_{12} and H_{21} are numbers), V_i and I_i are the input voltage and current. V_o and I_o are the output voltage and current. Every H_{ij} contain polarization and parasitic information.

EQ. 2.6 is equivalent to **EQ. 2.7**:

$$\begin{aligned} V_i &= H_{11} I_i + H_{12} V_o \\ I_o &= H_{21} I_i + H_{22} V_o \end{aligned} \tag{2.7}$$

As the power is conserved in the passive quadripole Q, ($P = I_i V_i = I_o V_o$), $H_{12} = H_{21}$.

Z_{sample} is given by $Z_{sample} = \frac{V_o}{I_o}$ so **EQ. 2.7** can be rewritten as follows:

$$\frac{V_i}{I_i} = H_{11} + \frac{H_{12}^2}{\frac{1}{Z_{sample}} - H_{22}} = Z_i \tag{2.8}$$

In order to know completely the hybrid matrix, three measurements must be performed:

- A short circuit measurement, done by putting in contact the two electrodes of the test fixture. In this case, $Z_{sample} \to 0$, which leads to $\lim_{Z_{sample} \to 0} \frac{V_i}{I_i} = H_{11} = Z_{SC}$, enabling the determination of the first hybrid matrix term.

- An open circuit measurement, done by letting far away the two electrodes (large air gap) of the test fixture. In this case, $Z_{sample} \to \infty$, which leads to $\lim_{Z_{sample} \to \infty} \frac{V_i}{I_i} = H_{11} - \frac{H_{12}^2}{H_{22}} = Z_{OC}$, enabling the determination of a relation between hybrid matrix terms.

- A reference material reference, done by measuring the impedance of a material which has an already known impedance Z_{ref}. We decided to use a pure PDMS polymer sample as reference. In this case:

$$H_{11} + \frac{H_{12}^2}{\frac{1}{Z_{ref}} - H_{22}} = Z_{ref\ measured} \tag{2.9}$$

Where $Z_{ref\ measured}$ is the measured value of Z_{ref}. It leads to the determination of the last hybrid matrix term H_{22}:

$$H_{22} = \frac{1}{Z_{ref}(1 + \frac{H_{11} - Z_{OC}}{Z_{ref\ measured} - H_{11}})} \tag{2.10}$$

Finally, the determination of the real value of the tested material Z_{sample} will be determined by the measured value of impedance $Z_{measured}$ given by the impedance meter at a given frequency, with:

$$Z_{sample} = \frac{1}{H_{22} + \frac{H_{12}^2}{Z_{measured} - H_{11}}} \tag{2.11}$$

With H_{11}, H_{22}, H_{12} are determined by the short circuit, open circuit and reference measurements as follows:

$$H_{11} = Z_{SC}$$

$$H_{22} = \frac{1}{Z_{ref}(1 + \frac{H_{11} - Z_{OC}}{Z_{ref\ measured} - H_{11}})} \qquad H_{12} = \sqrt{H_{22}(H_{11} - Z_{OC}H_{22})}$$

1.1.4 Relation between capacitance, resistance and conductivity, permittivity:

As seen previously, the response of materials to alternating fields is characterized by an equivalent complex impedance, given by (**EQ. 2.4**):

$$Z_{eq}^* = \frac{R}{1 + R^2C^2\omega^2} - j\frac{R^2C\omega}{1 + R^2C^2\omega^2} \tag{2.4}$$

As complex permittivity Z_{eq}^* depends on material geometry (thickness and area), complex permittivity $\varepsilon^*(\omega)$ will be used to characterize materials independently of its dimensions (**EQ. 2.12**).

$$\varepsilon^*(\omega) = -\frac{jd}{\omega A Z^*(\omega)} \tag{2.12}$$

Where A is the material's surface and d its thickness. Since the response of materials to alternating fields is characterized by a complex number, it is natural to separate its real and imaginary parts, which is done by convention in the following way:

$$\varepsilon^*(\omega) = \varepsilon' - j\varepsilon'' \tag{2.13}$$

Where ε' is the real part of the permittivity, ε'' is the imaginary part of the permittivity. Henceforth, the two contributions of the permittivity are calculated using the following equations from values of R and C.

$$\varepsilon' = \frac{dC}{A} \qquad \varepsilon'' = \frac{d}{\omega A R} \tag{2.14}$$

EQ. 2.14 shows that real part of the permittivity is directly links to the capacitance of the material while the imaginary part is links to the dielectric loss. Sometimes, the complex conductivity is preferred to the permittivity. For a given excitation (ω fixed), $\sigma^*(\omega)$ is homogeneous to $j\omega\varepsilon^*(\omega)$, which allows establishing the following relation.

$$\sigma^*(\omega) = j\omega\varepsilon^*(\omega) \tag{2.15}$$

where $\sigma^*(\omega)$ is the complex conductivity (by convention $\sigma^*(\omega) = \sigma' + j\sigma''$) and $\varepsilon^*(\omega)$ the complex permittivity. **EQ. 2.15** leads to the relations between real and imaginary parts of the conductivity and permittivity.

$$\begin{cases} \sigma'(\omega) = \omega\varepsilon''(\omega) = \dfrac{d}{AR} \\ \sigma''(\omega) = \omega\varepsilon'(\omega) = \dfrac{\omega dC}{A} \end{cases} \tag{2.16}$$

The real part of the complex conductivity $\sigma'(\omega)$, can be seen as the material's conductivity at fixed ω due to its finite resistance R and geometric dimensions. Actually, this conductivity is linked to the dielectric loss of the material from the related charges. Nevertheless, dielectric composites contains both free charges and related charges. They may conduct electrical current by adding conductive charges beyond percolation threshold and may exhibit polarization when an alternating electric field is applied thereto. This is an intermediate case between pure dielectric and conductive materials.

In this case, the conductivity due to free charges σ_{DC} (independent of the electrical frequency) must be added to the complex conductivity:

$$\sigma^*(\omega) = \sigma_{DC} + j\omega\varepsilon^*(\omega) \tag{2.17}$$

Thus

$$\sigma'(\omega) = \sigma_{DC} + \omega\varepsilon''(\omega) \tag{2.18}$$

where $\sigma'(\omega)$ denotes all the phenomena leading to an energy dissipation. σ_{DC} represents the loss due to free charges (Joule's effect) and $\omega\varepsilon''(\omega)$ represents the dielectric relaxation. In practice, the DC contribution is always measured by the impedancemeter. When one is interested only in the phenomena of polarization, this contribution must be subtracted. For the rest we will only focus on the real parts of the conductivity and the dielectric constant: $\sigma'(\omega)$ and $\varepsilon'(\omega)$ which are linked to the materials dimensions thanks to the relations (**EQ. 2.19**):

$$R = \frac{d}{A(\sigma_{DC} + \omega\varepsilon''(\omega))} = \frac{d}{A\,\sigma} \qquad C = \frac{A\,\varepsilon'}{d} \tag{2.19}$$

For simplification reasons, $\sigma'(\omega)$ and $\varepsilon'(\omega)$ will be noted respectively σ and ε.

1.1.5 Dielectric loss:

The loss tangent, $\tan\delta$, can be defined as the ratio between the real part of the conductivity $\sigma'$and the imaginary part σ'' as defined by:

$$\tan\delta = \frac{\sigma'}{\sigma''} = \frac{\sigma_{DC} + \omega\varepsilon''}{\omega\varepsilon'} = \frac{\sigma}{\omega\varepsilon} \tag{2.20}$$

In the case of pure dielectric materials (no conductivity due to free charges), the loss tangent would be simply $\frac{\varepsilon''}{\varepsilon'}$. This loss tangent can be understood as the gap of a material to the perfect capacitor. It represents how lossy the material is for AC signals caused by the dipoles orientation and by conduction. For isolating materials, $\tan\delta \to 0$ while for conducting materials $\tan\delta \gg 1$.

1.1.6 Practical procedure for measuring ε′, σ and tan δ as a function of frequency:

The experimental impedance measuring device is shown **FIG. 2.4** and its general principle is described below. The capacity (C) and resistance (R) measurements are performed across the thickness of the samples. They are loaded between two metallic disc electrodes (stainless steel) that have a diameter of 24 mm. The top electrode is controlled by a micrometric screw and a piezoactuator (Physik instruments P-842.30, travel range 45 µm) allowing a fine control of the applied strain. C and R are measured under a voltage of 1000 mV applied in the frequency range of $10-10^6$ Hz using a

computer-controlled impedance analyzer (Bio-Logic Impedance Analyser, MTZ-35). The previous described compensation procedure is used to remove the parasitic impedance (Q) of the sample holder and to get the real value of the material properties as a function of the frequency ($f = \frac{2\pi}{\omega}$). ε and σ were then calculated from **EQ. 2.19** after measuring the geometry of the sample. The dielectric losses, $tan\,\delta\,(\omega)$, were calculated from $\varepsilon(\omega)$ and $\sigma(\omega)$ by using **EQ. 2.20**. All the experiments were performed at room temperature.

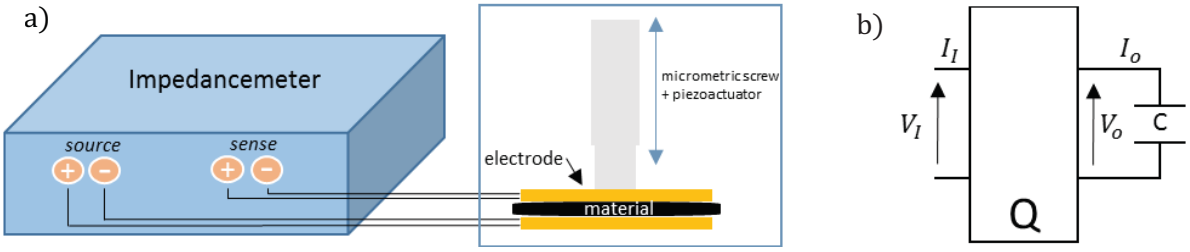


FIG. 2.4 - a) Impedance setup b) electrical equivalent of the setup

1.2 Determination of electromechanical performances:

1.2.1 Measurement and calculation of the intrinsic electrostrictive modulus M_{33} in static configurations:

As defined previously in Chapter 1, intrinsic electrostriction can be seen as a variation of permittivity, $\Delta\varepsilon_{33}$, when a stress is applied to material in the 3-direction :

$$M_{33}^{electrostriction} = \frac{\Delta\varepsilon_{33}}{2YS_3}$$

This a consequence of a change in the conductive fillers repartition due to the stress. However, the stress induced a strain leading to a change in the distance between the electrodes and a change of the material's permittivity. Both changes lead to a variation of the capacitance ΔC. For measuring the intrinsic electrostriction, only the contribution relative to the change of the material's permittivity will be considered. As $C = \frac{\varepsilon A}{e}$ at rest, the variation of the capacitance for small deformations and considering an unchanged surface, can be written (**EQ. 2.21**):

$$\frac{\Delta C}{C} = \frac{\Delta\varepsilon}{\varepsilon} - \frac{\Delta e}{e} \qquad (2.21)$$

Thus, the contribution relative to the change of the material's permittivity is $\Delta_C^{\varepsilon} = \frac{C\,\Delta\varepsilon}{\varepsilon}$, where C, ε are the capacitance and the permittivity at rest. Although, the contribution due to the change in thickness is $\Delta_C^{e} = -\frac{C\,\Delta e}{e}$, where e is the thickness at rest.

Thus, by measuring the change in capacitance ΔC_{33} using the impedancemeter, we can, after removing the contribution due to the change in distance, calculating $\Delta\varepsilon_{33}$.

The last step for calculating $M_{33}^{electrostriction}$ is to estimate the Young's modulus. The Young's modulus of the materials is measured using a tensile tester (Instron Model 4505). The initial dimensions (width and thickness) are measured before mounting the sample between the fixed and moving jaws. The force-displacement responses are acquired for each sample at a displacement rate of 0.067 mm s-1.

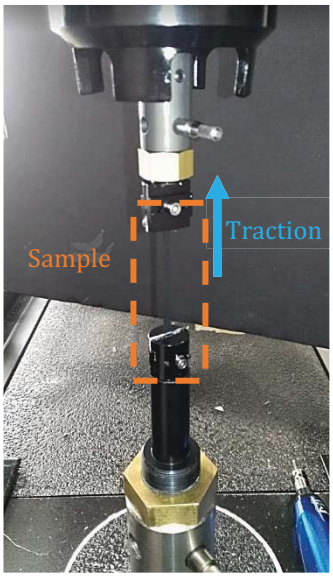


FIG. 2.5 - Uniaxial traction using Instron.

The tests ended when the specimens fractured. The Young's modulus is determined by measuring the slope of stress–strain curves in the elastic domain.

Consequently, we have all the desired information for the determination of $M_{33}^{electrostriction}$. Indeed, $\Delta\varepsilon_{33}$ is measured by the impedancemeter, S_3 is precisely controlled by the piezo actuator and Y is measured by the uniaxial traction machine.

1.2.2 Vibrational energy harvesting setup:

The experimental setup illustrated in **FIG. 2.6** is used to determine the recovering performance of the materials. It consists of a piezoelectric actuator (Physik Instrumente P-842.30) driven by a function generator (Keysight 33611A Waveform Generator) that applies a sinusoidal or square mechanical strain at a chosen frequency. The sample is placed between two electrodes: the top electrode is connected to the piezo actuator and moves at the same frequency as the actuator, the bottom electrode is fixed to the sample holder and does not move. As such, a modulated strain is applied along the thickness of the material. The strain is controlled by a computer linked to a function generator which controls the stroke of the actuator. An electric field E_{dc} is applied to the composite along the height (3-direction in **FIG. 2.6**) by a DC generator. To measure the current and generated power, a load resistance (R) is connected in series with the sample.The voltage U_R over the resistance is recorded by an oscilloscope (Keysight InfiniiVision 1000 X) and the current is determined using the Ohm's law ($I = U_R / R_l$)

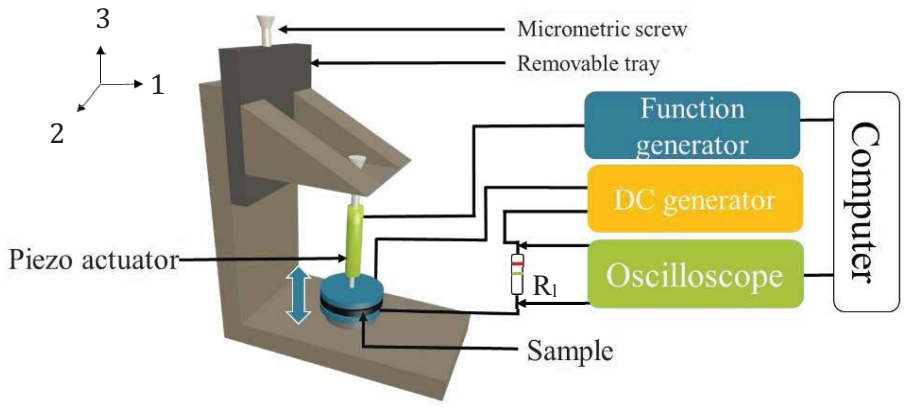


FIG. 2.6 - Schematic of the experimental setup

1.3 Formulation of the emulsion based electrostrictive composites:

1.3.1 Oil in water emulsion:

1.3.1.1. Materials:

The PDMS (polydimethylsiloxane), Sylgard 184, is purchased from Dow Corning as a kit of PDMS base and curing agent. The range of temperature for stable performances is −55 °C to 220 °C. This parameter is essential to avoid any degradation of the composite materials during the thermal reduction treatment of graphene oxide. The aqueous solution of graphene oxide (GO) monolayers is purchased from Graphenea, and the GO concentration is about 0.4 wt%. The GO particles are nonconducting. We first reduce them into reduced graphene oxide(r-GO) using a chemical reduction. 50 mL of solution at 0.4 wt % is heated under reflux for 1 h at 110 °C in the presence of 120 mg of ascorbic acid and 10 g of Tween 60. The solution turns from brown to black. The surfactant Tween 60 (Sigma Aldrich) allows us to stabilize the dispersion in water. The mean GO sheet size is about 2−3 µm. The solution is centrifuged in order to increase the GO concentration. Centrifugation is performed with a Sorval RC 6+, rotor SE-12, centrifuge at 22000 rpm (i.e., 50 000g) for 45 min. After centrifugation, the supernatant is removed. The bottom phase that contains GO monolayers is collected. The solid content of the material is determined by dry extracts after evaporation of the water under the vacuum at 100 °C. The mean final weight fraction of rGO is 5.8%.

1.3.1.2. Preparation of the composites:

The present method consists of building networks of carbon based fillers in between emulsion droplets of cross-linked PDMS polymer. Direct emulsions are made of oil droplets dispersed in an aqueous phase (see **FIG. 2.7**). As liquid drops are deformable, they can pack efficiently with a very small amount of remaining water continuous phase. The possibility to use water-based dispersions which are well controlled and which can

be stabilized with commercial surfactants is a major advantage of this approach. A mixture of PDMS and curing agent (10% in weight with respect to the PDMS phase) is first prepared as the oil phase (step a) **FIG. 2.7**). Emulsions are prepared by progressively adding the oil phase to an aqueous solution of Tween 60 surfactant under mechanical stirring provided by a mechanical mixer (IKA Eurostar 40 digital) (step b) **FIG. 2.7**). The gap between the paddle and inner wall of the container is about 7.5 mm. The surfactant weight fraction in the water phase is 4 wt %. Oil is added dropwise until its weight fraction reaches 85 wt % (step c) **FIG. 2.7**). Shear can be increased by raising the rotational speed of the mixer in order to form smaller droplets. The size of the obtained droplets is characterized using a Mastersizer Malvern 2000 particle size analyzer. The droplet sizes are broadly distributed using mechanical stirring. They range from 80 to 15 µm.

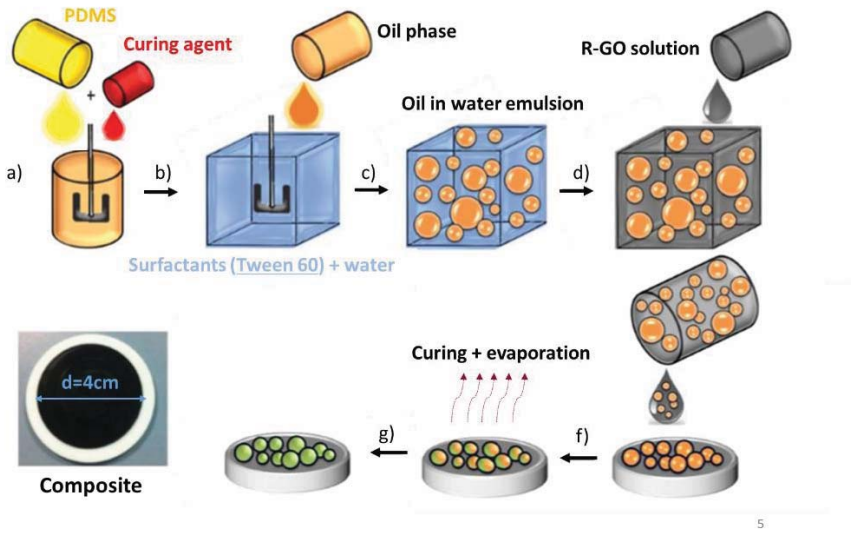


FIG. 2.7 - Scheme of preparation steps of the composites.

The emulsions are then gently mixed with a rGO aqueous dispersion (step d) **FIG. 2.7**). The number of fillers is varied in order to obtain different filler loadings in the final composites obtained after drying and curing. The emulsions loaded with the carbon-based fillers are placed in circular homemade Teflon molds (step f) **FIG. 2.7**). The diameter of the Teflon molds is 40 mm. Solid materials are obtained by evaporating water from the emulsion and by curing the PDMS polymer. The obtained samples are under the form of elastomer disks with a black color. They look perfectly homogeneous on a macroscopic scale. In order to obtain a comprehensive reduction of GO particles, the samples are heated at 200 °C for 2 h.

1.3.2 Water in oil emulsion:

1.3.2.1. Materials:

The emulsion consists of an aqueous solution of carbon black droplets dispersed in a matrix of PDMS and a curing agent. We use the following procedure (**FIG. 2.8**). The oil phase is prepared by mixing PDMS (Dow Corning), the curing agent (Dow Corning, 10% in weight with respect to the PDMS phase), and the surfactant lauryl PEG-8 dimethicone

(Silube J208-812, Siltech, 5.0 wt% of the final mixture) (step a) **FIG. 2.8**) . The water phase is prepared by mixing 5 g of arabic gum (Sigma Aldrich) and 95 g of deionized water (step b) **FIG. 2.8**). The desired concentration of carbon black powder (Alfa Aesar) is added and the mixture is tip sonicated for 1 hour at 400 W to homogeneously disperse the carbon black (CB) particle (step c) **FIG. 2.8**). The emulsion is prepared by progressively adding the carbon black solution to the oil phase under manual stirring up to a mass ratio of water:oil=1:1 (step d) **FIG. 2.8**). The mean droplet size depends on the viscosity of the continuous phase and ranges between 10—30 µm. The water-in-oil emulsion loaded with carbon black particles is spread with a stencil that has a depth of 500 µm on a plastic surface with a diameter of 24 mm. A second plastic surface is placed on the spread emulsion such that the emulsion remains confined between two flat surfaces. Solid materials are obtained by curing the PDMS polymer without evaporation in a warm water bowl (90°C) for 4 hours (step e) **FIG. 2.8**). The relative humidity in these conditions is 100%. Then, the solid material layer is removed from the two plastic surfaces and dried in an oven for 1 hour at 150°C (step g) **FIG. 2.8**). As PDMS is permeable to water vapor, droplets from carbon black solution dried and leave a structure with spherical-shaped pores covered by carbon black particles. Curing and drying are critical stages which strongly influence the final morphology of the porous composite.

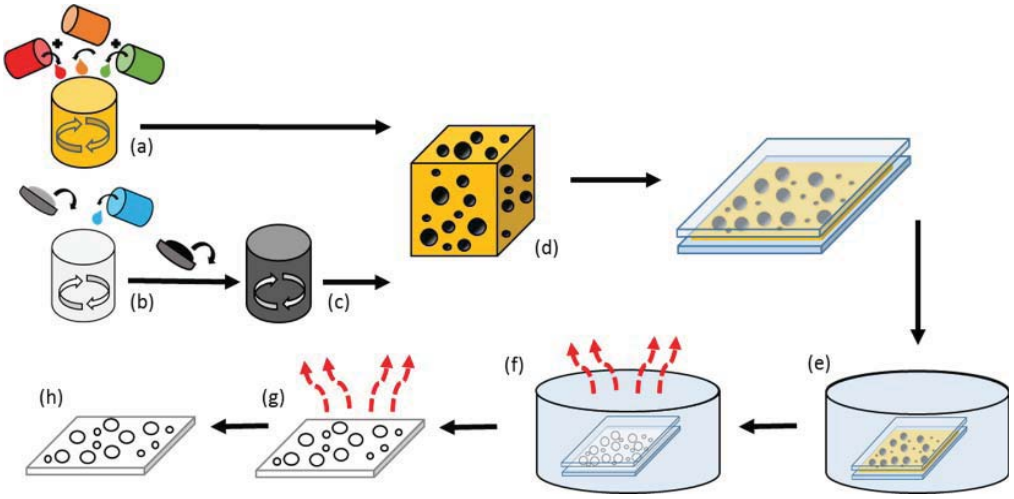


FIG. 2.8 - Scheme of the preparation of the microporous materials with pores covered by carbon black particles.

1.4 Scanning Electron Microscopy (SEM) analysis:

Each material was cut at its edge to reveal the view of the material's inner structure. A tabletop SEM Microscope Hitachi TM3000 was used to analyze the structure with the 15kV mode to get the best resolution.

1.5 Sensibivity measurements:

The experimental setup illustrated in **FIG. 2.9** is used to determine the pressure-induced capacitance changes for linear loading-unloading cycles. Capacitances were measured using the Agilent E4980A Precision LCR meter at 1 kHz frequency with a 1 V a.c. signal.

The connections between the point at which the shielding ends (BNC) and electrodes are kept as short as possible. The internal correction functions (cable length correction, open and short corrections) of the LCR-meter are used to correct errors due to the test fixture and the test leads. To perform the open correction, BNC and wires are connected to the electrodes and LCR-meter. A 5 mm air gap is maintained between the electrodes. The short correction is made by shorting the two electrodes. A DHR-3 rheometer (TA Instruments) is used as mechanized z-axis stage and force gauge. A top electrode is connected to the z-axis stage while the bottom electrode is fixed. The rheometer applies linear loading-unloading cycles to the sensing materials. The force, the displacement, the capacitance and the resistance are measured through an interfaced computer.

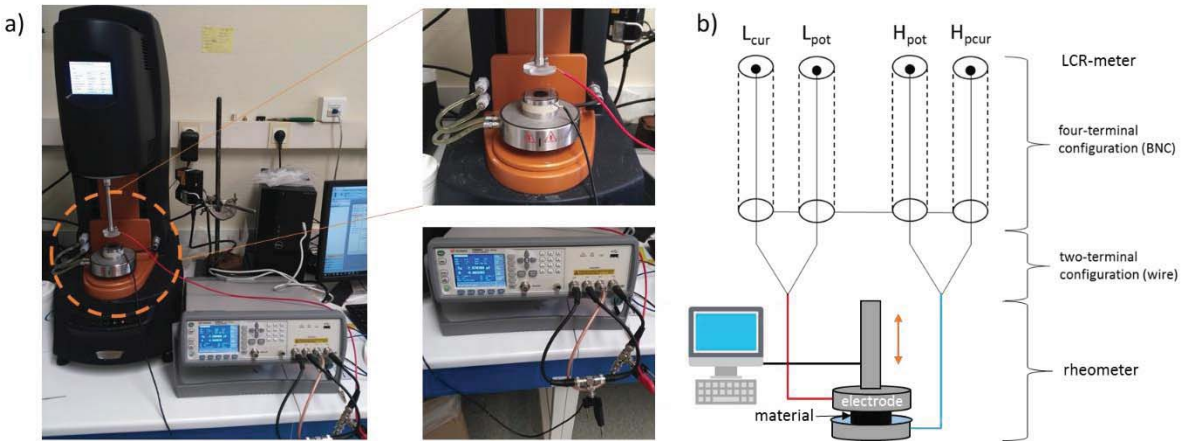


FIG. 2.9: Experimental setup for pressure sensing measurements a) photographs of the setup b) equivalent scheme.

Take home message – Chapter 2

This chapter presents general considerations on impedance and practical methods for measuring dielectric properties of materials. Then, we expose two new routes to synthesize electroactive composites via emulsions templating effects.

1. We first describe the way we measure the dielectric properties of materials and how we deal with the parasitic impedances.

2. We develop characterization methods and setups for the measurement of the electrostrictive coefficients and the power recovering of dielectric materials. This method provides an evaluation of the electromechanical properties while the materials are submitted to mechanical compressions.

3. Two process paths have been created for making electrostrictive composites. The first is based on an oil-in-water emulsion loaded with reduced graphene oxide conductive fillers. The second is based on a water-in-oil emulsion loaded with carbon black fillers. We expect to finely control the dielectric properties for developing materials with high permittivity while keeping the conductivity very low.

[1] O. GALLOT-LAVALLEE, P. GONON, Caractérisation des polymères par spectroscopie diélectrique, Techniques de l'ingénieur Propriétés Générales Des Plastiques. base documentaire : TIB152DUO. (2016). https://www.techniques-ingenieur.fr/base-documentaire/materiaux-th11/proprietes-generales-des-plastiques-42152210/caracterisation-des-polymeres-par-spectroscopie-dielectrique-am3141/.

[2] Broadband dielectric spectroscopy., Springer, Place of publication not identified, 2013.

[3] Impedance Corrections, in: Short Circuits in Power Systems: A Practical Guide to IEC 60909-0, Wiley-VCH Verlag GmbH & Co. KGaA, Weinheim, Germany, 2017: pp. 127–131. doi:10.1002/9783527803378.ch9.

3. Electrostrictive response and piezoresistivity of r-GO composites based on an (O/W) emulsion template.

This chapter is based on the following article:

Luna, M Pruvost, J Yuan, C Zakri, W Neri, C Monteux, P Poulin, A Colin. Giant Electrostrictive Response and Piezoresistivity of Emulsion Templated Nanocomposites. *Langmuir*, 33 (18), 4528-4536, 2017

Summary:

Using an emulsion road and optimizing the dispersion process, we prepare polymer-reduced graphene oxide (rGO) composites. The introduction of conductive nanoparticles into polymer matrices modifies the electronic properties of the material. We show that these materials exhibit giant electrostriction coefficients in the intermediate filler concentration (1.4 wt %). This makes them very promising for applications such as actuators but their dielectric losses prevent them from harvesting applications. In addition, the piezoresistivity measured in the high filler concentration situation exhibits a GF around 6 for a low 8% strain. This opens the way to use these materials for resistive stress or strain sensor applications considering their giant responses to mechanical deformations.

1 Introduction:

The investigation of the electrical properties of composites has been driven by the technological importance of developing flexible materials with high permittivity. In particular, these materials are convenient for building a flexible and low-cost electronic in the fields of sensing and energy harvesting [1,2]. To do so, the use of conductive fillers in an isolating polymer matrix is an interesting solution to increase the permittivity of materials. The dispersion of these fillers causes a charge accumulation at the interface between the insulating matrix and the conductive particles [3]. These free charges therefore contribute to increasing the interfacial polarization and thus the permittivity as described in Chapter 2. However, they also contribute to the increase in static conductivity σ_{DC} of the material. Indeed, when the concentration of the fillers approaches a critical value called *the percolation threshold*, the fillers come into contact with each other and a continuous path extends through the material. At this point, an abrupt change occurs in electrical properties of the composites (**FIG. 3.1**): both conductivity (σ) and permittivity (ε) diverge. The distribution of fillers in polymer matrix plays a key role in the value of the percolation threshold, which is influenced by the particle shape, size and orientation [4–6]. The challenge will consist in finding the best balance between high permittivity and low dielectric losses.

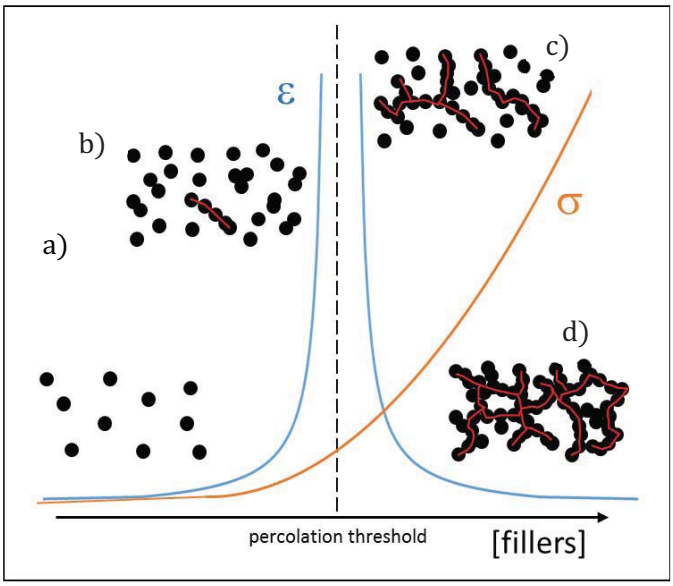


FIG. 3.1- Schematic evolution of electrical properties (ε, σ) as a function of the fillers concentration near the percolation threshold (dashed black line). a) randomly dispersed b) below the percolation, dispersed fillers start aggregating but no main conducting path exists c) above the percolation, dispersed fillers are aggravating and main conducting path exists d) filler network is fully percolated.

Before presenting our results based on r-GO/PDMS composites, let's provide a comprehensive understanding of dielectric composites formulation and identify the issues and difficulties.

1.1 Percolation theory:

The theory of percolation was originally used as a simple model of statistical physics to describe disordered systems [7]. However, this theory is very powerful for describing the electrical properties of heterogeneous materials (composite materials) and their huge changes as illustrated **FIG. 3.1.**

1.1.1 Evolution of the conductivity:

When highly conductive fillers (σ_{filler}) are added to an isolating matrix (σ_{matrix}), an abrupt change of conductivity is observed in the vicinity of the percolation threshold, especially if $\sigma_{filler} >> \sigma_{matrix}$. At this concentration, the composite displays a metal–insulator transition from an electrical point of view. In percolation theory, three behaviors can be distinguished depending on the fillers concentration [8]:

- $f < f_C$ (**FIG. 3.1** a)): there is no percolating path, the matrix isolates the conductive fillers. σ_c is described by **EQ.3.1**.

$$\sigma_c \propto \sigma_{matrix}(f_c - f)^{-s} \tag{3.1}$$

  where s is a critical exponent (s =0.7 – 1.3), f_c is the percolation threshold and σ_c refers to the composite conductivity.

- $|f - f_C| \to 0$ (**FIG. 3.1** c)):

$$\sigma_c \propto \sigma_{matrix}^{u} \sigma_{fillers}^{1-u} \tag{3.2}$$

  where $u = \frac{t}{t+s}$

- $f > f_C$ (**FIG. 3.1** d)): the conductivity of the composite σ_c is mainly determined by σ_{filler} as described by (**EQ.3.3**)

$$\sigma_c \propto \sigma_{fillers}(f - f_c)^{t} \tag{3.3}$$

  where f is the filler concentration, f_c is the percolation threshold and t is a critical exponent (t =1.1 - 2.0)

1.1.2 Evolution of the permittivity:

When the filler concentration is approaching the percolation threshold, from below, the composite permittivity ε_c starts diverging as described by equation (**EQ.3.4**) [8,9]

$$\varepsilon_c \propto \varepsilon_{matrix}|f - f_c|^{-s} \quad (3.4)$$

where s is a critical component close to 1. This equation illustrates that huge permittivity values can be achieved in composites as $|f - f_C| \to 0$

The dramatic change of permittivity, near percolated network, is physically explained by the formation of large conducting clusters, which are separated by a small layer of dielectric material (polymer matrix) [10]. This effect creates local microcapacitors, which contribute to an increase in the intensity of local electric field when the conductive fillers are adjacent to each other near the percolation threshold. The local electric field helps the migration and accumulation of electric charges, injected from the external electrodes, at the interfaces between the fillers and the matrix. This interfacial polarization (Maxwell-Wagner effect) induced an enhancement of the composite permittivity at low frequency [11].

1.1.3 Variable permittivity (electrostriction):

For applications in the field of variable capacitors (energy harvesting and sensing), high-permittivity materials with low-dielectric-loss, in frequency ranges of interest, are required. The drawback of high-permittivity materials is that the high permittivity originates from the structure of microcapacitors close to the percolation threshold which makes the control of the structure extremely challenging. The window for high-permittivity materials and low-dielectric-loss is very narrow. It means that a small deviation in the concentration can lead to huge electrical changes. Nevertheless, these electrical changes can be smartly used to create electrostrictive materials. Indeed, when a close to percolation material is strained, a local variation of filler concentration Δf can be induced. Consequently, a variation of permittivity $\Delta\varepsilon$ is observed leading to an electrostrictive material as represented **FIG. 3.2**.

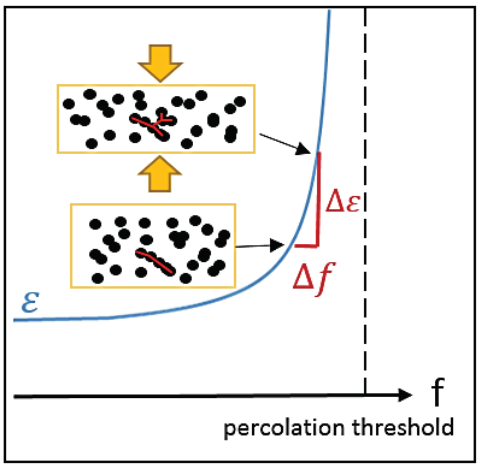


FIG. 3.2 - Variation of permittivity due to local fillers concentration changes

The variation of permittivity can be used to highly enhance capacitance variations when variable capacitors are submitted to strains. Indeed, when electrostrictive material are used as dielectric layer, capacitance variations result from thickness variation Δ_e and from permittivity variation Δ_ε (**FIG. 3.3**). Althought, when classic dielectrics are submitted to strain, low capacitance variations are observed because resulting from low geometrical changes (Δ_s).

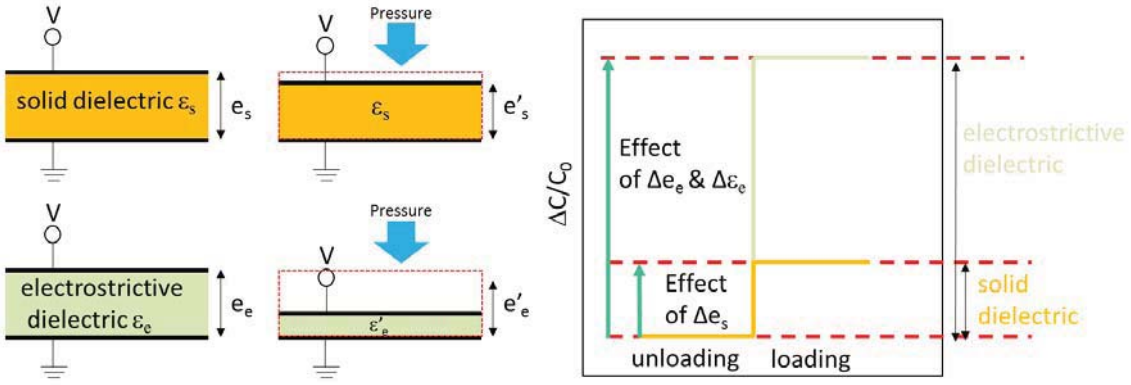


FIG. 3.3 - Effect of electrostriction on capacitance variations.

1.2 Interest of reduced graphene oxide flakes:

1.2.1 Description and properties:

In the field of conductive particles, graphene flakes have attracted interest due to their uncommon properties such as high electrical conductivity [12] or high mechanical strength (Young's modulus of 1 TPa [13]). These excellent properties show the high potential of graphene to improve physico-chemical properties of polymers in the field of composites. Graphene composites have varied applications for energy and related systems. Indeed, they have been mainly exploited as electrodes for supercapacitors or batteries [14,15], and for fuel cell membranes[16]. For a structure point of view, graphene flakes are pure bounded carbon atoms with atom-thick 2D structure and a large aspect ratio (**FIG. 3.4** a)).

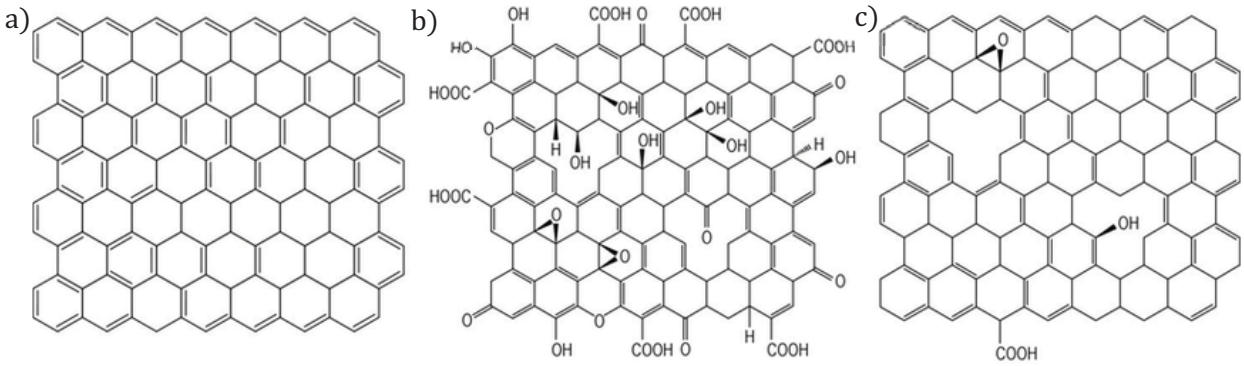


FIG. 3.4 - Graphene materials. a) Graphene b) Graphene oxide (GO) c) Reduced graphene oxide (r-GO)

Nevertheless, graphene flakes have a main drawback: their insolubility in water and organic solvents making the production of graphene based composites difficult. To facilitate their dispersion, the oxidized version of graphene flakes (graphene oxide—GO) is preferred. The main advantage of GO compared to its non-oxidized counterpart is its ability to form stable solutions in several solvents [17]. A variety of oxygen functionalities (-OH, =O, and—COOH) considered as "defects" are located at the edge (**FIG. 3.4** b)). These new groups make the GO flakes soluble in water and in polar solvents[17]. However contrary to graphene, graphite oxide is an electrical insulator[18]. This lack of conductivity is a bareer to the making of high-permittivity materials. For restoring electrical properties, a reduction of the oxygen groups can be performed by several methods such as chemical reduction or thermal reduction. More than 50 types of reducing agents have been studied to chemically reduce graphene oxide [19], including very toxic agents such as hydrazine[20] or softer agent such as L-ascorbic acid [21]. Each method leads to variable restoration of the electrical properties[19]. The thermal method is a greener method because no hazardous chemicals are used. However, this process requires a high temperature heating (above or around 1000 °C [22])for evaporating oxygen functional groups. This is a limitation for the selection of polymer matrix that can host the fillers. Indeed, many polymers do not bear such high temperature and start decomposing. For examples, the weight loss of PDMS begins around 250 °C [23] and some polyurethane products may begin their degradation at temperature as low as 150 °C [24]. Because no degradation of the materials is desirable, we assume that working at low temperature will lead to partial recovery of the electrical properties.

1.2.2 Self assembly of the GO flakes: a way to decrease electrical losses:

Recently J.Yuan et *al.* [4], have shown experimentally that graphene flakes could self-assemble into nematic liquid crystals before the percolation threshold. This new result provides an interesting road for making composites with graphene oxide flakes as conductive fillers (**FIG. 3.5**). Indeed, this phenomenon would make possible the use of graphene for making high permittivity composites because it will promote the formation of locally large microcapacitors. Moreover, a low conductivity is expected as conductive contacts are reduced.

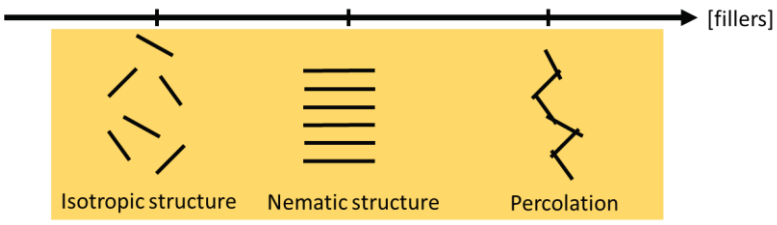


FIG. 3.5 - Reduced graphene oxide nematic-percolating transition as a function of the fillers concentration. r-GO flakes are symbolized by black rods.

The process requires a chemical modification of the GO flakes with a diblock copolymer polyaminopropylmethylsiloxane-b-PDMS (**FIG. 3.6** a)). This functionalization aims at transferring GO flakes from a water-based solution to an organic one (diethyl ether)

where PDMS can be solubilized (**FIG. 3.6** b)). The possibility to dissolve GO flakes into the organic phase eases their dispersion into PDMS. After a curing and evaporation steps, a solid material is obtained (**FIG. 3.6** c)). Thanks to this strategy, they successfully developed a PDMS-r-GO composite which exhibits a permittivity of 753 at 100 Hz along with a loss tangent of only 0.4.

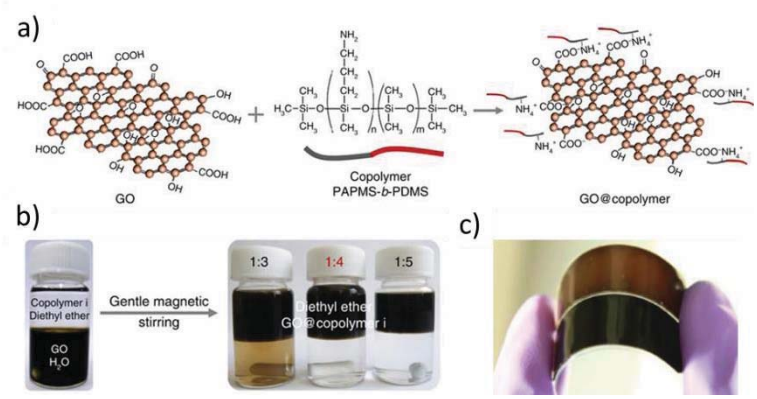


FIG. 3.6 - Liquid crystalline graphene-based PDMS composites

1.3 Strategies to disperse conductive fillers:

The distribution refers to the arrangement of all the phases with respect to each other. A more controlled distribution of the fillers inside the polymer matrix could prevent particles from forming conductive paths and keep the microcapacitors isolating. Additionally, it could ensure a homogeneous distribution of conductive particles within the material. This strategy could expand the formulation window and lead to materials with high permittivity and low conductivity. The filler distribution is directly linked to the fabrication process of composites. In this context, several processes have been developed to achieve this goal. A first dispersion path has been described in the previous paragraph, where a phase transfer was employed [4].

Other examples of fine dispersion were achieved by further methods:

- by *in-situ polymerization* of monomers in the presence of the fillers. Usually, in-situ polymerization leads to better fillers/matrix interactions which could enhanced electrical and mechanical properties. Numerous works have used this method for making CNT/polymer composites. For example, M.Cochet *et al.* developped composites by polymerisation of aniline with CNT [25].

- by solution casting where the matrix and the filler particles are dispersed in a common solvent. K. Wongtimnoi et al. [26] dissolved and homogenized PU granules in N,Ndimethylformamide (DMF). Meanwhile fractions of carbon black particles were dispersed in DMF using an ultrasonic probe. P.Fan *et al.* [27]

dispersed, with ultrasonic method, r-GO flakes in dimethylacetamide (DMAc) at the same time as PVDF powder.

- by mixing polymer beads and fillers by *melt processing.* Compared to solution mixing, melt mixing is considered cost-effective because no solvent is used. Nevertheless, studies suggest that polymer mixing provides lower level of filler dispersion as other methods [28].

1.4 Our approach:

The present Chapter draws attention to the elaboration of r-GO-PDMS composites made by an O/W emulsion approach. As described in detail in Chapter 2, the materials are synthesized by mixing r-GO sheets and PDMS emulsion droplets in water. r-GO-PDMS emulsions are molding, curing and drying to finally get solid materials.

1.4.1 Reduction paths:

The recovery of the electrical properties was achieved by two steps: an *in* and *ex-situ* reductions. As we are limited by *ex-situ* thermal reduction of the composites at 200 °C due to the PDMS degradation, this reduction will lead to partial recovery of the electrical properties. For improving the reduction, we have chosen to associate this thermal step with an *in-situ* chemical reduction. This step is directly performed on the GO commercial solution by using L-acid ascorbic (vitamin C) as chemical agent. The latest has been preferred to other chemicals thanks to its low toxicity for humans and environment[21] and has shown good electrical properties recovery[21]. It is worth noticing that the success of the chemical reduction can be observed easily as the graphene oxide solution turns from brown to black when the flakes are reduced.

1.4.2 Dispersion process:

Contrary to the usual dispersion processes, we have chosen to work with an unconventional method to disperse the conductive fillers: the emulsion approach. This is a recent strategy to efficiency homogenize the composite where PDMS droplets will play the role of molds for the r-GO fillers. It has been recently described by A.Luna *et al.*[29] with PDMS/CNT composites. They studied the role of the drying-curing procedure as well as the importance of the emulsion droplet size. For an emulsion size 1 order of magnitude higher than the length of the carbon nanotubes, they measure a giant permittivity larger than 20 000 at 100 Hz and a conductivity of 10^{-4} S/m ($\tan\delta = 1.8$). Unfortunately, the dielectric losses remain too high for using the material as the dielectric layer in capacitors. The origin of the dielectric losses may be attributed to the absence of nematic structuration in the case of CNT. Actually, when the filler concentration increases, the CNT evolve from an isotropic structure to a percolating one. The last one builds an interconnected network of conductive particles and increase the losses.

The use of r-GO flakes could delay the percolation as they self-structure into a nematic phase. From a structural point of view, the PDMS droplets will be larger than r-GO flakes and will force the conducting particles to accumulate in the Plateau borders. Compared to *in-situ* polymerization of PDMS with randomly dispersed r-GO sheets, this template effect presents several advantages. First, r-GO sheets can be efficiency dispersed in the aqueous phase of the emulsion, by using commercial surfactants. As water is environmentally friendly, the possibility to use this solvent is a major process advantage. We chose to work with Tween 60 as dispersant ; this preference was motivated by the absence of electrical charge on this surfactant (non-ionic surfactant). As we will apply, electrical fields to the composites, chemically inert surfactants were preferable. Second, the mixing of the oil phase (PDMS droplets) and the aqueous phase (r-GO solution) will be gently operating as the r-GO solution will be fully soluble in the PDMS emulsion. Plus, PDMS emulsion and r-GO solution are both dispersed by the same non-ionic surfactant (Tween 60). Finally, after water evaporation and cure, we could expect a nematic distribution of the fillers between the PDMS droplets (**FIG. 3.7**). Thus a greater degree of control of the conductive inclusions is expected. Indeed, the r-GO emulsion double the possibilities to reduce the dielectric losses by first segregating the fillers between the PDMS droplets and then by orientating the r-GO in a parallel system.

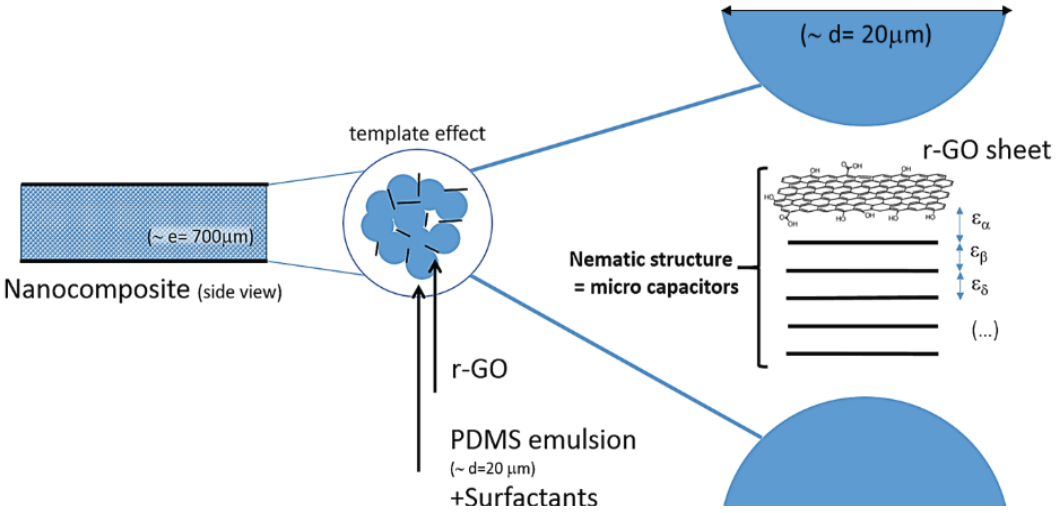


FIG. 3.7 - Focus on the r-GO sheets distribution between the PDMS droplets.

2 Results and discussion:

2.1 Microscopy and emulsion distribution:

For keeping the PDMS droplets, curing and drying are critical stages as they take place simultaneously and could lead to coalescence. Indeed, two characteristic times have to be controlled: the curing time (PDMS curing) and drying time (water evaporation). Fast-drying and slow curing times lead to the formation of faceted drops (**FIG. 3.8** a) b) c)) where r-GO flakes are located at the Plateau borders. The slow curing time aims at deforming the PDMS drops before their solidification and to highly pack them. The electronic microscopy pictures confirmed the lamellar phase structure of the r-GO between the droplets. This orientation of the platelets lowers their contact probability which results in a greater percolation threshold and limited dielectric losses. The dynamic light scattering (DLS) is used to determine the size distribution profile of the PDMS emulsion. The size distribution is log normal with a mean diameter <d> of 15 µm (**FIG. 3.9**). It is important to keep in mind that the size of the PDMS drops have to be larger than the r-GO fillers so as to decrease the possibility to build a fully connected network of conductive fillers.

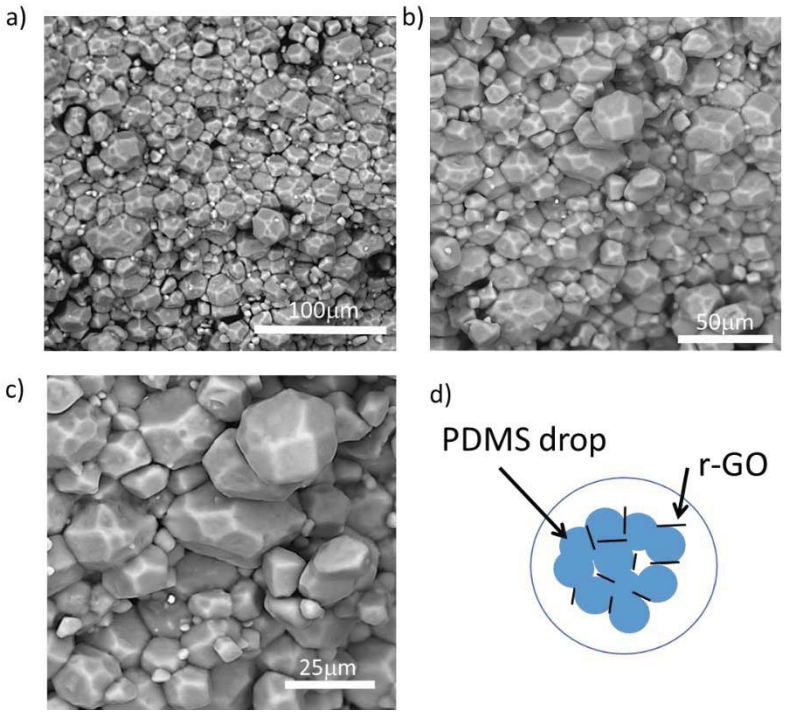


FIG. 3.8- Electronic microscopy (SEM) pictures of rGO composite at different scales. d) schematic illustration of the r-GO/PDMS emulsions

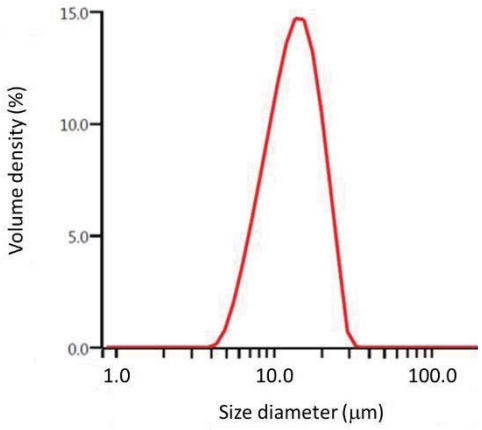


FIG. 3.9 - Size distribution of the PDMS emulsion, mean diameter =15 µm.

2.2 Dielectric measurements:

2.2.1 Influence of the reduction on the dielectric properties:

As previously discussed, the recovery of the electrical properties was achieved by two steps: an *in* and *ex-situ* reductions, with respectively a chemical and thermal methods. The use of the two paths is justified by the poor dielectric properties in absence of any thermal treatment. Indeed, **FIG. 3.10** a) and b) show the evolution of the permittivity and conductivity before and after the thermal reduction. Although a permittivity around 10 at 100 Hz was measured for the 1.4 wt% sample, the thermal treatment helped it to get a value around 640. An increase in conductivity by a factor 100 was also observed (**FIG. 3.10** b)). The thermal reduction of the r-GO flakes into more reduced graphene clearly lead to enhanced properties. The further reduction of r-GO is macroscopically observable by a change of color. As shown **FIG. 3.11**, the poorly conductive samples are dark brown but after the thermal reduction the color of the r-GO samples become completely black. In the following part, all the samples have been treated by both reduction methods.

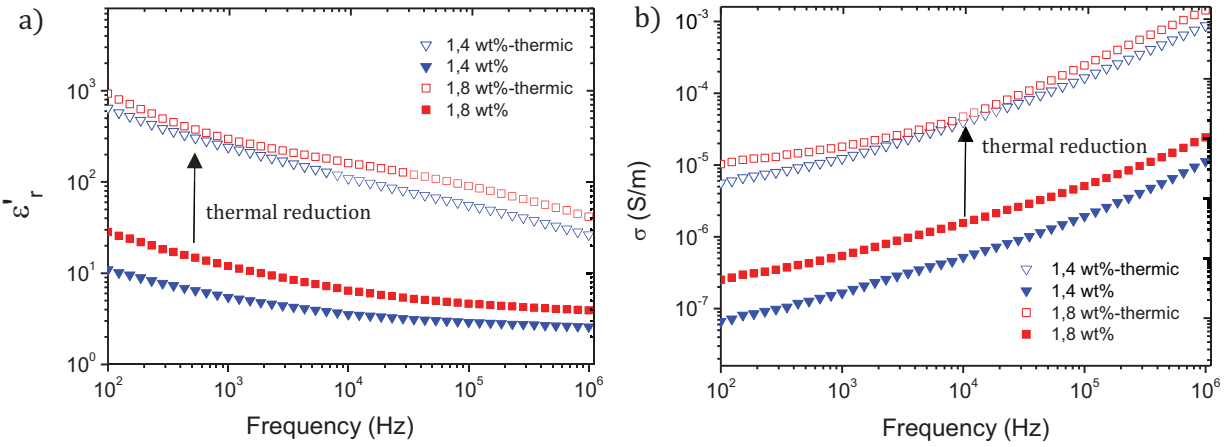


FIG. 3.10 - Influence of the thermal reduction on the a) composites permittivity b) composites conductivity.



FIG. 3.11 - Photographs of the r-GO/PDMS composites before (left) and after (right) the thermal reduction.

2.2.2 Dielectric response as a function of the filler concentration:

FIG. 3.12 displays the electric conductivity (σ), the relative permittivity (ε_r'), and the loss tangent ($\tan\delta$) at 100 Hz and room temperature for different r-GO samples. The electrical conductivity increases as a function of the r-GO concentration (**FIG. 3.12** blue scale). The percolation threshold is reached for a weight fraction of about 1.3 %. Bellow (0.8 wt%) and above (1.4 wt%) the threshold, the composites show an insulator-to-conductor transition with an increase in the conductivity of a factor 40 at 100 Hz. Theoretically, the composite conductivity should vary as $\sigma_c \propto \sigma_{matrix}(f_c - f)^{-s}$ below the percolation threshold. The **FIG. 3.13** a) shows the good fits of experimental data to theoretical behavior with s around 1.5 and $f_c = 1.3\,wt\%$. Above the percolation, the conductivity should vary as $\sigma_c \propto \sigma_{fillers}(f - f_c)^t$ which is confirmed **FIG. 3.13** b) with t around 1.4 and $f_c = 1.3\,wt\%$. The change in conductivity happens at the same time as an intense increase in the permittivity (permittivities are 410 and 3180 at 100 Hz for respectively 0.8 and 1.4 wt%). Below the percolation, the variation of the permittivity is theoretically depicted by the power law: $\varepsilon_c \propto \varepsilon_{matrix}|f - f_c|^{-s}$. **FIG. 3.13** b) confirms this evolution with $s = 1.2$ as critical exponent and $fc = 1.3\,wt\%$. It is worth noticing that similar values of the critical exponent s have been obtained, below percolation, for both conductivity and permittivity studies.

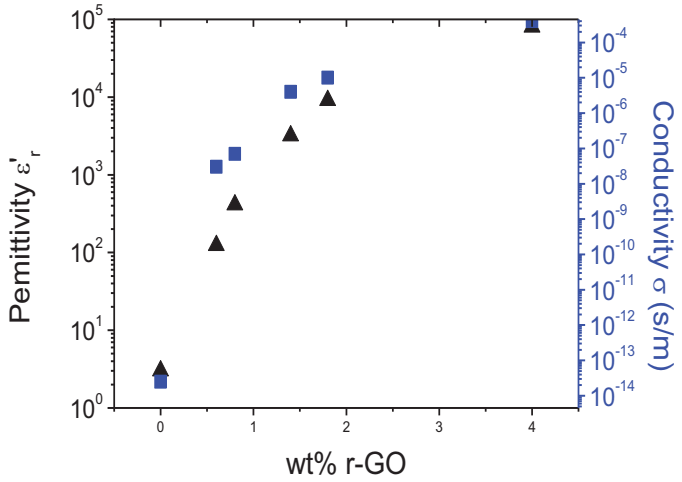


FIG. 3.12 - Relative permittivity ε'_r (black triangles) and electrical conductivity σ (blue squares) at 100 Hz as a function of the r-GO concentration obtained after solidification of the matrix.

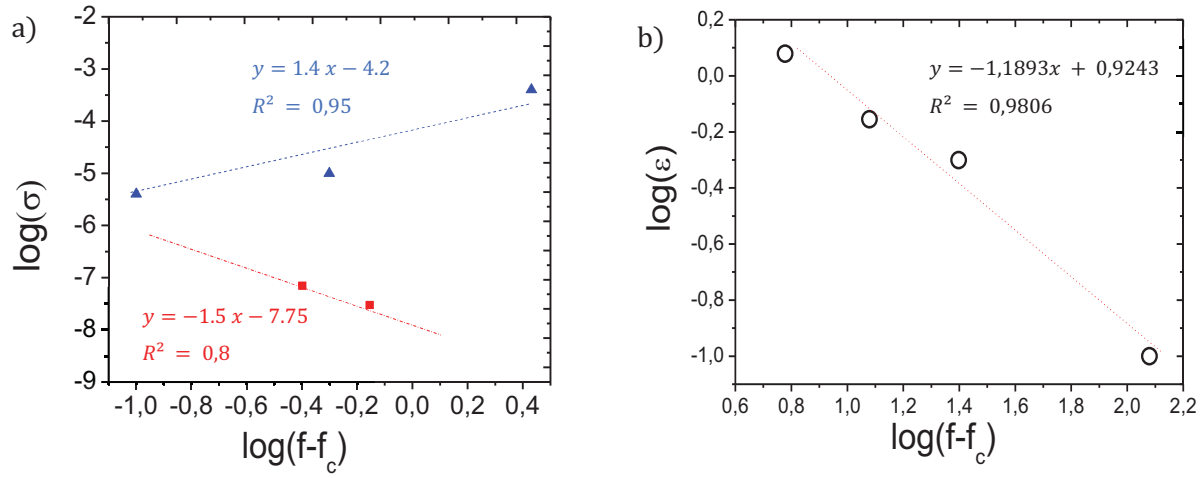


FIG. 3.13 - a) logarithm evolution of the conductivity at 100 Hz in function of the absolute difference f-fc, below the percolation (red squares), fc=1.3 and s=1.5; above the percolation (blue triangles), fc=1.3 and t=1.4 b) logarithm evolution of the permittivity at 100 Hz in function of the difference f-f_c, below the percolation. f_c=1.3 and s=1.2

As the volume fraction of r-GO is sometimes preferred and used in the literature[30], the weight fraction f can be transformed into the volume fraction v by using the equation (**EQ.3.5**):

$$v = \frac{\frac{f}{\rho_{rGO}}}{\frac{f}{\rho_{rGO}} + \frac{1-f}{\rho_{PDMS}}} \tag{3.5}$$

where ρ_{rGO} and ρ_{PDMS} are respectively the densities of r-GO (2.26 g/mL) and PDMS (1.05g/mL [31]). Thus, the weight percolation threshold corresponds to a volume fraction of 2.2 vol%.

We note that higher percolation thresholds were found in previous r-GO/polymer studies. Indeed, L. Seveyrat *et al.* [32] developed graphene based composites using solvent dispersion. The percolation threshold was found to be different for the two systems: 7.2% vol. for the r-GO/polyurethane films and 3.0% vol. for the r-GO/ P(VDF-TrFE-CFE) one. Permittivities of 70 and 120 were respectively measured at 100 Hz associated with loss tangent of 0.05 and 1.

2.2.3 Comparison with CNT/PDMS composites:

The electrical properties and percolation thresholds achieved with graphene based composites are often compared with those reported for CNT/polymer. A high percolation threshold has been found for our r-GO composites (1.3 *wt*% ; 2.2 vol%) compared to the

CNT based (0.2%wt [33]). This variation is due to the shape of the r-GO particles. As previously described, the platelets are known to exhibit an isotropic-nematic transition at low concentration below the percolation transition. Correlations of orientations of the platelets lower in fact their contact probability which results in a greater percolation threshold. This analysis is confirmed by electronic microscopy pictures that point out the lamellar phase structure of the rGO between the droplets (**FIG. 3.8**).

2.2.4 Dielectric response as a function of the electrical frequency:

FIG. 3.14 displays the frequency dependence (from 10^2 to 10^6 Hz) of the electric conductivity (σ), the relative permittivity (ε_r'), and the loss tangent ($\tan\delta$) at room temperature with different r-GO contents. At low r-GO concentrations, the permittivity exhibits a slow decrease trend along with the increasing frequency (**FIG. 3.14** a)). After the percolation threshold (1.3 wt%), the permittivity curves exhibit a different profile as they significantly decrease exponentially in function of the frequency. For example, the permittivity of the sample (1.8% wt) exhibits a decrease from 1000 to 40 as the frequency changes from 100 to 10^5. Above the percolation threshold and for all of the r-GO samples, the conductivity depends on the frequency, and no plateau is evidenced even at low frequencies (**FIG. 3.14** b)). Usually, for composites made with conductive fillers, the conductivity is mainly caused by the leakage current. The latest should lead, above the percolation, to a conductivity σ_{DC} independent on frequency. However, our results suggest a large contribution of dielectric losses to the conductivity instead of the free charges carriers. For low r-GO concentration, the dielectric losses are below 0.4 for the total frequency range. Above the percolation, the increase in the loss factor is the direct result of the considerably enhanced conductivity of the composites (**FIG. 3.14** c)). A value of 3 at 100 Hz is measured for the two samples at 1.4 and 1.8 wt%. For the highest value of filler concentration, a dielectric loss around 1 is measured. This decrease in the losses is a consequence of the huge measured permittivity ($\varepsilon'_{4\,wt\%} = 10^5$).

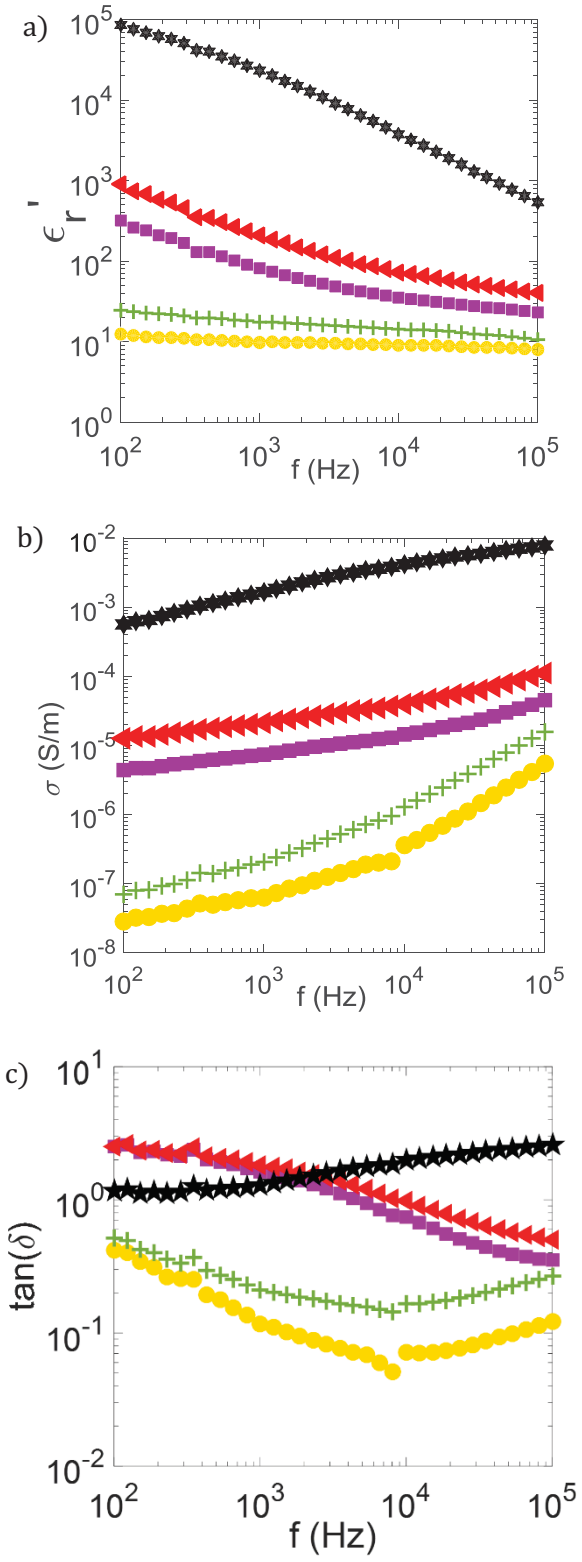


FIG. 3.14 - a) Evolution of the conductivity as a function of the frequency for various r-GO concentrations. 0.6%wt (yellow circle), 0.8%wt (green crosses), 1.4 %wt (purple square), 1.8%wt (red left triangle), 4%wt (black stars). b) Evolution of permittivity as a function of the frequency for various rGO concentrations (same symbols as in panel a). c) Evolution of tan(δ) as a function of the frequency for various rGO concentrations (same symbols as in panel a).

2.2.5 Influence of the r-GO concentration on the electrostriction modulus:

The electrostriction of our composites is measured directly by linking impedancemetry and piezoelectric actuator (see Chapter 2 for method details). In this method, a very low voltage 1 V is used (corresponding to a field of only 0.8 V/µm). The dielectric properties are measured using an 8% strain in the mechanical linear regime. Both electrostrictive contributions ($M_{33}^{Intrinsic}$ *and* $M_{33}^{Maxwell}$) were distinguished. We note that contrary to previous reported works[32,34], the Maxwell response is very close to the intrinsic response and that this effect can not be neglected.

TAB. 3.1 - Evolution of the Young modulus, ε'_r at 100 Hz, $M_{33}^{Maxwell}$, and $M_{33}^{Intrinsic}$ as a function of the rGO concentration.

wt% r-GO	**0,6**	**0,9**	**1,4**	**1,8**	**4**
Y (kPa)	$1.0\ 10^{2}$	$2.1\ 10^{1}$	$2.75\ 10^{2}$	$3.0\ 10^{2}$	$9.5\ 10^{1}$
ε_r (100Hz)	$1.23\ 10^{1}$	$4.10\ 10^{1}$	$3.18\ 10^{2}$	$9.09\ 10^{2}$	$7.99\ 10^{4}$
$M_{33}^{Maxwell}$ (100 Hz)	$-1.09\ 10^{-15}$	$-1.74\ 10^{-14}$	$-1.02\ 10^{-14}$	$-2.68\ 10^{-14}$	$-7.42\ 10^{-12}$
$M_{33}^{Intrinsic}$ (100 Hz)	$-4.79\ 10^{-16}$	$-4.75\ 10^{-15}$	$-1.51\ 10^{-14}$	$-6.11\ 10^{-15}$	$-1.80\ 10^{-13}$
$Q_{33}^{Intrinsic}$ (100 Hz)	$-4.77\ 10^{4}$	$-3.74\ 10^{3}$	$-1.91\ 10^{3}$	$-9.46\ 10^{1}$	$-3.60\ 10^{-1}$

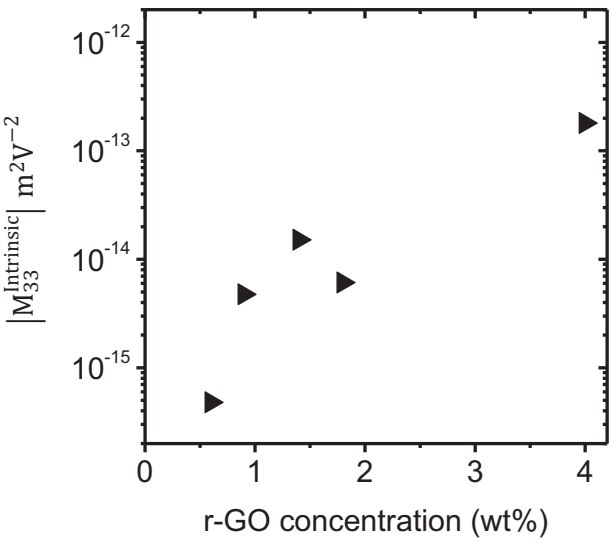


FIG. 15 - Evolution of the absolute value of the electrostrictive coefficient $M_{33}^{Intrinsic}$ at 100 Hz as function of the r-GO weight fraction.

M_{33} values are always negative whatever the concentration of r-GO (**TAB. 3.1**) and increase as a function of the filler weight fraction. Giant $M_{33}^{Intrinsic}$ values, as high as -1.8 $\times\ 10^{-13}$ m^2V^{-2} at 100 Hz are measured for f = 4wt %. However, this value comes with a high relative value of dielectric loss, equals to 1 at 100 Hz. This makes them unsuitable

for energy harvesting in spite of their giant electrostriction. Indeed, building an autonomous device requires very low losses in order to avoid discharging during the action phases. We also investigate the effect of graphene liquid phase of the near-percolated r-GO/PDMS composites (0.9 wt% and 1.4 wt%) on the electrostrictive modulus. Respectively, -4.75 × 10^{-15} and -1.51 × 10^{-14} m^2V^{-2} were measured, corresponding to a significative variation of permittivity from 41.3 to 54.8 and 318 to 881 for the 0.9 wt% and 1.4 wt% samples. This important electrostriction is due to the applied pressure which leads to contact changes between the particles and changes in their orientation. Unfortunately, high value of loss tangent 2.5 for 1.4 wt% and 2.8 for 0.9 wt% were measured at rest. We note that the performances of these materials remain classical and similar values have been reported for r-GO/PDMS composites. J.Yuan *et al.* [34] developed composites formulated by a phase-transfer method which allows the solubilization of GO flakes into nonpolar solvents. An intrinsic electrostriction of -1.2 × 10^{-14} m^2V^{-2} was reported with a loss tangent around 2.5 at 0.1 Hz. We also note that previously reported CNT/PDMS composites [33] exhibit similar electrostriction $M_{33}^{Intrinsic} = -10^{-13}\ m^2V^{-2}$ than our materials but with lower dielectric losses : $tan\,\delta = 0.5$ at 100 Hz below the percolation threshold (0.2 wt% of CNT).

2.2.6 Piezoresistivity:

The resistivity of the sample indeed varies as a function of the compression. It decreases when the sample is compressed, and the sample exhibits negative piezoresistivity. This effect is due to the change of the contact conditions for electronic conduction such as break in contact upon compression. **FIG. 3.16** displays the evolution of the gauge factor $GF = \frac{R_0 - R_s}{R_0 \gamma}$ as a function of the r-GO weight fraction, where R_s is the value of the strained sample and R_0 the initial value.

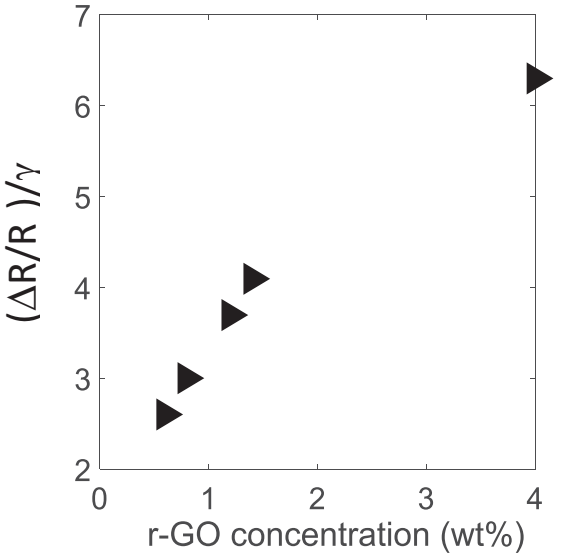


FIG. 3.16 - Evolution of the gauge factor as a function of r-GO weight fraction

The gauge factor increases from 2.5 to more than 6 above the percolation threshold. The latter value is higher than the metal resistive strain gauges which typically exhibit gauge factors in the range of 0.8−3. Similar values have been reported for graphene based composites. C.Yan et al.[35] reported a stretchable piezoresistive graphene–nanocellulose composite which exhibits a GF around 6 but for a strain up to 80% while only 8% strain was required in our case. However, higher GF have been measured for CNT/PDMS composites based on the same templating effect as our work [33]. The GF increases from 1 to more than 1000 above the percolation threshold (2 wt% of CNT). This higher performance is due to the easier change of the contact conditions when rod fillers (CNT) are preferred instead of flake fillers (r-GO). Nevertheless, the piezoresistivity we measured in our work, still opens the path for making low cost and flexible resistive strain sensors. Note that a full validation of the sensor applications, it would require further characterizations, including studies of cycling repeatability, reversibility, linear, or nonlinear calibration.

3 Conclusion:

We developed electrostrictive composites based on liquid crystalline r-GO flakes in a PDMS matrix. The intrinsic electrostriction of composites was directly measured and isolated from the Maxwell effect. The structure of graphene flakes promotes the formation of microcapacitors which leads to an enhancement of the dielectric response. Composites display high permittivity up to 10^5. The reported giant electrostrictive modulus, make the dielectric properties very sensitive to external mechanical stimuli. However, high dielectric losses were measured too, between 1 and 2 for the percolated systems. To bypass this drawback, it is thus mandatory to reduce the value of the conductivity as low as possible. In order to do so, the use of inverse emulsion (W/O) to prepare the sample might be an appropriate approach. It will allow us to confine the conductive particles inside droplets and to avoid many contacts and losses. This is the purpose of Chapter 4.

Take home message – Chapter 3

In this Chapter, we report the realization of electrostrictive materials based on liquid crystalline r-GO flakes in a PDMS matrix. Emulsion path aims at finely dispersed the fillers. We investigate the dielectric properties and electrostrictive properties.

1. The structure of graphene flakes promotes the formation of microcapacitors which leads to an enhancement of the dielectric response. Composites display high permittivity up to 10^5 at 100 Hz.

2. The materials present dielectric losses, between 1 and 2 for the percolated systems. This makes them too conductive for energy harvesting applications.

3. The materials show piezoresistivity and a gauge factor around 6 above the percolation threshold.

[1] H.S. Nalwa, Handbook of Low and High Dielectric Constant Materials and Their Applications, Academic Press, San Diego, 1999. http://search.ebscohost.com/login.aspx?direct=true&scope=site&db=nlebk&db=nlabk&AN=249073 (accessed May 26, 2018).

[2] H.R. Huff, H.R. Huff, H.R. Huff, High dielectric constant materials: VLSI MOSFET applications, Springer, Berlin, 2005.

[3] Z.-M. Dang, J.-K. Yuan, J.-W. Zha, T. Zhou, S.-T. Li, G.-H. Hu, Fundamentals, processes and applications of high-permittivity polymer–matrix composites, Progress in Materials Science. 57 (2012) 660–723. doi:10.1016/j.pmatsci.2011.08.001.

[4] J. Yuan, A. Luna, W. Neri, C. Zakri, T. Schilling, A. Colin, P. Poulin, Graphene liquid crystal retarded percolation for new high-k materials, Nature Communications. 6 (2015) 8700. doi:10.1038/ncomms9700.

[5] S.-H. Yao, Z.-M. Dang, M.-J. Jiang, H.-P. Xu, J. Bai, Influence of aspect ratio of carbon nanotube on percolation threshold in ferroelectric polymer nanocomposite, Applied Physics Letters. 91 (2007) 212901. doi:10.1063/1.2817746.

[6] Y.R. Hernandez, A. Gryson, F.M. Blighe, M. Cadek, V. Nicolosi, W.J. Blau, Y.K. Gun'ko, J.N. Coleman, Comparison of carbon nanotubes and nanodisks as percolative fillers in electrically conductive composites, Scripta Materialia. 58 (2008) 69–72. doi:10.1016/j.scriptamat.2007.08.025.

[7] D. Stauffer, A. Aharony, Introduction to percolation theory, Rev. 2. ed., transferred to digital print, Routledge, London, 2003.

[8] C.-W. Nan, Y. Shen, J. Ma, Physical Properties of Composites Near Percolation, Annual Review of Materials Research. 40 (2010) 131–151. doi:10.1146/annurev-matsci-070909-104529.

[9] C.-W. Nan, Physics of inhomogeneous inorganic materials, Progress in Materials Science. 37 (1993) 1–116. doi:10.1016/0079-6425(93)90004-5.

[10] C. Pecharromán, J.S. Moya, Experimental Evidence of a Giant Capacitance in Insulator-Conductor Composites at the Percolation Threshold, Advanced Materials. 12 (2000) 294–297. doi:10.1002/(SICI)1521-4095(200002)12:4<294::AID-ADMA294>3.0.CO;2-D.

[11] Broadband dielectric spectroscopy., Springer, Place of publication not identified, 2013.

[12] B. Marinho, M. Ghislandi, E. Tkalya, C.E. Koning, G. de With, Electrical conductivity of compacts of graphene, multi-wall carbon nanotubes, carbon black, and graphite powder, Powder Technology. 221 (2012) 351–358. doi:10.1016/j.powtec.2012.01.024.

[13] C. Lee, X. Wei, J.W. Kysar, J. Hone, Measurement of the Elastic Properties and Intrinsic Strength of Monolayer Graphene, Science. 321 (2008) 385–388. doi:10.1126/science.1157996.

[14] L. Jin, G. Wang, X. Li, L. Li, Poly(2,5-dimercapto-1,3,4-thiadiazole)/sulfonated graphene composite as cathode material for rechargeable lithium batteries, Journal of Applied Electrochemistry. 41 (2011) 377–382. doi:10.1007/s10800-010-0246-z.

[15] R. Liang, H. Cao, D. Qian, J. Zhang, M. Qu, Designed synthesis of SnO2-polyaniline-reduced graphene oxide nanocomposites as an anode material for lithium-ion batteries, Journal of Materials Chemistry. 21 (2011) 17654. doi:10.1039/c1jm13934g.

[16] C. Xu, Y. Cao, R. Kumar, X. Wu, X. Wang, K. Scott, A polybenzimidazole/sulfonated graphite oxide composite membrane for high temperature polymer electrolyte membrane fuel cells, Journal of Materials Chemistry. 21 (2011) 11359. doi:10.1039/c1jm11159k.

[17] D. Konios, M.M. Stylianakis, E. Stratakis, E. Kymakis, Dispersion behaviour of graphene oxide and reduced graphene oxide, Journal of Colloid and Interface Science. 430 (2014) 108–112. doi:10.1016/j.jcis.2014.05.033.

[18] Y. Zhu, S. Murali, W. Cai, X. Li, J.W. Suk, J.R. Potts, R.S. Ruoff, Graphene and Graphene Oxide: Synthesis, Properties, and Applications, Advanced Materials. 22 (2010) 3906–3924. doi:10.1002/adma.201001068.

[19] C.K. Chua, M. Pumera, Chemical reduction of graphene oxide: a synthetic chemistry viewpoint, Chem. Soc. Rev. 43 (2014) 291–312. doi:10.1039/C3CS60303B.

[20] S. Stankovich, D.A. Dikin, R.D. Piner, K.A. Kohlhaas, A. Kleinhammes, Y. Jia, Y. Wu, S.T. Nguyen, R.S. Ruoff, Synthesis of graphene-based nanosheets via chemical reduction of exfoliated graphite oxide, Carbon. 45 (2007) 1558–1565. doi:10.1016/j.carbon.2007.02.034.

[21] J. Zhang, H. Yang, G. Shen, P. Cheng, J. Zhang, S. Guo, Reduction of graphene oxide via L-ascorbic acid, Chem. Commun. 46 (2010) 1112–1114. doi:10.1039/B917705A.

[22] H.C. Schniepp, J.-L. Li, M.J. McAllister, H. Sai, M. Herrera-Alonso, D.H. Adamson, R.K. Prud'homme, R. Car, D.A. Saville, I.A. Aksay, Functionalized Single Graphene Sheets Derived from Splitting Graphite Oxide, The Journal of Physical Chemistry B. 110 (2006) 8535–8539. doi:10.1021/jp060936f.

[23] T.S. Radhakrishnan, Thermal degradation of poly(dimethylsilylene) and poly(tetramethyldisilylene-co-styrene), Journal of Applied Polymer Science. 99 (2006) 2679–2686. doi:10.1002/app.22813.

[24] H. Wang, Q. Wang, J. He, Z. Mao, J. Sun, Study on the Pyrolytic Behaviors and Kinetics of Rigid Polyurethane Foams, Procedia Engineering. 52 (2013) 377–385. doi:10.1016/j.proeng.2013.02.156.

[25] M. Cochet, W.K. Maser, A.M. Benito, M.A. Callejas, M.T. Martínez, J.-M. Benoit, J. Schreiber, O. Chauvet, Synthesis of a new polyaniline/nanotube composite: "in-situ" polymerisation and charge transfer through site-selective interaction, Chemical Communications. (2001) 1450–1451. doi:10.1039/b104009j.

[26] K. Wongtimnoi, B. Guiffard, A. Bogner-Van de Moortèle, L. Seveyrat, C. Gauthier, J.-Y. Cavaillé, Improvement of electrostrictive properties of a polyether-based polyurethane elastomer filled with conductive carbon black, Composites Science and Technology. 71 (2011) 885–892. doi:10.1016/j.compscitech.2011.02.003.

[27] P. Fan, L. Wang, J. Yang, F. Chen, M. Zhong, Graphene/poly(vinylidene fluoride) composites with high dielectric constant and low percolation threshold, Nanotechnology. 23 (2012) 365702. doi:10.1088/0957-4484/23/36/365702.

[28] H. Kim, Y. Miura, C.W. Macosko, Graphene/Polyurethane Nanocomposites for Improved Gas Barrier and Electrical Conductivity, Chemistry of Materials. 22 (2010) 3441–3450. doi:10.1021/cm100477v.

[29] A. Luna, J. Yuan, W. Néri, C. Zakri, P. Poulin, A. Colin, Giant Permittivity Polymer Nanocomposites Obtained by Curing a Direct Emulsion, Langmuir. 31 (2015) 12231–12239. doi:10.1021/acs.langmuir.5b02318.

[30] D. Wang, X. Zhang, J.-W. Zha, J. Zhao, Z.-M. Dang, G.-H. Hu, Dielectric properties of reduced graphene oxide/polypropylene composites with ultralow percolation threshold, Polymer. 54 (2013) 1916–1922. doi:10.1016/j.polymer.2013.02.012.

[31] H. Hocheng, C.-M. Chen, Y.-C. Chou, C.-H. Lin, Study of novel electrical routing and integrated packaging on bio-compatible flexible substrates, Microsystem Technologies. 16 (2010) 423–430. doi:10.1007/s00542-009-0930-2.

[32] L. Seveyrat, A. Chalkha, D. Guyomar, L. Lebrun, Preparation of graphene nanoflakes/polymer composites and their performances for actuation and energy harvesting applications, Journal of Applied Physics. 111 (2012) 104904. doi:10.1063/1.4718577.

[33] A. Luna, M. Pruvost, J. Yuan, C. Zakri, W. Neri, C. Monteux, P. Poulin, A. Colin, Giant Electrostrictive Response and Piezoresistivity of Emulsion Templated Nanocomposites, Langmuir. 33 (2017) 4528–4536. doi:10.1021/acs.langmuir.6b04185.

[34] J. Yuan, A. Luna, W. Neri, C. Zakri, A. Colin, P. Poulin, Giant Electrostriction of Soft Nanocomposites Based on Liquid Crystalline Graphene, ACS Nano. 12 (2018) 1688–1695. doi:10.1021/acsnano.7b08332.

[35] C. Yan, J. Wang, W. Kang, M. Cui, X. Wang, C.Y. Foo, K.J. Chee, P.S. Lee, Highly Stretchable Piezoresistive Graphene-Nanocellulose Nanopaper for Strain Sensors, Advanced Materials. 26 (2014) 2022–2027. doi:10.1002/adma.201304742.

4. Microporous electrostrictive materials for vibrational energy harvesting

This chapter is based on the following article:

Mickaël Pruvost,Wilbert J. Smit, Cécile Monteux, Philippe Poulin, Annie Colin. Microporous electrostrictive materials for vibrational energy harvesting. *Multifunct. Mater*. 00 (2018) 000000

Summary:

We present electrostrictive materials with excellent properties for vibrational energy harvesting applications. The developed materials consist of a porous carbon black composite, which is processed using water-in-oil emulsions. In combination with an insulating layer, the investigated structures exhibit a high effective relative dielectric permittivity (up to 182 at 100 Hz) with very low effective conductivity (down to 2.53 $10^{-8}\ S\ m^{-1}$). They can generate electrical energy in response to mechanical vibrations with a power density of 0.38 $W\ m^{-3}$ under an applied bias electric field of 32V. They display figures of merit for energy harvesting applications well above reference polymer materials in the field, including fluorinated co- and ter-polymers synthesized by heavy chemical processes. The production process of the present materials is based on non-hazardous and low-cost chemicals. The soft dielectric materials are highly flexible (Young's modulus of ~1 MPa) making them also suited for highly sensitive capacitive sensors.

1 Introduction:

The Internet of Things (IoT) is a new and fast-growing concept which aims at connecting everyday physical objects into the Internet without any human interaction [1,2]. The IoT requires the usage of numerous wireless sensors. Providing the electrical energy to run these wireless sensors is of major concern. Use of batteries with limited lifetime is a severe constraint. To overcome this problem, several environmental energy sources such as thermal, solar, salinity gradients, vibrations can be used to fulfill energy demands [3–5]. It could thus make sensors, MEMS, communicating devices, etc. self-sufficient in energy supply and as such highly increase their lifetime. A promising method to resolve this challenge is to harvest mechanical energy from the ambient environment and convert it into electrical power. An apparently convenient method consists in using piezoelectric materials. The most efficient piezoelectric ceramics can produce up to 0.2—30 mW cm^{-1} [6–9]. However, these materials are stiff and brittle which limits their implementation in embedded applications [10]. Triboelectric nanogenerators have recently demonstrated volume power density up to 0.49 W cm^{-3} [11,12]. However, their performances are largely affected by the environment such as humidity [12]. Moreover, their low durability as a result of two materials in physical friction is still a limiting factor [11]. A more recent approach consists in using electrostrictive polymers to convert energy from mechanical vibrations [13–19]. These polymers have high dielectric permittivity and are used as the dielectric layer inside variable capacitors. Capacitance variations in response to mechanical variations are enhanced by changes of dielectric permittivity of the electrostrictive polymers. This principle can be used to convert mechanical energy of vibrations into electrical energy. The interest in electrostrictive polymers is rapidly growing because polymer-based high-permittivity materials are flexible, low cost, and easily tunable, which makes them good candidates for IoT applications. A recent approach for obtaining high permittivity electrostrictive polymers is the use of polymers loaded with conductive nanoparticles [15–19]. These composite materials exhibit a large increase of dielectric permittivity in the vicinity of their percolation threshold but suffer from a weakness due to the substantial increase of losses near and above percolation [19,20].

2 Our strategy:

To overcome the limitations due to the high dielectric losses, we design a new bilayer structure based on a microporous dielectric layer associated with a thin insulating layer of polydimethyl siloxane (PDMS). Flexible porous materials of which the internal pores are covered with carbon black particles are prepared using a water-in-oil emulsion. This new composite possesses a high dielectric permittivity along with a very low conductivity. The fabrication of the microporous dielectric layer using a water-in-oil emulsion provides a fine control of the location of the conductive inclusions. The latter remain confined in the emulsions droplets. The micropores significantly deform upon compression resulting in a large change of the dielectric permittivity [21]. As such, the porous dielectric material can be used in a variable-capacitance engine to harvest mechanical energy [22]. The energy harvesting performance can be improved by combining the porous dielectric with a thin insulating layer of PDMS. This reduces the

conductivity of the system, and allows an increase of the filler concentration above the percolation threshold in the high permittivity layer.

In this chapter, we will first present the method for making carbon black/PDMS composites and then we will present their dielectric properties. In the second part, we will focus on the bilayer composites with theoretical considerations and experimental dielectric measurements. Finally, the last part will be devoted to the harvesting capabilities of the materials and we will open the discussion by comparing our performances to the previous reported works.

3 Carbon black/PDMS composites based on a W/O emulsion template:

3.1 Carbon black as conductive fillers:

Carbon black (CB) is massively produced by the petrochemical industry as a by-product of incomplete combustion of hydrocarbons [23]. It makes this filler low-cost and easily accessible. CB, as fillers in elastomers, plastics and paints, afford materials with outstanding electrical [24] and mechanical properties [25]. From a structural point of view, carbons form layer structures composed of hexagonal carbon rings, which tend to stack in three to four layers, forming crystallographic structures (**FIG. 4.1** a)). Then form primary particles, which further get together into primary aggregates (**FIG. 4.1** b)) Van der Waals forces cause these aggregates to join in more loosely assembled agglomerates (**FIG. 4.1** c)) [26].

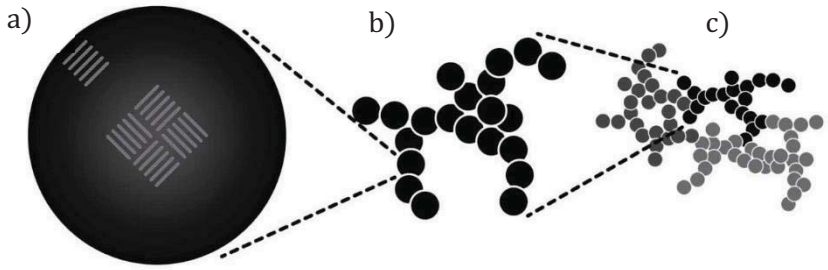


FIG. 4.1 - a) nodule (15-300 nm) b) aggregate (80-500 nm) c) agglomerate (1-100 µm)

It is well known that CB develops pore structures and high internal surface area. This property has ensured the development of many industrial applications: in the field of water purification where CB is used as absorbent for removing contaminants [26] and in the field of supercapacitors where huge specific surface areas are required for developing electrodes with high capacitances [28,29]. Supercapacitors benefit from high surface but from the high conductivity and electrochemical stability of carbon black too. Then, a huge part of carbon black production is devoted to the use as enhancer in polymer industries to improve the mechanical performances over other established materials [30]. For example, CB is used as filler in rubber for increasing the wear resistance of tires. Moreover, carbon black is extensively used as a conductive filler in elastomer composites to enhance the dielectric behavior of materials [31–33]. Although metal particles are intrinsically more conductive than CB, metal has a tendency to oxidize to form an insulating layer on its surface and cannot be used as easily as CB.

Concentration, nature, surface of carbon are examples of parameters which will influence the dielectric parameters [34].

3.2 Dispersion and coating processes:

3.2.1 Water solubilization of carbon black:

As carbon black particles are poorly soluble in water, we have chosen to work with a dispersant. In our formulations, Arabic gum is used as an emulsifier to make carbon particles suspensions. Note that surfactants such as SDS could lead to well-dispersed particles too, but Arabic gum has the advantage to be non-electrochemically active. From a chemistry point of view, Arabic gum is a sugar, which is used for centuries for making Chinese ink and has shown good dispersion of carbon particles [20]. Moreover, we choose to work with carbon black acetylene (Alfa Aesar, d=100g/L, surface area=80m^2/g), one of the purest carbon black, which has shown excellent electrical properties [20]. To make the dispersion, the water phase is prepared by mixing 5 wt % of Arabic gum (Sigma Aldrich) in deionized water. Carbon black particles are then added in variable proportions depending on the formulation, from 3 wt % to 10 wt %. The blend is then handshaked during several minutes until the carbon black is totally wetted by the aqueous solution. Finally, to homogenize the dispersion, the mixture is tip sonicated for 1 hour at 400 W. **FIG. 4.2** illustrates the carbon dispersion for a 1%wt CB.

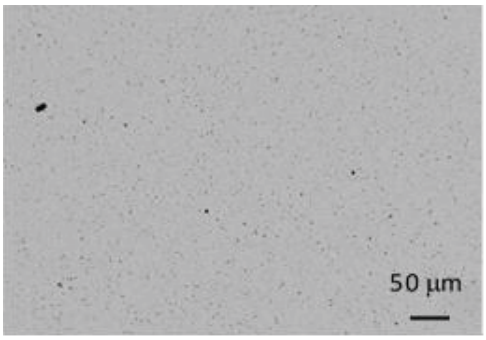


FIG. 4.2 - Microscopic picture of carbon black dispersion

3.2.2 Water in oil dispersion:

Contrary to Chapter 3 where R-GO fillers were dispersed using an oil-in-water dispersion process, the water-in-oil emulsion path has been preferred for developing carbon black composites. Indeed, W/O emulsion provides a fine control of the location of the conductive inclusions as the latter remain confined in the water droplets. The composites are synthesized by mixing CB solution to a PDMS oil phase by using a commercial oil-soluble surfactant (lauryl PEG-8 dimethicone) (see Chapter 2 § 1.3.2.1 for details). After molding, curing and drying, the materials become solid and carbon blacks particles create a conductive shell inside each air cavities (**FIG. 4.3**). We expect to get a close porosity (closed pores) where conductive pores will be isolated from each other. In this way, the probability to create conductive paths is reduced while maintaining the possibility to get high global permittivity by Maxwell-Wagner's effect. Indeed, if the CB inclusions are well dispersed, the large surface area of pores will serve as electrode of numerous small capacitors, and PDMS will play the role of a dielectric

layer between two conductive pores. The capacitor network within the composite can thus give a large capacitance and dielectric constant. The dielectric properties of the material can be finely tuned by varying the concentration of conductive particles. Note that when we talk about weight percentage of CB particles, we refer to the weight of CB regarding the total dried weight of the composites after water evaporation as:

$$CB\ wt\% = \frac{m_{\mathrm{CB}}}{m_{\mathrm{CB}} + m_{PDMS}} \tag{4.1}$$

Two possibilities exist for increasing the weight percentage of CB. First, for a given concentration of CB solution, we can increase the fraction of dispersed phase versus the continuous phase. Second, we can keep the ratio water/oil constant and increase the concentration of CB solution. Both methods have their limitations. Indeed, we will not be able to dispersed water phase above a critical fraction ($\phi = 60\%$) where the emulsion will start dephasing. Moreover, the solubilized quantity of carbon in water is limited. After a certain CB concentration, the viscosity of the solution will be too high to assure a good dispersion in the PDMS matrix.

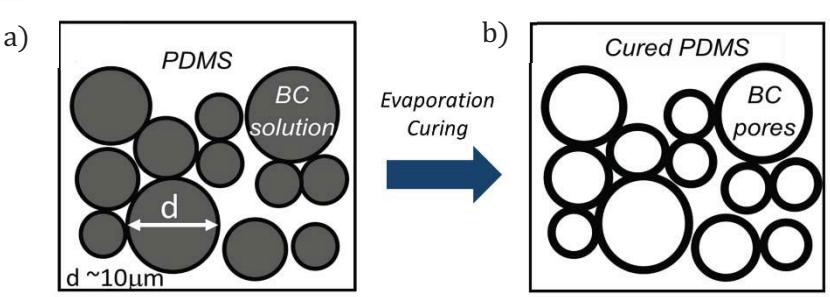


FIG. 4.3 - a) water-in-oil emulsion with PDMS as oil matrix and carbon black solution as aqueous part b) evaporation and thermal curing steps create a porous material.

3.2.3 Emulsion coating and curing parameters:

The water-in-oil emulsion loaded with carbon black particles can be easily shaped and coated with the desired geometric dimensions. The emulsion is spread with a micrometer adjustable film applicator (adjustable thickness) on a 250 μm thick PET plastic film (**FIG. 4.4** a)). A second plastic surface is placed on the spread emulsion such that the emulsion remains confined between two flat surfaces. Solid materials are obtained by curing the PDMS polymer without evaporation in a warm water bowl (90°C) for 4 hours. The relative humidity in these conditions is 100%. Then, the solid material layer is removed from the two plastic surfaces and dried in an oven for 1 hour at 150°C (**FIG. 4.4** b)). As PDMS is permeable to water vapor, droplets of carbon black solution dried and leave a structure with spherical-shaped pores covered by carbon black particles. Curing and drying are critical stages which strongly influence the final morphology of the porous composite. For example, a curing step with a temperature

higher than ebullition temperature of water would lead to the destruction of the emulsion and the loss of the porosity.

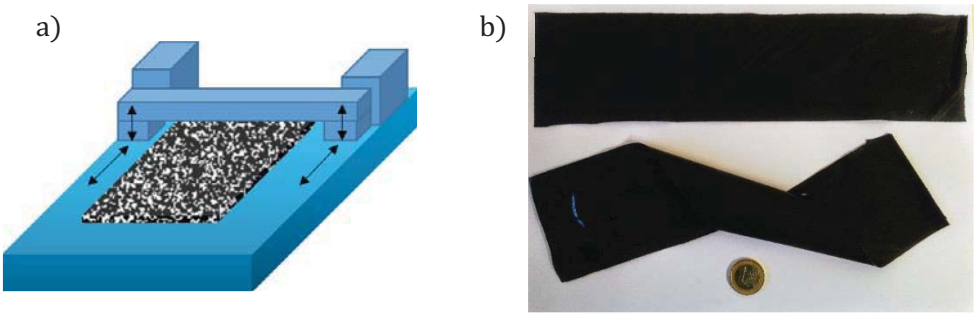


FIG. 4.4 – a) film-coater with adjustable film applicator b) macroscopic view of the composite film (200 µm X 7.5 cm X 18cm) coated with a doctor blade.

3.3 Interest in porous structures:

The micropores significantly deform upon compression resulting in a large change of the dielectric permittivity (**FIG. 4.5**). Indeed, the material can be seen as a composite where air inclusions coated with a conductive shell are dispersed in a PDMS matrix. Permittivity of air-CB pores is very different compared to PDMS matrix. Compressing the material amount to change the individual volume of the conductive inclusion which can lead to huge changes of global permittivity of the material as we decrease the volume fraction of conductive pores inside the PDMS matrix.

Besides, increasing the porosity helps at decreasing the Young's modulus of materials. Indeed, as the carbon black is known to reinforce the mechanical properties of materials, increasing the quantity of pores will offset the reinforcement. Developing materials with low Young's modulus is a key to success for efficient mechanical to electrical conversion. Indeed, softer materials will require less stress than others to get the same strain and thus less mechanical energy.

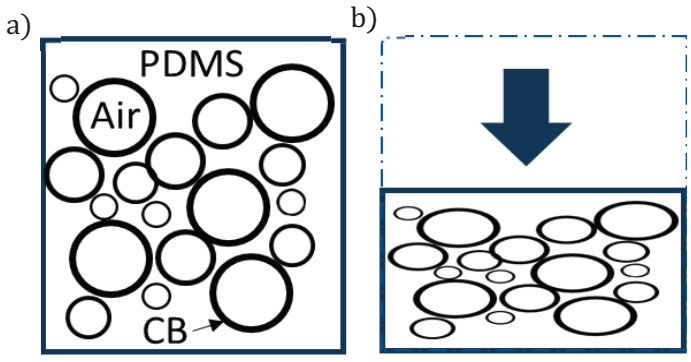


FIG. 4.5 - Schematic representation of the micropores a) at rest b) under deformation.

3.4 Microscopic analysis:

The final morphology of materials depends strongly on the competition between the curing and evaporation times. Fast curing along with a high relative humidity leads to spherical water drops surrounded by cured PDMS. The PDMS has time to solidify before

starting the water evaporation. This is evidenced by SEM investigation. **FIG. 4.6** illustrates a cross-cut of a porous carbon black composite (BC=5wt% ; oil:water=1:1). A high porosity is clearly observable, resulting of previous formed water droplets, with size pores between 1-10 µm. Each pores are globally isolated but some are connected and leads to partially opened porosity.

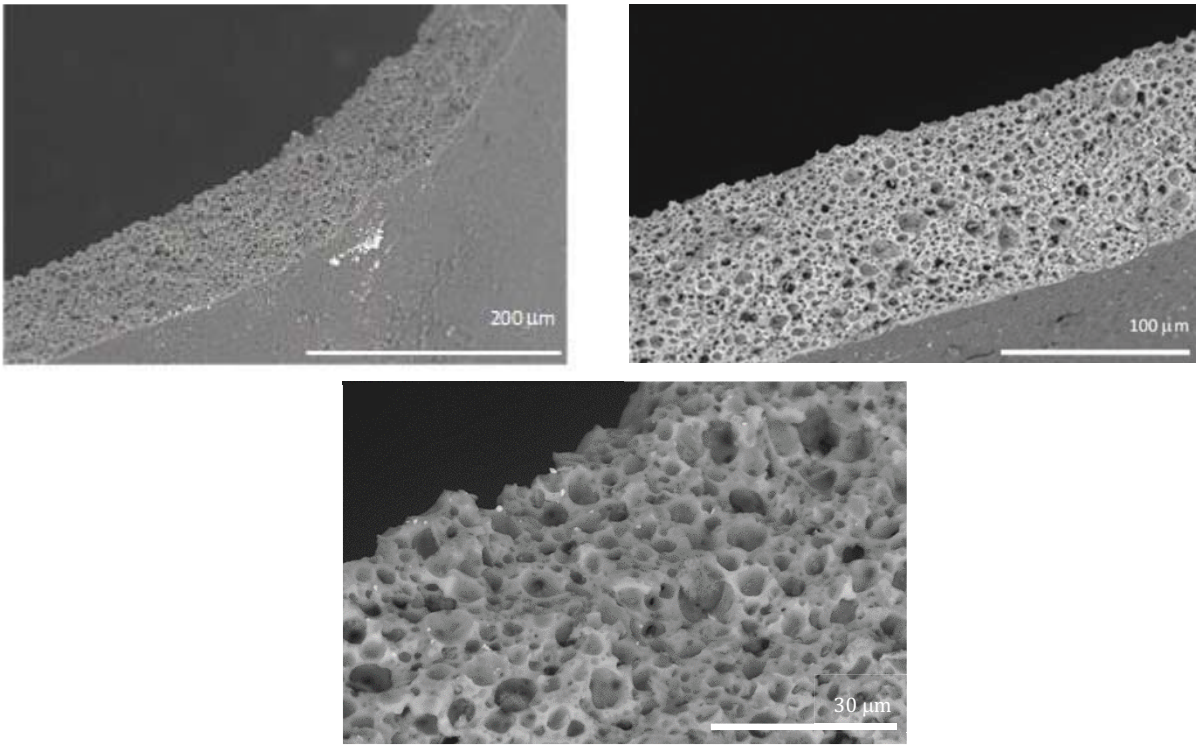


FIG. 4.6 - Electron microscope pictures of a cross-cut of a porous carbon black composite. BC=5wt% ; oil:water=1:1. Scale bars in the pictures.

3.5 Dielectric response:

3.5.1 Frequency dependence:

We measure the electrical conductivity and dielectric permittivity of CB/PDMS composites as the same way as rGO/PDMS samples, precise method is described in Chapter 2 §1.1.3. We just remind that we use a calibration procedure for removing the parasitic impedances and that all the experiments are performed at room temperature. **FIG. 4.7** Illustrates the results as a function of the CB weight fraction, the ratio water:oil is kept constant and is equal to 1:1. Both conductivity and dielectric permittivity increase as a function of CB weight fractions. The percolation threshold is reached for a weight fraction below 6%. Below the percolation threshold, the conductivity is frequency dependent and arises from dielectric losses due to bound charges. In the meantime, the dielectric permittivity remains constant for the full range of investigated frequencies. Above the percolation threshold, and at low frequencies, the conductivity is constant because essentially due to the transport of free charges brought by the carbon black particles. By contrast, the dielectric permittivity presents frequency dependence and is enhanced by the interfacial polarization of the carbon black particles. In the high filler concentration regimes, the values of conductivity (above 10^{-6} S m^{-1}) make the materials unsuitable for vibrational energy harvesting.

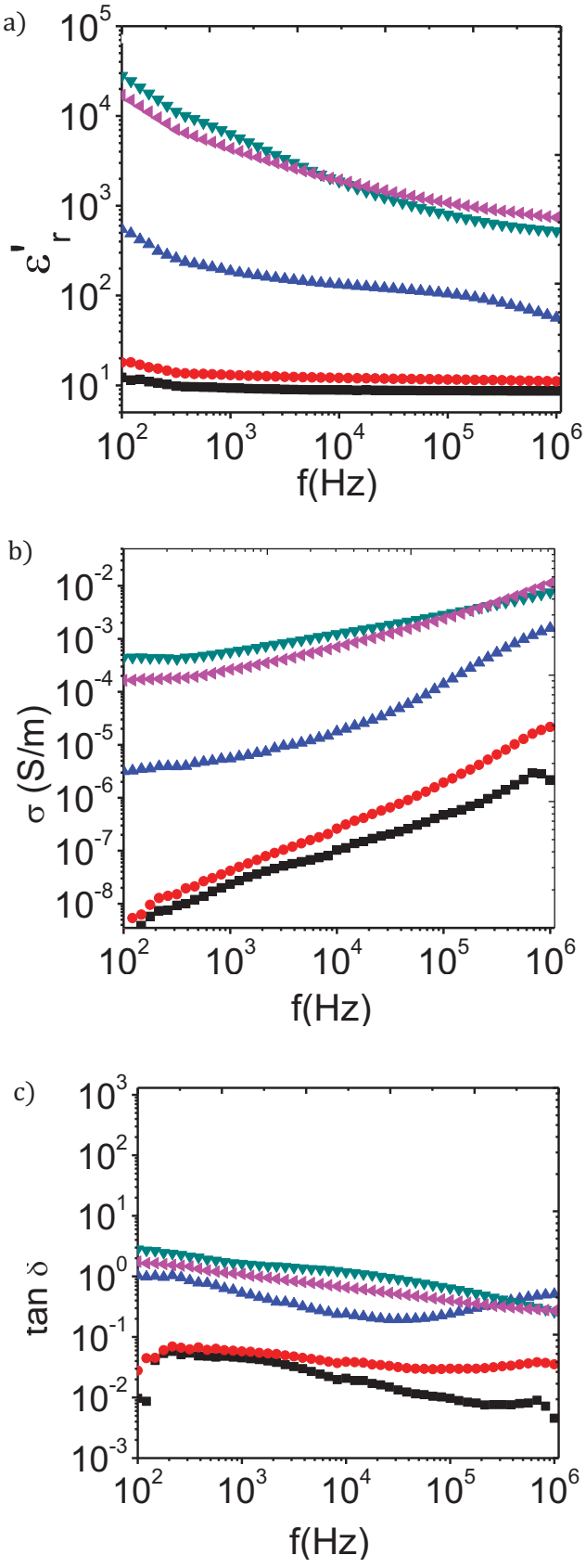


FIG. 4.7 - a) Evolution of the dielectric permittivity b) conductivity c) and loss tangent as a function of the frequency for various CB particle concentrations. 3.0 wt % (black squares), 4.0 wt % (red circles), 6.0 wt% (purple top triangles), 8.0 wt% (green down triangles), 10 wt% (pink left triangles). Phase fractions are fixed: oil:water = 1:1

3.5.2 Influence of the formulation on dielectric properties:

We have studied the influence of CB weigh fractions and aqueous fraction on permittivity at 100 Hz. **FIG. 4.8** illustrates the results, each spot correspond to an experiment and color map are simulated isoresponse curves based on experimental results. Simulations have been performed using software JMP (statistical software). It can be seen that whatever the aqueous fraction (CB solution), the percolation threshold is kept constant, around 4.5-5 wt%. At this concentration, the permittivity (**FIG. 4.8** a)) and *tan δ* (**FIG. 4.8** b)) show a dramatic increase. It is worth noticing that for a fixed CB fraction, increasing the aqueous fraction requires increasing the CB concentration of water solutions. It means that for a low aqueous fraction, the CB concentration inside pores will be higher than in the case of a high aqueous fraction. The results show that whatever the way carbon is dispersed inside the PDMS matrix, it will not significantly

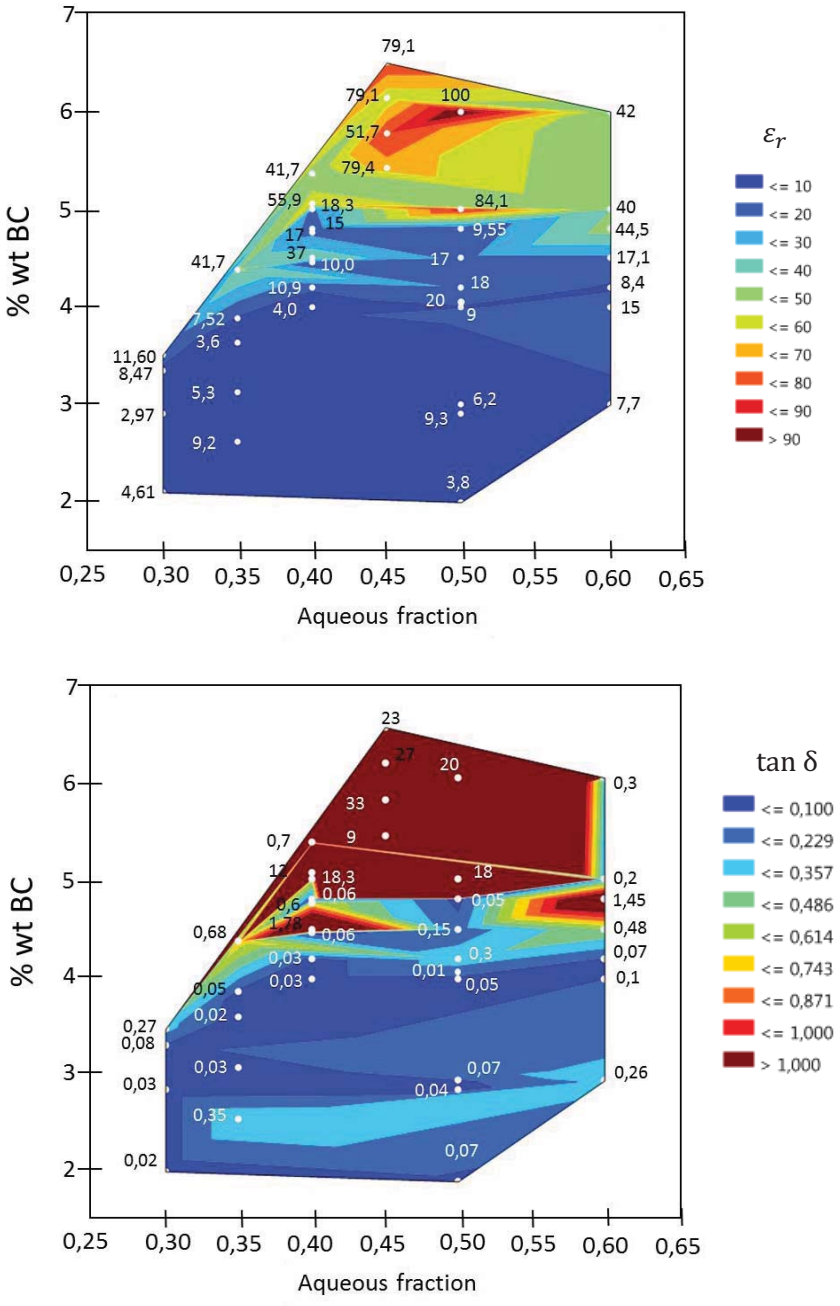


FIG. 4.8 - Isoresponse curves of a) permittivity and b) *tan δ* as a function of the CB weigh percent and the aqueous fraction at 100 Hz.

affect the percolation threshold. The main parameter remains the carbon weight fraction for determining the percolation threshold. Obviously, this conclusion has limitations. Indeed, if all the carbon particles were at the same place, no percolation would be observable.

Otherwise, the porosity will affect the mechanical properties. For a fixed CB concentration, increasing the porosity will lead to materials with lower Young's modulus.

3.5.3 Conclusion on dielectric response of porous BC/PDMS composites:

In this part, we proposed a new formulation to easily prepare porous BC/PDMS composites using water in oil emulsions as a way for improving the fillers dispersion. Dielectric responses have been studied on several formulations. In part §3.3.1, we studied the frequency response of materials having a fixed water:oil ratio of 1.1 and different CB concentrations. A good compromise between high permittivity and low dielectric loss has been found for materials close to the percolation threshold. Indeed, for 4.0 wt% of CB, a permittivity of 20 with a $tan\ \delta$ equal to 0.02 has been measured at 100 Hz. These performances are very close to those delivered by the polyvinylidene fluoride (PVDF)[35], considered as a reference in the field of electroactive polymers. Nevertheless, the soft process (solvent free, PDMS, low operating temperatures) we used is an advantage compared to fluorinated polymers synthesized by heavy chemical processes. Plus, the high stretchability of PDMS composites (Young's modulus of ~1 MPa) could open the application window as PVDF materials developed Young's modulus three decades higher [36] than our materials. As we showed §3.3.2, the dispersed fraction (aqueous phase) weakly influences on the percolation threshold and dielectric properties. However, changing the dispersed fraction could be used to tune the mechanical properties.

We are aware that dielectric composites based on conductive fillers show limitations and drawbacks. Indeed, the dielectric properties of porous materials highly depend upon the materials synthesis protocol in the vicinity of the percolation transition. It leads to a very limited composition window, making the process poorly reliable. Moreover, developing materials with higher permittivity than 20 and low dielectric losses, is still a challenge.

To overcome the limitations due to the high dielectric losses, we design a new bilayer structure. It is based on the previously described microporous CB material associated with a thin insulating layer of polydimethyl siloxane (PDMS). This new composite is the purpose of the next parts.

4 Interest of bilayer composites:

4.1 Bilayer composites:

Facing the huge challenge to develop dielectric composites with low dielectric losses by incorporation of conductive fillers, some reported works [37] proposed a new approach. The main idea is to use a two-layer system based on a high permittivity material and a small air gap which is by definition easily deformable and completely isolating. The developed system enables changes of capacitance in response to thickness variations of the air gap. As it is not easy processable to maintain an air gap above a dielectric material, we have chosen to work with another approach. Indeed, we design a bilayer structure based on the previous described microporous dielectric layer associated with a thin insulating layer of polydimethyl siloxane (PDMS). This composite possesses a high dielectric permittivity along with a very low conductivity. Before discussing the experimental results, we provide a comprehensive clarification about the impedance of two-layer system.

4.2 Effective impedance of the bilayer composites:

The high conductivity (free charge carriers and dielectric loss) of near and above percolated composites is a drawback for energy harvesting applications. Indeed, such applications do not allow any leakage for yielding a positive energy conversion. For keeping high values of effective dielectric permittivity and low values of conductivity, we associate a thin insulating layer to a high permittivity layer. The isolating layer has low dielectric losses and no free charge carriers. It acts as a blocking layer and prevents

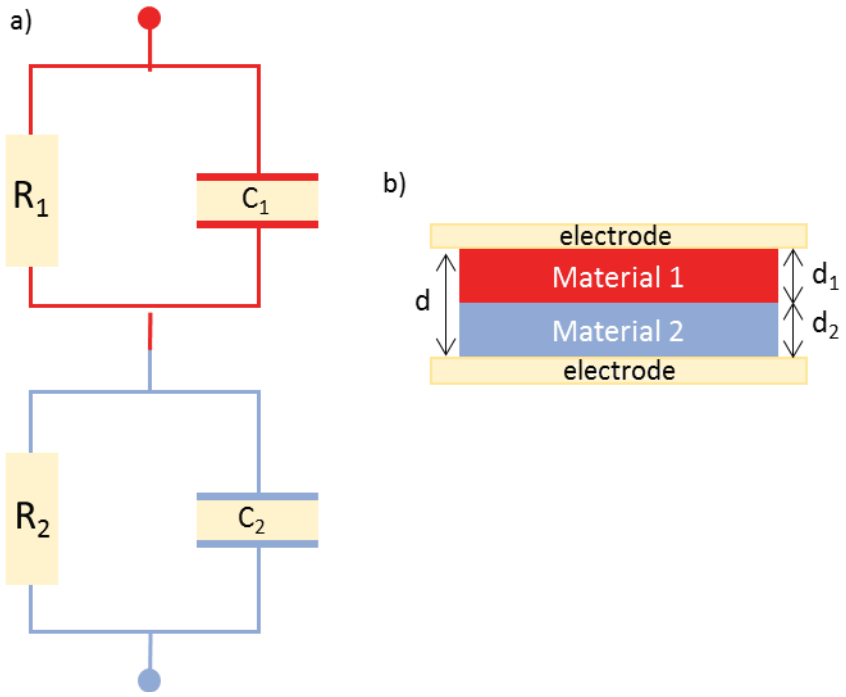


FIG. 4.9 a) Equivalent electric circuits for the bilayer composite b) schematic representation of the bilayer composite. Red refers to material 1 and blue to material 2.

leaks of the capacitor. We call the association of two layers, a *bilayer composite* (**FIG. 4.9** b)).

To fully understand the interest in bilayer composites, we express the effective dielectric properties of such a structure. The equivalent electrical circuit for a bilayer material is a junction of two RC circuits in series (**FIG. 4.9** a)). For the calculation, 1 refers to the layer 1 and 2 for the layer 2. The effective conductivity and dielectric constant of the bilayer structure depend on the thicknesses (d_1, d_2) and dielectric properties of both layers ($\sigma_1, \sigma_2, \varepsilon_1, \varepsilon_2$).

The impedance Z for a parallel RC circuit can be expressing for each material as:

$$R_1 = \frac{d_1}{\sigma_1(f)\mathrm{A}} \qquad R_2 = \frac{d_2}{\sigma_2(f)\mathrm{A}} \tag{4.2}$$

$$C_1 = \frac{\varepsilon_0\varepsilon_1(f)\mathrm{A}}{d_1} \qquad C_2 = \frac{\varepsilon_0\varepsilon_2(f)\mathrm{A}}{d_2} \tag{4.3}$$

$$Z_1 = \frac{R_1}{1 + j\omega C_1 R_1} \qquad Z_2 = \frac{R_2}{1 + j\omega C_2 R_2} \tag{4.4}$$

where A is surface area, $d = d_1 + d_2$, σ is the conductivity, ε is the dielectric permittivity, C is the capacitance, R is the resistance, Z is the impedance, $j^2 = -1$. As two layers are stacked and as each one is modeled by an RC circuit, the impedance Z^* for the association of two RC circuits in series is

$$Z^* = Z_1 + Z_2 = \frac{R_1}{1 + j\omega C_1 R_1} + \frac{R_2}{1 + j\omega C_2 R_2} \tag{4.5}$$

We recall, as seen Chapter 2 § 1.1.4, that complex permittivity ε^* and conductivity σ^* can be calculated from the complex impedance Z^* as:

$$\sigma^* = \frac{d}{AZ^*} \tag{4.6}$$

$$\varepsilon^* = \frac{\sigma^*}{j\omega\varepsilon_0} \tag{4.7}$$

It leads to:

$$\varepsilon^* = \varepsilon_h + \frac{\varepsilon_l - \varepsilon_h}{1 + j\,2\pi f\,\tau} - j\frac{\sigma_l}{2\pi f \varepsilon_0} \tag{4.8}$$

with:

$$\varepsilon_h(f) = \frac{\varepsilon_1(f)\varepsilon_2(f)d}{\varepsilon_1(f)d_2 + \varepsilon_2(f)d_1}$$

$$\varepsilon_l(f) = \frac{\varepsilon_1(f)\sigma_2(f)^2 d_1 d + \varepsilon_2(f)\sigma_1(f)^2 d_2 d}{(\sigma_1(f)d_2 + \sigma_2(f)d_1)^2}$$

$$\tau(f) = \varepsilon_0 \frac{\varepsilon_1(f)d_2 + \varepsilon_2(f)d_1}{\sigma_1(f)d_2 + \sigma_2(f)d_1}$$

$$\sigma_l(f) = \frac{\sigma_1(f)\sigma_2(f)d}{\sigma_1(f)d_2 + \sigma_2(f)d_1}$$

Finally:

$$\begin{aligned} \varepsilon_{bilayer} &= \mathcal{R}e(\varepsilon^*) \\ \sigma_{bilayer} &= -Im(\varepsilon^*)\varepsilon_0 2\pi f \end{aligned} \tag{4.9}$$

The effective permittivity $\varepsilon_{bilayer}$ and conductivity $\sigma_{bilayer}$ of bilayer composites depend on the thickness of each layer (d_1, d_2) and individual dielectric properties (σ_1, σ_2, ε_1, ε_2). The challenge will be to optimize all these parameters to succeed in having the highest $\varepsilon_{bilayer}$ while keeping the $\sigma_{bilayer}$ as low as possible. Theoretical calculations will help us to estimate the thicknesses required to meet the challenge.

4.3 Theoretical plots:

We studied the effective permittivity $\varepsilon_{bilayer}$ and tanδ of a bilayer composite depending on the thickness of each layer (**FIG. 4.10**), the results are based on **EQ. 4.8** and **4.9. TAB. 1** shows the dielectric properties of individual layer, used to make the theoretical calculations.

TAB. 1- Dielectric properties of each layer.

@100 Hz	Permittivity ε	Conductivity σ	*Tan δ*
Isolating layer (PDMS)	2	1 x 10^{-13}	9 x 10^{-6}
Active layer (CB/PDMS)	2 x 10^{4}	4 x 10^{-4}	1.8 x 10^{0}

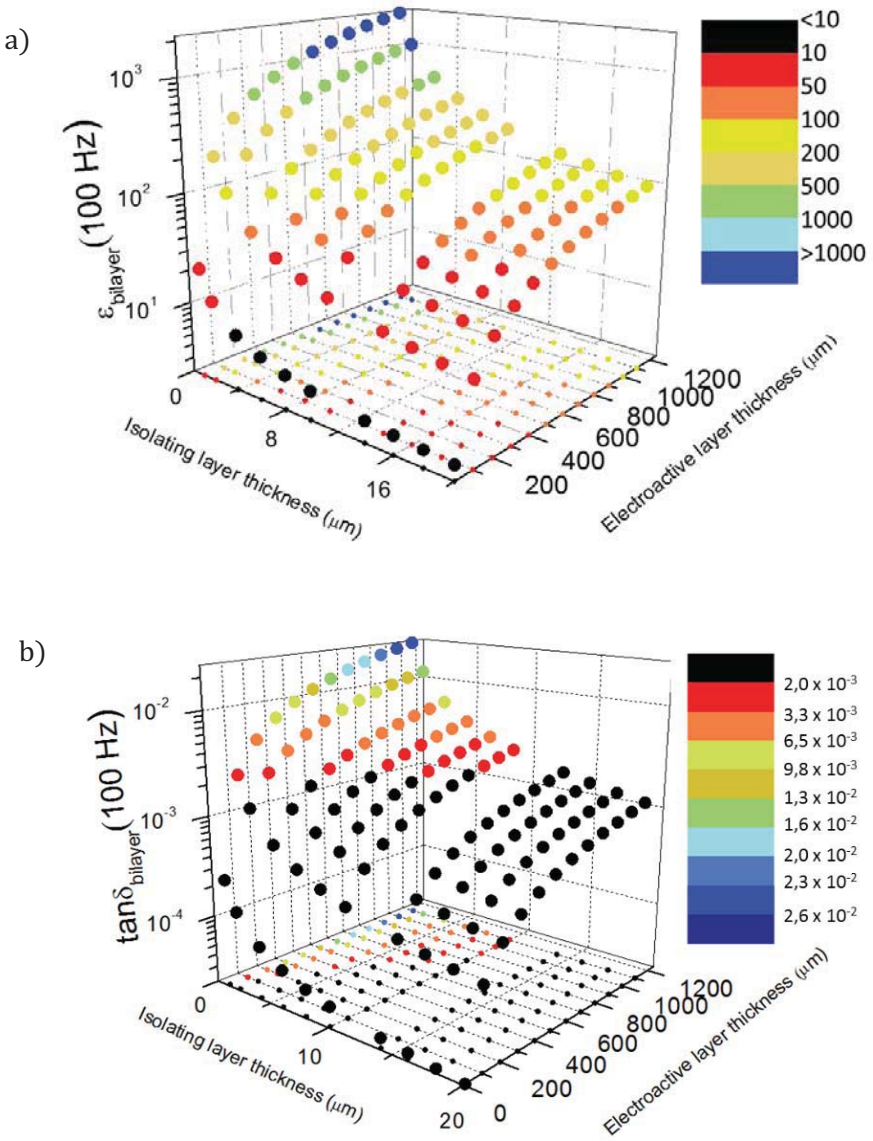


FIG. 4.10 – 3D curves of the $\varepsilon_{bilayer}$ a) and tan δ b) responses depending on material thicknesses for f=100 Hz.

As expected, using an isolating layer decreases the global permittivity of the material. Starting with an active layer with giant permittivity, this is the case for materials formulated after the percolation threshold, the final permittivity decreases from 1 to 3 orders of magnitude. A higher ratio electroactive layer thickness/isolating layer thickness leads to better effective permittivity. However, increasing this ratio leads to more conductive materials as illustrated by the increase of *tan δ.* Nevertheless, these loss tangents are largely below the one measured for the active layer. The theoretical plots confirm the efficiency of using an isolating layer for preventing the materials from conductivity. The choise of the thicknesses will be driven by the possibility of making isolating layers as thin as possible without any default.

4.4 Experimental dielectric response of bilayer composites:

4.4.1 Isolating layer deposition:

As predicted by the previous described theoretical calculations, the microporous materials have to be combined with a very thin insulating layer of PDMS to decrease the dielectric losses. To do so, the insulating layer is spin coated on conductive aluminum

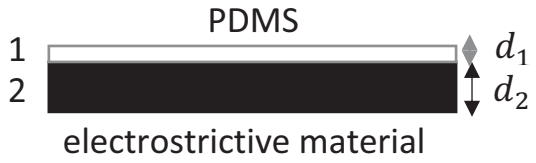


FIG. 4.11 - Schematic representation of the bilayer composite.

substrates with a diameter of 24 mm. For the spin-coating, 3 g of PDMS with a curing agent (10% in weight with respect to the PDMS phase) is deposited at rest on an aluminum substrate. Then a spin-coater is used at 8000 rpm for 60 s at an acceleration of 1000 rpm s^{-1} to attain a thickness of the PDMS layer of 5 μm. The aluminum substrate covered by the PDMS layer is then softly baked at 100 º C for 30 minutes to cure the PDMS. The thickness of the layer is measured by a mechanical profilometer (Dektak 150) after scratching the surface. Note that microporous layer are just held in contact with the insulating layer (deposited onto an aluminum substrate). As coating an isolating layer is an irreversible process, this structuration is justified by the fact that we wanted, as many times as necessary, characterize the microporous layers without the insulating layer. Nevertheless, nothing prevents the PDMS isolating layer from being directly coated on the microporous layer (**FIG. 4.11**).

4.4.2 Dielectric response of bilayer composites:

The effective conductivity and dielectric permittivity of the bilayer structure depend on the thicknesses and dielectric properties of both layers. The blocking layer 1 is a cured PDMS layer ($\varepsilon_{PDMS} = \varepsilon_2 = 2$ and $\sigma_2 = 10^{-13}$ S m^{-1} in the range 10—10^6 Hz at 25°C) of constant thickness 5 μm. The high permittivity layer 2 is the porous carbon black material ($\varepsilon_1 \ll \varepsilon_2$ and $\sigma_2 \gg \sigma_1$) of variable thickness depending on carbon black concentration (see **TAB. 2**).

TAB. 2 - Properties of the carbon black (CB) composites.

% CB	CB (g L^{-1})	Thickness (μm)
3	31	500
4	42	510
6	64	510
8	87	750
10	110	800

For comparison, we investigate the dielectric properties of the electrostrictive composites at rest with and without insulating layer. **FIG. 4.12** shows the relative

dielectric permittivity, electrical conductivity, and loss tangent at 100 Hz as a function of the carbon black weigh fractions. First, we consider the electrostrictive composites without insulating layer. At carbon black concentrations below the percolation threshold (~5 wt%), the dielectric permittivity has a nearly constant value of ~10 with an electric conductivity of ~1 nS m^{-1}. Above the percolation threshold, the dielectric permittivity rapidly increases to 550 at 6 wt%. However, the electrical conductivity also increases by a factor of 103, leading to a loss tangent above 1. A further addition of conductive carbon black particles enhances the interfacial polarization, which leads to an increase in permittivity but also leads to further increase of the electrical conductivity to 0.6 mS m^{-1} at ~8 wt%. Such a high conductivity does not allow the efficient use of the materials as a dielectric layer in variable capacitors.

The effective dielectric properties of the electrostrictive composites with an insulating layer are very different at carbon black concentrations above the percolation threshold. The PDMS layer limits the electric conductivity below 1—10 nS m^{-1}. The insulating layer also leads to a decrease of the effective dielectric permittivity to 157 and 182 for the 8 and 10 wt% black carbon weight fractions, respectively. However, the obtained dielectric loss tangents are very low with $1.5 \cdot 10^{-2}$ and $2.5 \cdot 10^{-2}$ for the 8 and 10 wt% carbon black systems, respectively, making them well suited for energy harvesting applications. Theoretical calculations of the conductivity based on calculations from § 4.2 predict values slightly lower than the ones found experimentally, probably as a result of small holes and defects in the insulating PDMS layer.

Let us stress that the materials with insulating film are a new concept. The properties of the porous material highly depend upon the materials synthesis protocol in the vicinity of the percolation transition. A 5% carbon black particles sample without insulating film may in principle have the same properties as an 8% material with an insulating layer. However, we note that the conductivity of the 5% carbon black particles sample depends a lot upon the preparation conditions in a very limited composition window, making the process poorly reliable. 2 orders of magnitude of variation have been measured for two different samples from two different batches. Using an insulating film allows us to prepare materials with reproducible properties and makes the technology sufficiently robust for realistic applications. Only 20% of variations have been measured for two different samples from two different batches with an insulating film.

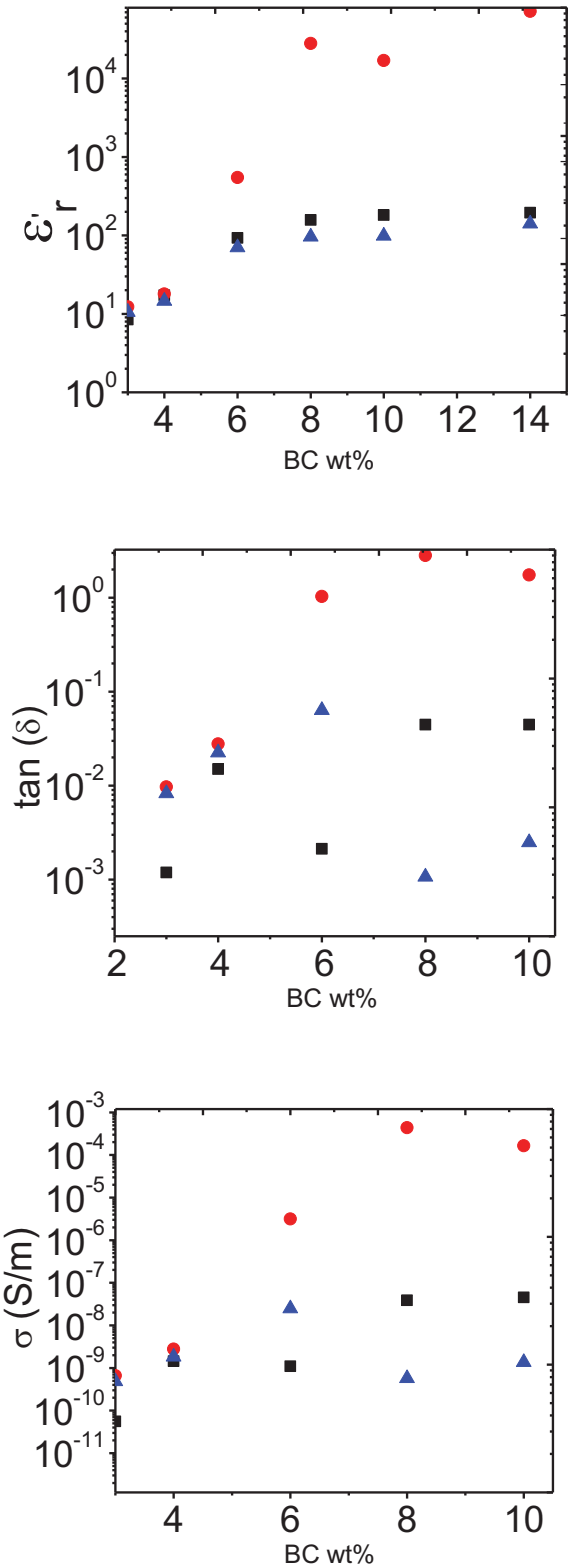


FIG. 4.12 - Effective dielectric properties at 100 Hz of the porous carbon black layer (red circles), bilayer polymer—carbon black composites (black squares), and theoretical predictions of the latter (blue triangles), as a function of carbon black concentration.

5 Harvesting mechanical energy with electrostrictive materials:

The bilayer composite approach allowed us to meet the requirements for developing stretchable materials with high permittivity and low dielectric losses. Materials with effective dielectric permittivity of 157 and 182 for 8 and 10 wt% BC with insulating layer have been obtained at 100 Hz. The associated dielectric loss tangents are very low with 1.5 10^{-2} and 2.5 10^{-2} for the 8 and 10 wt% carbon black systems. In the next parts, we take advantage of these good electrical properties to determine the recovering possibilities of them.

5.1 General considerations:

Several methods are conceivable for recovering electrical energy from a mechanical source, using electrostrictive materials (see Chapter 1 § 3.1.2.4). All of them have their specificities but for a general comprehension, we can use **FIG. 4.13** to illustrate the idea of the electromechanical conversion. From top, moving clockwise, mechanical energy is put into the system to compress the material which increases its capacitance. Electrical energy (charges) is introduced to the system for charging the material. The material is then released, decreases its capacitance, and mechanical energy is transferred to the material as electrical energy. The later does not create new charges but place the previous charges in a higher electrical energy state (higher voltage). The charges are then extracted, the cycle can restart. This method allows to convert one unit of mechanical energy into one unit of electrical energy using another unit of electrical energy.

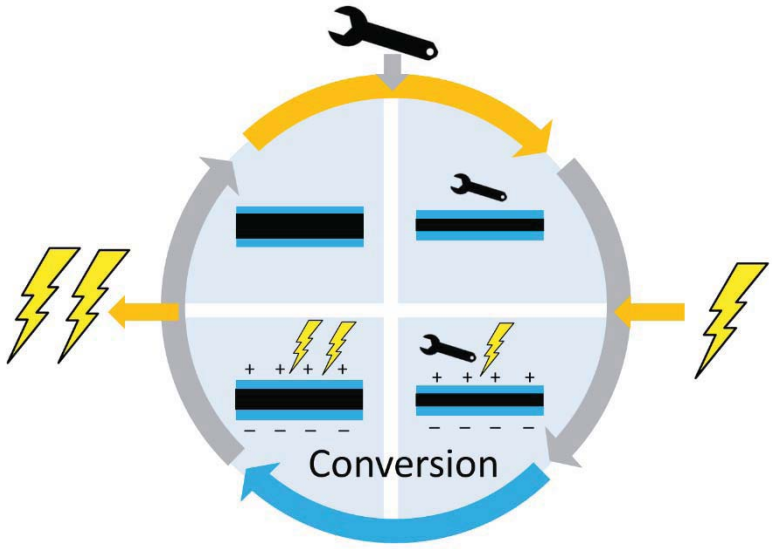


FIG. 4.13 – Schematic representation of an ideal electromechanical conversion.

In this thesis, the pseudo-piezoelectric mode [38–40] is preferred for energy recovering. This choice is motivated because of the ease of its implementation and its efficiency for characterizing the recovering capabilities of materials. Indeed, this method does not require fine control of the charge and the strain; it means that no complex power circuits will be required for implementing the characterization.

5.2 Theoretical calculation of the harvested current:

Here, we expose a theoretical calculation of the harvested current I_h for a pure electrostrictive material (i.e. no piezoelectric behavior) at the terminals of a load resistance R_l (**FIG. 4.14**). We remind that electrostrictive polymers are not piezoelectric, it is thus necessary to induce polarization with a DC bias to obtain a pseudo-piezoelectric behavior.

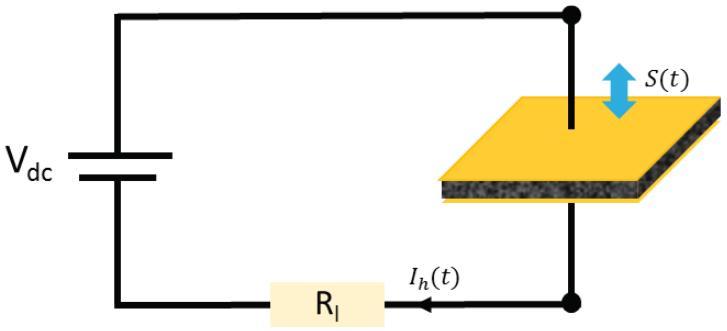


FIG. 4.14 - Equivalent electrical diagram

We start from the differential equation (**EQ. 4.10**) for the harvested current $I_h$as derived by Lallart *et al.* [41,42] for a small transversal strain S:

$$I_h(t) = -\frac{AR_l\varepsilon\varepsilon_0}{d}\frac{\partial I_h(t)}{\partial t} + 2\,A\,M_{33}^{*}\,Y\,E_{dc}\frac{\partial S(t)}{\partial t} \tag{4.10}$$

Where A is the area of the sample, Y is the Young's modulus, M_{33}^{*} is the apparent electrostrictive coefficient, E_{dc} is the applied bias electric field, S is the sinusoidal strain amplitude, ε is the relative dielectric permittivity, ε_0 is the vacuum permittivity, d is the material thickness and R_l is the load resistance.

For convenience, we define $\mathcal{A} \equiv \frac{AR_l\varepsilon\varepsilon_0}{d}$ and $\mathcal{B} \equiv 2\,A\,M_{33}^{*}Y\,E_{dc}$. EQ.4.10 can then be rewritten as

$$\frac{I_h(t)}{\mathcal{A}} + \frac{\partial I_h(t)}{\partial t} = \frac{\mathcal{B}}{\mathcal{A}}\frac{\partial S(t)}{\partial t} \tag{4.11}$$

Multiplying both sides by $e^{\frac{t}{\mathcal{A}}}$ gives

$$e^{\frac{t}{\mathcal{A}}}\left(\frac{I_h(t)}{\mathcal{A}} + \frac{\partial I_h(t)}{\partial t}\right) = e^{\frac{t}{\mathcal{A}}}\frac{\mathcal{B}}{\mathcal{A}}\frac{\partial S(t)}{\partial t} \tag{4.12}$$

Integrating both sides yields

$$e^{\frac{t}{\mathcal{A}}}I_h(t) = \mathcal{C} + \frac{\mathcal{B}}{\mathcal{A}}\int_{-\infty}^{t} dt'\, e^{\frac{t'}{\mathcal{A}}}\frac{\partial S(t')}{\partial t'} \tag{4.13}$$

$$I_h(t) = \mathcal{C}\mathrm{e}^{\frac{-t}{\mathcal{A}}} + \frac{\mathcal{B}}{\mathcal{A}}\mathrm{e}^{\frac{-t}{\mathcal{A}}}\int_{-\infty}^{t} \mathrm{d}t'\ \mathrm{e}^{\frac{t'}{\mathcal{A}}}\ \frac{\partial S(t')}{\partial t'}$$

where $\mathcal{C}$ is an integration constant, which we set to zero as $\lim_{t\to\pm\infty} I_h(t)$ is finite. This leaves us with the following integral:

$$I_h(t) = \frac{\mathcal{B}}{\mathcal{A}}\mathrm{e}^{\frac{-t}{\mathcal{A}}}\int_{-\infty}^{t} \mathrm{d}t'\ \mathrm{e}^{\frac{t'}{\mathcal{A}}}\ \frac{\partial S(t')}{\partial t'} \tag{4.14}$$

For a sinusoidal strain with amplitude S and angular frequency $\omega=2\pi f$, i.e. $S(\mathrm{t}) = \mathrm{S}\sin(\omega t)$, the harvested current becomes:

$$I_h(t) = \omega S\frac{\mathcal{B}}{\mathcal{A}}\mathrm{e}^{\frac{-t}{\mathcal{A}}}\int_{-\infty}^{t} \mathrm{d}t'\ \mathrm{e}^{\frac{t'}{\mathcal{A}}}\ \cos(\omega t') \tag{4.15}$$

By applying integration by parts twice, we get

$$I_h(t) = \frac{\omega}{1+\omega^2\mathcal{A}^2} S\mathcal{B}[\omega\mathcal{A}\sin(\omega t) + \cos(\omega t)\ ] \tag{4.16}$$

We now insert the definitions for $\mathcal{A}$ and $\mathcal{B}$ and obtain

$$I_h(t) = \frac{2\ M_{33}^{*}YE_{dc}\omega AS}{1+\left(\frac{\omega AR_l\varepsilon\varepsilon_0}{d}\right)^2}\left[\frac{\omega AR_l\varepsilon\varepsilon_0}{d}\ \sin(\omega t) + \cos(\omega t)\ \right] \tag{4.17}$$

5.3 Expression of the harvested power:

The average harvested power of a cycle $\bar{P}$, which is dissipated in the load resistance R_l by Joule's effect, can be obtained by calculating:

$$\bar{P} = \frac{R_l}{T}\int_0^T \mathrm{d}t\ \ {I_h}^2(t) \tag{4.18}$$

where $T = 2\pi/\omega$ is the period of the cycle.

Inserting **EQ. 4.17** in the above average harvested power expression, we obtain

$$\bar{P} = \frac{R_l}{T}\left[\frac{2\ M_{33}^{*}YE_{dc}\omega AS}{1+\left(\frac{\omega AR_l\varepsilon\varepsilon_0}{d}\right)^2}\right]^2 \int_0^T \mathrm{d}t\ \left[\frac{\omega AR_l\varepsilon\varepsilon_0}{d}\sin^2(\omega t) + \cos^2(\omega t)\right] \tag{4.19}$$

$$\bar{P} = \frac{R_l}{2} \frac{(2\, M_{33}^{*} Y E_{dc} \omega A S)^2}{1 + \left(\frac{R_l \varepsilon \varepsilon_0 \omega A}{d}\right)^2} \tag{4.20}$$

The power $\bar{P}$ is optimal for a given load resistance $R_{l,max}$ which can be found by deriving the expression of the power with respect to R_l (**EQ. 4.21**)

$$\frac{\partial \bar{P}}{\partial R_l} = \frac{\left(1 + \left(\frac{R_l \varepsilon \varepsilon_0 \omega A}{d}\right)^2\right) - 2{R_l}^2 \left(\frac{\varepsilon \varepsilon_0 \omega A}{d}\right)^2}{(1 + \left(\frac{R_l \varepsilon \varepsilon_0 \omega A}{d}\right)^2)^2} \tag{4.21}$$

When **EQ. 4.21** is equal to zero, $\bar{P}$ is maximal for:

$$R_{l,max} = \frac{d}{A \varepsilon \varepsilon_0 \omega} \tag{4.22}$$

5.4 Loss power and efficiency:

Until now, the dielectric materials were assumed perfect ($tan\,\delta \to 0 \equiv R_i \to \infty$), no leakage was considered. Nevertheless, to get a positive energy balance, the dissipated power must be smaller than the harvested power. Indeed, as we used a bias voltage V_{dc} for operating in piezo-active mode, it is crucial to determine whether the power recovered is not weaker than the polarization power. Otherwise, we will lose electric power instead of recovering power. The difference between harvested power and loss power will give us the net power production.

We remind that dielectric composites can be represented by a leak resistance R_i (ω) in parallel with a capacitance C (ω), they respectively denote the losses of the materials (by charge carriers and dielectric losses) and the intrinsic capacitance (**FIG. 4.15**).

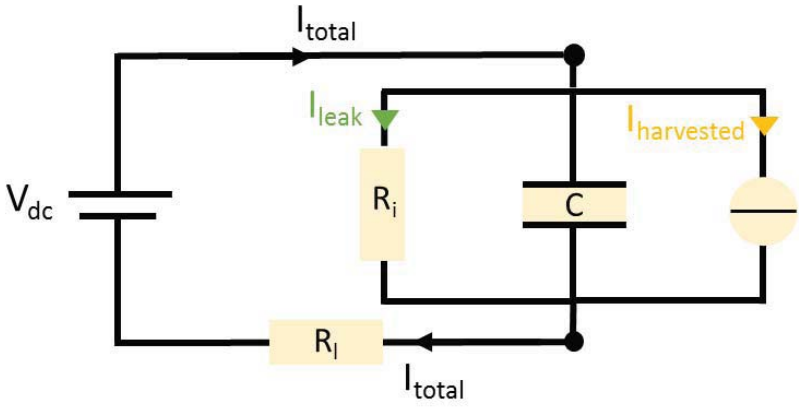


FIG. 4.15 - Equivalent electrical diagram.

The current circulating in the electrical circuit I_{total} can be separated into two contributions (**FIG. 4.15**): the harvested current I_h and a static current I_{leak} with $I_{total} = I_h + I_{leak}$. The term I_{leak} corresponds to the direct current (DC) required to polarize, with a static field, the materials at rest (no mechanical excitation). It can be expressed as:

$$I_{leak} = \frac{V_{dc}}{R_i + R_l} \tag{4.23}$$

where R_i is the internal leak resistance at f=0 Hz, R_l is the load resistance values, and V_{dc} is the applied voltage difference The internal leak resistance is calculated using $R_i = \frac{d}{\sigma A}$ with the geometrical parameters of the materials and its conductivity. The harvested current I_h is the recovering current due to compression-decompression cycles of the composite. In the equivalent electrical circuit, it is modeled by an alternative current generator. This current has the same frequency as the mechanical excitation. Its expression has already been discussed previously.

The dissipated power for maintaining a polarization of the composite, which is due to the leak direct current is given by:

$$P_{\text{loss}} = \frac{V_{dc}^2}{R_i + R_l} \tag{4.24}$$

As $R_i \gg R_l$, P_{loss} can be rewritten:

$$P_{\text{loss}} = \frac{V_{dc}^2}{R_i} \tag{4.25}$$

Finally, the electrical energy gain will be calculated by considering the ratio of power harvestable to electrical polarization losses.

$$electrical\ gain = \frac{P_{harvested}}{P_{\text{loss}}} \tag{4.26}$$

Using the definition of harvested power $P_{harvested}$ found **EQ. 4.20** and the definition of the loss power **EQ. 4.25**, the electrical gain can be theoretically expressed as:

$$electrical\ gain = \frac{(R_i)}{V_{dc}^2}\ \frac{R_l}{2}\frac{(2\ M_{33}^* Y E_{dc} \omega A S)^2}{1 + \left(\frac{R_l \varepsilon \varepsilon_0 \omega A}{d}\right)^2} = \frac{1}{2}\frac{R_l\ R_i (2\ M_{33}^* Y \omega A S)^2}{d^2 + (R_l \varepsilon \varepsilon_0 \omega A)^2} \tag{4.27}$$

It is worth mentioning that the electrical gain will not depend on the applied bias voltage.

5.5 Dynamic measurement of electrostrictive modulus:

Contrary to Chapter 3, where electrostrictive performances of r-GO/PDMS composites were measured using a direct approach (impedancemetry), we use, in this part, a dynamic approach for the determination of the electrostrictive modulus of bilayer composites. The determination is based on the theoretical model of harvested current. As predicted by the expression of $I_h(t)$, see below, the harvested current is linked to the electric field E_{dc}.

$$I_h(t) = \frac{2\, M_{33}^{*} Y E_{dc} \omega A S}{1 + \left(\frac{\omega A R_l \varepsilon \varepsilon_0}{d}\right)^2} \left[\frac{\omega A R_l \varepsilon \varepsilon_0}{d} \sin(\omega t) + \cos(\omega t)\right] \tag{4.28}$$

The time-derivative current is given by:

$$\frac{\partial I_h}{\partial t}(t) = \frac{2\, M_{33}^{*} Y E_{dc} \omega A S}{1+\left(\frac{\omega A R_l \varepsilon \varepsilon_0}{d}\right)^2} \left(\frac{\omega A R_l \varepsilon \varepsilon_0}{d} cos(\omega t) - sin(\omega t)\right)\omega) \tag{4.29}$$

$$\text{Which is maximum for } t = \frac{\arctan\left(\frac{\omega A R_l \varepsilon \varepsilon_0}{d}\right)}{\omega}$$

So the expression for the maximum value of the harvested current is

$$I_{h,max} = \frac{2\, M_{33}^{*} Y E_{dc} \omega A S}{1+\left(\frac{\omega A R_l \varepsilon \varepsilon_0}{d}\right)^2} \left(\frac{\omega A R_l \varepsilon \varepsilon_0}{d} sin\left(\arctan\left(\frac{\omega A R_l \varepsilon \varepsilon_0}{d}\right)\right) + cos\left(\arctan\left(\frac{\omega A R_l \varepsilon \varepsilon_0}{d}\right)\right)\right) \tag{4.30}$$

Hence, a linear relation between $I_{h,max}$ and E_{dc} is obtained for a constant strain, frequency, and load resistance. The product $M_{33}{}^{*}Y$ can be easily estimated from the slope of the $I_{h,max} - E_{dc}$ curves. The apparent electrostrictive coefficient $M_{33}{}^{*}$ is calculated by division of the measured Young's modulus Y.

5.6 Energy harvesting results:

This part is devoted to the presentation of the experimental results which be commented in the discussion part.

5.6.1 Figure of merit:

We investigate the performance of the bilayer composites for energy harvesting purposes. First, the electromechanical performances are assessed by calculating the figure of merit (FoM) proposed by Guyomar et al. [43,44]:

$$\text{FoM} = \left(\frac{2\pi}{\varepsilon}\right)\left(M_{33}{}^{*}Y\right)^2 \quad (\text{J m}^{-1}\,\text{V}^{-2}\,\text{cycle}^{-1}) \tag{4.31}$$

The FoM depends only on material properties (M_{33}^*, Y, ε) and aims at comparing electromechanical performances of materials without any external parameters such as geometry and measurement details. Three compositions (6, 8, and 10 CB wt% + PDMS layer) are used for performance comparisons. Properties of the materials are reported in **TAB. 3**. M_{33}^* is measured using the method described in the section § 5.5 and Y with traction machine (see Chapter 2 § 1.2.1 for the precise method). In the following, in the presence of an insulating film, M_{33}^* will be an effective coefficient. It will average the properties of the material and those of the insulating film.

TAB. 3 - Materials properties:

% CB	Oil fraction	CB (g L-1)	Thickness (µm)	Surface (m^2)	M* Y	Y (MPa)	M_{33}^*(m2 V−2)
6.0	0.5	$6.4 \cdot 10^{1}$	$5{,}1 \cdot 10^{2}$	$1.1 \cdot 10^{-3}$	$2.2 \cdot 10^{-10}$	1,38	$1{,}60 \cdot 10^{-16}$
8.0	0.5	$8{,}7 \cdot 10^{1}$	$7.5 \cdot 10^{2}$	$6.2 \cdot 10^{-4}$	$1.5 \cdot 10^{-9}$	1,40	$1{,}07 \cdot 10^{-15}$
10.0	0.5	$1.1 \cdot 10^{2}$	$8.0 \cdot 10^{2}$	$1.0 \cdot 10^{-3}$	$3.6 \cdot 10^{-9}$	1,61	$8{,}46 \cdot 10^{-15}$

5.6.2 Power harvested:

Next, we examine the power generation properties of the bilayer composites by discharge over a load resistance R_l, for a 100 Hz sinusoidal strain. As shown in **FIG. 4.16**, the voltage drop over the resistance U_r and the instantaneous harvested power are monitored as a function of time. The average harvested power per cycle $\bar{P}$ is calculated using **EQ. 4.20**.

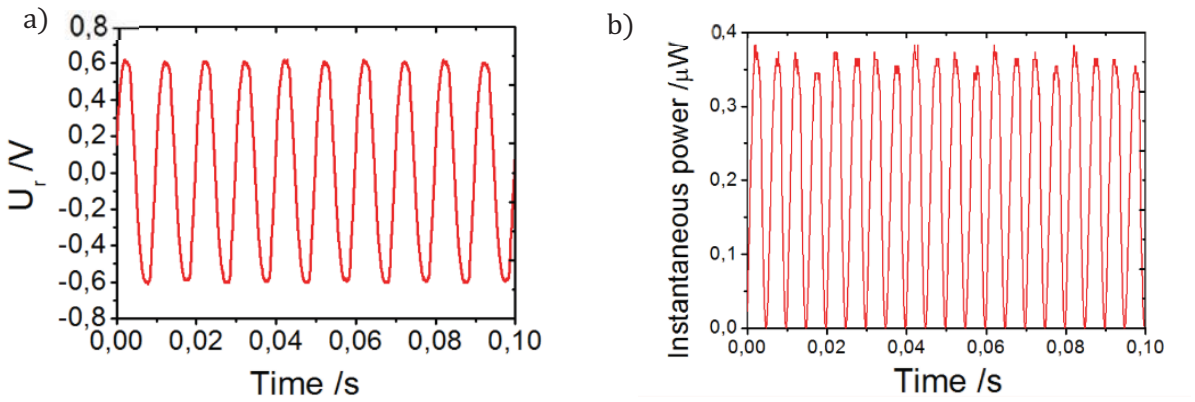


FIG. 4.16 - a) The voltage difference and b) instantaneous power across a load resistance of 1 MΩ for a 100 Hz sinusoidal strain. The applied bias voltage over the bilayer composite with 8 wt% carbon black is 32 V.

5.6.3 Influence of the load resistance on the harvested current:

FIG. 4.17 shows the value of the theoretical and experimental power harvestable as a function of the load resistance. Theoretical predictions are determined using **EQ. 4.20**. Best values are obtained for a load resistance of about 1 MΩ for both materials, which corresponds to the resistance with optimal power production ($R_{l,max} = \frac{d}{A\varepsilon\varepsilon_0\omega}$). Good agreement is observed between the experimental data and theoretical powers. In addition, the increase in FoM by a factor 5 between 8 CB wt% and 10 CB wt% leads to an increase in harvested power by a factor 6.

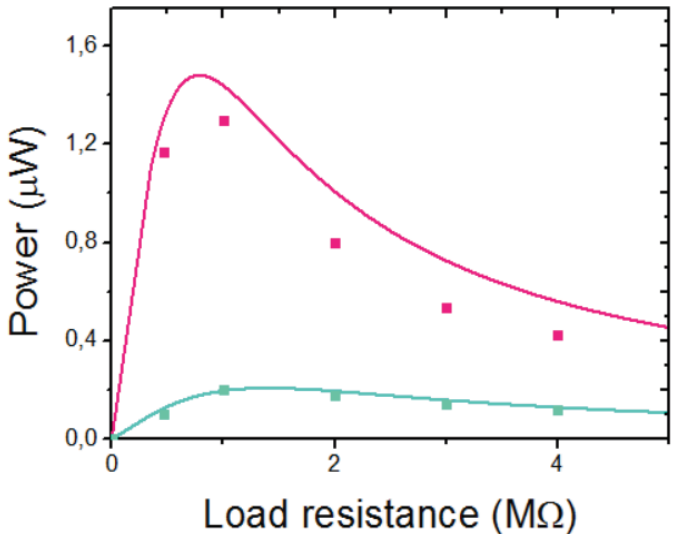


FIG. 4.17 - Harvested power of the composites with 8 CB wt% (green) and 10 CB wt% (pink) with insulating layer as a function of the load resistance. Squares are experimental data and lines are theoretical predictions using **EQ. 4.20**. The strain frequency is 100 Hz and the applied voltage over the composite V_{dc}= 32 V.

The internal leak resistance is calculated by Ri = $\frac{d}{\sigma A}$ with the geometrical data from **TAB. *4*** for a bias voltage of V_{dc} = 32 V and a load resistance of R_l =1 MΩ.

TAB. 4 - Efficiency of the bilayer composites for different carbon black concentrations:

% CB	Harvested power (µW)	Power loss (µW)	Net power production (µW)	Electrical gain factor
8.00	0.20	0.12	0.08	1.74
10.0	1.3	1.0	0.3	1.31

5.7 Discussion:

The use of an insulating layer limits the electric conductivity below 1–10 nS m^{-1} and allows us to use our materials for energy harvesting. Data given in **TAB. *4*** show that the energy balance is largely positive for both materials. The power produced by the mechanical-electrical conversion for the 8 wt% composite is 1.74 times higher than the power dissipated to polarize it and the net power harvestable is around 0.17 W m^{-3}. We can see that increasing the CB wt% enables to increase the net harvested power by almost a factor 4, i.e. up to 0.38 W m^{-3}. This is a consequence of the increase of permittivity of the material at 10 wt%. But at the same time, the conductivity of the 10 wt% composite is 1.9 higher than that of the 8 wt% composite which has a conductivity of 1.30 10^{-8} S m^{-1}; leading to a net decrease in the energy balance, but to an increased overall power production. These excellent performances can be explained by the porous structure of the materials and insulating properties of the thin polymer layer. As a result, the electric field required to polarize the material is decreased, which is crucial for vibrational energy harvesting applications.

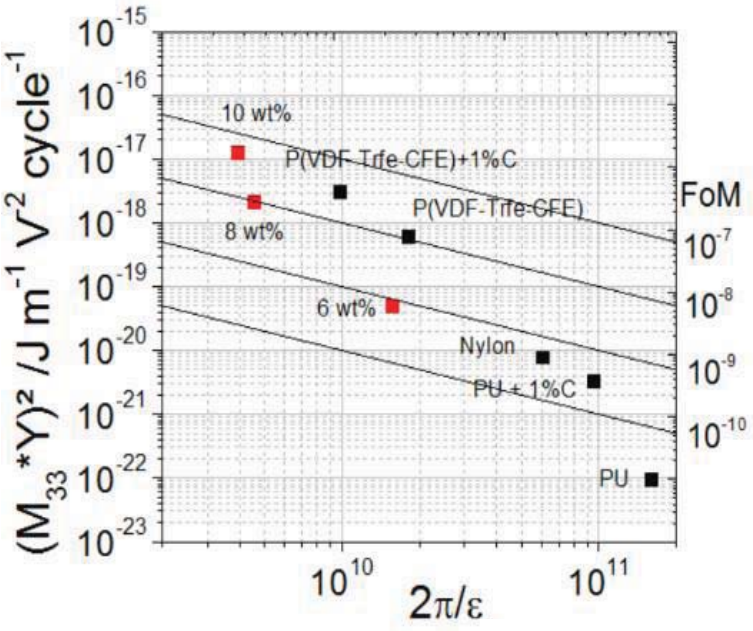


FIG. 4.18 - Comparison of the electromechanical performances at 100 Hz using the figure of merit (FoM) proposed by Guyomar et al. [43,44]. Thick lines have the same FOM. Black spots refer to materials from the literature [43,44].

FIG. 4.18 presents the FoM of materials from the literature, and of composites developed in this work. The values of the FOM are enhanced by increasing the filler concentration. For 10 wt% CB, the FoM is equal to 5.06·10-8 J m^{-1} V^{-2} $cycle^{-1}$. This result exceeds the previous-best electrostrictive materials based on a mixture of Polyvinylidene fluoride (PVDF) terpolymers and carbon black by a factor 1.7. In addition, it outperforms in terms of process and material cost and toxicity [21–22]. Increasing the FoM is a key point for increasing the power harvestable as we show below. Besides, their low Young's modulus compared to PVDF polymers (~ GPa) could enlarge the scope of applications using low stress vibrations.

5.8 Conclusion:

We have presented microporous electrostrictive composites with improved properties for vibrational energy harvesting. These systems are made of carbon black particles dispersed in a porous PDMS matrix. An inverted emulsion templating approach provides a fine control of the location of the particles which is a key factor to achieve high permittivity and low losses. A thin insulating layer was added to limit further losses. The resulting structure possesses a very large effective relative dielectric permittivity of 182 at 100 Hz in combination with a very low loss tangent of $2.5 \cdot 10^{-2}$. We succeeded in evaluating the energy scavenging abilities of these composites. More than 300 nW has been harvested with the 10 wt% carbon black composites which leads to a power density of 0.4 μ W cm^{-3}. The present materials exhibits a figure of merit as high as $5.06 \cdot 10^{-8}$ J m^{-1} V^{-2} $cycle^{-1}$ which is 1.7 times higher than the best reference fluorinated polymers and 3350 times higher than pure polyurethane [21]. The low cost process and low toxicity make the carbon black bilayer composites very promising materials for vibrational energy harvesting. The power harvested with our materials is good enough to provide a significant boost to the battery life of ultra-low power devices. For example, the Phoenix processor [45,46] has a sleep power consumption of only 30 pW and 200 nW in active mode which makes our materials suitable for this application. In addition, these carbon black bilayer composites, with excellent dielectric properties, could find potential applications as low cost flexible capacitor sensors in the printed electronics industry.

Take home message – Chapter 4

We present microporous electrostrictive composites with improved properties for vibrational energy harvesting. These systems are made of carbon black particles dispersed in a porous PDMS matrix thanks to an inverted emulsion templating. A thin insulating layer is added to limit further losses. We succeed in evaluating the energy scavenging abilities of these composites.

1. Using a thin isolating layer is the key to success to obtain dielectric materials compatible with energy harvesting applicatons. The resulting structure possesses a very large effective relative dielectric permittivity of 182 at 100 Hz in combination with a very low loss tangent of $2.5 \cdot 10^{-2}$.

2. The materials exhibits a figure of merit as high as $5.06 \cdot 10^{-8}$ J m^{-1} V^{-2} $cycle^{-1}$ which is 1.7 times higher than the best reference fluorinated polymers and 3350 times higher than pure polyurethane.

3. More than 300 nW has been harvested with the 10 wt% carbon black composites which leads to a power density of 0.4 µ W cm^{-3}. This is good enough to provide a significant boost to the battery life of ultra-low power devices.

[1] J. Gubbi, R. Buyya, S. Marusic, M. Palaniswami, Internet of Things (IoT): A vision, architectural elements, and future directions, Future Generation Computer Systems. 29 (2013) 1645–1660. doi:10.1016/j.future.2013.01.010.

[2] F. Xia, L.T. Yang, L. Wang, A. Vinel, Internet of Things, International Journal of Communication Systems. 25 (2012) 1101–1102. doi:10.1002/dac.2417.

[3] D. Brogioli, Extracting Renewable Energy from a Salinity Difference Using a Capacitor, Physical Review Letters. 103 (2009). doi:10.1103/PhysRevLett.103.058501.

[4] M. Janssen, A. Härtel, R. van Roij, Boosting Capacitive Blue-Energy and Desalination Devices with Waste Heat, Physical Review Letters. 113 (2014). doi:10.1103/PhysRevLett.113.268501.

[5] N.E. Dutoit, B.L. Wardle, S.-G. Kim, Design considerations for mems-scale piezoelectric mechanical vibration energy harvesters, Integrated Ferroelectrics. 71 (2005) 121–160. doi:10.1080/10584580590964574.

[6] H.A. Sodano, D.J. Inman, G. Park, A Review of Power Harvesting from Vibration Using Piezoelectric Materials, The Shock and Vibration Digest. 36 (2004) 197–205. doi:10.1177/0583102404043275.

[7] S.R. Anton, H.A. Sodano, A review of power harvesting using piezoelectric materials (2003–2006), Smart Materials and Structures. 16 (2007) R1–R21. doi:10.1088/0964-1726/16/3/R01.

[8] Y. Yan, J.E. Zhou, D. Maurya, Y.U. Wang, S. Priya, Giant piezoelectric voltage coefficient in grain-oriented modified PbTiO3 material, Nature Communications. 7 (2016) 13089. doi:10.1038/ncomms13089.

[9] F.R. Fan, W. Tang, Z.L. Wang, Flexible Nanogenerators for Energy Harvesting and Self-Powered Electronics, Advanced Materials. 28 (2016) 4283–4305. doi:10.1002/adma.201504299.

[10] O. Guillon, F. Thiebau, D. Perreux, Tensile fracture of soft and hard PZT, International Journal of Fracture. (2002). doi:https://doi.org/10.1023/A:1022072500963.

[11] Z.L. Wang, Triboelectric nanogenerators as new energy technology and self-powered sensors – Principles, problems and perspectives, Faraday Discuss. 176 (2014) 447–458. doi:10.1039/C4FD00159A.

[12] V. Nguyen, R. Yang, Effect of humidity and pressure on the triboelectric nanogenerator, Nano Energy. 2 (2013) 604–608. doi:10.1016/j.nanoen.2013.07.012.

[13] D. Jaaoh, C. Putson, N. Muensit, Enhanced strain response and energy harvesting capabilities of electrostrictive polyurethane composites filled with conducting polyaniline, Composites Science and Technology. 122 (2016) 97–103. doi:10.1016/j.compscitech.2015.11.020.

[14] X. Yin, J.-F. Capsal, D. Guyomar, A comprehensive investigation of poly(vinylidene fluoride-trifluoroethylene-chlorofluoroethylene) terpolymer nanocomposites with carbon black for electrostrictive applications, Applied Physics Letters. 104 (2014) 052913. doi:10.1063/1.4864160.

[15] A. Luna, M. Pruvost, J. Yuan, C. Zakri, W. Neri, C. Monteux, P. Poulin, A. Colin, Giant Electrostrictive Response and Piezoresistivity of Emulsion Templated Nanocomposites, Langmuir. 33 (2017) 4528–4536. doi:10.1021/acs.langmuir.6b04185.

[16] A. Luna, J. Yuan, W. Néri, C. Zakri, P. Poulin, A. Colin, Giant Permittivity Polymer Nanocomposites Obtained by Curing a Direct Emulsion, Langmuir. 31 (2015) 12231–12239. doi:10.1021/acs.langmuir.5b02318.

[17] J. Yuan, A. Luna, W. Neri, C. Zakri, T. Schilling, A. Colin, P. Poulin, Graphene liquid crystal retarded percolation for new high-k materials, Nature Communications. 6 (2015) 8700. doi:10.1038/ncomms9700.

[18] J.Y. Li, C. Huang, Q. Zhang, Enhanced electromechanical properties in all-polymer percolative composites, Applied Physics Letters. 84 (2004) 3124–3126. doi:10.1063/1.1702127.

[19] X. Yin, M. Lallart, P.-J. Cottinet, D. Guyomar, J.-F. Capsal, Mechanical energy harvesting via a plasticizer-modified electrostrictive polymer, Applied Physics Letters. 108 (2016) 042901. doi:10.1063/1.4939859.

[20] H. Parant, G. Muller, T. Le Mercier, J.M. Tarascon, P. Poulin, A. Colin, Flowing suspensions of carbon black with high electronic conductivity for flow applications: Comparison between carbons black and exhibition of specific aggregation of carbon particles, Carbon. 119 (2017) 10–20. doi:10.1016/j.carbon.2017.04.014.

[21] S.B. Jones, S.P. Friedman, Particle shape effects on the effective permittivity of anisotropic or isotropic media consisting of aligned or randomly oriented ellipsoidal particles, Water Resources Research. 36 (2000) 2821–2833. doi:10.1029/2000WR900198.

[22] S. Boisseau, G. Despesse, B. Ahmed, Electrostatic Conversion for Vibration Energy Harvesting, in: M. Lallart (Ed.), Small-Scale Energy Harvesting, InTech, 2012. http://www.intechopen.com/books/small-scale-energy-harvesting/electrostatic-conversion-for-vibration-energy-harvesting (accessed September 27, 2017).

[23] J.-B. Donnet, R.C. Bansal, M.-J. Wang, eds., 2nd ed., rev. and expanded, Dekker, New York, 1993.

[24] J. Sánchez-González, A. Macías-García, M.F. Alexandre-Franco, V. Gómez-Serrano, Electrical conductivity of carbon blacks under compression, Carbon. 43 (2005) 741–747. doi:10.1016/j.carbon.2004.10.045.

[25] J.W.M. Noordermeer, W.K. Dierkes, Carbon Black Reinforced Elastomers, in: S. Kobayashi, K. Müllen (Eds.), Encyclopedia of Polymeric Nanomaterials, Springer Berlin Heidelberg, Berlin, Heidelberg, 2015: pp. 1–14. doi:10.1007/978-3-642-36199-9_287-1.

[26] J.-C. Huang, Carbon black filled conducting polymers and polymer blends, Advances in Polymer Technology. 21 (2002) 299–313. doi:10.1002/adv.10025.

[27] N. Savage, M.S. Diallo, Nanomaterials and Water Purification: Opportunities and Challenges, Journal of Nanoparticle Research. 7 (2005) 331–342. doi:10.1007/s11051-005-7523-5.

[28] P. Simon, Y. Gogotsi, Materials for electrochemical capacitors, Nature Materials. 7 (2008) 845–854. doi:10.1038/nmat2297.

[29] N. Jäckel, P. Simon, Y. Gogotsi, V. Presser, Increase in Capacitance by Subnanometer Pores in Carbon, ACS Energy Letters. 1 (2016) 1262–1265. doi:10.1021/acsenergylett.6b00516.

[30] S. Ojha, S.K. Acharya, G. Raghavendra, Mechanical properties of natural carbon black reinforced polymer composites, Journal of Applied Polymer Science. 132 (2015). doi:10.1002/app.41211.

[31] K. Wongtimnoi, B. Guiffard, A. Bogner-Van de Moortèle, L. Seveyrat, C. Gauthier, J.-Y. Cavaillé, Improvement of electrostrictive properties of a polyether-based polyurethane elastomer filled with conductive carbon black, Composites Science and Technology. 71 (2011) 885–892. doi:10.1016/j.compscitech.2011.02.003.

[32] X. Zhao, J. Zhao, J.-P. Cao, X. Wang, M. Chen, Z.-M. Dang, Tuning the Dielectric Properties of Polystyrene/Poly(vinylidene fluoride) Blends by Selectively Localizing Carbon Black Nanoparticles, The Journal of Physical Chemistry B. 117 (2013) 2505–2515. doi:10.1021/jp310021r.

[33] J. Yacubowicz, M. Narkis, Dielectric behavior of carbon black filled polymer composites, Polymer Engineering and Science. 26 (1986) 1568–1573. doi:10.1002/pen.760262207.

[34] O.A. Al-Hartomy, F. Al-Solamy, A. Al-Ghamdi, N. Dishovsky, M. Ivanov, M. Mihaylov, F. El-Tantawy, Influence of Carbon Black Structure and Specific Surface Area on the Mechanical and Dielectric Properties of Filled Rubber Composites, International Journal of Polymer Science. 2011 (2011) 1–8. doi:10.1155/2011/521985.

[35] J.-W. Zha, X. Meng, D. Wang, Z.-M. Dang, R.K.Y. Li, Dielectric properties of poly(vinylidene fluoride) nanocomposites filled with surface coated BaTiO, Applied Physics Letters. 104 (2014) 072906. doi:10.1063/1.4866269.

[36] A. Vinogradov, F. Holloway, Electro-mechanical properties of the piezoelectric polymer PVDF, Ferroelectrics. 226 (1999) 169–181. doi:10.1080/00150199908230298.

[37] T. Vu-Cong, C. Jean-Mistral, A. Sylvestre, Electrets substituting external bias voltage in dielectric elastomer generators: application to human motion, Smart Materials and Structures. 22 (2013) 025012. doi:10.1088/0964-1726/22/2/025012.

[38] L. Lebrun, D. Guyomar, B. Guiffard, P.-J. Cottinet, C. Putson, The Characterisation of the harvesting capabilities of an electrostrictive polymer composite, Sensors and Actuators A: Physical. 153 (2009) 251–257. doi:10.1016/j.sna.2009.05.009.

[39] P.-J. Cottinet, M. Lallart, D. Guyomar, B. Guiffard, L. Lebrun, G. Sebald, C. Putson, Analysis of AC-DC conversion for energy harvesting using an electrostrictive polymer P(VDF-TrFE-CFE), IEEE Transactions on Ultrasonics, Ferroelectrics and Frequency Control. 58 (2011) 30–42. doi:10.1109/TUFFC.2011.1771.

[40] R. Liu, Q. Zhang, L.E. Cross, Experimental investigation of electrostrictive polarization biased direct apparent piezoelectric properties in polyurethane elastomer under quasistatic conditions, Journal of Applied Polymer Science. 73 (1999) 2603–2609. doi:10.1002/(SICI)1097-4628(19990923)73:13<2603::AID-APP7>3.0.CO;2-R.

[41] P.-J. Cottinet, D. Guyomar, B. Guiffard, C. Putson, L. Lebrun, Modeling and experimentation on an electrostrictive polymer composite for energy harvesting, IEEE Transactions on Ultrasonics, Ferroelectrics and Frequency Control. 57 (2010) 774–784. doi:10.1109/TUFFC.2010.1481.

[42] M. Lallart, P.-J. Cottinet, L. Lebrun, B. Guiffard, D. Guyomar, Evaluation of energy harvesting performance of electrostrictive polymer and carbon-filled terpolymer composites, Journal of Applied Physics. 108 (2010) 034901. doi:10.1063/1.3456084.

[43] P.-J. Cottinet, D. Guyomar, B. Guiffard, C. Putson, L. Lebrun, Modeling and experimentation on an electrostrictive polymer composite for energy harvesting, IEEE Transactions on Ultrasonics, Ferroelectrics and Frequency Control. 57 (2010) 774–784. doi:10.1109/TUFFC.2010.1481.

[44] M. Lallart, P.-J. Cottinet, L. Lebrun, B. Guiffard, D. Guyomar, Evaluation of energy harvesting performance of electrostrictive polymer and carbon-filled terpolymer composites, Journal of Applied Physics. 108 (2010) 034901. doi:10.1063/1.3456084.

[45] S. Hanson, M. Seok, Y.-S. Lin, Z. Foo, D. Kim, Y. Lee, N. Liu, D. Sylvester, D. Blaauw, A Low-Voltage Processor for Sensing Applications With Picowatt Standby Mode, IEEE Journal of Solid-State Circuits. 44 (2009) 1145–1155. doi:10.1109/JSSC.2009.2014205.

[46] H. Jayakumar, K. Lee, W.S. Lee, A. Raha, Y. Kim, V. Raghunathan, Powering the internet of things, in: ACM Press, 2014: pp. 375–380. doi:10.1145/2627369.2631644.

5. Integration of electrostrictive materials in a cantilever device

Summary:

In this part, we present the integration of electrostrictive porous carbon black composites into a real-life application of mechanical energy harvesting. We made a mechanical energy harvester based on a cantilever beam. In combination with an insulating layer, the investigated structure maintains its conversion abilities although it was integrated into an all-organic resonator. Using a sinusoidal acceleration amplitude of 2 g at 25 Hz, we succeed in generating an electrical power density of 0.4 $\mu W/cm^3$. Although a bias voltage is used to polarize materials, we show that the energy balance is positive. The production process of the present cantilever is based on non-hazardous and low-cost chemicals.

1 Introduction:

In chapter 4, we described the synthesis of new electrostrictive materials, very efficient for the recovery of vibrational energy. These new materials exhibit a figure of merit as high as $5.06 \cdot 10^{-8}$ J m^{-1} V^{-2} $cycle^{-1}$. Their conversion capacity and electrical losses were assessed using a test bench and a piezoelectric actuator to simulate vibrations. The use of materials in this configuration is very useful for the laboratory scale characterizations and helps at orientating the materials formulation. Nevertheless, for real-life operations of electrostrictive materials in the energy harvesting field, they have to be integrated into well-designed devices. Moreover, the majority of ambient mechanical vibration sources provide frequencies lower than 100 Hz [1]. In order to use ambient vibrations, energy harvesters should be able to vibrate at this frequency range. Due to their flexibility, low resonant frequency and high stress generation, cantilever beam structures are promising systems. They afford efficient electromechanical conversion once an active layer is integrated into their structure. Indeed, a thin and flat form factor allows electrostrictive elements to readily react to the motion of the host vibrating structure. Usually they are designed with a triangular shape including a seismic mass which allows a low resonant frequency and a high strain. Researchers have investigated classical piezoelectric materials such as PZT, for making cantilever beams [2]. However, as a lead compound, PZT materials are very dangerous for the environment. Moreover, cracks can occur inside the structure due to excessive stresses and fatigue [3]. Lead-free materials like $BaTiO_3$ require high temperature (700-900 °C) for their deposition process [4,5] which is not compatible with most of substrate materials. Our previous described CB/PDMS composites are particularly interesting for making cantilevers. Indeed, they are easy processing, low cost, very lightweight and high stretchable. Plus, their integration is easily reached by the soft chemistry required for making the active materials (low temperature, water as solvent, etc.). Previous work reported the fabrication of a cantilever harvester based on an electrostrictive r-GO/PDMS composite [6]. Even if 6 $\mu W/cm^3$ were successfully harvested, the electrical losses were not discussed. However, this is a crucial point for making viable such a system, as the balance energy harvested – energy dissipated has to be positive.

In this chapter, we report the fabrication of a mechanical energy harvester based on a porous CB/PDMS composite. We succeed in maintaining its conversion abilities although it was integrated into an all-organic resonator. Moreover, we place special emphasis on the dielectric losses and the real electrical energy recovered.

2 Materials and methods:

2.1 Cantilever fabrication :

4.3 cm^2 square pieces of poly(téréphtalate d'éthylène) (PET-Mylar, Radiospare) of 125 µm thick are cut. This plastic substrate acts as a supporting layer for the cantilever. The first step consists of depositing the bottom electrode on PET substrate. Double-sided adhesive tape of conductive carbon is used as electrode (Neyco). Carbon tape has the advantage to present high flexibility and conductivity. The next step is to place on the

adhesive carbon electrode, a 2.5 µm thick PET film (Mylar, Neyco), which acts as an isolating layer. Then a piece of porous CB/PDMS composite (4.3 cm^2 x 90 µm) is deposited on the isolating layer. The formulation of the electrostrictive material is described in Chapter 2 (10%wt CB; 1:1 PDMS/CB solution). The PET film is stacked on the solid CB/PDMS composites by using a surface plasma treatment (Plasma Diener Pico) for 3 minutes. This method aims at making stickable, the thin plastic film, on PDMS-composites. Then the two elements are stuck together for 15 min by applying a pressure at 90°C. The bottom electrode is deposited on the latter and is a piece of double-sided adhesive tape of conductive carbon too. At that time, the shape of the cantilever is simply defined by cutting a triangular shape into the structure (**FIG. 5.2**). Then the cantilever is glued to a glass slide, which works as a support. Finally, the electrical contact is established by bonding conductive wires to both electrodes using pieces of conductive copper tape. A seismic mass is added at the tip of the cantilevers by depositing a small metallic piece (0.35 g). In this process, it is worth noticing that the electrostrictive cantilever is based on all organic, non-hazardous and low-cost chemicals.

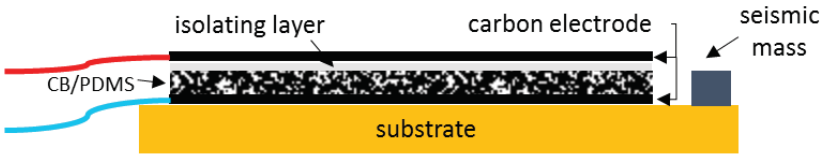


FIG. 5.1 – Schematic lateral view of the cantilever.



FIG. 5.2 - Photograph of the cantilever, top view.

2.2 Static characterization:

We measure the resistance and capacitance at rest of the electrostrictive cantilever so as to characterize the evolution of the conductivity of the system depending on the beam deformation Both dielectric properties are measured with a DC (0 Hz) voltage. To do so, the cantilever is bent between its two extremum positions by applying a force at its end using a non-conductive rod. The properties are measured using a precise LCR-meter (Agilent E4980A) with a 1 V DC signal at room temperature. A compensation procedure is used to remove parasitic impedances.

2.3 Dynamic characterization:

The cantilever is connected to a load resistance R_{load} with an external voltage source of V_{DC}=32 V, while an oscilloscope (Keysight InfiniiVision 1000 X) measures the voltage U_R at the terminals of the load resistance (see **FIG. 4.3** a)). Then the cantilever is put under vibrations with a shaker (4810 Bruel & kjaer) which drives it into different mechanical frequency from 1 Hz to 50 Hz. An accelerometer (IEPE Bruel & kjaer, 10mV/g,) is fixed on the cantilever to record the acceleration. The recovering current is determined using the Ohm's law ($I = U_R / R_{load}$). It is worth mentioning that the recovering current can be composed of several frequencies. The main one is the mechanical excitation frequency but other harmonic frequencies or electrical noise can add also frequency contributions to the recovering current. We choose to filter with an FFT the electrical signal to keep only the frequency corresponding to the mechanical excitation.

Then the average harvested power per cycle $\bar{P}$ is calculated using (**EQ. 5.1**):

$$\bar{P} = \frac{1}{T}\int_0^T P(t)\,dt = \frac{1}{R_{load}\,T}\int_0^T U_r(t)^2\,dt \qquad (5.1)$$

where T is the period of the mechanical excitation.

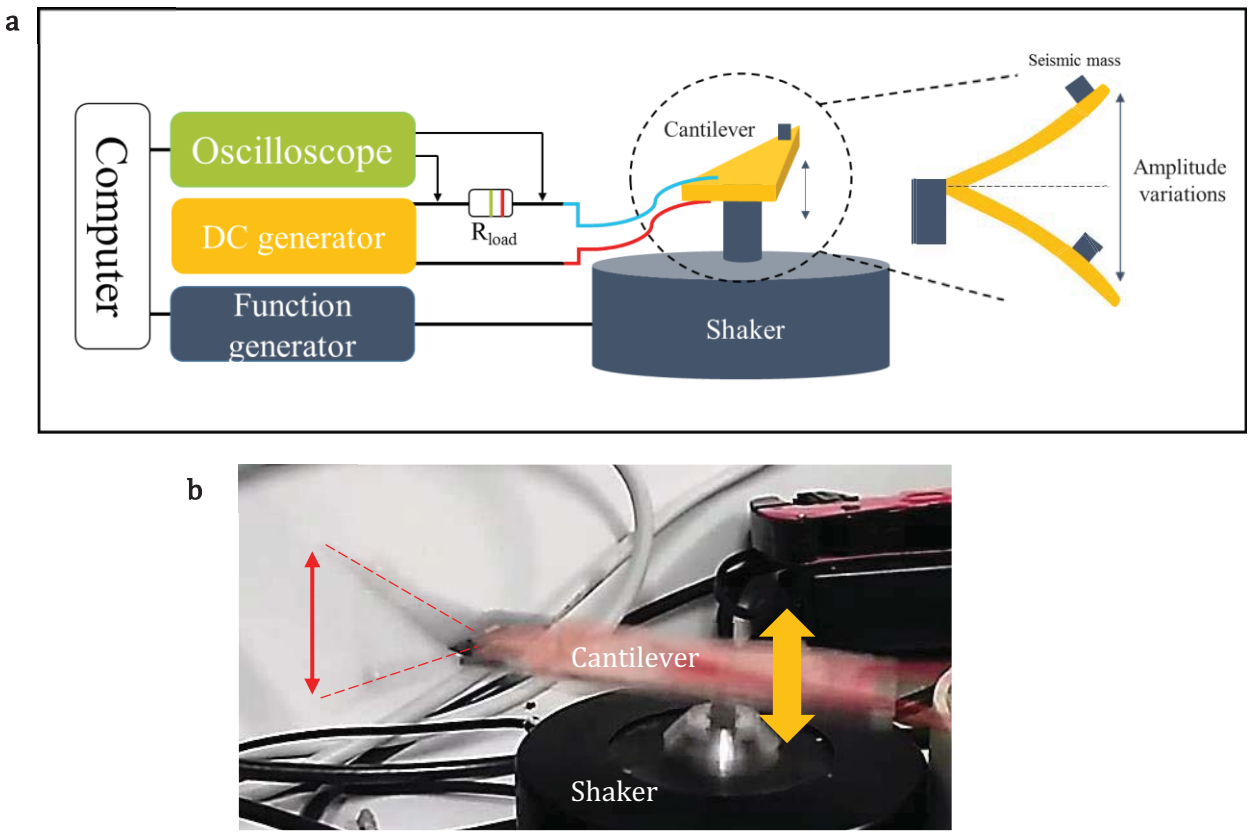


FIG. 4.3- a) Schematic of the experimental setup. b) Photograph of the setup at resonance.

3 Results and discussion:

3.1 Recovering power optimization:

We first investigate the performances of the bilayer composites for mechanical energy harvesting purposes. We measure the harvested current by discharge over a load resistance R_{load}, when the cantilever is mechanically excited using a shaker as depicted **FIG. 4.3**. Primary, the cantilever is studied without any seismic mass at its tip. **FIG. 5.4** a) presents the variation in harvested power versus the frequency of the mechanical excitation. The load resistance is fixed at R_{load}=8 MΩ and an acceleration of 9 g (90 m/s-2). It is highlighted that the output power is maximized for a frequency of 37 Hz which corresponds to the fundamental natural resonant frequency of the cantilever. A power of 151 nW is measured at this frequency although a significative decrease of 10 percent was observable for an offset of 3 Hz from the resonant frequency. Also, the output power depends on the load resistance R_{load}, which must be optimized to recover the maximum power. **FIG. 5.4** b) illustrates this optimization. Successive measurements are made with different values of R_{load} varying between 4 MΩ to 14 MΩ. The maximum power is measured for a load resistance of 8 MΩ using an acceleration amplitude of 9 g at the resonant frequency. It corresponds to the resistance with optimal power production. Taking into account the surface (4.3 cm^2) and the thickness (90 µm) of the electrostrictive layer, it leads to a maximum power density of 4 $\mu W/cm^3$ at the resonant frequency, the optimal resistance and an acceleration of 9g. For lower acceleration amplitudes the power density is decreasing quasi-linearly as shown **FIG. 5.4** c) with a slope around 16 nW/g. A power density of 0.3 $\mu W/cm^3$ is measured using an acceleration of 2g.

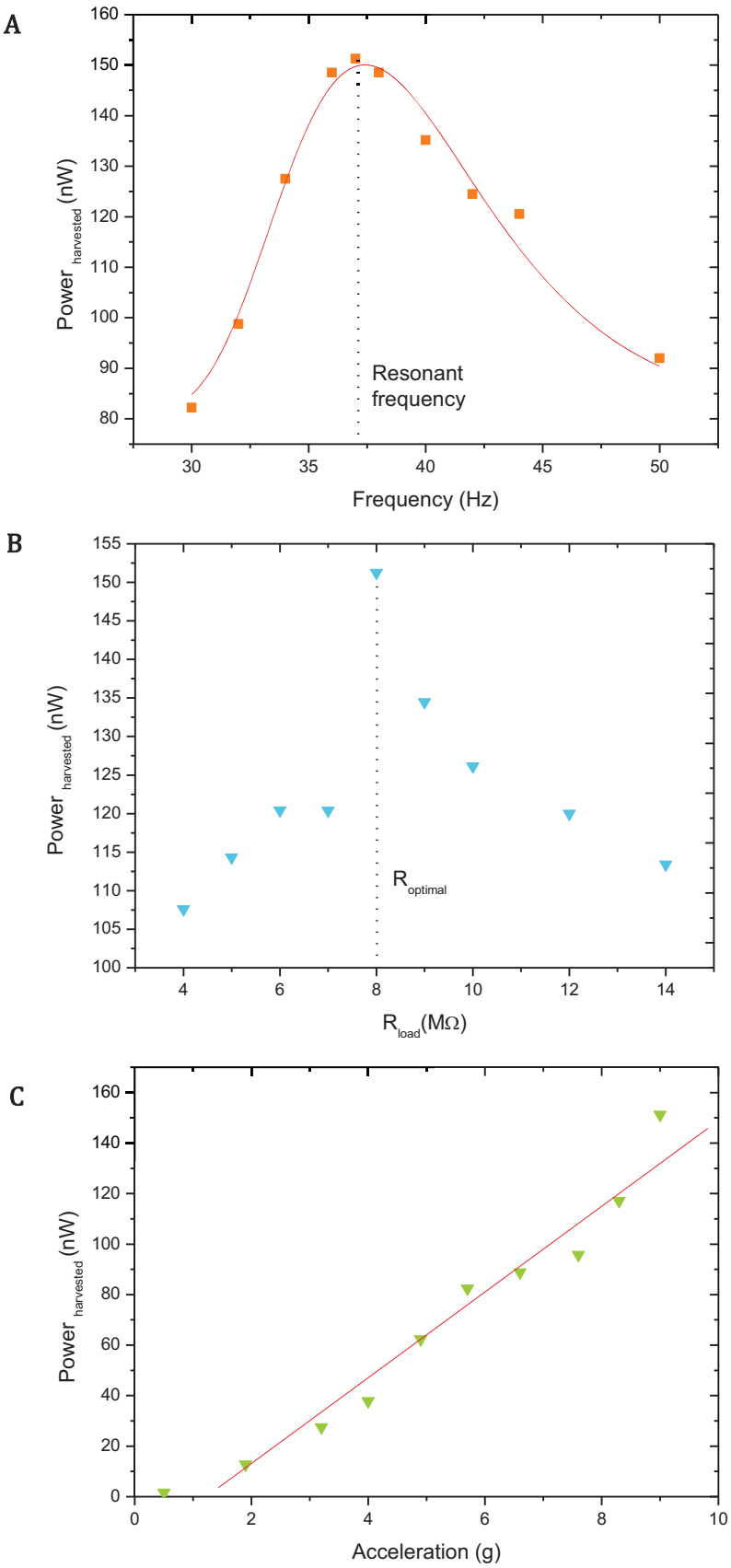


FIG. 5.4 – Power harvested related to the cantilever without seismic mass. a) Power harvested in function of the cantilever excitation frequency at R_{load}=8 MΩ and an acceleration of 9g. Resonant frequency (37 Hz) is highlighted by a black dot line. b) Power harvested in function of the load resistance at f=37 Hz an acceleration of 9g. Optimal load resistance is highlighted by a black dot line. c) Power harvested in function of the acceleration at R_{load}=8 MΩ and f=37 Hz.

For comparison, we investigate the performances of the same cantilever with a seismic mass (0.35g) at its tip. It is necessary to attach a tip mass to the beam in order to tune its fundamental natural frequency to a lower value and to improve its dynamic flexibility[7]. The recovering power is illustrated **FIG. 5.5**. As expected, the seismic mass reduces the resonant frequency of the cantilever to a value down to 25 Hertz (**FIG. 5.5** a)). At this frequency, a maximum power of 75 nW is measured when the cantilever is accelerated under 3g. The load resistance optimization is illustrated **FIG. 5.5** b). The optimal load resistance (6 MΩ) is lower than the one found without seismic mass. Finally, a linear increase of the recovering power with the acceleration of the beam is determined experimentally as shown **FIG. 5.5** c). The cantilever harvests around 23.7 nW/g. Taking into account the dimensions of the electroactive layer, a power density of 0.9 $\mu W/cm^3$ is measured using an acceleration of 2g. We remind that a power density of 0.3 $\mu W/cm^3$ was measured without mass using an acceleration of 2g. The cantilever with a seismic mass clearly provides the highest electrical response and the lowest resonant frequency. We succeed in increasing by almost a factor 3 the recovering power density while keeping the resonant frequency very low (25 Hz). These results confirm the abilities for electrostrictive materials to harvest electrical energy when they are integrated into a cantilever resonator.

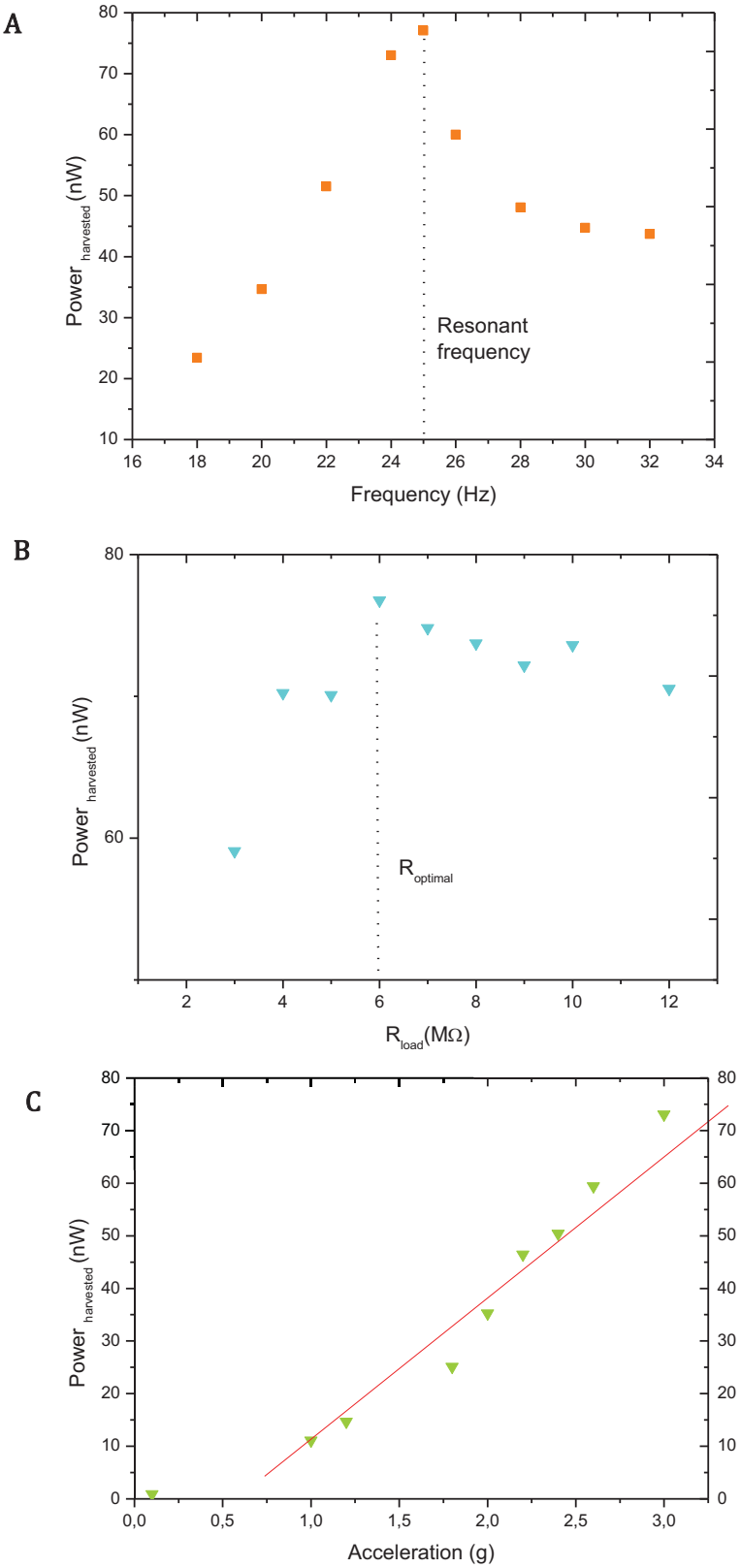


FIG. 5.5 - Power harvested related to the cantilever with a seismic mass of 350 mg. a) Power harvested in function of the cantilever excitation frequency at R_{load}=6 MΩ. Resonant frequency (25Hz) is highlighted by a black dot line. b) Power harvested in function of the load resistance at f=25 Hz. Optimal load resistance is highlighted by a black dot line. c) Power harvested in function of the acceleration at R_{load}=6 MΩ and f=25 Hz.

3.2 Electrical balance:

3.2.1 Leak resistance:

For recovering electrical power, we used the recently described “pseudo-piezoelectric” road [8–10] which is much easier than classic electrostatic cycles (constant charge or voltage)[11–13] because not requiring fine control of the charge and the strain. The pseudo-piezoelectric behavior is induced by the use of an electric field bias V_{dc}. Indeed, electrostrictive polymers are not piezoelectric, it is necessary to induce polarization with a DC bias to obtain a pseudo-piezoelectric behavior.

Nevertheless, for feasible energy harvesting applications, the energy balance has to be positive. It means that for efficient electrical conversion, the dissipated power must be smaller than the harvested power. We remind that the dissipated power for maintaining a polarization of the composite comes from the leak direct current (DC). This current is a consequence of the finite resistance R_i (ω) of the electrostrictive composite submitted to a DC bias voltage V_{dc}. Indeed, dielectric composites can be represented by a leak resistance R_i (ω) in parallel with a capacitance C (ω), denoting respectively the losses of the materials (by charge carriers and dielectric losses) and the intrinsic capacitance. **TAB. 1** shows the resistance value depending on the cantilever position (up, at rest, down). These values have been recorded using the up and down positions in the case of the resonating cantilever with a seismic mass at 25 Hz and for an acceleration amplitude of 3g. In these conditions, the cantilever amplitudes are recorded using a fast camera and reproduce in no vibrating conditions using a non-conductive rod.

TAB. 1 – Leak resistance R_i values depending on the cantilever position:

Cantilever positions		Leak Resistance (Ω0at f=0Hz
Up		0.8×10^{12}
At rest		1.0×10^{12}
Down		0.7×10^{12}

3.2.2 Loss power:

Now we expose the calculations of the loss powers. When the dielectric material is submitted to a voltage bias V_{dc}, the loss of power is given by:

$$P_{\text{loss}} = \frac{V_{dc}^2}{R_i} \quad (5.2)$$

where R_i is the internal leak resistance and V_{dc} is the applied voltage difference. **EQ. 5.2** leads to the loss powers in the case of a up and down positions, respectively 1.3 nW and 1.4 nW. The loss powers are very low and confirm the role of the PET isolating film for preventing the cantilever from electrical leakages even when the beam is stretched. Finally, the electrical energy gain will be calculated by considering the ratio of power harvestable to electrical polarization losses.

TAB. 2 shows the electrical efficiency in the case of the beam with the seismic mass at resonance. The maximum loss power has been considered to deduce the net power production. A net recovery power density of 1.9 μW/cm³ is calculated for an acceleration of 3g while 0.2 μW/cm³ were recovered for 1g.

TAB. 2 - Efficiency of the electrostrictive composite integrated in a cantilever beam.

% CB	a (g)	Harvested power (nW)	Power loss (nW)	Net power production (nW)	Electrical gain factor
10,0	3	75	1.4	73.6	53
10.0	2	35	1.4	33,6	25
10.0	1	10	1.4	8,6	7

Discussion :.

Working with a triangular cantilever with seismic mass was motivated as this shape has provided the highest electrical response and the lowest resonant frequency [6]. Indeed, triangular shape allows a uniform strain along their top surface, comparatively to rectangular ones, where strain is concentrated in the clamped area of the microcantilever [14]. Depositing an electrostrictive layer and an isolating film allows the recovery of mechanical energy when the active layer is submitted to strain. Data given in **TAB. 2** show that the energy balance is largely positive whatever the applied acceleration. We can see that increasing the tip's mass aims at increasing the power density by a factor 3 while a linear increase with the acceleration is reported. Tuning the tip's mass is a better strategy than increasing the acceleration for increasing the power density as ambient vibrations are mostly reported with accelerations below 2g [15]. However, the reported results are lower than the previous reported electrostrictive cantilever [6]. Nevertheless, the latter study does not discuss the losses which are probably not negligible as applied materials are close to the percolation threshold. At 2g, we report a higher power density, 0.9 μW/cm³, than the best material studied in Chapter 4 (0.4 μW/cm³).

4 Conclusion :

We presented a new cantilever resonator, specifically developed for real vibratory energy harvesting. Our microporous electrostrictive composite was associated with a thin insulating layer PET to limit losses. We succeeded in evaluating the energy scavenging abilities of this cantilever. 8.6 nW were recovered with a seismic mass and a 10 wt% carbon black composite using an acceleration amplitude of 1 g at the resonant frequency of 25 Hz. It leads to a power density of 0.12 $\mu W/cm^3$. The low resonant frequency of the triangular cantilever including a seismic mass at its tip, makes the device very promising for ambient energy harvesting. We discussed about the losses and electrical balance. An electrical gain factor of 7 is reported for an acceleration of 1g. In addition, the low-cost process and low toxicity are criteria encouraging their future development. Further improvements of the presented system lie in the design of the cantilever. We believe that optimization of the layers thickness could increase the power density by increasing the strain of the electroactive material. Indeed, the change of capacitance of electrostrictive materials, key parameter for increasing the harvested energy, is dominated by the applied strain. Moreover as mechanical vibrations are broadly dispersed, a larger resonant frequency bandwidth can be simply done by a parallel arrangement of single beam structures using different seismic masses[14]. In addition, the resonant electrostrictive cantilever could find applications for low-cost frequency or accelerator sensors in vibrating structures.

Take home message – Chapter 5

In this chapter, we sought to integrate electrostrictive CB/PDMS composite into a resonant cantilever. The developed prototype shows good potential for recovering natural mechanical vibrations.

1. We succeeded in maintaining the conversion abilities of an electrostrictive material although it was integrated into an all-organic resonator.

2. A 10 wt% carbon black composite using an acceleration amplitude of 1 g at the resonant frequency of 25 Hz recovered a power density of 0.12 $\mu W/cm^3$.

3. Geometric optimization of the cantilever (layers thickness, etc.) should increase the power density by increasing the strain of the electroactive material.

[1] L.B. Kong, T. Li, H.H. Hng, F. Boey, T. Zhang, S. Li, Waste Mechanical Energy Harvesting (I): Piezoelectric Effect, in: Waste Energy Harvesting, Springer Berlin Heidelberg, Berlin, Heidelberg, 2014: pp. 19–133. doi:10.1007/978-3-642-54634-1_2.

[2] Y. Tsujiura, E. Suwa, H. Hida, K. Suenaga, K. Shibata, I. Kanno, Lead-free piezoelectric MEMS energy harvesters of stainless steel cantilevers, in: IEEE, 2013: pp. 474–477. doi:10.1109/Transducers.2013.6626806.

[3] M. Shoaib, N.H. Hamid, M. Tariq Jan, N.B. Zain Ali, Effects of Crack Faults on the Dynamics of Piezoelectric Cantilever-Based MEMS Sensor, IEEE Sensors Journal. 17 (2017) 6279–6294. doi:10.1109/JSEN.2017.2737044.

[4] K.-I. Park, S. Xu, Y. Liu, G.-T. Hwang, S.-J.L. Kang, Z.L. Wang, K.J. Lee, Piezoelectric $BaTiO_3$ Thin Film Nanogenerator on Plastic Substrates, Nano Letters. 10 (2010) 4939–4943. doi:10.1021/nl102959k.

[5] J. Ihlefeld, B. Laughlin, A. Hunt-Lowery, W. Borland, A. Kingon, J.-P. Maria, Copper Compatible Barium Titanate Thin Films for Embedded Passives, Journal of Electroceramics. 14 (2005) 95–102. doi:10.1007/s10832-005-0866-6.

[6] H. Nesser, H. Debéda, J. Yuan, A. Colin, P. Poulin, I. Dufour, C. Ayela, All-organic microelectromechanical systems integrating electrostrictive nanocomposite for mechanical energy harvesting, Nano Energy. 44 (2018) 1–6. doi:10.1016/j.nanoen.2017.11.036.

[7] W.G. Kaval, R.A. Coutu, R.A. Lake, Electrostrictive polymers for mechanical-to-electrical energy harvesting, in: IEEE, 2016: pp. 323–327. doi:10.1109/NAECON.2016.7856823.

[8] L. Lebrun, D. Guyomar, B. Guiffard, P.-J. Cottinet, C. Putson, The Characterisation of the harvesting capabilities of an electrostrictive polymer composite, Sensors and Actuators A: Physical. 153 (2009) 251–257. doi:10.1016/j.sna.2009.05.009.

[9] P.-J. Cottinet, M. Lallart, D. Guyomar, B. Guiffard, L. Lebrun, G. Sebald, C. Putson, Analysis of AC-DC conversion for energy harvesting using an electrostrictive polymer P(VDF-TrFE-CFE), IEEE Transactions on Ultrasonics, Ferroelectrics and Frequency Control. 58 (2011) 30–42. doi:10.1109/TUFFC.2011.1771.

[10] R. Liu, Q. Zhang, L.E. Cross, Experimental investigation of electrostrictive polarization biased direct apparent piezoelectric properties in polyurethane elastomer under quasistatic conditions, Journal of Applied Polymer Science. 73 (1999) 2603–2609. doi:10.1002/(SICI)1097-4628(19990923)73:13<2603::AID-APP7>3.0.CO;2-R.

[11] K. Ren, Y. Liu, H. Hofmann, Q.M. Zhang, J. Blottman, An active energy harvesting scheme with an electroactive polymer, Applied Physics Letters. 91 (2007) 132910. doi:10.1063/1.2793172.

[12] Yiming Liu, Kai Liang Ren, H.F. Hofmann, Qiming Zhang, Investigation of electrostrictive polymers for energy harvesting, IEEE Transactions on Ultrasonics, Ferroelectrics and Frequency Control. 52 (2005) 2411–2417. doi:10.1109/TUFFC.2005.1563285.

[13] M. Lallart, P.-J. Cottinet, D. Guyomar, L. Lebrun, Electrostrictive polymers for mechanical energy harvesting, Journal of Polymer Science Part B: Polymer Physics. 50 (2012) 523–535. doi:10.1002/polb.23045.

[14] H. Nesser, C. Ayela, I. Dufour, H. Debéda, Highly deformable printed organic trapezoidal micro-beams for vibration energy harvesting, Flexible and Printed Electronics. 2 (2017) 015001. doi:10.1088/2058-8585/aa5310.

[15] S. Roundy, P.K. Wright, J.M. Rabaey, Energy Scavenging for Wireless Sensor Networks: with Special Focus on Vibrations, Springer US, Boston, MA, 2004. http://public.eblib.com/choice/publicfullrecord.aspx?p=3079287 (accessed July 9, 2018).

6. Highly sensitive flexible pressure sensors based on electrostrictive materials

Summary: Capacitive pressure sensors have attracted much attention in the recent past due to their potential for a variety of applications as a key component in e-skin systems. In particular, they are required for long-term heart monitoring and for increasing the natural interaction of robots with humans. In this work, we report the development of a flexible capacitive pressure sensor with a maximum sensitivity of 36 kPa^{-1} in the pressure range of 0-0.2 kPa. The stability over 100 cycles of the capacitive pressure response is demonstrated. The arrangement of a microstructured carbon filled polydimethylsiloxane and a PET isolating layer enabled us to operate the devices in different pressure regimes (0-20kPa), where the capacitance change upon compression with no electronic amplification and very low voltage (1V). We demonstrate that our sensor can be used for non-invasive and continuous radial artery pulse wave monitoring. Such a low-cost and easy processable technology may constitute an alternative to conventional invasive methods such as the arterial catheter system. Coupled with modern communication technologies, our sensor paves the way for heart monitoring system allowing patients to continue to live in their home environment instead of expensive healthcare.

1 Introduction:

Artificial intelligence that comes into direct contact with humans requires electronics on flexible and stretchable substrates. In this field, pressure sensors have attracted much attention in recent years due to their potential for a variety of applications. In particular, the demand for pressure sensors with high sensitivity in low pressure regions (<10kPa) is very high, for systems in healthcare and medical diagnosis as well as in electronic systems, in particular for the so-called "e-skin" systems [1–3]. The latter are materials able to mimic functionalities of human skin and have the sensing abilities to detect environmental factors such as changes in heat or pressure. E-skin systems are particularly adapted for continuously measuring arterial blood pressure (BP). Indeed, deposited on human skin, they combine two essential clinical standards: noninvasivity and real time measurements. Usually, the first criterion is respected by using non-invasive upper arm tensiometer, also known as sphygmomanometer (**FIG. 6.1**) and the second by using invasive arterial catheter systems (**FIG. 6.2**) [4,5].

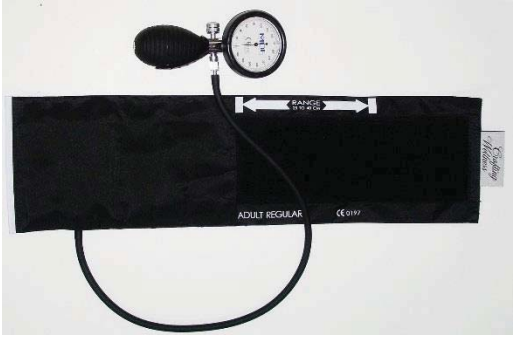


FIG. 6.1- Photograph of a noninvasive and non-continuous tensiometer for blood pressure measurements.

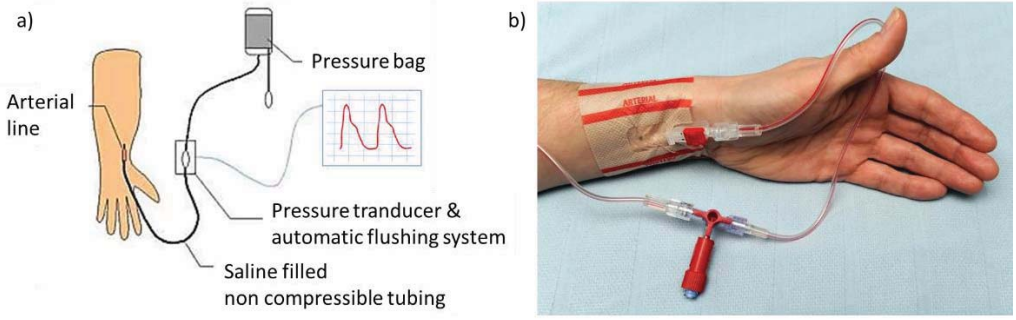


FIG. 6.2 – a) Schematic representation and b) photograph of an invasive arterial catheter system for continuous blood pressure measurements.

During major surgeries or in intensive cares, continuous and invasive arterial pressure measurement using arterial catheter is chosen to closely monitor the changes in blood pressure [6]. In other cases, especially for high-risk patients, the non-invasive intermittent measurement based on tensiometry is preferred, because of the possible

surgical complications of the first technique [7,8], but its accuracy depends on the correct positioning of the device on patients and may be lowered by patient conditions such as obesity [9].

The development of e-skin systems providing reliable and continuous BP measurements is motivated by the fact that cardiovascular disease is the leading cause of death worldwide accounting for 30% of the total deaths every year in the world (World Health Organization). Healthcare providers have recognized the need for early diagnosis and treatment to decrease this high death rate [6]. Non-invasive, non-intrusive sensors are needed elements of ambulatory and long-term heart monitoring systems. Coupled with modern communication technologies, they pave the way for blood pressure monitoring systems allowing patients to continue to live in their home environment instead of expensive healthcare facilities.

Until now, very few technologies are available for noninvasive and continuous blood pressure measurements. The most widespread is *the volume clamp method* [10]. The BP is measured at the finger with an inflatable cuff joined with a photodiode (**FIG. 6.3** a)). The diameter of the artery in the finger is measured by the photodiode; the pressure in the cuff is adjusted to keep the diameter of the artery constant. From the pressure changes in the cuff, a BP curve can be calculated [11].

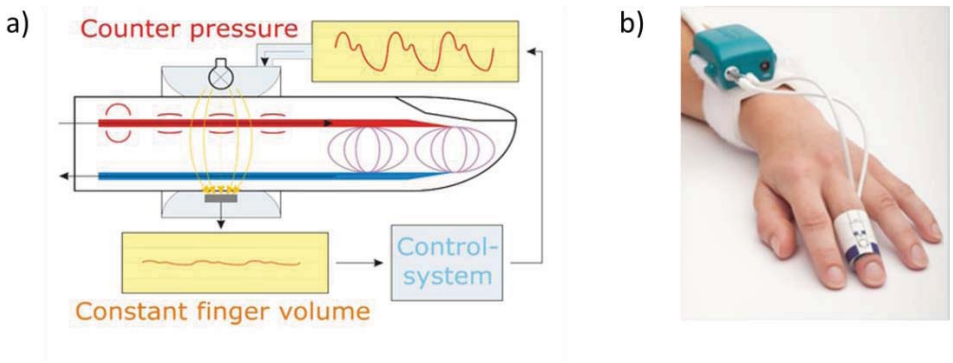


FIG. 6.3 – a) Schematic representation of the volume clamp method b) real blood pressure fingertip sensor.

Nevertheless, different medical reasons make volume clamp method inadequate in many cases. For examples, severe vasoconstriction, distorted fingers due to arthritis, etc. lead to difficulties to obtain a valid waveform using finger cuffs. Moreover, patients report discomfort from the congestion of the fingertip (**FIG. 6.3** b)) and need to change the cuff to another finger after a certain period of monitoring.

Consequently, the development of noninvasive continuous blood pressure monitoring methods is a field of great interest. The next generation of continuous blood pressure technologies is based on flexible e-skins, requiring materials with high pressure sensitivity. We remind that sensitivity to pressure P for piezocapacitive materials is defined as $S = \frac{\Delta C}{C_0 P}$. Several micro- or nano-structures [12–14] have been suggested to improve the sensitivity of piezocapacitive materials in particular in the low pressure

range. However, they usually require complex and expensive fabrication processes. Previously reported works have been vastly discussed in Chapter 1 but the main ones are reminded. Many recent works have based their investigations into pyramid-structured PDMS film. A sensitivity of 0.55 kPa^{-1} was reported compared to 0.02 kPa^{-1} for an unstructured PDMS film [12]. The structured film aims at subtly changing the permittivity value of the sensitive layer under pressure. To increase sensitivity to pressure, several groups [3,12,15] decided to integrate dielectric polymers as a gate dielectric layer in OFET (organic field effect transistor). Indeed, OFET could play the role of amplification and thus improve the sensibility. Still using the pyramid-structured PDMS and its integration in OFET, Schwartz et *al.* [3] advanced high sensitivity (8.4 kPa^{-1}).

Many drawbacks are observable on the current piezocapacitive materials. First, materials based on OFET need to be used with a high bias voltage to present high sensitivity. It could, consequently, constitute a limitation for wearable electronic. Then, the necessity of a very sensitive patterning process (Si mold) for making pyramid-structured film makes the process, time consuming and less reproducibility.

In this chapter, we present a new type of flexible, capacitive pressure sensors with unprecedented sensitivity. This new device can be economically fabricated over large areas by using thin films of microporous CB/PDMS composites associating with an isolating layer. The direct dependence of the applied pressure on the capacitance of CB/PDMS composites make them very suitable for low pressure capacitive sensors as porous materials developed very low Young's modulus.

2 Materials and methods:

The key component or our sensitive device is a porous thin film of PDMS filled with carbon black. The materials were fabricated using the water-in-oil emulsion method previously described in Chapter 2. They have shown good dielectric properties (up to $\varepsilon = 182$ at 100 Hz and loss tangent of $2.5 \cdot 10^{-2}$), when they were associated with an insulating layer (see Chapter 4). Moreover, PDMS is well known for its good mechanical properties and its compatibility with human tissues [16]. Making porous the PDMS allows a huge decrease of the Young's modulus compared to bulk PDMS, depending on the porosity and the carbon fraction. As the sensitivity is directly dependent on the applied pressure, making the materials deformable at low pressure will help them at increasing their sensitivity. Finally, the dielectric properties and the flexibility of these materials, are properties making the CB/PDMS composites, materials of choice for pressure-sensitive dielectric thin films.

However, there are two main differences in the formulation of porous materials with respect to our energy harvesting study. First, we decided to change the type of PDMS by switching from Sylgard 134 (Dow Corning) to another one (*confidential*). Even if theoretically both types are chemically identical, main differences have been observed in the quantity of dispersable phase. Indeed, 80 wt% of carbon solution were dispersable

in the other PDMS contrary to only 50 wt% for the Sylgard. Above these two maximal concentrations a phase separation was observable. This change is thus motivated as increasing the dispersed fraction aims at decreasing the final Young's modulus. High flexibility is required as materials will be used for the realization of "e-skin" systems. Using 10 wt% of carbon black and a dispersed fraction of 0.8, the material is highly strechtable and twisting as illustrated **FIG. 6.4**. **FIG. 6.5** illustrates this high flexibility as a strain of 140 % was required to fracture the material. In traction configuration, a non-linearity has been measured for a stress range between 0 and 275 kPa. A Young's modulus comprised between 0.4 and 0.1 kPa, depending on the stress range, is calculated. This modulus is one order of magnitude below those measured with the 1:1 CB/PDMS (Sylgard) (see Chapter 4) and confirm the interest of increasing the dispersed phase for decreasing the Young's modulus.



FIG. 6.4 - CB/PDMS porous material (10 w% of BC and 80 w% of dispersed phase) a) at rest b) stretching c) twisting.

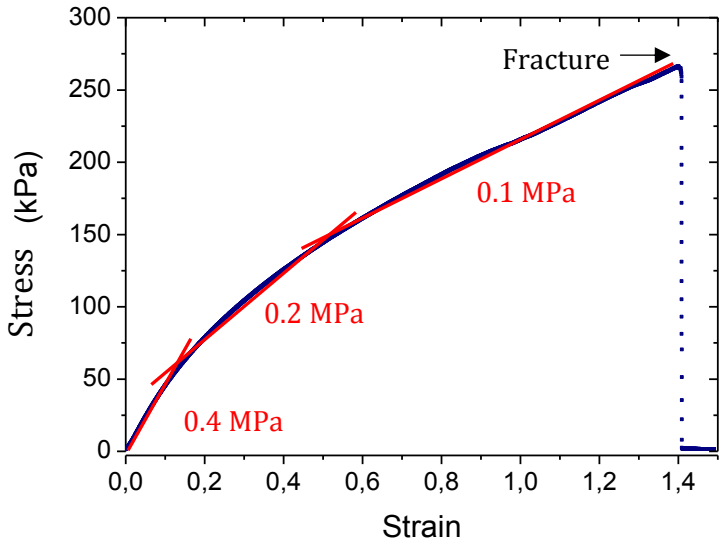


FIG. 6.5 - Stress-strain traction curve (10 w% of BC and 80 w% of dispersed phase).

The second change concerns the isolating layer. A thin plastic film of Mylar (polyethylene terephthalate, 2.5 µm) has been preferred compared to unstructured (bulk) PDMS for

making the isolation layer as small holes and defects could appear in the PDMS coating when its thickness was decreased. This change was motivated as the isolating layer is crucial for keeping the loss tangent as low as possible. For our study, the Mylar film is stacked on the solid CB/PDMS composites by using a surface plasma treatment (Plasma Diener Pico) for 3 minutes. This method aims at making stickable, the thin plastic film, on PDMS-composites. Then the two elements are stuck together for 15 min by applying a pressure at 90°C.

The sensitivity to compression tests of the bilayer composites was measured in capacitor configuration. To apply a well-controlled load, a rheometer is used as mechanized z-axis stage and force gauge. A top electrode (stainless steel) is connected to the z-axis stage while the bottom electrode is fixed. The rheometer applies linear loading-unloading cycles to the sensing materials. At the same time the dielectric properties are measured under 1V at 1kHz using an LCR-meter (Agilent). The force, the displacement, the capacitance and the resistance are recorded through an interfaced computer. The size of the pressure-sensitive material was 3.1cm^2. The practical procedure is detailed Chapter 2, especially the impedance compensation procedure.

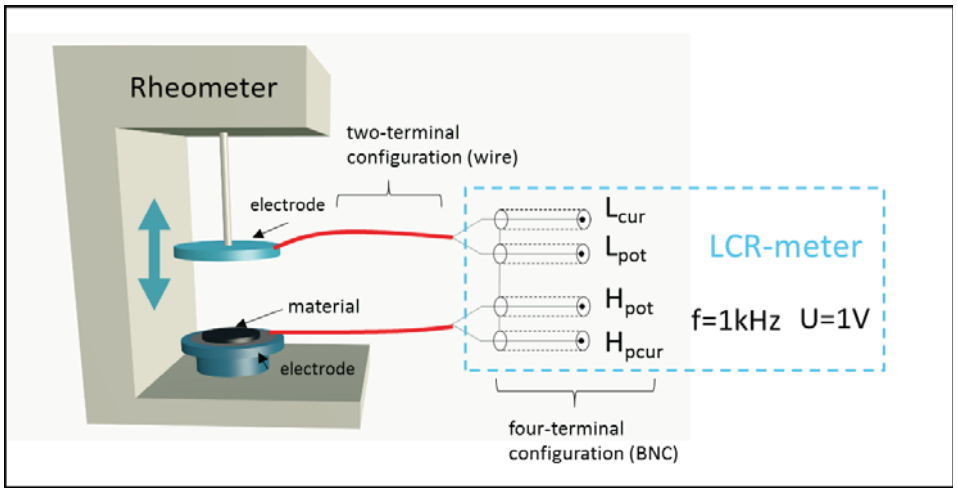


FIG. 6.6 – Schematic representation of the experimental setup for sensitivity measurements. Rheometer is used as mechanized z-axis stage and force gauge. Dielectrics properties are measured using an LCR-meter, under 1V at 1kHz. Both devices are computer controlled.

3 Results:

The sensitivity of the capacitive pressure sensor is investigated for a material disc with a diameter of 20 mm. Its formulation has been described in §2. **FIG. 6.7** a) shows the pressure sensitivity responses for 1, 100 and 100 loading-unloading consecutive cycles. Capacitance is measured at 1kHz under a voltage of 1 V. The sensitivity to pressure $\boldsymbol{S}$ can be defined as the slope of the pressure-capacitance response curves ($\boldsymbol{S} = \frac{\Delta \boldsymbol{C}}{\boldsymbol{C_0 P}}$, where $\boldsymbol{P}$ represents the applied pressure, $\boldsymbol{C_0}$ and $\Delta \boldsymbol{C}$ represent the capacitance at rest and the capacitance variation after applying pressure) as illustrated **FIG. 6.7** c).

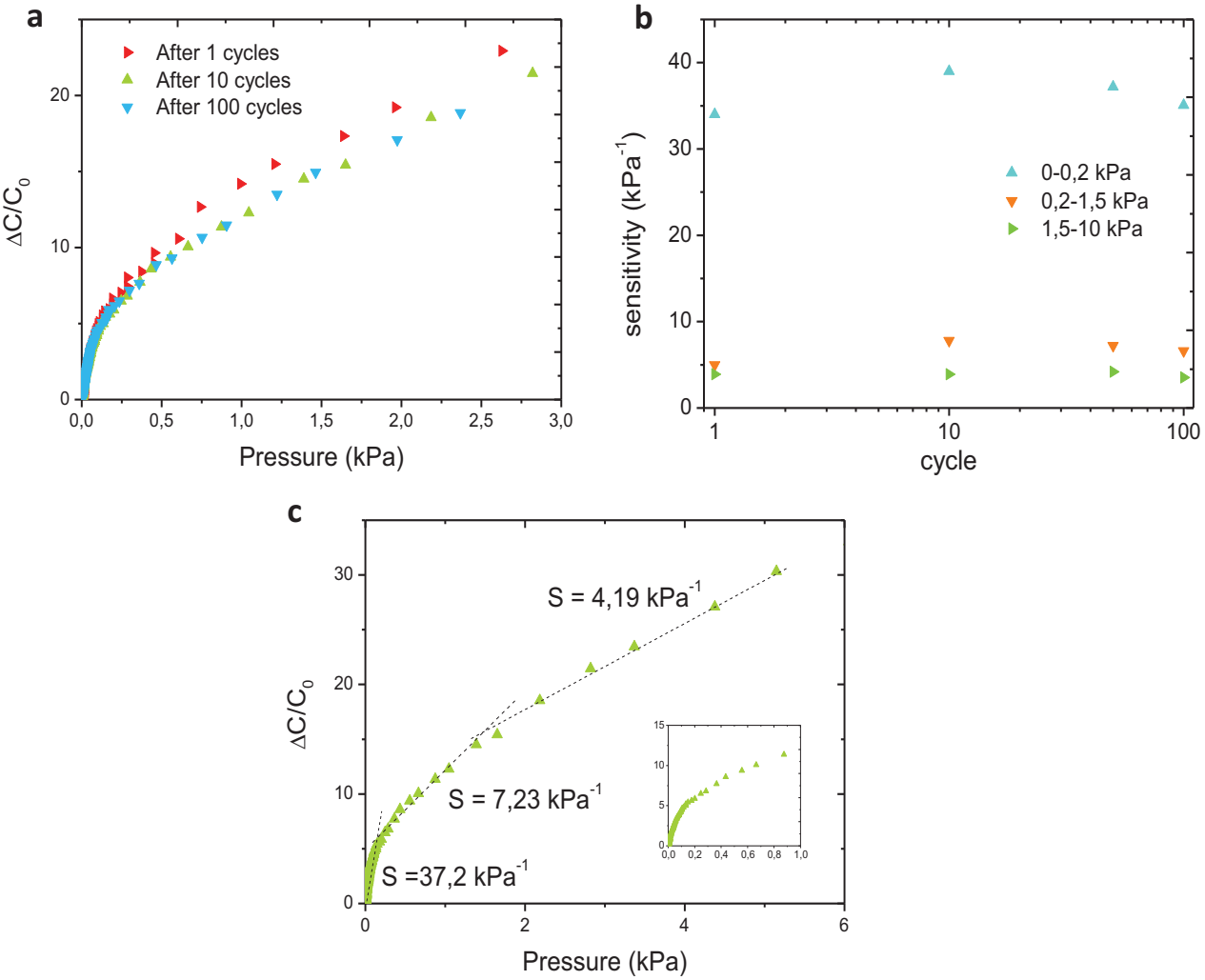


FIG. 6.7 - a) Pressure-response curves for successive loading-unloading cycles (right red triangles for 1 cycle, top green triangles for 10 cycles and bottom blue triangles for 100 cycles) b) Sensitivity evolution depending on the cycle number of different pressure ranges (top blue triangles 0-0.2 kPa, bottom orange triangles 0.2-1.5 kPa, right green triangles, 1.5-10 kPa). c) sensitivity measurements after 10 cycles for different pressure ranges. All capacitances are measured at 1kHz under a voltage of 1 V.

The composite exhibits different sensitivities depending on the pressure ranges as represented **FIG. 6.7** b). The maximum slope of the relative capacitive change is measured in the 0-0.2 kPa range with an average value of 36 kPa^{-1}. Then average values of 6.7 kPa^{-1} and 3.9 kPa^{-1} are respectively measured in the 0.2-1.5 kPa and 1.5-10 kPa range. Moreover, the microstructured film exhibits a very low hysteresis. Thousand loading-unloading consecutive cycles have been performed without significant change in the pressure-response curves (**FIG. 6.7** a)) and in the sensitivity (**FIG. 6.7** b)). Compared to previous reported works, we achieved a sensitivity far above the literature without using any OFET configuration or electronic amplification (**TAB. 6.1**). Until now, the best reported sensitivity (8,2 kPa-1) for a pressure range of 0 – 4 kPa was reached by Schwartz *et Al.* [3] with an OFET amplification although a sensitivity of 0.7 kPa-1 in the pressure range of 0 – 1 kPa was reported by Park *et Al.* [17]. With no amplification, we achieve a sensitivity one order of magnitude above the latest with a larger pressure range. Moreover, our sensitivity is very close to the one achieved with amplification.

TAB. 6.1 – Maximum sensitivities achieved in previous reported works:

active materials	pressure range (kPa)	sensitivity (kPa-1)	references.
PDMS pyramids OFET	0 -1,5	0,55	[12]
PDMS microhairy	0 - 1	0,58	[18]
Porous PDMS/air gap	0 - 1	0,7	[17]
Fluorosilicone/air gap	0 - 0,5	0,91	[19]
PDMS pyramids OFET	0 - 4	8,2	[3]
Suspended gate OFET	15 - 20	158,6	[15]

The huge reported sensitivities of the microporous CB/PDMS composite arise from the enhanced dielectric constant of the materials and from the low Young's modulus achieved. For developing e-skin systems measuring, inter alia, arterial blood pressure, we remind that high sensitivity in the low pressure range (<10kPa) is required.

The origin of the sensitivities variations, depending on the pressure range, has been investigated using mechanical studies. Stress-strain curves are measured for different loading-unloading consecutive cycles and compared to capacitance variations (**FIG. 6.8**). Three different mechanical behaviors are observable as illustrated **FIG. 6.8** a) by blue increments. The first value of sensitivity at very low pressure range (0-0.2 kPa) corresponds to an electrical contact area where the elastic resistance is very low (**FIG. 6.8** a)). Even if creating/removing an electrical contact could not appear reproducible, a quasi-constant value of sensitivity has been measured (**FIG. 6.7** c) in this pressure range. Then the second range (0.2-1.5 kPa), corresponds to the closure of porosity of the dielectric composite. At this range, the elastic resistance is low (Young's modulus=0.09 MPa) as the material is filled of pores which start to be removed by applying pressure (**FIG. 6.8** a)). Latter, for higher pressure range (1.5-10 kPa), the material is solicited in

its bulk (Young's modulus=0.3 MPa) and does not depend on any electrical contact (**FIG. 6.8** a)). The achieved Young's modulus, in the bulk phase, is one order of magnitude below the ones achieved with the materials developed in the energy harvesting part of this thesis. We remind that we succeeded in decreasing the modulus by increasing the weight fraction of the dispersed phase from 0.5 to 0.8, using another PDMS. Stress-strain curves measured for different loading-unloading consecutive cycles (**FIG. 6.8** b)), show very low hysteresis and confirm the origin of the stable sensitivities after 100 cycles (**FIG. 6.4** b)).

The electrical resistance, at 1kHz, of the studied sensitive material has been measured for the 100 loading-unloading cycles. The evolution of this resistance is presented in **FIG. 6.9**, for the 100th cycle, depending on the applied pressure. A linear evolution is observed

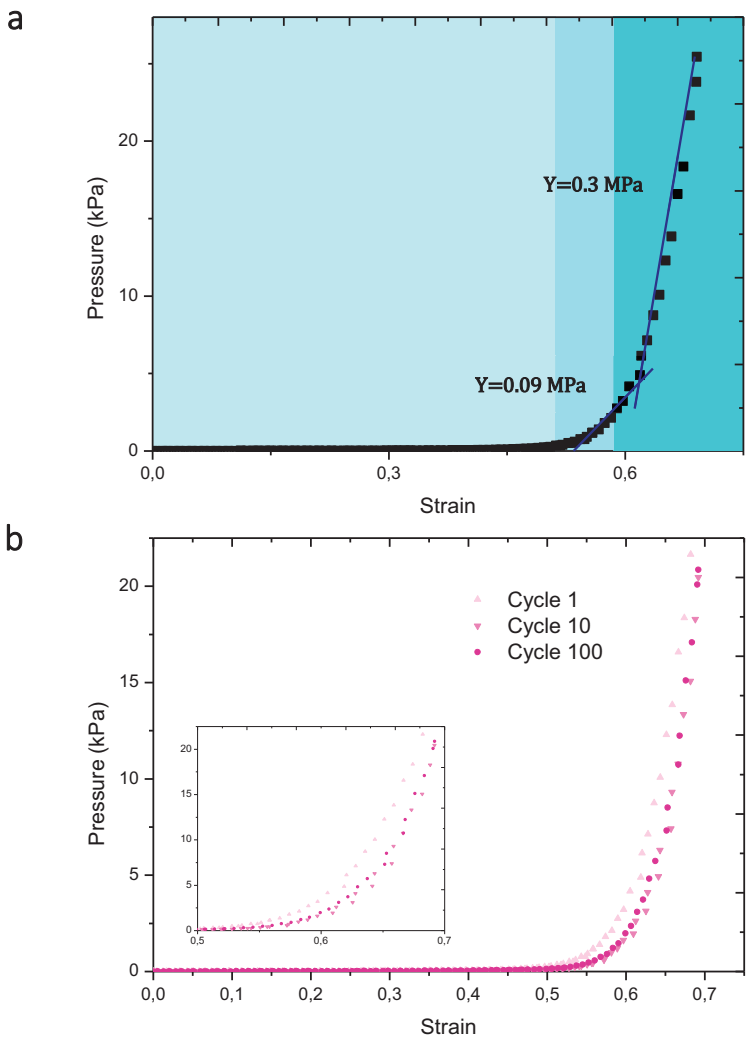


FIG. 6.8 – a) Pressure-strain curve after 100 cycles. Pressure ranges are highlighted by blue increments : light blue (0-0.2kPa), medium blue (0.2-1.5kPa), dark blue (1.5-10kPa). Young's modulus for the medium blue area is 0.09 MPa while for the dark area is 0.3 MPa. b) Pressure-strain curves depending on the cycle number. Light pink (cycle 1), medium pink (cycle 10), dark pink (cycle 100).

in the pressure range of 0.01 - 10 kPa, from 1 GΩ to 1.5 MΩ and attest of the piezoresistivity of the CB/PDMS composite. Nevertheless, the use of the PET isolating film affords using material as the dielectric layer in capacitive configuration, as the resistance is high enough. Besides, working with isolating materials helps to decrease the power consumption of the sensor (see Chapter 4).

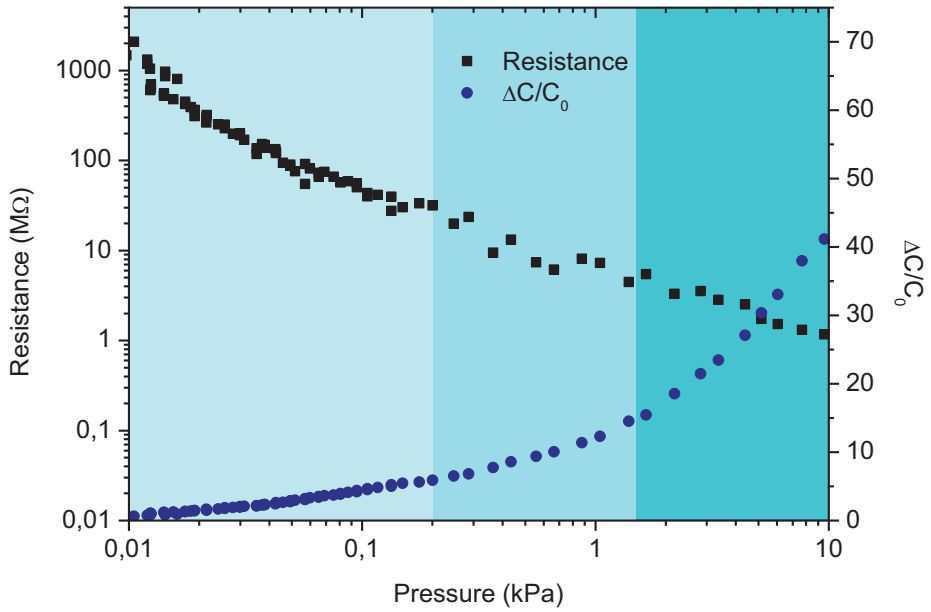


FIG. 6.9 - Evolution of the capacitance and resistance at 1kHz in function of the applied pressure. Pressure ranges are highlighted by the same colors as **FIG. 6.8.**

To further investigate the stability of the pressure sensor, the capacitive changes of the material were measured when alternatively load/unload, for more than 100 cycles, an applied pressure of 13.2 Pa or 9 Pa (**FIG. 6.10**). The material was submitted to pressure variations by using a piezoelectric actuator and a function generator applying a 0.1 Hz square signal. The results reveal that the capacitive pressure sensor exhibits high repeatability with very low hysteresis. Material shows immediate response and relaxation times after applying or releasing the pressure.

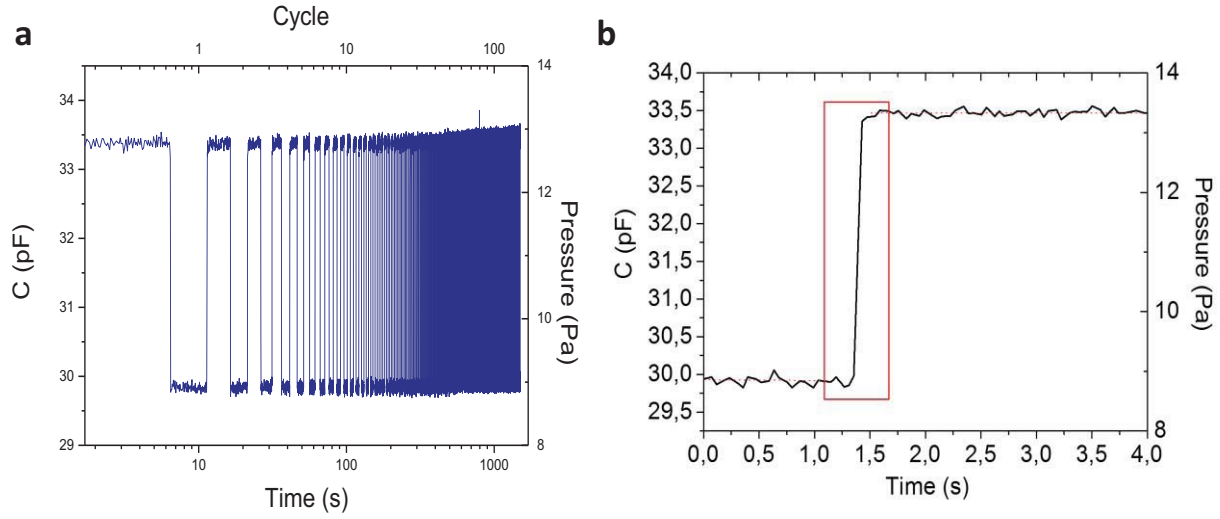


FIG. 6.10 – a) Real-time C-t curves of the sensitive material for more than 100 square loading/unloading cycles, 10 seconds for each cycle, with an applied pressure comprised between 9 and 13 Pa. b) Enlarged view on sensor response to pressure.

The stability cycling test is also performed in the bulk mechanical range as illustrated **FIG. 6.11**. Hundred sinus loading/unloading cycles are applied on the sensitive material, at 0.1 Hz, with an applied pressure comprised between 1.75 and 2.35 kPa. Capacitances values follow perfectly the sinus mechanical excitation (**FIG. 6.11** b)) and low decrease in capacitance is measured after 100 cycles(**FIG. 6.11** a)). This cycling test confirms the high stability of the sensitive material.

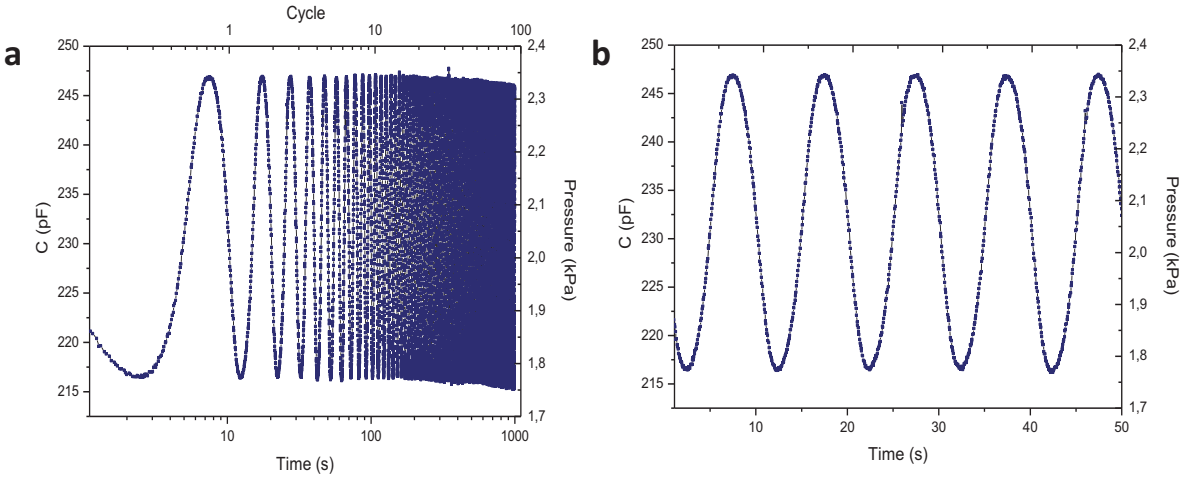


FIG. 6.11 - a) Real-time C-t curves of the sensitive material for more than 100 sinus loading/unloading cycles, 10 seconds for each cycle, with an applied pressure comprised between 1.75 and 2.35 kPa. b) Enlarged view on sensor response to stress.

Beyond the high sensitivities to pressure, our material has shown high capacitive gauge factor (GF) in its bulk domain (see **FIG. 6.8**). **FIG. 6.12** illustrates the capacitance variation in function of the strain for a mechanical compression. We remind that the gauge factor can be defined as the slope of the capacitance variation vs strain curves ($GF = \frac{\Delta C}{C_0 \varepsilon}$, where $\boldsymbol{\varepsilon}$ is the strain). The sensor device showed reliable, linear performance over thousands of cycles at up to 10% strain and the highest reported GF for a device of this class : 31,7[20].

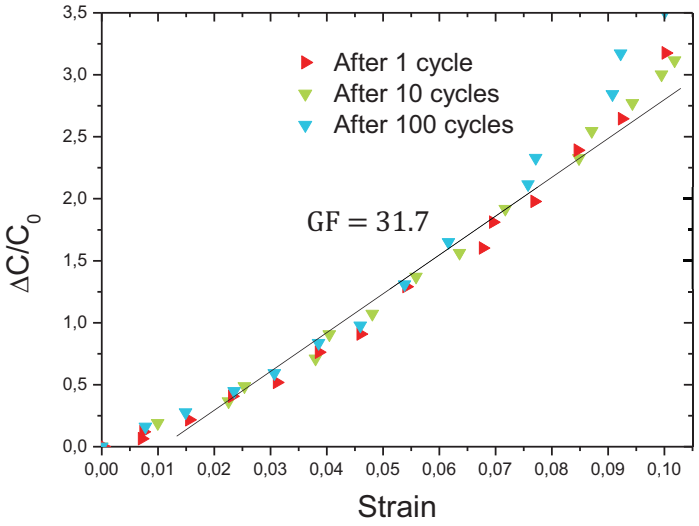


FIG. 6.12 - Capacitance variations in function of the strain for successive loading-unloading cycles (right red triangles for 1 cycle, top green triangles for 10 cycles and bottom blue triangles for 100 cycles).

Usually, capacitive strain sensors use the deformation for bringing electrodes closer together (geometrical effect), resulting in an increase in capacitance. The theoretical value of GF for incompressible materials due to this geometrical change is 1 [21] [22]. As our materials have shown electrostrictive properties (permittivity variation under compression), we succeed in increasing the GF by a factor 30. The huge reported GF makes our material very adapted for measuring deformation of objects or monitoring human motions such as walking, running, etc.

Application to arterial pressure measurements. In the medical field, arterial pulse wave is a key indicator as it aims at measuring the blood pressure and the heart rate. The previously described highly sensitive pressure sensor has been placed over the radial artery of the wrist to measure the subtile pressure variations. To do so, the sensitive material was completed by two flexible electrodes by depositing conductive flexible carbon tape on the top and the bottom of the materials surfaces as illustrated **FIG. 6.13** a). The system electrode-material-electrode is deposited on a copper tape, used as a substrate. The device, completed by wires, is simply deposited on the wrist and fixed with non-conductive tape (**FIG. 6.13** c)). It is worth mentioning that contrary to usual tensiometry techniques no compressive cuff is required. This advantage makes our device very useful for non-invasive and continuous blood pressure monitoring. The fast

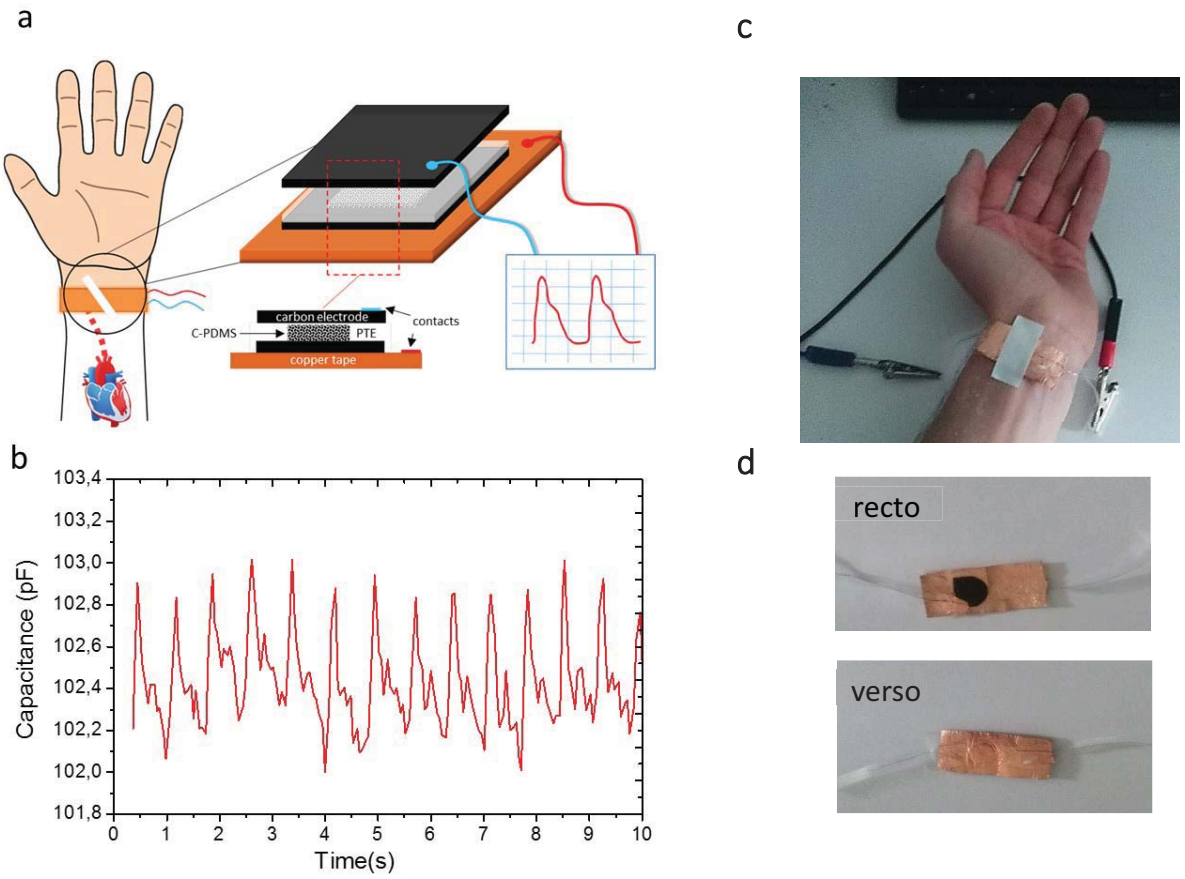


FIG. 6.13 – a) Schematic illustration of the e-skin device for detection of the wrist pulse b) Capacitive signals over time of a wrist pulse of a test person c) Photograh of the pressure-sensitive device on human wrist d) Photographs of the sensor.

response time of the e-skin provides high resolution which aims at getting the detailed clinical information from wrist pulse wave. **FIG. 6.13** b) shows noticeably the pulse frequency of a healthy person, measured at 75 beats/min (period of 0.8 s) with regular and repeatable pulse waves. For measuring the blood pressure, calibration between the measured capacitance and the pressure must be precisely established. For healthy people, systolic pressure is 90-120 mmHg [23] (10.5 – 16 kPa) and diastolic pressure is

60-79 mmHg [23] (8 - 10.5 kPa), meaning that the pressure range of interest, for blood pressure measurements, ranges between 8 and 16 kPa. These two pressures are easily distinguishable on the pulse a wave signal as $P_{systolic}$ is the pressure measured at the top of the pulse wave and $P_{diastolic}$ constitutes the pressure at the based line of the pulse wave (**FIG. 6.14**) [20]. The pulse wave illustrated **FIG. 6.13** b) shows that blood pressure is clearly measurable as the two picks are distinguishable. For the future, building wearable electronics and software for real time pulse waves monitoring could make accessible to healthcare professionals blood pressure information anywhere and anytime. It is worth noticing that only 1 volt was required for measuring capacitances. Although, high voltages were necessary in reported works [3,12,15], this low tension allows to avoid the use of large batteries. which can be incompatible with wearable sensors.

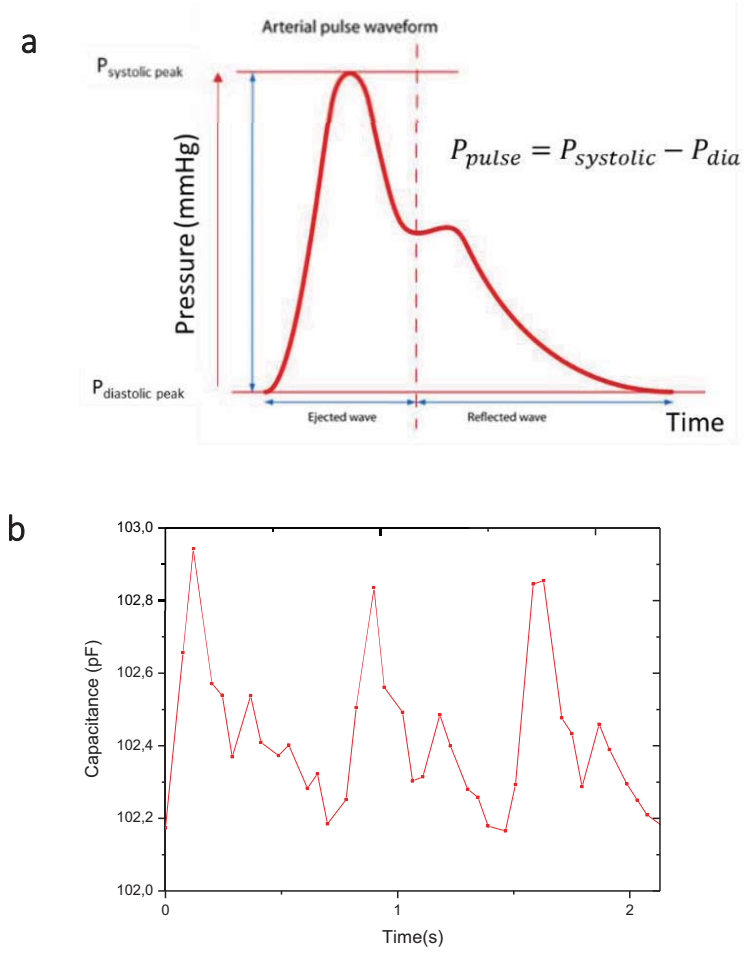


FIG. 6.14 – a) Theroritical curve of the radial arterial pressure during one cardiac cycle. Blood pressure P_{pulse} can be evaluated by the difference between $P_{systolic}$ and $P_{diastolic}$. b) Capacitance signal recorded with our pressure sensor.

4 Discussion and conclusion:

In summary, we developed a new capacitive pressure sensor by combining porous CB/PDMS composites with a thin PET isolating layer. The association of a porous material filled with high-k particles address the mechanical and dielectric requirements for developing deformable dielectric layers. The material shows unprecedented properties affording sensitivities of 36 kPa^{-1} in the 0-0.2 kPa pressure range and 6.7 kPa^{-1} in the 0.2-1.5 kPa range. These performances are one order of magnitude higher than those recently reported (**FIG. 6.15**). Until now, capacitive sensors based on rubber were mostly obtained using very delicate patterning process (pyramid-structured PDMS [3,12,13]). Moreover, they achieved high sensitivities by operating them with thin-film transistors (OFET) for signal amplification. This could be a limitation for developing wearable capacitive sensors, as OFET required high voltages. No amplification was required for measuring low pressure-capacitive changes with our sensor. Only 1V was used to record the capacitive response. Furthermore, our sensor performs stable pressure-capacitance changes and sensitivities after thousands of cycles. Low hystereris has been measured on the pressure-strain curves after performing these cycles. We also demonstrate the possibility of continuously recording arterial pulse waves in a noninvasive way. The sensor is successfully employed to assess the pulse frequency and to measure systolic and diastolic peaks. This new e-skin offers opportunities to make highly sensitive and wearable capacitive sensors and pave the way for low-cost and low power consumption heart monitoring systems. It also provides a solution to the dilemma of combining noninvasivity and continuous blood pressure monitoring. Besides, considering that components are fully commercial raw materials and that the process is relatively simple a low cost ($2/sensor) has been predicted for their fabrication.

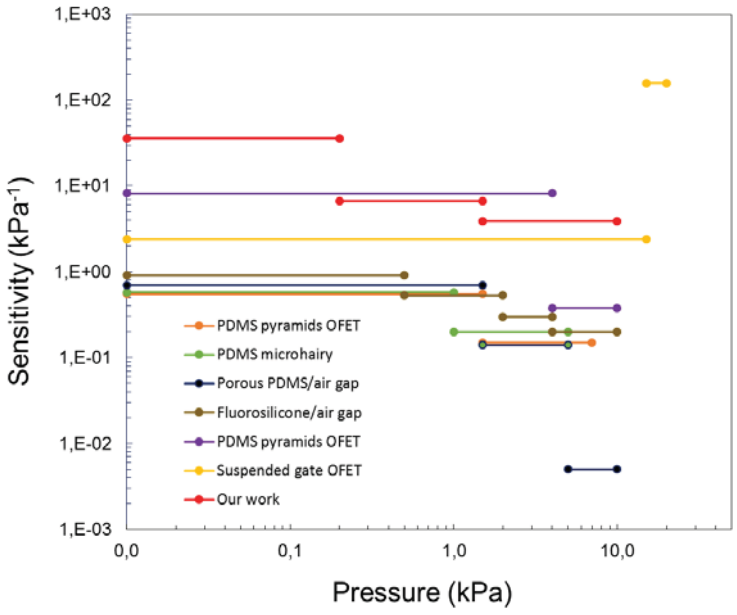


FIG. 6.15 - Comparison of the sensitivity of capacitive pressure sensors reported in the literature depending on the pressure range. The colors correspond to different materials: orange [12], green [18], black [17], brown [19], purple [3], yellow [15], red (our sensor).

5 Outlooks:

Using an innovative design, we have developed a new material that meets the integration and sensitivity specifications. We envision that this work will contribute to a new type of flexible e-skins, reliable for heart monitoring and adapted to large-scale production with cost-effective methods. The low cost of production and its high added value are criteria that will allow the material to find a place in a rapidly expanding heart monitoring market. The development of multifonctionnal wearable sensors that allows the detection of different stimuli such as temperature, humidity, etc. will be the subject of future investigations. For example, incorporation of metal organic framework (MOF) particles into polymer matrix could add the temperature sensing capacity to our materials. D.Zhao recently reported the development of mixed-lanthanide MOF with high relative sensitivity of luminescence properties in the physiological temperature regime [25]. In addition, integrating sensors into fully wearable systems where electronics such as data storage and data transmission (wireless), is a coming challenge for long-term continuous recording.

Take home message – Chapter 6

In this Chapter, we presented highly sensitive flexible pressure and strain sensors based on electrostrictive materials.

1. We reported the development of a capacitive pressure sensor, with sensitivities far above the literature : 36 kPa^{-1} in the 0-0.2 kPa pressure range and 6.7 kPa^{-1} in the 0.2-1.5 kPa range with easy processable materials. Moreover, we operated with no OFET amplification. Only 1V was used to record the capacitive response.

2. Then we showed that our sensor can perform as a capacitive strain sensor too. The device showed reliable, linear performances over thousands of cycles at up to 10% strain and the highest reported GF for a device of this class : 31,7.

3. We then demonstrated the possibility of continuously recording arterial pulse waves in a noninvasive way. The pressure sensor was successfully employed to assess the pulse frequency and to measure systolic and diastolic peaks.

[1] M.L. Hammock, A. Chortos, B.C.-K. Tee, J.B.-H. Tok, Z. Bao, 25th Anniversary Article: The Evolution of Electronic Skin (E-Skin): A Brief History, Design Considerations, and Recent Progress, Advanced Materials. 25 (2013) 5997–6038. doi:10.1002/adma.201302240.

[2] S. Gong, D.T.H. Lai, B. Su, K.J. Si, Z. Ma, L.W. Yap, P. Guo, W. Cheng, Highly Stretchy Black Gold E-Skin Nanopatches as Highly Sensitive Wearable Biomedical Sensors, Advanced Electronic Materials. 1 (2015) 1400063. doi:10.1002/aelm.201400063.

[3] G. Schwartz, B.C.-K. Tee, J. Mei, A.L. Appleton, D.H. Kim, H. Wang, Z. Bao, Flexible polymer transistors with high pressure sensitivity for application in electronic skin and health monitoring, Nature Communications. 4 (2013) 1859. doi:10.1038/ncomms2832.

[4] J.E. Fischer, ed., Fischer's mastery of surgery, Seventh edition, Wolters Kluwer, Philadelphia, 2019.

[5] L.A. Geddes, Handbook of blood pressure measurement., Humana, Place of publication not identified, 2013.

[6] J.J. Vos, M. Poterman, E.A.Q. Mooyaart, M. Weening, M.M.R.F. Struys, T.W.L. Scheeren, A.F. Kalmar, Comparison of continuous non-invasive finger arterial pressure monitoring with conventional intermittent automated arm arterial pressure measurement in patients under general anaesthesia, British Journal of Anaesthesia. 113 (2014) 67–74. doi:10.1093/bja/aeu091.

[7] E.E. Frezza, H. Mezghebe, Indications and complications of arterial catheter use in surgical or medical intensive care units: analysis of 4932 patients, Am Surg. 64 (1998) 127–131.

[8] T.R. Cousins, J.M. O'Donnell, Arterial cannulation: a critical review, AANA J. 72 (2004) 267–271.

[9] K. Lakhal, C. Macq, S. Ehrmann, T. Boulain, X. Capdevila, Noninvasive monitoring of blood pressure in the critically ill: Reliability according to the cuff site (arm, thigh, or ankle), Critical Care Medicine. 40 (2012) 1207–1213. doi:10.1097/CCM.0b013e31823dae42.

[10] J. Penáz, A. Voigt, W. Teichmann, [Contribution to the continuous indirect blood pressure measurement], Z Gesamte Inn Med. 31 (1976) 1030–1033.

[11] A.S. Meidert, B. Saugel, Techniques for Non-Invasive Monitoring of Arterial Blood Pressure, Frontiers in Medicine. 4 (2018). doi:10.3389/fmed.2017.00231.

[12] S.C.B. Mannsfeld, B.C.-K. Tee, R.M. Stoltenberg, C.V.H.-H. Chen, S. Barman, B.V.O. Muir, A.N. Sokolov, C. Reese, Z. Bao, Highly sensitive flexible pressure sensors with microstructured rubber dielectric layers, Nature Materials. 9 (2010) 859–864. doi:10.1038/nmat2834.

[13] C.M. Boutry, A. Nguyen, Q.O. Lawal, A. Chortos, S. Rondeau-Gagné, Z. Bao, A Sensitive and Biodegradable Pressure Sensor Array for Cardiovascular Monitoring, Advanced Materials. 27 (2015) 6954–6961. doi:10.1002/adma.201502535.

[14] X. Wang, Y. Gu, Z. Xiong, Z. Cui, T. Zhang, Silk-Molded Flexible, Ultrasensitive, and Highly Stable Electronic Skin for Monitoring Human Physiological Signals, Advanced Materials. 26 (2014) 1336–1342. doi:10.1002/adma.201304248.

[15] Y. Zang, F. Zhang, D. Huang, X. Gao, C. Di, D. Zhu, Flexible suspended gate organic thin-film transistors for ultra-sensitive pressure detection, Nature Communications. 6 (2015). doi:10.1038/ncomms7269.

[16] M.C. Bélanger, Y. Marois, Hemocompatibility, biocompatibility, inflammatory and in vivo studies of primary reference materials low-density polyethylene and polydimethylsiloxane: a review, J. Biomed. Mater. Res. 58 (2001) 467–477.

[17] S. Park, H. Kim, M. Vosgueritchian, S. Cheon, H. Kim, J.H. Koo, T.R. Kim, S. Lee, G. Schwartz, H. Chang, Z. Bao, Stretchable Energy-Harvesting Tactile Electronic Skin Capable of Differentiating Multiple Mechanical Stimuli Modes, Advanced Materials. 26 (2014) 7324–7332. doi:10.1002/adma.201402574.

[18] C. Pang, J.H. Koo, A. Nguyen, J.M. Caves, M.-G. Kim, A. Chortos, K. Kim, P.J. Wang, J.B.-H. Tok, Z. Bao, Highly Skin-Conformal Microhairy Sensor for Pulse Signal Amplification, Advanced Materials. 27 (2015) 634–640. doi:10.1002/adma.201403807.

[19] L. Viry, A. Levi, M. Totaro, A. Mondini, V. Mattoli, B. Mazzolai, L. Beccai, Flexible Three-Axial Force Sensor for Soft and Highly Sensitive Artificial Touch, Advanced Materials. 26 (2014) 2659–2664. doi:10.1002/adma.201305064.

[20] T.Q. Trung, N.-E. Lee, Flexible and Stretchable Physical Sensor Integrated Platforms for Wearable Human-Activity Monitoringand Personal Healthcare, Advanced Materials. 28 (2016) 4338–4372. doi:10.1002/adma.201504244.

[21] D.J. Cohen, D. Mitra, K. Peterson, M.M. Maharbiz, A Highly Elastic, Capacitive Strain Gauge Based on Percolating Nanotube Networks, Nano Letters. 12 (2012) 1821–1825. doi:10.1021/nl204052z.

[22] S. Yao, Y. Zhu, Wearable multifunctional sensors using printed stretchable conductors made of silver nanowires, Nanoscale. 6 (2014) 2345. doi:10.1039/c3nr05496a.

[23] P.K. Whelton, R.M. Carey, W.S. Aronow, D.E. Casey, K.J. Collins, C. Dennison Himmelfarb, S.M. DePalma, S. Gidding, K.A. Jamerson, D.W. Jones, E.J. MacLaughlin, P. Muntner, B. Ovbiagele, S.C. Smith, C.C. Spencer, R.S. Stafford, S.J. Taler, R.J. Thomas, K.A. Williams, J.D. Williamson, J.T. Wright, Guideline for the Prevention, Detection, Evaluation, and Management of High Blood Pressure in Adults: A Report of the American College of Cardiology/American Heart Association Task Force on Clinical Practice Guidelines, Hypertension. 71 (2018) e13–e115. doi:10.1161/HYP.0000000000000065.

[24] R.E. Klabunde, Cardiovascular physiology concepts, 2nd ed, Lippincott Williams & Wilkins/Wolters Kluwer, Philadelphia, PA, 2012.

[25] D. Zhao, X. Rao, J. Yu, Y. Cui, Y. Yang, G. Qian, Design and Synthesis of an MOF Thermometer with High Sensitivity in the Physiological Temperature Range, Inorganic Chemistry. 54 (2015) 11193–11199. doi:10.1021/acs.inorgchem.5b01623.

Conclusion and perspectives

The electrostrictive project was the core of my PhD research project over the past three years. This project was multipurpose in the sense that it combined:

- Formulation and chemical skills to synthetize composite materials
- Electronic and mechanical abilities to deal with the materials characterization
- Applied research and engineering to develop prototypes of integrated electrostrictive materials.

First, we developed composites via the addition of conductive fillers to soft elastomeric polymers. The feature of our investigations is that the fillers are added into a continuous phase by using emulsion paths (O/W or W/O). The use of emulsions offers opportunities to control the fillers dispersion and to tune the materials microstructure. In the case of O/W emulsions and r-GO fillers (**Chapter 3**), we successfully increased the permittivity of composites. The structure of graphene flakes promotes the formation of microcapacitors which leads to high permittivity up to 10^5 at 100 Hz. Eventhough, we expected to get low loss tangents thanks to a nematic structuration of the fillers, moderate dielectric losses have been obtained, between 1 and 2 for the percolated systems at 100 Hz. It makes them too conductive for energy harvesting applications but very adapted for making piezoresistive sensors (gauge factor around 6 above the percolation threshold).

As we were aware of the limitations of our first system for energy harvesting applications, we decided to focus on a second system: W/O emulsion based materials filled with carbon black particles (**Chapter 4**). The materials consist of a porous carbon black composite, where carbon blacks particles create conductive shells inside each air cavities. A good compromise between high permittivity and low dielectric loss has been found for materials close to the percolation threshold. Indeed, for 4.0 wt% of CB, a permittivity of 20 with a $tan\,\delta$ equal to 0.02 has been measured at 100 Hz. These performances are very close to those delivered by the polyvinylidene fluoride (PVDF) but with a Young's modulus three decades lower. Nevertheless, the dielectric properties of porous materials highly depend upon the materials synthesis protocol in the vicinity of the percolation transition. It leads to a very limited composition window, making the process poorly reliable. To overcome this limitation, we decided to design a new bilayer structure. It is based on the previously described microporous CB material associated with a thin insulating layer. This new

investigated structure exhibits a high effective relative dielectric permittivity (up to 182 at 100 Hz) with very low effective conductivity (down to 2.53 $10^{-8}\ S\ m^{-1}$).

As our bilayer approach leads to materials possessing the dielectric and mechanical requirements, we evaluated the energy harvesting possibilities using a test bench and a piezoelectric actuator to simulate vibrations. We succeeded in generating electrical energy in response to mechanical vibrations with a power density of $0.38\ W\ m^{-3}$ under an applied bias electric field of 32V. Materials display figures of merit well above materials classically used or published in the litterature, including fluorinated co- and ter-polymers synthesized by heavy chemical processes. The production process of the present materials is based on non-hazardous and low-cost chemicals.

Then we succeeded in integrating the electrostrictive porous carbon black composites into a mechanical energy harvesting device (**Chapter 5**). We made a mechanical energy harvester based on a cantilever beam. In combination with an insulating layer, the investigated structure maintains its conversion abilities although it was integrated into an all-organic resonator. Using a sinusoidal acceleration amplitude of 2 g at 25 Hz, we succeeded in generating an electrical power density of 0.4 μW/cm^3.

Finally, we presented highly sensitive flexible pressure and strain sensors based on electrostrictive materials (**Chapter 6**). Sensors were tested over thousands of cycles. We demonstrated the possibility of continuously recording arterial pulse waves in a noninvasive way. The pressure sensor is successfully employed to assess the pulse frequency and to measure systolic and diastolic peaks.

Based on the performed proofs of concept, we fully believe in the benefits of our technology for making highly sensitive and wearable capacitive sensors and for paving the way for low-cost and low power consumption heart monitoring systems. It will be the starting points of a competitive product adapted to the needs of the health market. That is why we want to promote our technology and its 4 patents, in the future, by creating a startup.

Value creation: publications and patents

The research presented in this thesis gave rise to two papers published in international reviews. Another one, reporting the sensing performances of the CB/PDMS composites is being drafted.

Publications:

- Luna, M Pruvost, J Yuan, C Zakri, W Neri, C Monteux, P Poulin, A Colin. Giant Electrostrictive Response and Piezoresistivity of Emulsion Templated Nanocomposites. Langmuir, 33 (18), 4528-4536, 2017

- Mickaël Pruvost, Wilbert J. Smit, Cécile Monteux, Philippe Poulin, Annie Colin. Microporous electrostrictive materials for vibrational energy harvesting. Multifunct. Mater. 00 (2018) 000000

Patterns:

Structured composites useful as low force sensors, applied in 2018, first-to-invent (50%):

- PCT/EP2018/050002
- PCT/EP2018/050003
- PCT/EP2018/059956
- PCT/EP2018/059957

LANGMUIR

Article

pubs.acs.org/Langmuir

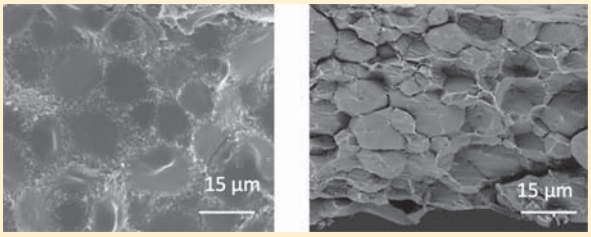
Giant Electrostrictive Response and Piezoresistivity of Emulsion Templated Nanocomposites

Alan Luna,[†] Mickael Pruvost,[‡] Jinkai Yuan,[†] Cécile Zakri,[†] Wilfrid Neri,[†] Cécile Monteux,[‡] Philippe Poulin,[†] and Annie Colin*[,‡]

[†]Centre de Recherche Paul Pascal, CNRS, Université de Bordeaux, 115 Avenue Schweitzer, 33600 Pessac, France

[‡]ESPCI Paris, PSL Research University, CNRS, Laboratoire Sciences et Ingénierie de la Matière Molle, UMR 7615, 10 rue Vauquelin, 75231 Paris cedex 05, France

ABSTRACT: Using an emulsion road and optimizing the dispersion process, we prepare polymer carbone nanotubes (CNT) and polymer reduced graphene oxide (rGO) composites. The introduction of conductive nanoparticles into polymer matrices modifies the electronic properties of the material. We show that these materials exhibit giant electrostriction coefficients in the intermediate filler concentration (below 1 wt %). This makes them very promising for applications such as capacitive sensors and actuators. In addition, the values of the piezoresistivity measured in the high filler concentration situation are at least an order of magnitude greater than the one reported in the literature. This opens the way to use these materials for stress or strain sensor applications considering their giant responses to mechanical deformations.



Downloaded via E S P C I on July 9, 2018 at 10:11:17 (UTC).
See https://pubs.acs.org/sharingguidelines for options on how to legitimately share published articles.

INTRODUCTION

In the large field of nanotechnology, polymer matrix based nanocomposites have become a prominent area of current research and development.[1] The introduction of conductive nanoparticles into polymer matrices represents a promising avenue for the development of new materials for electronics. These materials are flexible, of low cost, and have original mechanical and electronic properties. The latter may be tuned by varying the amount of included particles.[2] From a theoretical point of view, by gradually filling insulating polymer matrices with conductive particles, four types of behavior can be defined. In the low concentration situation, the particles are more or less dispersed in the matrix. The electronic conductivity of the material is low, but the introduction of polarizable domains induces an increase of the dielectric permittivity. In the vicinity of the percolation threshold and below it, the electronic conductivity remains low, but the dielectric permittivity diverges. This is physically explained by the formation of large conducting clusters, which are separated by small distances in near percolated networks. This effect creates locally large capacitors, which contribute to the increase of the permittivity of the material.[3] This range of particle concentration is thus perfectly suited to get materials with huge dielectric permittivity for energy storage but also with huge electrostrictive coefficients.[4] Electrostrictive materials are used in the fabrication of sensors and actuators[5] (ink jet printing, printhead, adaptive optics devices, and ultrasonic motor). More recently, it has been proposed to use them as dielectric in variable capacitors to harvest energy from mechanical vibrations. In the vicinity of the percolation threshold but slightly above, the sample becomes electronically conductive. In this concentration range, deformable networks might exhibit huge variation of electronic resistance as a function of the deformation considering the large susceptibility of near percolated networks. These materials are piezoresistive and may be used to build stress or strain sensors.[5−11] Well above the percolation threshold, the sample is conductive. The value of the percolation threshold depends upon the shape of the particles.[12,13] In practice, finite size effects, difficulties to homogeneously incorporate particles in a matrix, and resistive contacts between the conducting particles make the achievement of the ideal behavior diagram challenging. In addition, the polymer composite technology suffers from a weakness due to the substantial increase of losses near and above percolation. These losses arise from dielectric losses related to the motion of bound charges of the dielectric medium and from the intrinsic conductivity brought by the free charges of the conducting particles. High permittivity and low losses in frequency ranges of interest below the percolation threshold are expected to be found by developing a fine degree of the structure of the nanoparticles within the polymer matrix. Progress toward this goal has been achieved in the recent years particularly in the dispersion of nanoparticles in polymer matrices. Examples of fine carbon nanotube (CNT) dispersions were achieved by in situ polymerization of monomers in the presence of CNTs,[14] by mixing polymer beads and CNTs[15] by melt processing, and by solution casting where the matrix and the CNTs are dispersed in a common solvent.[16]Following this path, Park et

Received: November 21, 2016
Revised: April 9, 2017
Published: April 20, 2017

 © 2017 American Chemical Society

DOI: 10.1021/acs.langmuir.6b04185
Langmuir 2017, 33, 4528−4536

al.[17] improved the electrostrictive properties of polyimide by including a highly uniform dispersion of single wall nanotubes (SWNTs) to the polymer. The uniformity and the homogeneity of the dispersion is possible due to the donor−acceptor interaction between the SWNTs and the polyimide.[18] Park and co-workers[18] have measured negative out-of-plane strain in polyimide matrix composites in response to a low-frequency (0.02 Hz)-applied electric field and have found electrostrictive coefficients ranging between $M_{33} = -3.8 \times 10^{-15}$ m^2/V^2 and -1.2×10^{-13} m^2 V^{-2} at 0.02 Hz with a conductivity ranging between 10^{-9} S/m and 10^{-2} S/m. The best compromise between low conductivity and high electrostrictive coefficient (i.e., −3.8 × 10−15 m^2/V^2, 10^{-9} S/m) is achieved at an intermediate concentration equal to 0.0035% by the weight of nanotubes. The high electrostrictive coefficient results from the creation of deformable micro and nanocapacitors formed by the CNTs. In addition, the donor−acceptor interactions between the fillers and the matrix bring additional polarization to the system. The same performances are obtained by Wongtimnoi et al.,[16] using a polyether-based polyurethane elastomer filled with conductive carbon black. Adding single walled carbon nanotubes to a nonactuating polyimide, Deshmukh[19] et al. have obtained an electrostrictive coefficient equal to 10^{-12} m^2/V^2 but with a conductivity equal to 10^{-3} S/m. These values of electrostrictive coefficients are much higher than the ones obtained with neat polymers or classical nanocomposites that usually comprise between 10^{-17} m^2 V^{-2} and 510^{-16} m^2 V^{-2}.[20]

These recent results demonstrate the potential of CNT-polymer composites to achieve electrostrictive materials with promising properties, but a greater degree of control of the structuration of the conductive inclusions is still needed to achieve improvements of properties. We show in this work that the fabrication of composites using an emulsion approach[21] provides such a control and yields unprecedented performances. The emulsion droplets are greater than the size of the conductive particles. As a consequence, the particles remain segregated in between the emulsions droplets. The polymer is cross-linked after the composite has been molded and dried in order to end up with a solid state nanocomposite. Varying the concentration of conductive particles allows the electrostrictive properties of the sample to be tuned. Close to the percolation, giant electrostrictive coefficients are evidenced. Description and discussion of the present results are provided in the following sections. The first section of the article is devoted to the preparation and characterization of the samples. In the second section, we display the influence of the nature of the conductive particles (carbon nanotubes or reduced graphene oxide) on the dielectric properties at rest. The third section is devoted to the characterization of the dielectric properties under mechanical stress. Finally, the last part deals with the discussion of the data and includes some comments about potential applications.

MATERIALS AND CLASSICAL METHODS

Materials. The PDMS (polydimethylsiloxane), Sylgard 184, was purchased from Dow Corning as a kit of PDMS base and curing agent. The range of temperature for stable performances is −55 °C to 220 °C. This parameter is essential to avoid any degradation of the composite materials during the thermal reduction treatment of graphene oxide. The sodium dodecyl sulfate (SDS) was purchased from Sigma-Aldrich and used as received. The aqueous solution of the graphene oxide (GO) monolayers was purchased from Graphenea, and the GO concentration is about 0.4 *wt*%. The GO particles[22] are nonconducting. We first reduced them into reduced graphene oxide(rGO) using a chemical reduction. 50 mL of solution at 0.4 *wt* % was heated under reflux for 1 h at 110 °C in the presence of 120 mg of ascorbic acid and 10 g of Tween 60. The solution turns from brown to black. The surfactant Tween 60 allows us to stabilize the dispersion in water. The mean GO sheet size is about 2−3 μm.[13] The solution was centrifuged in order to increase the GO concentration. Centrifugation was performed with a Sorval RC 6+, rotor SE-12, centrifuge at 22000 rpm (i.e., 50 000*g*) for 45 min. After centrifugation, the supernatant was removed. The bottom phase that contains GO monolayers was collected. The solid content in the material was determined by dry extracts after evaporation of the water under vacuum at 100 °C. The mean final weight fraction of rGO was 5.8%. Thin multiwall CNTs (MWCNTs) were purchased from Nanocyl under the reference Nanocyl 7000 and used as received. The average diameter of the nanotubes is about 10 nm, and the average length is about 1.5 μm. Their dispersion was carried out in 10 mL flat-bottomed flasks by mixing 0.9 and 1.2 wt % of CNT and SDS. Tip sonication using a Branson Sonifier 450A is performed during 1 h at 20 W to unbundle and homogeneously disperse the CNTs. The sample is cooled down during sonication employing an ice bath. Carbon nanotubes were cut during the sonication treatment, and their length decreased down to an average length of about 500 nm.[23,24]

Preparation of the Sample. The present method consists of building networks of carbon based fillers in between emulsion droplets of cross-linked PDMS polymer. Direct emulsions are made of oil droplets dispersed in an aqueous phase (see Figure 1). As liquid drops

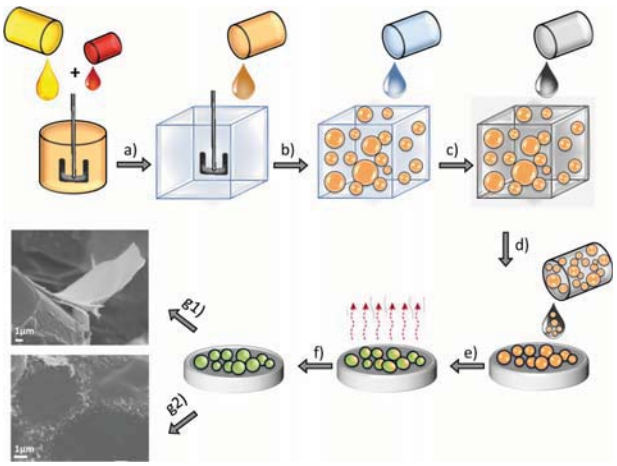


Figure 1. Scheme of the procedure allowing for the preparation of the sample.

are deformable, they can pack efficiently with a very small amount of remaining water continuous phase. The possibility to use water based dispersions which are well controlled and which can be stabilized with commercial surfactants is a major advantage of this approach. A mixture of PDMS and curing agent (10% in weight with respect to the PDMS phase) is first prepared as the oil phase. Emulsions are prepared by progressively adding the oil phase to an aqueous solution of SDS surfactant under mechanical stirring provided by a mechanical mixer (IKA Eurostar 40 digital). The gap between the paddle and inner wall of the container is about 7.5 mm. The surfactant weight fraction in the water phase is 4 wt %. Oil is added dropwise until its weight fraction reaches 85 wt %. Shear can be increased by raising the rotational speed of the mixer in order to form smaller droplets. The size of the obtained droplets is characterized using a Mastersizer Malvern 2000 particle size analyzer. Different mean droplets sizes were achieved by modifying the shear stress applied to the emulsion. The droplet sizes are broadly distributed using mechanical stirring. They range from 80 to 15 μm. In order to obtain smaller droplets, higher shear stress has to be applied to the emulsions. To this end, smaller emulsion droplets are produced using a Couette emulsification instrument.[25] The Couette mixer consists of a rotor stator system that enables the production of small

DOI: 10.1021/acs.langmuir.6b04185
Langmuir 2017, 33, 4528−4536

and monodisperse emulsions due to high shear induced droplet rupturing. In this method, a premixed emulsion of large, polydisperse droplets is first introduced into a syringe. The premixed emulsion is prepared manually. It is pushed by a piston into the gap between the rotor and the stator. The sheared monodisperse emulsion is recovered at the top of the mixer. The mean droplet size depends on the shear rate and on the oil volume fraction. Experimentally, we decided to shear emulsions at a fixed volume weight (85 wt %). Therefore, the obtained mean droplet sizes are ranging in between 20 and 5 μm. Once the desired mean droplet size is obtained, the emulsions are then gently mixed with a carbon based aqueous dispersion of CNTs or rGO. A previous study[21] has shown that the length of the filler and the droplet size have a significant influence on the dielectric properties of the material. We recall that the optimum formulation for high permittivity composites is achieved when the mean droplet size is about 10 times higher than the mean filler's length.[21] Accordingly, the mean droplet size of emulsions loaded with CNT (respectively rGO) is equal to 5 μm (rep.20 μm). In addition, the amount of fillers is varied in order to obtain different filler loadings in the final composites obtained after drying and curing. The emulsions loaded with the carbon based fillers are placed in circular homemade Teflon molds. The diameter of the Teflon molds is 38 mm. Solid materials are obtained by evaporating water from the emulsion and by curing the PDMS polymer. The obtained samples are under the form of elastomer disks with a black color. They look perfectly homogeneous on a macroscopic scale. In the GO situation and in order to obtain a comprehensive reduction of GO particles, the samples are heated at 200 °C for 2 h. We have checked that longer time or higher temperature do not change the values of the electronic properties suggesting that the reduction is optimal under this process.

Measurements of the Dielectric Properties at Rest. The alternating current (AC) electrical conductivity measurements were performed across the thickness of the molded disc samples of 38 mm in diameter and 0.38 mm in thickness. The sample is placed between two metallic disc electrodes that have the same diameter as the samples. The electrical conductivity was measured under a voltage of 100 mV applied in the frequency range of $10-10^6$ Hz using a computer-controlled impedance analyzer (Materials Mates 7260). A classical calibration procedure removing the contribution of the polarization of the electrodes[26] is used to determine the dielectric permittivity and the conductivity of the sample as a function of the frequency. All of the experiments are performed at room temperature.

Measurements of the Electrostrictive Coefficients. *Definition of the Electrostrictive Coefficient, Maxwell Stress, and Intrinsic Contribution.* Electrostriction is a property of all dielectrics due to the presence of electric domains randomly distributed inside the material. When an electric field is applied, each domain polarizes along the axis of the field. The opposing sides of the domains are oppositely charged and attract each other, causing a reduction in their size in the direction of the electric field (and jointly an extension of their dimensions perpendicular to the field in the proportions of the Poisson's coefficient). The resulting deformation is proportional to the square of the electric field modulus. Electrostriction must be distinguished from the inverse piezoelectric effect. Piezoelectricity is the property that certain bodies possess to electrically polarize under the action of a mechanical stress (direct piezzoelectric effect) and reciprocally to deform under the action of an electrical field (inverse piezzoelectric effect). The direct and inverse effects are inseparable. Electrostriction is an effect of the second order, proportional to the square of the electric field.[27,28] Thus, opposite electric fields create an identical deformation. Conversely, the piezoelectric effect is a linear effect, and the deformation is proportional to the electric field (first-order effect). Opposing electric fields therefore create opposite deformations in the piezoelectric situation. Moreover, if the inverse piezoelectric effect is always associated with the direct piezoelectric effect, there is no equivalent for electrostriction: an applied stress does not create any electrical polarization variation.

Electrostriction is generally defined as a quadratic coupling between strain (S_{ij}) and polarization (P_m) following eqs 1 and 2.

$$E_m = \epsilon'_{mn} P_n + 2Q_{klmn}\tau_{kl}P_n \tag{1}$$

$$S_{ij} = s_{ijkl}T_{kl} + Q_{ijmn}P_mP_n \tag{2}$$

s^P_{ijkl} is the elastic compliance, Q_{ijkl} is the polarization-related electrostriction coefficient, ϵ'_{jk} is the inverse of the linear dielectric permittivity in the absence of mechanical strain, τ_{kl} is the stress, and E_m the electric field. Assuming a linear relationship between the polarization and the electric field, the strain S_{ij} and electric flux density D_i are expressed as independent variables of the electric field intensity E_k, E_l, and stress τ_{kl} by the constitutive relationships according to eqs 3 and 4:

$$D_i = \epsilon_{ik}E_k + 2M_{ijkl}\tau_{kl}E_j \tag{3}$$

$$S_{ij} = s_{ijkl}\tau_{kl} + M_{ijkl}E_kE_l \tag{4}$$

ϵ_{ik} is the dielectric permittivity of the sample in the absence of mechanical strain. In the nonlinear dielectric systems situation, the M coefficients depend upon the electrical field, whereas Q coefficients do not. When an electric field is applied to a thin dielectric film, charges with different signs on two electrode sides will attract each other, resulting in a electrostatic force which is known as Maxwell stress. It is important to note at this stage that total electrostrictive strain originates from both electrostrictive effect and Maxwell effect. In the conductive sample situtation, the electrostrictive coefficients are complex numbers. This is the case in our study. In the following, we report the real part of the electrostrictive coefficient.

Measurements of the Dielectric Properties under Mechanical Stress: A Direct Determination of the Electrostrictive Coefficient M_{33}. The following paragraph is devoted to the development of a methodology to determine the intrinsic electrostrictive coefficient M_{33}. We consider a 3−3 situation, i.e., a geometry where the electrical field is applied along the 3 direction and the deformation is the compression measured along the 3 direction, i.e., S_{33}. We use two homemade metal electrodes that enable the study of the dielectric properties and application of the mechanical stress at the same time. The homemade aluminum electrodes of diameter 40 mm were equipped with a PVC-insulator adaptor. Its main role is to insulate the measurement performed by the electrode from the rest of the ZWICK 2.5 traction machine. This traction machine was used to measure the Young's modulus in quasi-static deformations. Not forgetting that it ensures a reliable mechanical contact with the force sensor and the steel base of the traction machine. The electrodes are connected to a Materials Mates 7260 impedance analyzer enabling the characterization of the impedances under mechanical stress imposed by the traction machine. The impedances under dynamic stress are studied at an electrical frequency (f = 100 Hz) at 0.1 V and following the typical compensation procedure. For all of the characterized samples, we apply a prestrain force of about 0.5 N. We note that the prestrain is to ensure a good electrical contact between the electrodes and the sample. An electrical contact is found when the force sensor detects a non-null positive force. We define a mechanical cycle as the mechanical step for which the strain increases from 0% to 8% and decreases back to 0% strain. This cycle is repeated successively 20 times and studied. The frequency of the mechanical measurement is 0.2 Hz. The measurements were carried out at room temperature of about 20 °C.

This setup allows a direct characterization of the intrinsic electrostrictive coefficient: we apply a mechanical stress and measure the modification of the impedances. We remind that the composite materials are modeled by an RC parallel circuit. The mechanical stress is controlled and cycled by a traction machine, inducing mechanical loads and unload cycles to the material. These cycles provoke an increase and decrease of the capacitance of the material. In addition, the traction machine enables the determination of the stress, strain, and Young's modulus during the entire experiment. Measurements of the dielectric properties are started at the same time as the mechanical cyclic loadings. Consequently, we can obtain the intrinsic change of capacitance in response to a stress τ_{33}. As $D_3 = \epsilon_{33}^{effective}E_3$, where $\epsilon_{33}^{effective}$ is the effective dielectric permittivity in the presence of strain, we get

DOI: 10.1021/acs.langmuir.6b04185
Langmuir 2017, 33, 4528−4536

Table 1. Evolution of Young's Modulus, ϵ_r at 100 Hz, $M_{33}^{Maxwell}$, and $M_{33}^{intrinsic}$ as a Function of the Concentration in Nanotubes[a]

% CNT	0.05	0.1	0.2	0.5	1	2
Y (kPa)	4×10^1	3.1×10^1	4.2×10^1	5.1×10^1	4.4×10^1	4×10^1
ϵ_r (100 Hz)	2×10^1	8×10^1	2.5×10^2	3×10^2	3×10^3	2×10^4
$M_{33}^{Maxwell}$ (100 Hz)	-4.45×10^{-15}	-2.2×10^{-14}	-5.2×10^{-14}	-5.2×10^{-14}	$-6.\ 0^{-13}$	-5×10^{-12}
$M_{33}^{intrinsic}$ (100 Hz)	-2×10^{-16}	-4×10^{-15}	-2×10^{-13}	-9×10^{-13}	-5×10^{-12}	$+10^{-12}$
$Q_{33}^{intrinsic}$ (100 Hz) (m^4C^{2-})	-6×10^3	-8×10^3	-4×10^4	-1.2×10^5	-710^3	$+ 1.5 \times 10^2$

[a] $M_{33}^{Maxwell}$ is estimated through $M_{33}^{\text{Maxwell}} = \frac{\epsilon_r \epsilon_o (1+2\nu)}{2Y}$, ν is the Poisson ratio and is taken to 0.5. $Q_{33}^{intrinsic} = M_{33}^{intrinsic}/\epsilon_o^2(\epsilon_r - 1)^2$. The samples were prepared using the emulsion process.

$\epsilon_{33}^{effective} = \epsilon_{33}^{Maxwell} + \epsilon_{33}^{intrinsic}$. $\epsilon_{33}^{Maxwell}$ is due to the variation the permittivity due to the geometrical variation of the distance between the two electrodes. Taking into account these geometrical corrections, we measure $\epsilon_{33}^{intrinsic}$ through the measurement of the impedance, and we get $M_{33}^{\text{intrinsic}} = \frac{\epsilon_{33}^{\text{intrinsic}} - \epsilon_{33}}{2\tau_{33}}$. Note that for nonlinear dielectrics,[28] the M coefficient depends upon the electrical field value. We will show in the following that it is not the case for our samples as the electrostrictive strain is a quadratic function of the electric field.

Measurements of the Dielectric Properties under Mechanical Stress: Determination of the Electrostrictive Coefficient M13 in Actuator Mode. The objective is to obtain the electrostrictive coefficient M_{13} of an emulsion based composite by analyzing the bending of a system made of stacked layers in response to an electrical field. The two outer layers (i.e., layers 2 and 3) act as compliant electrodes. They are made of gold using a coating sputtering technique. Their thickness is 2 μm. Layer 1 is composed of the emulsion based electrostrictive material. Layer 4 is prepared with a pure dielectric PDMS neat polymer. Layers 1 and 4 are expected to respond differently to the electric field. If individually considered, both layers would be compressed in their thickness and expand laterally under an electrical field, but here, the two layers are mechanically coupled. One will expand, whereas the second one will contract or at least display a smaller expansion compared to that of the other layer, resulting in a bending of the whole system. The bending is in fact dictated by the layer that has the greater electrical energy. This dominant layer is layer 1 because of its much greater permittivity compared to that of layer 4. h_1, h_2, h_3, and h_4 are the thicknesses of the layers, b_1, b_2, b_3, and b_4 are the widths of the layers, and L is the length of the layers at rest. We note that the PDMS base and curing agent ratio for layer 4 is modified to a 7:1 ratio. The ratio used for the electrostrictive material is 10:1. The difference of ratios between the two layers enable a better adhesion of the two inner layers of the stack and prevent possible delamination problems upon bending. A mechanics model is used to calculate the electrostrictive coefficient M_{13} from the induced curvature K, and the mechanical properties of the four-layer material A setup that are reminiscent of those commonly used to characterize electrostrictive coefficients M_{13} of polymer films were implemented. The strip composite material is subjected to a triangular AC electric field, produced by a TTi-TGA 1230 waveform generator and amplified by a TREK high voltage amplifier model 609 $\times 10^{-6}$. We used plastic tweezers to hold the sample and the electrodes. A high voltage is applied between the two copper electrodes. The voltage was kept below 1.5 V/μm to avoid air and dielectric breakdown. The strip composite material is enlightened by a light emitting diode, LED, to ensure a reliable video recording. The bending of the strip composite material induced by the electric field is monitored by a PHANTOM high speed camera MR110. The influence of the frequency was evaluated in the range of 0.5 Hz−10 Hz under electrical fields ranging from 0 to 1.5 V/μm. As explained above, the strain induced by the electric field is the result of two mechanisms: the Maxwell stress and the true electrostriction. The effective electrostriction coefficient M_{13} is given by $S_{13} = M_{13}E_3^2$ (9), where S_{13} is the induced in plane strain of the electrostrictive layer 1. E_3 is the applied electric field perpendicular to the plane. The applied electric field is given by $E_3 = \frac{V}{h1 + h4}$, where V is the voltage applied between the compliant electrodes 2 and 3. From the tip displacement (w), the curvature of the film K is measured, $K = 2w/L^2$. The electrostrictive coefficient of the layer 1 is obtained through the following equations:[18]

$$M_{13} = \frac{S_{11}(h1 + h4)^2}{V^2} \tag{5}$$

$$S_{11} = \frac{-KN1^2}{(2Y_1b_1h_1Den)} + \frac{2KG(A + B + C + D)}{3Y_1b_1h_1Den} \tag{6}$$

$$N_1 = (Y_1b_1h_1(h_1 + 2h_3) + Y_2b_2h_2(2h_1 + h_2 + 2h_3 + 2h_4) + Y_3b_3h_3^2 + Y_4b_4h_4(2h_1 + 2h_3 + h_4))^2 \tag{7}$$

$$Den = (Y_2b_2h_2(h_1 + h_2 + 2h_4) - Y_3b_3h_3(h_1 + h_3) + Y_4b_4h_4(h_1 + h_4)) \tag{8}$$

$$A = Y_1b_1h_1(h_1^2 + 3h_1h_3 + 3h_3^2) \tag{9}$$

$$B = Y_3b_3h_3^3 \tag{10}$$

$$C = Y_4b_4h_4(3h_1^2 + 3h_3^2 + h_4^2 + 6h_1h_3 + 3h_1h_4 + 3h_3h_4) \tag{11}$$

$$D = Y_2b_2h_2(3h_1^2 + h_2^2 + 3\cdot h_3^2 + 3\cdot h_4^2 + 3h_1h_2 + 6h_1h_3 + 6h_1h_4 + 6h_3h_4 + 3h_2(h_3 + h_4)) \tag{12}$$

$$G = Y_1b_1h_1 + Y_2b_2h_2 + Y_3b_3h_3 + Y_4b_4h_4 \tag{13}$$

In our set up, the thickness of the gold electrodes $h_3 = h_2$ is equal to 2 μm, the thickness of the active material h_1 is equal to 70 μm for the 0.1% CNT sample, 74 μm for the 0.2% CNT sample, and 75 μm for the 0.5% CNT sample, and the thickness of the PDMS layer is set to h_4 = 400 μm. The Young's modulus of the gold electrodes is equal to 83 GPa, and the Young's modulus of the PDMS pure layer is equal to 3.5 MPa. The Young's modulus of the investigated samples is reported in Table 1.

RESULTS

Measurements at Rest. *Polymer CNT Composites.* We study the dielectric properties of the electrostrictive materials used at rest for comparisons with the dynamic measurements. Figure 2 a shows the electric conductivity as a function of the frequency for different CNT samples. The electrical conductivity shows three regimes as a function of the CNT concentration. First, for CNT concentrations below the percolation threshold, the conductivity is characterized by a frequency dependence. It is observed for samples loaded with less than 0.1 wt %. This behavior arises from dielectric losses due to bound charges. Second, for CNT concentrations largely higher than the percolation threshold (i.e., 2 wt %), the sample is frequency independent since the conductivity is dominated by free-charges. The third case is for CNT concentrations around the percolation threshold. At high frequencies, the

DOI: 10.1021/acs.langmuir.6b04185
Langmuir 2017, 33, 4528−4536

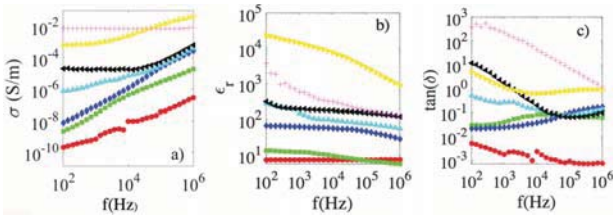


Figure 2. (a) Evolution of the conductivity as a function of the frequency for various CNT concentrations. 0%*wt* (red circles), 0.05% *wt* (green squares), 0.1%*wt* (blue diamond), 0.2%*wt* (cyan up triangle), 0.5%*wt* (black left triangle), 1%*wt* (yellow right triangle), and 2%*wt* (magenta cross). (b) Evolution of the dielectric permittivity as a function of the frequency for various concentrations (same symbols as in panel a). (c) Evolution of the $\tan(\delta) = \frac{\sigma}{\epsilon_r \epsilon_0 2\pi f}$ as a function of the frequency for various CNT concentrations (same symbols as in panel a).

conductivity is dominated by dielectric losses due to bound charges, while at low frequencies the conductivity is driven by the transport of free charges brought by the CNTs. The electrical conductivity at 100 Hz varies between 10^{-8} S/m at 0.1 wt % and 10^{-5} S/m at 0.5 wt %. The relative dielectric permittivity ϵ_r, (see Figure 2b) remains constant on almost the entire frequency range for the samples loaded with 0, 0.05, and 0.1 wt % CNT. By contrast, the permittivity of the samples loaded with 0.2 wt %, 0.5 wt % 1 wt %, and 2% wt presents frequency dependences. The addition of conductive particles, such as CNTs, to a dielectric matrix enhances the interfacial polarization leading to an increase of the permittivity. We note that the relative permittivity values are broad and range from 10 to 10^4 depending on the CNT concentration at 100 Hz. The permittivity increases with the CNT concentration within the range of 0 to 1 wt % CNT, as a result of the formation of microcapacitors made of neighboring clusters of nanotubes. The permittivity of the 2 wt % CNT, above the percolation threshold, decreases because of shorts between the previously mentioned microcapacitors

Polymer rGO Composites. Figure 4 displays the electric conductivity as a function of the frequency for different rGO samples. The electrical conductivity increases as a function of the rGO concentration. The percolation threshold is reached for a weight fraction of about 0.8%, i.e., for an 8 times higher concentration than for the CNTs. The variation of the percolation threshold is due to the shape of the rGO particles. The platelets are known to exhibit an isotropic- nematic transition at low concentration below the percolation transition. Correlations of orientations of the platelets lower in fact their contact probability which results in a greater percolation threshold.[13,29] This analysis is confirmed by electronic microscopy pictures that point out the lamellar phase structure of the rGO between the droplets (see Figure3).

Above the percolation threshold, the frequency dependences differ from the ones measured in CNT samples. For all of the rGO samples, the conductivity depends upon the frequency, and no Plateau is evidenced even at low frequencies. The conductivity varies as f^{α} with α comprised between 0.26 and 0.33. This behavior suggests a large contribution of dielectric losses to the conductivity. These materials are less conductive than the ones containing CNTs. 4% wt of rGO is required to get a conductivity equivalent to the one of materials containing 1% wt of CNT at 100 Hz. As for the samples loaded with CNTs,[21] huge permittivity values are reached. We note, however, that by contrast to the CNT polymer composites, the permittivity increases as a function of the rGO concentration. No maximum is evidenced at the percolation or above the percolation. This behavior might be explained by the presence of large conductive clusters which remain not connected with the main conductive percolated network.

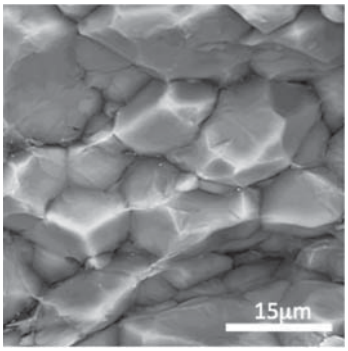


Figure 3. Electronic microscopy pictures of rGO composites.

Measurements under Mechanical Stress. *Polymer CNT Composites and Measurement of M_{33}.* The following section is devoted to the study of electrostrictive materials under mechanical stress. The sample is subjected to mechanical stress that is cycled several times. The mechanical frequency is equal to 0.2 Hz. The applied stress is situated within the linear elastic region, and its maximal value corresponds to an 8% strain. The linear elastic region ranges between 0% and 12% of mechanical strain. The quasi static values of the Young's modulus as a function of the CNT concentration are reported in Table. 1.

The absolute values of the electrostriction coefficients measured at 100 Hz (frequency of the electrical current) are shown in Figure 5 as a function of the CNT concentration. The electrostrictive coefficient value is negative and increases as a function of the filler weight fraction up to 1% in charge. For 2% and above the percolation threshold, the electrostrictive coefficient value is positive. The material is not purely dielectric and behaves differently from near percolated materials. The permittivity decreases when the sample is compressed and increases when the stress is released. In other words, the sign of the electrostriction coefficient is opposite to the one of nonpercolated and near-percolated networks. The compression may create new contacts between nanotubes and thus decrease the number of microcapacitors inside the sample. The obtained values at 100 Hz range between $M = -4 \times 10^{-15}$ m^2 V^{-2} for c = 0.1%, $M = -10^{-13}$ m^2 V^{-2} for c = 0.2%, and $M = -10^{-11}$ m^2 V^{-2} for c = 1 wt %. The conductivity of the sample for c = 0.1 wt % is 10^{-8} S/m, for c = 0.2 wt % 10^{-6} S/m, and for c = 1 wt % is 10^{-4} S/m. We stress that these values are actual direct measurements and not a calculated or extrapolated value. The sample for which the CNT concentration is near the percolation threshold (1 wt % CNT) yields the highest permittivity values.

The electrostrictive coefficient M_{33} of the latter sample is also the greatest and of about 10^{-11} m^2 V^{-2} at 100 Hz. The average value is calculated based on two different batches and for samples tested at 0.5 mm/min. We report two different values for M_{33} in the 1 wt % CNT situation. These variations seem to be related to the use of two different CNT batches. Slight differences of structure and chemical nature are enhanced in the percolation region, but even the lowest measured values remain exceptionally high and above previously reported values for

DOI: 10.1021/acs.langmuir.6b04185
Langmuir 2017, 33, 4528−4536

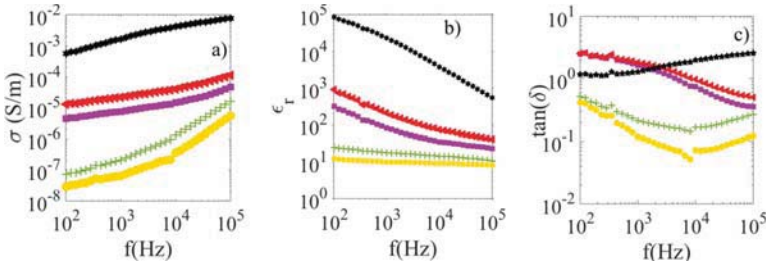


Figure 4. (a) Evolution of the conductivity as a function of the frequency for various concentrations. 0.6%*wt* (yellow circle), 0.8%*wt* (green crosses), 0.1%*wt* (purple square), 1.8%*wt* (red left triangle), 4%*wt* (black star). (b) Evolution of permittivity as a function of the frequency for various rGO concentrations (same symbols as in panel a). (c) Evolution of tan(δ) as a function of the frequency for various rGO concentrations (same symbols as in panel a).

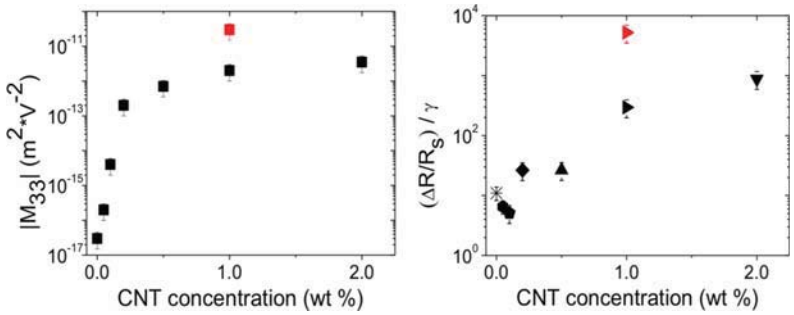


Figure 5. Left: Evolution of the absolute value of the electrostrictive coefficient M_{33} as a function of the CNT concentration. Right: Evolution of the gauge factor coefficient GF = $\frac{R-R_s}{R_s\gamma}$ as a function of the CNT concentration.

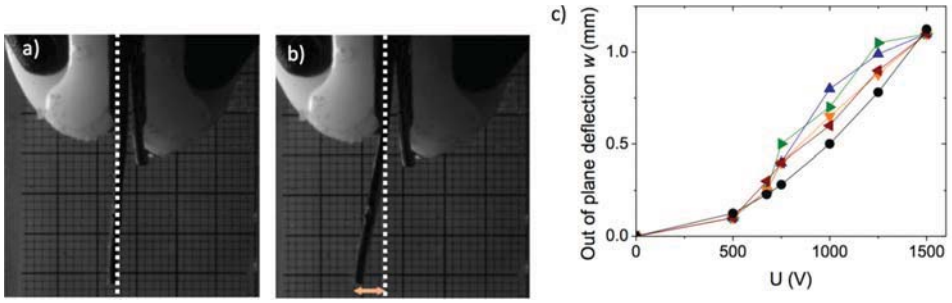


Figure 6. Comparison of the deflection of the bilayer composite tip under different voltages. Image a corresponds to U = 0 V, while b corresponds to U = 1000 V. The out of plane deflection w (pink arrow) enables the determination of the electrostrictive coefficient M13. The small squares are 1 mm per side. (c) The out of plane deflection of strip composites as a function of the applied voltage at different electrical frequencies for a 0.2*wt* % CNT composite: The up triangle corresponds to 0.5 Hz, the right triangle to 1 Hz, the down triangle to 2.5 Hz, the left triangle to 7.5 Hz, and the black circles to the square of the applied electric field. The thickness of the composite is equal to 450 μm, and its length is equal 3 cm.

related materials. It corresponds to an improvement of about an order of magnitude compared to the previous highest reports by Deshmukh et al.[19] and about 3 orders of magnitude in comparison with most data in the literature dealing with dielectric composites. Note that these samples have the same conductivity 10^{-3} S/m than the ones prepared by Deshmukh et al.[19] We note that the reported $Q_{33}^{intrinsic}$ values are much higher than the one reported for ceramics typically around[30] 0.05 m^4C^{2-} and PVDF[31] of 13.5 m^4C^{2-}.

Looking for the best compromise between a low conductivity and a high electrostrictive coefficient, we find that the range of CNT weight fractions comprised between 0.1% and 0.2% is the best suited. The obtained results are comparable or 1 order of magnitude higher than the ones reported in the literature[18] for comparable and even lower frequencies. It is important to note here that our data correspond to an electrical frequency of 100 Hz and a mechanical frequency of 0.2 Hz.

The achievement of high values of electrostrictive coefficients comes with the appearance of piezoresistivity. The resistivity of the sample indeed varies as a function of the compression. It decreases when the sample is compressed, and the sample exhibits negative piezoresistivity. Figure 5 displays the evolution of the gauge factor GF = $\frac{R-R_s}{R_s\gamma}$ as a function of the nanotube weight fraction, where R_s is the value of the strained sample and R the initial value. The gauge factor GF increases from 1 to more than 1000 above the percolation threshold. The latter value is about 1 order of magnitude higher than the best one already obtained. Metals strain gauges typically exhibit gauge factors in the range of 0.8−3. Another common type of strain sensor is the piezoresistive single crystal silicon strain sensor

DOI: 10.1021/acs.langmuir.6b04185
Langmuir 2017, 33, 4528−4536

compatible with the CMOS process and owing to a high gauge factor up to 135. However, these sensors are more expensive and more fragile than foil polymer based gauges. In addition, they are not suitable for flexible strain sensing applications. Note that a full validation of the sensor applications would require further characterizations, including studies of cycling repeatability, reversibility, linear, or nonlinear calibration.

Polymer CNT Composites and Measurement of M_{13}. The following section is devoted in the first place to the determination of the electrostrictive coefficient M_{13} as commonly done in the literature. Second, we will compare these values to the ones obtained using the more direct methodology. We anticipate that the aim of this section is not to give a comprehensive study of the actuator properties of our samples but rather to check the validity of the above data by making a separate measurement.

We study the deflection of the strip material when the electric field E is applied. The typical applied values for E are about 1 V/μm and lead to the displacement of the strip. The bending is the result of the compression and expansion of the different layers when the electric field is applied. The strip deflection is determined using a millimeter range sheet placed behind the strip. In order to verify the electrostrictive behavior of the nanocomposites, we measure the actuation response as a function of the amplitude of the electrical field.

Figure 6 shows the displacement of the strip as a function of the voltage U for a nanocomposite loaded with 0.2 wt % CNT. The displacement of the strip is proportional to U^2 regardless of the frequency. We attribute the slight differences from theoretical quadratic curves corresponding to uncertainties in the measurements of the maximal displacement itself. Henceforth, using the tip deflection we are able to determine the electrostrictive coefficient of the nanocomposite following eq 4. Figure 7 displays the results obtained as a function of the concentration.

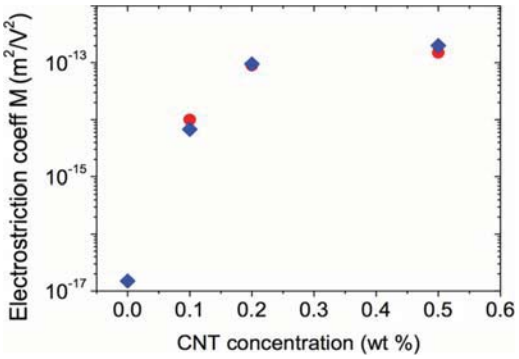


Figure 7. Comparison of the electrostrictive coefficient determined by two different setups for different CNT concentrations. The blue diamonds correspond to the direct compression setup (M33), while the red circles correspond to the actuator setup (M13).

We note a very good agreement between both measurements, suggesting first that our samples respond in a isotropic way, i.e., that $M_{13} = M_{33}$ and that second the Maxwell stress has a low contribution in our sample. We recall that in this geometry, we measure the sum of the Maxwell contribution and of the intrinsic contribution. This last point is not surprising since our samples have a rather large Young's modulus and a large $\Delta\epsilon_r$ (Table 2). This is in perfect agreement with the values $M_{33}^{Maxwell}$ calculated through $M_{33}^{\mathrm{Maxwell}} = \frac{1+2\nu}{2}\frac{\epsilon_r\epsilon_0}{Y}$ with ν the Poisson Coefficient and Y the Young's modulus shown in Table 1.

Polymer rGO Composites and the Measurement of M_{33}. As in the previous section, the properties are measured using a 8% strain in the mechanical linear regime. On the contrary to the polymer CNT composites, M_{33} values are always negative whatever the concentration of rGO (Figure 8). Values as high as 3×10^{-13} m^2 V^{-2} at 100 Hz are measured for c = 4%. This value comes with a conductivity equal to 10^{-3} S/m. The value of $\tan(\delta)$ is equal to 1 at 100 Hz. By contrast to CNT, very little piezoresistivity is observed for rGO materials. We note that the performances of these material remain more classical and not as promising as the ones obtained with CNTs. We also note that the intrinsic response is very close to the Maxwell response which was not the case for CNT composites.

■ DISCUSSION AND CONCLUSION

We have studied the dielectric properties of polymer nanocomposites at rest and under deformation. We have developed a device to directly measure the electrostrictive properties of the material. The polymer nanocomposites have been prepared using an emulsion pathway. This procedure allows us to disperse homogeneously the conductive charges in the sample. Even though it is good, this dispersion is not perfect, and finite size effects are observed. In the domain of the percolation threshold, some continuous carbon particle paths between the electrodes coexist with some large aggregates. Huge dielectrical permittivity and intermediate resistivity values are thus measured in this region. A number of effects at a microscopic level result from the imposed mechanical deformation. The distance between CNTs or rGO platelets can change in not always intuitive ways,[32] potentially leading to increases or decreases of conductivity and permittivity depending on the concentration of particles and on their structuration in the matrix. Also pressure changes between the contacting particles and changes of orientation can strongly alter the electrical properties of the nanocomposites. A clear identification of the presently involved dominant mechanisms is still missing. The properties obtained with CNTs[21] in terms of electrostrictive coefficients are more interesting than the one obtained with rGO. Nevertheless, the experimentally measured properties make the present materials suited for many applications. First, we note that the properties obtained with CNTs[21] in terms of electrostrictive coefficients are more interesting than the ones obtained with rGO. In the low filler concentration situation (i.e., less than 0.2% in weight), our materials are suited for energy harvesting from mechanical noise. They display performances comparable to or 1 order of magnitude better than in those in the literature at a frequency of 100 Hz, a typical relevant frequency for energy harvesting. In the high filler concentration situation, the values of the electrostrictive coefficients are giant. However, they come with a high value of conductivity (typically higher than 10^{-4} S/m). This makes them unsuitable for energy harvesting in spite of their giant electrostrictive response. Indeed, building an autonomous device requires very low losses in order to avoid discharging during the action phases. Unfortunately, this drawback is shared by most of nanocomposites reported in the literature. To bypass this drawback, it is thus mandatory to reduce the value of the conductivity at least around 10^{-7} S/m. In order to do so, the use of inverse emulsion to prepare the sample might be an

DOI: 10.1021/acs.langmuir.6b04185
Langmuir 2017, 33, 4528−4536

Table 2. Evolution of the Young Modulus, ϵ_r at 100 Hz, $M_{33}^{Maxwell}$, and $M_{33}^{intrinsic}$ as a Function of the Concentration in rGO[a]

% rGO	0.6	0.9	1,4	1,8	4
Y (kPa)	10^2	2.1×10^1	2.7510^2	3×10^2	9.510^1
ϵ_r (100 Hz)	1.23×10^1	4.1×10^1	3.18×10^2	9.09×10^2	7.99×10^4
$M_{33}^{Maxwell}$ (100 Hz)	-1.09×10^{-15}	-1.74×10^{-14}	-1.02×10^{-14}	-2.68×10^{-14}	$-7.42\ 10^{-12}$
$M_{33}^{intrinsic}$ (100 Hz)	-4.79×10^{-16}	-4.75×10^{-15}	-1.51×10^{-14}	-6.11×10^{-15}	-1.8^{-13}
$Q_{33}^{intrinsic}$ (100 Hz) (m^4C^{2-})	-4.77×10^4	-3.74×10^3	-1.9110^3	-9.46×10^1	-3.61^{-1}

[a] $M_{33}^{Maxwell}$ is estimated through $M_{33}^{\text{Maxwell}} = \frac{\epsilon_r \epsilon_o (1+2\nu)}{2Y}$, ν is the Poisson ratio and is taken to 0.5. $Q_{33}^{intrinsic} = M_{33}^{intrinsic}/\epsilon_o^2(\epsilon_r - 1)^2$. The samples were prepared using the emulsion process.

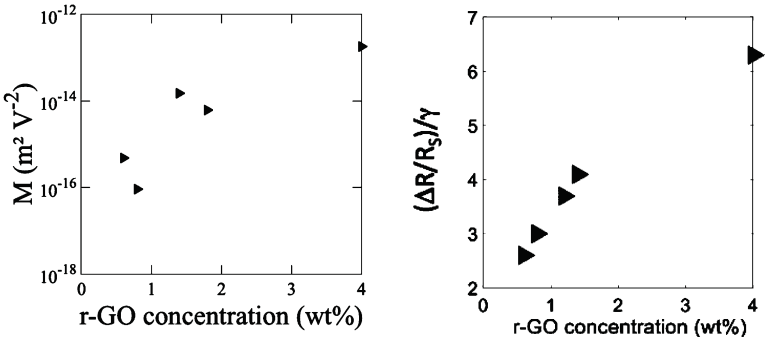


Figure 8. Left: Evolution of the absolute value of the electrostrictive coefficient M_{33} as a function of the rGO weight fraction, Right: Evolution of the gauge factor coefficient GF= $\frac{R-R_s}{R_s\gamma}$ as a function of the rGO weight fraction.

appropriate approach. Work along this axis is in progress. It will allow us to confine the conductive particles inside droplets and to avoid many contacts and losses. However, the giant electrostriction of the present nanocomposites makes them very promising for other applications including in particular capacitive sensors and actuators. In addition, the values of the piezoresistivity measured in the high filler concentration situation are at least an order of magnitude greater than the one reported in the literature. This opens the path to use these materials for stress or strain sensor applications considering their giant responses to mechanical deformations.

AUTHOR INFORMATION

Corresponding Author

*Phone: +33 0 1 40 79 47 45. E-mail: annie.colin@espci.fr.

ORCID

Jinkai Yuan: 0000-0003-2347-5191

Annie Colin: 0000-0001-8372-006X

Notes

The authors declare no competing financial interest.

REFERENCES

(1) Ajayan, P. M.; Schadler, L. S.; Braun, P. V. *Nanocomposite Science and Technology*; John Wiley & Sons: New York, 2006.

(2) Li, J.; Ma, P. C.; Chow, W. S.; To, C. K.; Tang, B. Z.; Kim, J.-K. Correlations between percolation threshold, dispersion state, and aspect ratio of carbon nanotubes. *Adv. Funct. Mater.* **2007**, *17*, 3207–3215.

(3) Efros, A. L.; Shklovskii, B. I. Critical Behaviour of Conductivity and Dielectric Constant near the Metal-Non-Metal Transition Threshold. *Phys. Status Solidi B* **1976**, *76*, 475.

(4) Zhao, X.; Suo, Z. Electrostriction in elastic dielectrics undergoing large deformation. *J. Appl. Phys.* **2008**, *104*, 123530.

(5) Guyomar, D.; Lebrun, L.; Putson, C.; Cottinet, P. J.; Guiffard, B.; Muensit, S. Electrostrictive energy conversion in polyurethane nanocomposites. *J. Appl. Phys.* **2009**, *106*, 014910.

(6) Cottinet, D.; Guyomar, P.; Guiffard, J.; Putson, C. B.; Lebrun, L. Modeling and Experimentation on an Electrostrictive Polymer Composite for Energy Harvesting. *Ieee Transactions on Ultrasonics Ferroelectrics and Frequency Control* **2010**, *57*, 774–784.

(7) Fiorido, T.; Galineau, J.; Salles, L.; Seveyrat, V.; Belhora, F.; Cottinet, P. J.; Hu, L.; Liu, B.; Guiffard, Y.; Bogner-Van De Moortele, A.; Epicier, T.; Guyomar, D.; Brioude, A. Bifunctional organic/inorganic nanocomposites for energy harvesting, actuation and magnetic sensing applications. *Sens. Actuators, A* **2014**, *211*, 105.

(8) Guyomar, D.; Cottinet, P. J.; Lebrun, C.; Putson, L.; Yuse, K.; Kanda, M.; Nishi, Y. The compressive electrical field electrostrictive coefficient M33 of electroactive polymer composites and its saturation versus electrical field, polymer thickness, frequency, and fillers. *Polym. Adv. Technol.* **2012**, *23*, 946–950.

(9) Jaaoh, D.; Putson, N.; Muensit, C. Enhanced strain response and energy harvesting capabilities of electrostrictive polyurethane composites filled with conducting polyaniline. *Compos. Sci. Technol.* **2016**, *122*, 97.

(10) Jomaa, M. H.; Masenelli-Varlot, K.; Seveyrat, L.; Lebrun, L.; Jawhar, M. C. D.; Beyou, J. Y.; Cavaille, E. Investigation of elastic, electrical and electromechanical properties of polyurethane/grafted carbon nanotubes nanocomposites. *Compos. Sci. Technol.* **2015**, *121*, 1–8.

(11) Seveyrat, L.; Chalkha, A.; Guyomar, D.; Lebrun, L. Preparation of graphene nanoflakes/polymer composites and their performances for actuation and energy harvesting applications. *J. Appl. Phys.* **2012**, *111*, 104904.

(12) He, F.; Lau, S.; Chan, H. L.; Fan, J. High dielectric permittivity and low percolation threshold in nanocomposites based on poly (vinylidene fluoride) and exfoliated graphite nanoplate. *Adv. Mater.* **2009**, *21*, 710–715.

(13) Yuan, J.; Luna, A.; Neri, W.; Zakri, C.; Schilling, T.; Colin, A.; Poulin, P. Graphene liquid crystal retarded percolation for new high-k materials. *Nat. Commun.* **2015**, *6*, 8700.

(14) Li, Q.; Xue, Q.; Hao, L.; Gao, X.; Zheng, Q. Large dielectric constant of the chemically functionalized carbon nanotube/polymer composites. *Compos. Sci. Technol.* **2008**, *68*, 2290–2296.

(15) Grossiord, N.; Kivit, P. J.; Loos, J.; Meuldijk, J.; Kyrylyuk, A. V.; van der Schoot, P.; Koning, C. E. On the influence of the processing

DOI: 10.1021/acs.langmuir.6b04185
Langmuir 2017, 33, 4528–4536

conditions on the performance of electrically conductive carbon nanotube/polymer nanocomposites. *Polymer* **2008**, *49*, 2866−2872.
(16) Wongtimnoi, K.; Guiffard, B.; Bogner-van de Moortele, A.; Seveyrat, L.; Gauthier, C.; Cavaillé, J.-Y. Improvement of electrostrictive properties of a polyether-based polyurethane elastomer filled with conductive carbon black. *Compos. Sci. Technol.* **2011**, *71*, 885−892.
(17) Park, C.; Ounaies, Z.; Watson, K. A.; Crooks, R. E.; Smith, J.; Lowther, S. E.; Connell, J. W.; Siochi, E. J.; Harrison, J. S.; St Clair, T. L. Dispersion of single wall carbon nanotubes by in situ polymerization under sonication. *Chem. Phys. Lett.* **2002**, *364*, 303−308.
(18) Park, C.; Kang, J. H.; Harrison, J. S.; Costen, R. C.; Lowther, S. E. Actuating single wall carbon nanotube−polymer composites: intrinsic unimorphs. *Adv. Mater.* **2008**, *20*, 2074−2079.
(19) Deshmukh, S.; Zoubeida, O. Single walled carbon nanotube (SWNT)−polyimide nanocomposites as electrostrictive materials Âż. *Sens. Actuators, A* **2009**, *155*, 246−52.
(20) Lallart, M.; Cottinet, P.-J.; Guyomar, D.; Lebrun, L. Electrostrictive polymers for mechanical energy harvesting. *J. Polym. Sci., Part B: Polym. Phys.* **2012**, *50*, 523−535.
(21) Luna, A.; Yuan, J.; Néri, W.; Zakri, C.; Poulin, P.; Colin, A. Giant Permittivity Polymer Nanocomposites Obtained by Curing a Direct Emulsion. *Langmuir* **2015**, *31*, 12231−12339.
(22) Huang, X.; Yin, Z.; Wu, S.; Qi, X.; He, Q.; Zhang, Q.; Yan, Q.; Boey, F.; Zhang, H. Graphene-based materials: synthesis, characterization, properties, and applications. *Small* **2011**, *7*, 1876.
(23) Lucas, A.; Zakri, C.; Maugey, M.; Pasquali, M.; van der Schoot, P.; Poulin, P. Kinetics of nanotube and microfiber scission under sonication. *J. Phys. Chem. C* **2009**, *113*, 20599−20605.
(24) Pagani, G.; Green, M. J.; Poulin, P.; Pasquali, M. Competing mechanisms and scaling laws for carbon nanotube scission by ultrasonication. *Proc. Natl. Acad. Sci. U. S. A.* **2012**, *109*, 11599−11604.
(25) Mason, T. G.; Bibette, J. Shear rupturing of droplets in complex fluids. *Langmuir* **1997**, *13*, 4600−4613.
(26) Alibert, I.; Coulon, C.; Bellocq, A.; Gulik-Krzywicki, T. Dielectric study of the dilute part of a SDS/brine/alcohol system: A new sequence of phases? *EPL (Europhysics Letters)* **1997**, *39*, 563.
(27) Newnham, R.; Sundar, V.; Yimnirun, R.; Su, J.; Zhang, Q. Electrostriction: nonlinear electromechanical coupling in solid dielectrics. *J. Phys. Chem. B* **1997**, *101*, 10141−10150.
(28) Li, F.; Jin, L.; Xu, Z.; Zhang, S. Electrostrictive effect in ferroelectrics: An alternative approach to improve piezoelectricity. *Appl. Phys. Rev.* **2014**, *1*, 011103.
(29) Mathew, M.; Schilling, T.; Oettel, M. Connectivity percolation in suspensions of hard platelets. *Phys. Rev. E* **2012**, *85*, 061407.
(30) Jin, L.; Huo, R.; Guo, R.; Li, F.; Wang, D.; Tian, Y.; Hu, Q.; Wei, X.; He, Z.; Yan, Y.; et al. Diffuse Phase Transitions and Giant Electrostrictive Coefficients in Lead-Free Fe3+-Doped 0.5 Ba (Zr0. 2Ti0. 8) O3−0.5 (Ba0. 7Ca0. 3) TiO3 Ferroelectric Ceramics. *ACS Appl. Mater. Interfaces* **2016**, *8*, 31109−31119.
(31) Zhang, Q. M.; Bharti, V.; Zhao, X. Giant Electrostriction and Relaxor Ferroelectric Behavior in Electron-Irradiated Poly(vinylidene fluoride-trifluoroethylene) Copolymer. *Science* **1998**, *280*, 2101.
(32) Grillard, F.; Jaillet, C.; Zakri, C.; Miaudet, P.; Derre, A.; Korzhenko, A.; Gaillard, P.; Poulin, P. Conductivity and percolation of nanotube based polymer composites in extensional deformations'. *Polymer* **2012**, *53*, 183−187.

DOI: 10.1021/acs.langmuir.6b04185
Langmuir 2017, 33, 4528−4536

IOP Publishing *Multifunct. Mater.* **00** (2018) 000000

Multifunctional Materials



RECEIVED
19 October 2017

REVISED
8 February 2018

ACCEPTED FOR PUBLICATION
28 February 2018

PUBLISHED
DD MM 2018

PAPER

Microporous electrostrictive materials for vibrational energy harvesting

Mickaël Pruvost[1], Wilbert J Smit[1], Cécile Monteux[1], Philippe Poulin[2] and Annie Colin[1,2]

[1] ESPCI Paris, PSL Research University, CNRS, Laboratoire Sciences et Ingénierie de la Matière Molle, UMR 7615, 10 rue Vauquelin, F-75231 Paris cedex 05, France

[2] Centre de Recherche Paul Pascal, CNRS, Université de Bordeaux, 115 Avenue Schweitzer, F-33600 Pessac, France

E-mail: annie.colin@espci.fr

Keywords: energy harvesting, polymers, electrostriction, capacitive sensors, electrostrictive material

Supplementary material for this article is available online

Abstract

We present electrostrictive materials with excellent properties for vibrational energy harvesting applications. The developed materials consist of a porous carbon black composite, which is processed using water-in-oil emulsions. In combination with an insulating layer, the investigated structures exhibit a high effective relative dielectric permittivity (up to 182 at 100 Hz) with very low effective conductivity (down to 2.53 10^{-8} S m^{-1}). They can generate electrical energy in response to mechanical vibrations with a power density of 0.38 W m^{-3} under an applied bias electric field of 32 V. They display figures or merit for energy harvesting applications well above reference polymer materials in the field, including fluorinated co- and ter-polymers synthetized by heavy chemical processes. The production process of the present materials is based on non hazardous and low-cost chemicals. The soft dielectric materials are highly flexible (Young's modulus of ~1 MPa) making them also suited for highly sensitive capacitive sensors.

1. Introduction

The Internet of Things (IoT) is a new and fast growing concept which aims at connecting everyday physical objects into the Internet without any human interaction [1, 2]. The IoT requires the usage of numerous wireless sensors. Providing the electrical energy to run these wireless sensors is of major concern. Use of batteries with limited lifetime is a severe constraint. To overcome this problem, several environmental energy sources such as thermal, solar, salinity gradients, vibrations can be used to fulfil energy demands [3–5]. It could thus make sensors, MEMS, communicating devices, etc self-sufficient in energy supply and as-such highly increase their life time. A promising method to resolve this challenge is to harvest mechanical energy from the ambient environment and convert it into electrical power. An apparently convenient method consists in using piezoelectric materials. The most efficient piezoelectric ceramics can produce up to 0.2–30 mW cm^{-1} [6–9]. However, these materials are stiff and brittle which limits their implementation in embedded applications [10]. Triboelectric nanogenerators have recently demonstrated volume power densities up to 0.49 W cm^{-3} [11, 12]. However, their performances are largely affected by the environment such as humidity [12]. Moreover, their low durability as a result of two materials in physical friction is still a limiting factor [11]. A more recent approach consists in using electrostrictive polymers to convert energy from mechanical vibrations [13–19]. These polymers have high dielectric permittivity and are used as the dielectric layer inside variable capacitors. Capacitance variations in response to mechanical variations are enhanced by changes of dielectric permittivity of the electrostrictive polymers. This principle can be used to convert mechanical energy of vibrations into electrical energy. The interest in electrostrictive polymers is rapidly growing because polymer-based high-permittivity materials are flexible, low cost, and easily tunable, which makes them good candidates for IoT applications. A recent approach for obtaining high permittivity electrostrictive polymers is the use of polymers loaded with conductive nanoparticles [15–19]. These composite materials exhibit a large increase of dielectric

© 2018 IOP Publishing Ltd

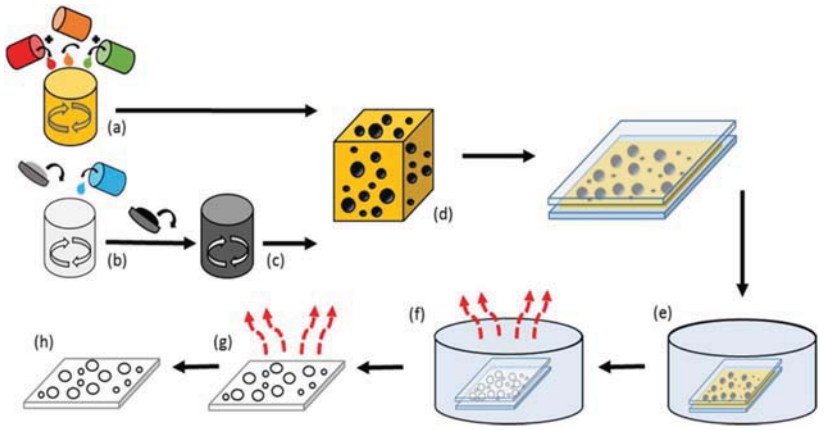


Figure 1. Scheme of the preparation of the microporous materials with pores covered by carbon black particles. (a) Preparation of the oil phase by mixing PDMS, curing agent, and surfactant. (b) Preparation of the water phase by mixing water and arabic gum. (c) Dispersion of black carbon powder in water phase. (d) Dispersion of water phase inside the oil phase. (e) Spreading of the emulsion between two surfaces and immersion in a water bowl. (f) The PDMS in the emulsion is cured by increasing the temperature of water. (g) Evaporation of the water by increasing the temperature outside the water bath. (h) Finally, a porous and dried composite is obtained.

permittivity in the vicinity of their percolation threshold but suffer from a weakness due to the substantial increase of losses near and above percolation [19, 20].

To overcome these limitations, we design a new bilayer structure based on a microporous dielectric layer associated with a thin insulating layer of polydimethyl siloxane (PDMS). Porous flexible materials of which the internal pores are covered with carbon black particles are prepared using a water-in-oil emulsion. This new composite possesses a high dielectric permittivity along with a very low conductivity. We show that the fabrication of the microporous dielectric layer using a water-in-oil emulsion provides a fine control of the location of the conductive inclusions. The latter remain confined in the emulsions droplets. The micropores significantly deform upon compression resulting in a large change of the dielectric permittivity [21]. As such, the porous dielectric material can be used in a variable-capacitance engine to harvest mechanical energy [22].The energy harvesting performance can be improved by combining the porous dielectric with a thin insulating layer of PDMS. This reduces the conductivity of the system, and allows an increase of the filler concentration above the percolation threshold in the high permittivity layer. The electrostrictive properties of the material can be finely tuned by varying the concentration of conductive particles. The presented bilayer structures exhibit high effective relative dielectric permittivity (up to 182 at 100 Hz) with a very low effective conductivity (down to $2.53 \cdot 10^{-8}$ S m^{-1}). They can generate electrical energy in response to mechanical vibrations with a power density of 0.4 μW cm^{-3}. The efficiency of electrostrictive materials for actual energy harvesting applications can be assessed by their so-called figure of Merit (FoM). FoM of the present materials exceeds the previous-best electrostrictive materials based on mixtures of fluorinated terpolymers and carbon black particles by a factor 1.7, and by almost four orders magnitude more conventional composites made of polyurethane and carbon black particles. They have also a low cost considering the components they are made of. In addition, considering their large flexibility (Young's modulus of about 1 MPa) and sensitivity of dielectric properties, the presented materials are well suited for capacitive sensors with high sensitivity.

2. Experimental details

2.1. Material synthesis

The emulsion consists of an aqueous solution of carbon black droplets dispersed in a matrix of PDMS and a curing agent. We used the following procedure (figure 1). The water phase is prepared by mixing 5 g of arabic gum (Sigma Aldrich) and 95 g of deionized water. The desired concentration of carbon black powder (Alfa Aesar) is added and the mixture is tip sonicated during 1 h at 400 W to homogeneously disperse the carbon black (CB) particles [20]. The oil phase is prepared by mixing PDMS (Dow Corning), the curing agent (Dow Corning, 10% in weight with respect to the PDMS phase), and the surfactant lauryl PEG-8 dimethicone (Silube J208-812, Siltech, 5.0 wt% of the final mixture). Note that composition of the curing agent is not divulgated but it is probably a mixture of dimethyl,methylhydrogen siloxane—dimethyl siloxane, dimethylvinyl terminated—dimethylvinylated and trimethylated silica—tetramethyl tetravinyl cyclotetra siloxane and ethyl benzene.

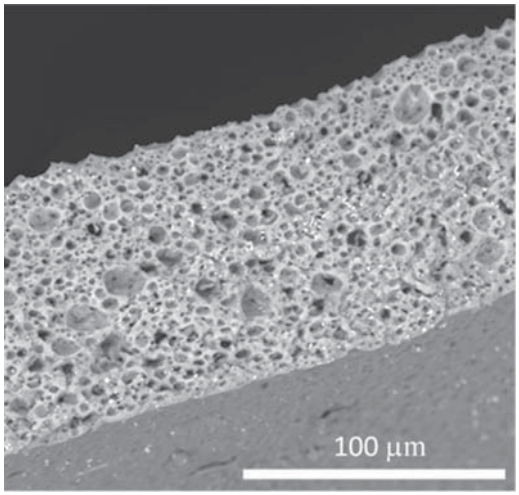


Figure 2. Electron microscope picture of a cross-cut of a porous carbon black composite.

The emulsion is prepared by progressively adding the carbon black solution to the oil phase under manual stirring up to a mass ratio of water:oil = 1:1. The mean droplet size depends on the viscosity of the continuous phase and ranges between 10–30 μm. The water-in-oil emulsion loaded with carbon black particles is spread with a stencil that has a depth of 500 μm on a plastic surface with a diameter of 24 mm. A second plastic surface is placed on the spread emulsion such that the emulsion remains confined between two flat surfaces. Solid materials are obtained by curing the PDMS polymer without evaporation in a warm water bowl (90 °C) for 4 h. The relative humidity in these conditions is 100%. Then, the solid material layer is removed from the two plastic surfaces and dried in an oven for 1 h at 150 °C. As PDMS is permeable to water vapor, droplets from carbon black solution dried and leave a structure with spherical-shaped pores covered by carbon black particles (figure 2). Curing and drying are critical stages which strongly influence the final morphology of the porous composite.

2.1.1. Isolating layer deposition

To decrease the dielectric losses, the microporous materials are combined with a thin insulating layer of PDMS. The insulating layer is spin coated on conductive aluminum substrates with a diameter of 24 mm. For the spin-coating, 3 g of PDMS with a curing agent (10% in weight with respect to the PDMS phase) is deposited at rest on an aluminum substrate. Then a spin-coater is used at 8000 rpm for 60 s at an acceleration of 1000 rpm s^{-1} to obtain a thickness of the PDMS layer of 5 μm. The aluminum substrate covered by the PDMS layer is then soft baked at 100 °C for 30 min to cure the PDMS. The thickness of the layer is measured by a mechanical profilometer (Dektak 150) after scratching the surface.

Note that in the following experiments, the micro porous layers are simply held in contact with the insulating layer which is deposited onto an aluminium substrate. However, it is possible to spin coat an insulating film on our materials. We have recovered a micro porous material with a five microns thick film of PDMS and curing agent. The comprehensive system has been cured at 100 °C for 30 min.

2.2. Determination of the dielectric properties

We measure the electrical conductivity and dielectric permittivity of the samples between two metallic disc electrodes in the frequency range of 10–10^6 Hz under an applied voltage of 1 V using an impedance analyzer (Bio-Logic Impedance Analyser, MTZ-35). A calibration procedure removing the contribution of the polarization of the electrodes is used to determine the dielectric permittivity and the conductivity of the sample as a function of frequency [16]. All the experiments are performed at room temperature.

2.3. Determination of the electromechanical performances

To determine the electrostrictive properties of the composites we use the experimental setup illustrated in figure 3, which consists of a piezoelectric actuator (Physik Instrumente P-842.30) driven by a function generator (Keysight 33611A Waveform Generator) that applies a sinusoidal mechanical strain at a frequency of 100 Hz. The sample is placed between two electrodes: the top electrode is connected to the piezo actuator and moves at the same frequency as the actuator, the bottom electrode is fixed to the sample holder and does not move. As such, a modulated strain is applied along the thickness of the material. The strain is controlled by a computer

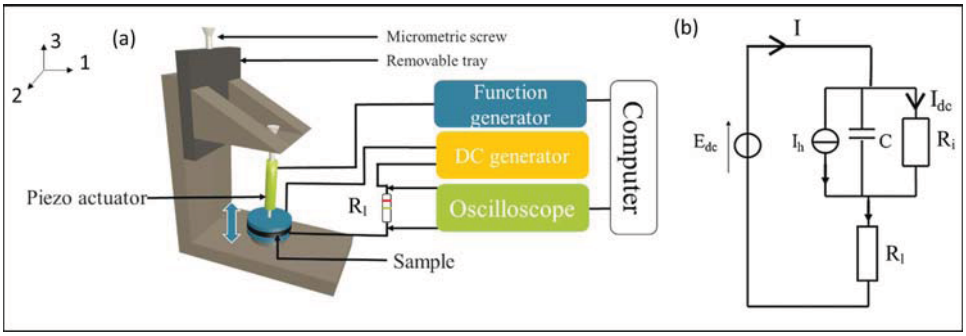


Figure 3. Schematic of the experimental setup (a) and the equivalent electric circuit (b).

linked to a function generator which controls the stroke of the actuator. An electric field E_{dc} is applied to the composite along the height (3-direction in figure 3) by a DC generator. To measure the current and generated power, a load resistance (R) is connected in series with the sample. The voltage U_R over the resistance is recorded by an oscilloscope (Keysight InfiniiVision 1000 X) and the current is determined using the Ohm's law ($I = U_R/R_l$).

The Young's modulus of the composites is measured using a tensile tester (Instron Model 4505). The initial dimensions (width and thickness) are measured before mounting the sample between the fixed and moving jaws. The force-displacement responses are acquired for each sample at a displacement rate of 0.067 mm s^{-1}. The tests ended when the specimens fractured. The Young's modulus is determined by measuring the slope of stress–strain curves in the elastic domain.

The composite material is modeled by a parallel RC circuit (see figure 3(b)). The observed current is composed of two parts: a leakage current I_{dc} and a harvested current I_h induced by compression-decompression cycles of the composite. According to the model developed by Guyomar *et al* [23, 24], for a sinusoidal strain the current I_h through a load resistance R_l is given by (see supporting information is available online at stacks.iop.org/MFM/0/000000/mmedia)

$$I_h(t) = \frac{2M_{33}{}^*YE_{dc}\omega AS}{1+\left(\frac{\omega AR_l\varepsilon\varepsilon_0}{d}\right)^2}\left[\frac{\omega AR_l\varepsilon\varepsilon_0}{d}\sin(\omega t) + \cos(\omega t)\right] \quad (1)$$

Here, A is the area of the sample, Y is the Young's modulus, $M_{33}{}^*$ is the apparent electrostrictive coefficient [15], E_{dc} is the applied bias electric field ($E_{dc} = 32$ V), S is the sinusoidal strain amplitude equaling the displacement induced by the piezo actuator (24 μm) divided by two times the material thickness, ε is the relative dielectric permittivity, ε_0 is the vacuum permittivity, d is the material thickness, and ω is the angular frequency of the applied strain. Hence, a linear relation between I_h and E_{dc} is obtained for a constant strain, frequency, and load resistance. As a result, the product $M_{33}{}^*Y$ can be easily estimated from the slope of the I-E_{dc} curves. The apparent electrostrictive coefficient $M_{33}{}^*$ is calculated by division of the Young's modulus Y. In the following, in presence of an insulating film, $M_{33}{}^*$ will be an effective coefficient. It will average the properties of the material and those of the insulating film.

3. Results

3.1. Polymer-carbon black composites

The dielectric properties of the polymer/carbon black composite, without insulating layer, are first studied at rest. The load fraction of carbon black particles inside composites is varied while keeping the oil:water ratio constant. Figure 4 shows the electrical conductivity, dielectric permittivity, and loss tangent ($\tan(\delta) = \frac{\sigma}{\varepsilon_0\varepsilon\omega}$, with σ the electrical conductivity) as a function of the frequency for different carbon black particle concentrations.

Both conductivity and dielectric permittivity increase as a function of CB concentration. The percolation threshold is reached for a weight fraction of 6%. Below the percolation threshold, the conductivity is frequency dependent and arises from dielectric losses due to bound charges. In the meantime, the dielectric permittivity remains constant for the full range of investigated frequencies. Above the percolation threshold, and at low frequencies, the conductivity is constant because essentially due to the transport of free charges brought by the carbon black particles. By contrast, the dielectric permittivity presents frequency dependence and is enhanced by

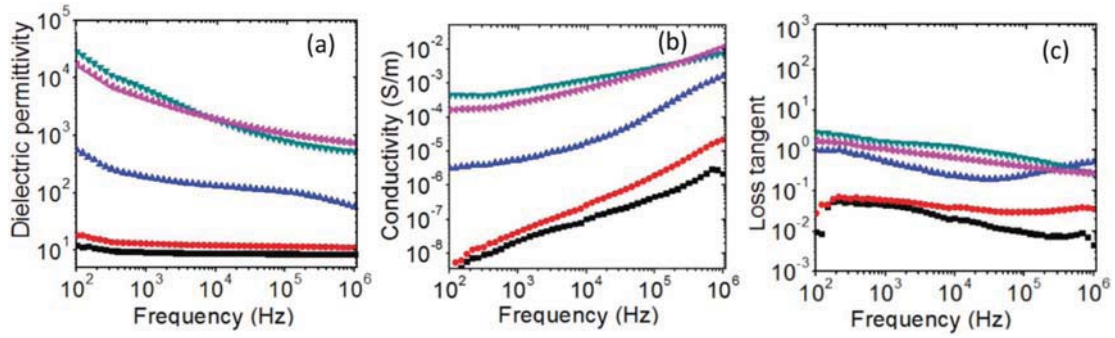


Figure 4. (a) Evolution of the dielectric permittivity (a), conductivity (b) and loss tangent (c) as a function of the frequency for various CB particle concentrations. 3.0 wt% (black squares), 4.0 wt% (red circles), 6.0 wt% (purple top triangles), 8.0 wt% (green down triangles), 10 wt% (pink left triangles)Phase fractions are fixed: oil:water = 1:1.

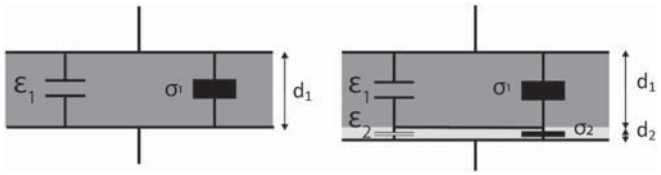


Figure 5. Equivalent electric circuits for the porous black carbon (a) and the bilayer (b) composite. ε_i, σ_i and d_i are the dielectric permittivity, the conductivity, and the thickness of the layer i, respectively.

Table 1. Properties of the carbon black (CB) composites.

% CB	CB (g L^{-1})	Thickness (μm)
3	31	500
4	42	510
6	64	510
8	87	750
10	110	800

the interfacial polarization of the carbon black particles. In the high filler concentration regimes, the values of conductivity (above 10^{-6} S m^{-1}) make the materials unsuitable for vibrational energy harvesting.

3.2. Bilayer polymer-carbon black composites

The high conductivity (free charges carriers and dielectric loss) of the carbon black composites is a drawback for energy harvesting applications [24]. Indeed, such applications do not allow any leakage for yielding a positive energy conversion. In this paper, we propose an original approach for keeping high values of effective dielectric permittivity and low values of conductivity by associating a thin insulating layer to the high permittivity layer. This layer has low dielectric losses and no free charge carriers. It acts as a blocking layer and prevents leaks of the capacitors (figure 5).

The electrical equivalent circuit for a bilayer material is a junction of two RC circuits in series. The expressions for the effective dielectric properties of the bilayer structure are given in the supporting information. The effective conductivity and dielectric constant of the bilayer structure depend on the thicknesses and dielectric properties of both layers. The blocking layer 2 is a cured PDMS layer ($\varepsilon_{PDMS} = \varepsilon_2 = 2$ and $\sigma_2 = 10^{-13}$ S m^{-1} in the range 10–10^6 Hz at 25 °C) of thickness 5 μm. The high permittivity layer 1 is the porous carbon black material layer ($\varepsilon_1 \gg \varepsilon_2$ and $\sigma_1 \ll \sigma_2$) of variable thickness depending on carbon black concentration (see table 1).

For comparison, we investigate the dielectric properties of the electrostrictive composites at rest with and without insulating layer. Figure 6 shows the relative dielectric permittivity, electrical conductivity, and loss tangent at 100 Hz as a function of the carbon black concentration. First, we consider the electrostrictive composites *without* insulating layer. At carbon black concentrations below the percolation threshold (~5 wt%),

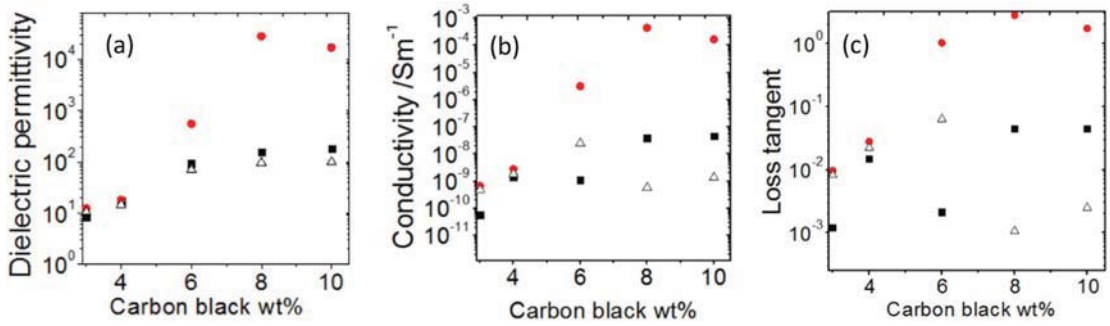


Figure 6. Effective dielectric properties at 100 Hz of the porous carbon black layer (red circles), bilayer polymer—carbon black composites (black squares), and theoretical predictions of the latter (open black triangles), as a function of carbon black concentration.

the dielectric permittivity has a nearly constant value of ~10 with an electric conductivity of ~1 nS m^{-1}. Above the percolation threshold, the dielectric permittivity rapidly increases to 550 at 6 wt%. However, the electrical conductivity also increases by a factor of 10^3, leading to a loss tangent above 1. A further addition of conductive carbon black particles enhances the interfacial polarization, which leads to an increase in permittivity but also leads to further increase of the electrical conductivity to 0.6 mS m^{-1} at ~8 wt%. Such a high conductivity does not allow the efficient use of the materials as a dielectric layer in variable capacitors.

The effective dielectric properties of the electrostrictive composites *with* an insulating layer are very different at carbon black concentrations above the percolation threshold. The PDMS layer limits the electric conductivity below 1–10 nS m^{-1}. The insulating layer also leads to a decrease of the effective dielectric permittivity to 157 and 182 for the 8 and 10 wt% black carbon weight fractions, respectively. However, the obtained dielectric loss tangents are very low with $1.5 \cdot 10^{-2}$ and $2.5 \cdot 10^{-2}$ for the 8 and 10 wt% carbon black systems, respectively, making them well suited for energy harvesting applications. Theoretical calculations of the conductivity (see supporting information) predict values slightly lower than the ones found experimentally, probably as a result of small holes and defects in the insulating PDMS layer.

Let us stress, that the materials with insulating film are a new concept. The properties of the porous material highly depend upon the materials synthesis protocol in the vicinity of the percolation transition. A 5% carbon black particles sample without insulating film may in principle have the same properties than a 8% material with an insulating layer. However, we note that the conductivity of the 5% carbon black particles sample depends a lot upon the preparation conditions. 2 orders of magnitude of variation have been measured on two different samples from two different batches. Using an insulating film allows us to prepare materials with reproducible properties. 20% of variations have been measured on two different sample from two different batches with an insulating film.

3.3. Electromechanical performances and power harvested estimation

We now investigate the performance of the bilayer composites for energy harvesting purposes. First, the electromechanical performances are assessed by calculating the figure of merit (FoM) proposed by Guyomar *et al* [23, 24]:

$$\mathrm{FoM} = \left(\frac{2\pi}{\varepsilon_r}\right)(M_{33}{}^{*}Y)^2 \quad (\mathrm{J\ m^{-1}\ V^{-2}\ cycle^{-1}}) \tag{2}$$

The FoM depends only on materials properties ($M_{33}{}^{*}$, Y, ε_r) and aims at comparing electromechanical performances of materials without any external parameters such as geometry and measurement details. Three compositions (6, 8, and 10 wt%) are used for performances comparisons (table 2). Properties of the materials are reported in table 2. FoM, $M_{33}{}^{*}$ and Y are measured using the methods described in the experimental section.

3.4. Determination of the harvested power

Next, we examine the power generation properties of the bilayer composites by discharge over a load resistance R_l. As shown in figure 7, the voltage drop over the resistance U_r and the instantaneous harvested power are monitored as a function of time. The average harvested power per cycle $\overline{P}$ is calculated using

$$\overline{P} = \frac{1}{T}\int_0^T P(t)\,\mathrm{d}t = \frac{1}{R_l\,T}\int_0^T U_r(t)^2\,\mathrm{d}t, \tag{3}$$

where T is the period of the cycle.

Table 2. Bilayers composite properties. $M_{33}{}^*$ is measured at 100 hertz. The thickness refers to the thickness of the porous material. The thickness of the film is 5 microns for all the samples.

% CB	Oil fraction	CB (g L^{-1})	Thickness (μm)	Surface (m^2)	$M^* Y$	Y(MPa)	$M_{33}{}^*$ (m^2 V^{-2})
6.0	0.5	$6.4 \cdot 10^1$	$5{,}1 \cdot 10^2$	$1.1 \cdot 10^{-3}$	$2.2 \cdot 10^{-10}$	1,38	$1{,}60 \cdot 10^{-16}$
8.0	0.5	$8{,}7 \cdot 10^1$	$7.5 \cdot 10^2$	$6.2 \cdot 10^{-4}$	$1.5 \cdot 10^{-9}$	1,40	$1{,}07 \cdot 10^{-15}$
10.0	0.5	$1.1 \cdot 10^2$	$8.0 \cdot 10^2$	$1.0 \cdot 10^{-3}$	$3.6 \cdot 10^{-9}$	1,61	$8{,}46 \cdot 10^{-15}$

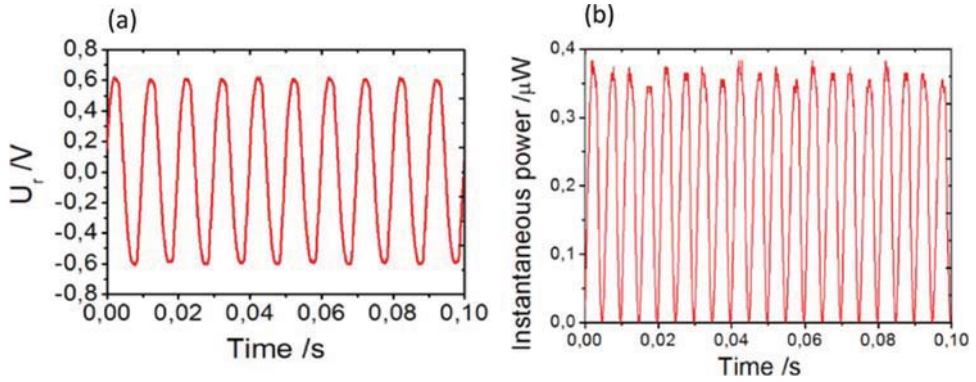


Figure 7. The voltage difference (a) and instantaneous power (b) across a load resistance of 1 MΩ for a 100 Hz sinusoidal strain. The applied bias voltage over the bilayer composite with 8 wt% carbon black is 32 V.

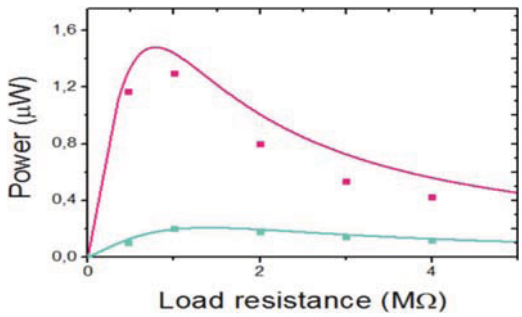


Figure 8. Harvested power of the composites with 8 CB wt% (green) and 10 CB wt% (pink) with insulating layer as a function of the load resistance. Squares are experimental data and lines are theoretical predictions using equation (7). The strain frequency is 100 Hz and the applied voltage over the composite $V_{dc} = 32$ V.

Q1

The theoretical harvested power is given by (see supporting information)

$$\overline{P_{\text{th}}} = \frac{R_l}{2} \frac{(2\, M_{33}{}^* Y)^2 E_{dc}{}^2 \omega^2 A^2 S^2}{1 + \left(\frac{R_l A \varepsilon_0 \varepsilon\, \omega}{d}\right)^2}, \tag{4}$$

where $\omega = 2\pi/T$.

Figure 8 shows the value of the theoretical and experimental power harvestable as a function of the load resistance. Best values are obtaining for a load resistance of about 1 M for both materials, which corresponds to the resistance with optimal power production $\left(R_{l,\,\max} = \frac{d}{A\varepsilon\varepsilon_0\omega}\right)$. Good agreement is observed between the experimental data and theoretical powers. In addition, the increase in FoM by a factor 5 between 8 CB wt% and 10 CB wt% leads to an increase in harvested power by a factor 6.

3.5. Efficiency

To get a positive energy balance, the dissipated power must be smaller than the harvested power. The dissipated power for maintaining a polarization of the composite is given by [24]:

Table 3. Efficiency of the bilayer composites for different carbon black concentrations.

% CB	Harvested power (μW)	Power loss (μW)	Net power production (μW)	Electrical gain factor
8.00	0.20	0.12	0.08	1.74
10.0	1.3	1.0	0.3	1.31

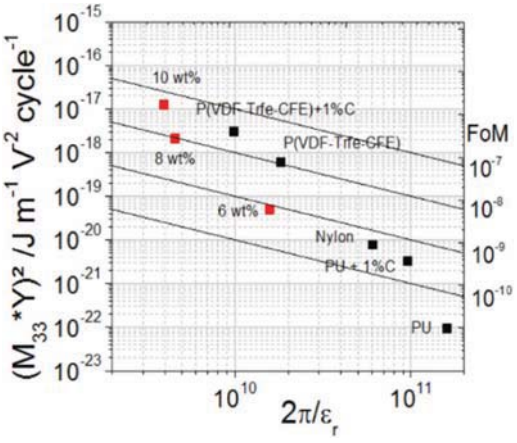


Figure 9. Comparison of the electromechanical performances at 100 Hz using the figure of merit (FoM) proposed by Guyomar *et al* [23, 24]. Thick lines have the same FOM. Black spots refer to materials from the literature [23, 24].

$$P_{\text{loss}} = R_l \left(\frac{V_{dc}}{R_i + R_l} \right)^2 \tag{5}$$

where R_i is the internal leak resistance, R_l is the load resistance values, and V_{dc} is the applied voltage difference. The internal leak resistance is calculated by $R_i = \frac{d}{\sigma A}$ with the geometrical data from table 2. The electrical energy gain is calculated by considering the ratio of power harvestable to electrical polarization losses for a bias voltage of $V_{dc} = 32$ V and a load resistance of $R_l = 1$ MΩ.

4. Discussions

The use of an insulating layer limits the electric conductivity below 1–10 nS m^{-1} and allows us to use our materials for energy harvesting. Data given in table 3 show that the energy balance is largely positive for both materials. The power produced by the mechanical-electrical conversion for the 8 wt% composite is 1.74 times higher than the power dissipated to polarize it and the net power harvestable is around 0.17 W m^{-3}. We can see that increasing the CB wt% enables to increase the net harvested power by almost a factor 4, i.e. up to 0.38 W m^{-3}. This is a consequence of the increase of permittivity of the material at 10 wt%. But at the same time, the conductivity of the 10 wt% composite is 1.9 higher than that of the 8 wt% composite which has a conductivity of $1.30 \cdot 10^{-8}$ S m^{-1}; leading to a net decrease in the energy balance, but to an increased overall power production. These excellent performances can be explained by the porous structure of the materials and insulating properties of the thin polymer layer. As a result, the electric field required to polarize the material is decreased, which is crucial for vibrational energy harvesting applications.

Figure 9 presents the FoM of materials from the literature, and of composites developed in this work. The values of the FOM are enhanced by increasing the filler concentration. For 10 wt% CB, the FoM is equal to $5.06 \cdot 10^{-8}$ J m^{-1} V^{-2} cycle^{-1}. This result exceeds the previous-best electrostrictive materials based on a mixture of Polyvinylidene fluoride (PVDF) terpolymers and carbon black by a factor 1.7. In addition, it outperforms in term of process and material cost and toxicity [21, 22]. Increasing the FoM is a key point for increasing the power harvestable as we show below. Besides, their low Young's modulus compared to PVDF polymers (~GPa) could enlarge the scope of applications using low stress vibrations.

Note that same behaviour has been measured at 10 hertz. M_{33} is greater by a factor of 2 to 5 at this frequency for all the samples. The use of a sweeping frequency excitation will be considered in a further work.

5. Conclusions

We presented microporous electrostrictive composites with improved properties for vibrational energy harvesting. These systems are made of carbon black particles dispersed in a porous PDMS matrix. An inverted emulsion templating approach provides a fine control of the location of the particles which is a key factor to achieve high permittivity and low losses. A thin insulating layer was added to limit further the losses. The resulting structure possesses a very large effective relative dielectric permittivity of 182 at 100 Hz in combination with a very low loss tangent of $2.5 \cdot 10^{-2}$. We succeeded in evaluating the energy scavenging abilities of these composites. More than 300 nW has been harvested with the 10 wt% carbon black composites which leads to a power density of 0.4 μW cm^{-3}. The present materials exhibits a figure of merit as high as $5.06 \cdot 10^{-8}$ J m^{-1} V^{-2} cycle^{-1} which is 1.7 times higher than the best reference fluorinated polymers and 3350 times higher than pure polyurethane [21]. The low cost process and low toxicity make the carbon black bilayer composites very promising materials for vibrational energy harvesting. The power harvested with our materials is good enough to provide a significant boost to the battery life of ultra-low power devices. For example, the Phoenix processor [25, 26] has a sleep power consumption of only 30 pW and 200 nW in active mode which makes our materials suitable for this application. In addition, these carbon black bilayer composites, with excellent dielectric properties, could find potential applications as low cost flexible capacitors sensors in the printed electronics industry.

Acknowledgments

We acknowledge financial support from the following organisms and projects: Université de recherche Paris Sciences et Lettres, the Université Pierre et Marie Curie, ANR Project ANR-12-NANO-0002 ELENA, and ANR in the Cluster of Excellence AMADEUS.

ORCID iDs

Annie Colin https://orcid.org/0000-0001-8372-006X

References

[1] Gubbi J, Buyya R, Marusic S and Palaniswami M 2013 Internet of things (IoT): a vision, architectural elements, and future directions *Future Gener. Comput. Syst.* **29** 1645–60
[2] Xia F, Yang L T, Wang L and Vinel A 2012 Internet of things *Int. J. Commun. Syst.* **25** 1101–2
Q2 [3] Brogioli D 2009 Extracting renewable energy from a salinity difference using a capacitor *Phys. Rev. Lett.* **103**
[4] Janssen M, Härtel A and van Roij R 2014 Boosting capacitive blue-energy and desalination devices with waste heat *Phys. Rev. Lett.* **113**
[5] Dutoit N E, Wardle B L and Kim S-G 2005 Design considerations for mems-scale piezoelectric mechanical vibration energy harvesters *Integr. Ferroelectr.* **71** 121–60
[6] Sodano H A, Inman D J and Park G 2004 A review of power harvesting from vibration using piezoelectric materials *Shock Vib. Dig.* **36** 197–205
[7] Anton S R and Sodano H A 2007 A review of power harvesting using piezoelectric materials (2003–2006) *Smart Mater. Struct.* **16** R1–21
[8] Yan Y, Zhou J E, Maurya D, Wang Y U and Priya S 2016 Giant piezoelectric voltage coefficient in grain-oriented modified PbTiO3 material *Nat. Commun.* **7** 13089
[9] Fan F R, Tang W and Wang Z L 2016 Flexible nanogenerators for energy harvesting and self-powered electronics *Adv. Mater.* **28** 4283–305
Q3 [10] Guillon O, Thiebau F and Perreux D 2002 Tensile fracture of soft and hard PZT *Int. J. Fract.* (https://doi.org/10.1023/A:1022072500963)
[11] Wang Z L 2014 Triboelectric nanogenerators as new energy technology and self-powered sensors—principles, problems and perspectives *Faraday Discuss.* **176** 447–58
[12] Nguyen V and Yang R 2013 Effect of humidity and pressure on the triboelectric nanogenerator *Nano Energy.* **2** 604–8
[13] Jaaoh D, Putson C and Muensit N 2016 Enhanced strain response and energy harvesting capabilities of electrostrictive polyurethane composites filled with conducting polyaniline *Compos. Sci. Technol.* **122** 97–103
[14] Yin X, Capsal J-F and Guyomar D 2014 A comprehensive investigation of poly(vinylidene fluoride-trifluoroethylene-chlorofluoroethylene) terpolymer nanocomposites with carbon black for electrostrictive applications *Appl. Phys. Lett.* **104** 052913
[15] Luna A, Pruvost M, Yuan J, Zakri C, Neri W, Monteux C, Poulin P and Colin A 2017 Giant electrostrictive response and piezoresistivity of emulsion templated nanocomposites *Langmuir* **33** 4528–36
[16] Luna A, Yuan J, Néri W, Zakri C, Poulin P and Colin A 2015 Giant permittivity polymer nanocomposites obtained by curing a direct emulsion *Langmuir* **31** 12231–9
[17] Yuan J, Luna A, Neri W, Zakri C, Schilling T, Colin A and Poulin P 2015 Graphene liquid crystal retarded percolation for new high-k materials *Nat. Commun.* **6** 8700
[18] Li J Y, Huang C and Zhang Q 2004 Enhanced electromechanical properties in all-polymer percolative composites *Appl. Phys. Lett.* **84** 3124–6
[19] Yin X, Lallart M, Cottinet P-J, Guyomar D and Capsal J-F 2016 Mechanical energy harvesting via a plasticizer-modified electrostrictive polymer *Appl. Phys. Lett.* **108** 042901

[20] Parant H, Muller G, Le Mercier T, Tarascon J M, Poulin P and Colin A 2017 Flowing suspensions of carbon black with high electronic conductivity for flow applications: comparison between carbons black and exhibition of specific aggregation of carbon particles *Carbon* **119** 10–20
[21] Jones S B and Friedman S P 2000 Particle shape effects on the effective permittivity of anisotropic or isotropic media consisting of aligned or randomly oriented ellipsoidal particles *Water Resour. Res.* **36** 2821–33
[22] Boisseau S, Despesse G and Ahmed B 2012 Electrostatic conversion for vibration energy harvesting ed M Lallart *Small-Scale Energy Harvest.* (Rijeka: InTech) (http://intechopen.com/books/small-scale-energy-harvesting/electrostatic-conversion-for-vibration-energy-harvesting) (accessed September 27, 2017)
[23] Lallart M, Cottinet P-J, Lebrun L, Guiffard B and Guyomar D 2010 Evaluation of energy harvesting performance of electrostrictive polymer and carbon-filled terpolymer composites *J. Appl. Phys.* **108** 034901
[24] Cottinet P-J, Guyomar D, Guiffard B, Putson C and Lebrun L 2010 Modeling and experimentation on an electrostrictive polymer composite for energy harvesting *IEEE Trans. Ultrason. Ferroelectr. Freq. Control* **57** 774–84
[25] Hanson S, Seok M, Lin Y-S, Foo Z, Kim D, Lee Y, Liu N, Sylvester D and Blaauw D 2009 A low-voltage processor for sensing applications with picowatt standby mode *IEEE J. Solid-State Circuits* **44** 1145–55
Q4 [26] Jayakumar H, Lee K, Lee W S, Raha A, Kim Y and Raghunathan V 2014 *Powering the Internet of Things* (ACM Press) pp 375–80
[27] Raicu V and Feldman Y (ed) 2015 *Dielectric Relaxation in Biological Systems: Physical Principles, Methods, and Applications* 1st edn
Q5 (Oxford, United Kingdom: Oxford University Press)

MICKAËL PRUVOST

130 rue Hoche
Apt C022
94200 Ivry sur Seine

+33 6 16 02 10 48

pruvost.mickael@gmail.com

@ Mickaël PRUVOST

Formations

2015-2018 PARIS
Ecole supérieure de physique et de chimie de la ville de Paris (ESPCI Paris)
Etudiant doctorant (bac+8)
Université : Paris Sciences et Lettres
Laboratoire : Science et ingénierie de la matière molle (SIMM)
Sujet: Formulation de matériaux electrostrictifs pour la récupération d'énergie vibratoire et le développement de capteurs cardiaques.
Mots clés: Electrostriction-composites-récupération d'énergie vibrationnelle-diélectrique-émulsion-capteurs de pression cardiaque.

2015 MONTREAL
Ecole Polytechnique de Montréal
Echange étudiant, études en génie chimique et management de la R&D

2012-2015 PARIS
Ecole nationale supérieure de chimie de Paris (Chimie ParisTech)
Diplôme d'ingénieur chimiste (bac+5)
Cours (60%) et travaux pratiques (40%) en chimie organique, chimie des matériaux, chimie analytique et physique, risques chimiques et génie chimique.

2010-2012 LILLE
Ecole nationale supérieure de chimie de Lille
Classe préparatoire intégrée aux écoles de chimie (bac+2)

Expériences

02/15 – 08/15 Stagiaire ingénieur
L'Oréal – PARIS
Mission en développement hygiène douche.
Sujet : Optimisation de formulations en termes de performance et coûts
Compétences: plans d'expériences – caractérisation de la mousse – caractérisation sensorielle- mesures de viscosité- chimie des tensio-actifs.

03/14 - 08/14 Stagiaire ingénieur
BASF – BASEL (SWITZERLAND)
Mission en R&D,
Sujet : développement de nouveaux matériaux pour les photodiodes organiques
Compétences : formulation d'encres pour l'impression de photodiodes organiques, optimisation des réponses spectrales.

07/13 - 08/13 Stagiaire ouvrier
SANOFI – PARIS
Mise en place d'un nouvel outil de gestion sur ligne de conditionnement

08/12 - 09/12 Stagiaire ouvrier
BRIDGESTONE – LILLE
Développement d'une base de données matières premières

08/11 - 09/11 Stagiaire ouvrier
KEEP – TOKYO
Serveur dans un hôtel restaurant

Emplois

2017- 2018
Solvay – MISSION DOCTORALE
Réalisation de matériaux electrostrictifs.

2016-2017 **ESPCI Paris - MISSION DOCTORALE**
Encadrement de travaux pratiques de thermodynamiques (70h)

2015-2018 **PROFESSEUR**
Cours particuliers de chimie et mathématiques

08/14 - 09/14 **PAUL – Gare de Lyon**
Employé polyvalent

07/12 **CENTRE HOSPITALIER**
Brancardier en radiologie

Compétences

Langues
ANGLAIS : Compétences professionnelles complètes (TOEIC:920)
ALLEMAND : Niveau scolaire

Permis B

Brevet de secourisme

Sujets qui me préoccupent :
Environnement, Cuisine, Arts, Voyages

Publications et brevets

2018 Microporous electrostrictive materials for vibrational energy harvesting. Multifunct. Mater. 00 (2018) 000000

2018 « Structured composites useful as low force sensors », 4 brevets, USA, Europe, Japon.

2017 Giant electrostrictive response and piezoresistivity of emulsion templated nanocomposites, Apr 20, 2017, Langmuir

2017 « CONVERTISSEUR D'ENERGIE VIBRATIONNELLE »
Brevet France n° 17 53184, extension Europe demandée.

Conférences

2016-2017
- GDR polynano, Juin 2016, Paris
- Soft Matter days, Juin 2017, Paris
- European Polymer Congress, Juillet2017, Lyon, KEYNOTE LECTURE
- European Advanced Materials Congress, Août 2017, Stockolm
- European Materials Research Society, Septembre 2017, Warsaw

Autoformations

2016-2017
- "Carbones et matériaux carbonés : du design aux applications », Clément Sanchez, Collège de France
- "Électrochimie appliquée : les différents systèmes de batteries", Jean-Marie Tarascon, Collège de France
- Séminaire résidentiel: « valorisez la recherche par la création d'entreprise", Cnano IDF

Résumé

L'objectif de ces travaux de thèse est de mettre à profit la matière molle pour le développement de matériaux composites électrostrictifs en vue de leur utilisation à des fins de récupération d'énergie vibrationnelle et de capteurs de pression haute sensibilité. Une approche par voie émulsion est proposée pour la réalisation de composites afin d'incorporer des particules conductrices telles que feuillets de graphène ou des particules de noir de carbone dans une matrice polymère élastique faite de polydimethylsiloxane (PDMS). Cette approche originale permet de contrôler la dispersion des charges et la microstructure des composites. Les propriétés diélectriques de ces matériaux sont contrôlées par le type de charges, leur concentration et leur voie de dispersion. L'optimisation de leviers de formulation permet d'atteindre des valeurs de permittivité diélectrique très élevées (ε_r'≈182 à 100 Hz) pour des composites polymères. Les matériaux développés au cours de ces travaux ont été utilisés avec succès dans des dispositifs de récupération d'énergie vibrationnelle. En combinaison avec une couche isolante, les structures étudiées présentent une permittivité diélectrique relative effective élevée avec une très faible conductivité effective (jusqu'à 2,53 10^{-8} $S.m^{-1}$). Nous avons développé un dispositif expérimental permettant de mesurer l'électrostriction des matériaux et de quantifier la génération d'énergie électrique en réponse à des vibrations mécaniques. Une densité de puissance de 0,38 $W.m^{-3}$ a été mesurée pour des excitations mécaniques de 100 Hz. Pour l'utilisation en conditions réelles des matériaux électrostrictifs et leur utilisation en récupérateur d'énergie mécanique ambiante, nous les avons intégrés dans des structures vibrantes de poutre en porte-à-faux. Grâce à la flexibilité de ces structures et à leur faible fréquence de résonnance, nous avons réussi à récupérer 0.4 $W.m^{-3}$ pour une excitation mécanique de 25 Hz. Dans la dernière partie de nos travaux, nous avons porté notre attention sur les capteurs de pression haute sensibilité, nécessaire pour la surveillance cardiaque à long terme et pour l'interaction naturelle des robots avec les humains. Nous démontrons que nos matériaux composites électrostrictifs peuvent être intégrés dans ces capteurs de pression souple. Les performances rapportées en termes de sensibilité à la pression sont au-dessus de celles de la littérature. Nous illustrons les performances de nos matériaux en réussissant à les utiliser pour enregistrer de manière continue et non invasive des ondes de pouls d'une artère radiale.

Mots Clés :

Electrostriction-composites-récupération d'énergie vibrationnelle-diélectrique-émulsion-capteurs de pression

Abstract

The goal of this thesis is to leverage soft matter for the development of electrostrictive composite materials for use in vibrational energy recovery and high sensitivity pressure sensors. An emulsion approach is proposed for making composites and incorporating conductive particles such as graphene foils or carbon black particles into an elastic polymeric matrix made of polydimethylsiloxane (PDMS). This original approach allows controlling the dispersion of the charges and the microstructure of the composites. The dielectric properties of these materials are controlled by the type of charges, their concentration and their dispersion path. Optimization of formulation levers makes it possible to achieve very high dielectric permittivity values (ε_r'≈182 at 100 Hz) for polymer composites. The materials developed during this work have been used successfully in vibrational energy recovery devices. In combination with an insulating layer, the studied structures have a high effective relative dielectric permittivity with a very low effective conductivity (up to 2,53 10^{-8} $S.m^{-1}$). We have developed an experimental device to measure the electrostriction of materials and to quantify the generation of electrical energy in response to mechanical vibrations. A power density of 0.38 W m^{-3} was measured for mechanical excitations of 100 Hz. For real-life use of electrostrictive materials and their use as an ambient mechanical energy harvester, we incorporated them into vibrating beam structures cantilevered. Thanks to the flexibility of these structures and their low resonance frequency, we managed to recover 0.4 $W.m^{-3}$ for a mechanical excitation of 25 Hz. In the last part of our work, we focused our attention on high sensitivity pressure sensors, necessary for long-term cardiac monitoring and for the natural interaction of robots with humans. We demonstrate that our electrostrictive composite materials can be integrated into these flexible pressure sensors. The reported performance in terms of pressure sensitivity is above that of the literature. We illustrate the performance of our materials by successfully using them to continuously and non-invasively record the pulse waves of a radial artery.

Keywords:

Electrostriction-composites-vibrational energy recovery-dielectric-emulsion-pressure sensors